high cycle fatigue behavior of additive manufactured stainless steel 316L : free surface effect and microstructural heterogeneity

Xiaoyu Liang

▶ **To cite this version:**

Xiaoyu Liang. high cycle fatigue behavior of additive manufactured stainless steel 316L : free surface effect and microstructural heterogeneity. Materials. HESAM Université, 2020. English. NNT : 2020HESAE017 . tel-02951486

HAL Id: tel-02951486
https://theses.hal.science/tel-02951486

Submitted on 28 Sep 2020

HAL is a multi-disciplinary open access archive for the deposit and dissemination of scientific research documents, whether they are published or not. The documents may come from teaching and research institutions in France or abroad, or from public or private research centers.

L'archive ouverte pluridisciplinaire **HAL**, est destinée au dépôt et à la diffusion de documents scientifiques de niveau recherche, publiés ou non, émanant des établissements d'enseignement et de recherche français ou étrangers, des laboratoires publics ou privés.

HESAM UNIVERSITÉ

Arts et Métiers Sciences et Technologies

ÉCOLE DOCTORALE SCIENCES DES MÉTIERS DE L'INGÉNIEUR
[LAMPA – Campus de Angers]

THÈSE

présentée par : **Xiaoyu LIANG**

soutenue le : **09 Juillet 2020**

pour obtenir le grade de : **Docteur d'HESAM Université**

préparée à : **École Nationale Supérieure d'Arts et Métiers**

Spécialité : **Mécanique-Matériaux**

High cycle fatigue behavior of additive manufactured stainless steel 316L: free surface effect and microstructural heterogeneity

THÈSE dirigée par :
Prof. MOREL Franck

et co-encadrée par :
Dr. ROBERT Camille et Dr. HOR Anis

Jury

Mme. Catherine MABRU, Professeure des Universités, ISAE-SUPAERO	Présidente
M. Eric CHARKALUK, Directeur de Recherche CNRS, Ecole Polytechnique	Rapporteur
M. Yves NADOT, Professeur des Universités, ISAE ENSMA	Rapporteur
M. Mehdi SALEM, Ingénieur de Recherche, Ecole des Mines d'Albi-Carmaux	Examinateur
M. Franck MOREL, Professeur des Universités, Arts et Métiers - Centre d'Angers	Examinateur
M. Camille ROBERT, Ingénieur de Recherche, Arts et Métiers - Centre d'Angers	Examinateur
M. Anis HOR, Maître de Conférence, ISAE-SUPAERO	Examinateur
M. Luis REIS, Professeur, University of Lisbon	Invité

THÈSE

Acknowledgement

Firstly, I would like to express my deepest gratitude to my supervisor Franck MOREL for the continuous support of my PhD stud, for his patience, motivation, and immense knowledge. His guidance helped me in all the time of research and writing of this thesis.

I wish to express my sincere appreciation to my co-supervisors Camille ROBERT and Anis HOR for the many selfless hours of their time that they have given on my behalf without which this work would not have materialized.

I would like to thank Catherine MABRU who has done me the honor of being the president of the jury of my thesis. I would like to thank Eric CHARKALUK and Yves NADOT, my two examiners of thesis, for their well-directed support and meticulous reading of my dissertation. I am really touched and thankful for their time and patience in reading carefully my manuscript. I would like to give my thanks to Mehdi SALEM and Luis REIS, my other jury members, for their time and their valuable advices. Especially, the help from Dr. SALEM for certain experiments is acknowledged. I am also indebted to Etienne PESSARD, who is my committee member with Prof. NADOT, for his suggestion and support.

I wish to thank all the people whose assistance was a milestone in the completion of my research: Nikita DOROFEEV, Marco SCARPETTA, Nicolas CHAMBRIN, Linamaria GALLEGOS, Idriss TIBA, Daniel BELLETT.

I would also like to express my great appreciate to the colleagues of LAMPA for a lot of happy moments and giving me this agreeable and unforgettable memory: Rou, Hela, Bessam, Siti, Hugo, Benoit, Driss, Houssem, Racha, Sana, Amandine, Antoine, Vincent, Viet-duc, Foued, …

I appreciate the financial support from China Scholarship Council during the first three years of my PhD study.

I would like to thank my parents and my sister for supporting me throughout writing this thesis and my life in general.

In the end, I would like to dedicate this dissertation to my small family: my wife Xiaodong WANG, my daughter Yilian, my cat Wanzi and myself.

“For many a lonely day sailed across the milky seas

Ne'er looked back, never feared, never cried”

- ’39, a Queen’s song

Contents

Acknowledgement i
Contents iii
List of figures vii
List of tables xv
Résumé étendu xvii
Introduction 1
Chapter I. Literature research 5
I.1. Generality 6
I.1.1. Selective laser melting of additive manufacturing 6
I.1.2. High cycle fatigue 9
I.1.3. Stainless steel 316L 10
I.2. The state-of-the-art research about fatigue behavior of SLM SS 316L 12
I.2.1. Effect of surface finish 13
I.2.2. Effect of heat treatment 18
I.2.3. Effect of building direction 21
I.2.4. Effect of processing parameters 23
I.2.5. Discussion 25
I.3. Summary 26
Syntheses 28
Chapter II. Material preparation and characterization 29
II.1. Specimens elaboration 30
II.1.1. Powder characterization 30
II.1.2. Fabrication of specimens 33
II.1.3. Heat treatment 35
II.2. Microstructural characterization 38
II.2.1. Macrostructure of the SLM SS 316L 39
II.2.2. Microstructure of the SLM SS 316L 41
II.2.3. Grain morphology and Crystallographic texture 44
II.3. Inherent defect characterization 48

II.3.1. Surface state characterization 48
II.3.2. Porosity characterization 51
II.4. Mechanical behavior 54
II.4.1. Hardness 54
II.4.2. Monotonic tensile test 55
II.4.3. Cyclic tensile test 59
II.5. Conclusions 63
Syntheses 65
Chapter III. Fatigue experiments and analysis 67
III.1. Experimental fatigue test set-ups and conditions 68
III.1.1. Tensile fatigue tests 68
III.1.2. Bending and torsional fatigue tests 68
III.1.3. Surface preparation 70
III.2. Fatigue strength results and analysis 71
III.2.1. S-N curves 71
III.2.2. Effect of the surface state 73
III.2.3. Effect of loading type 73
III.2.4. Discussion 74
III.3. Fractographic analysis 76
III.3.1. Bending samples 76
III.3.2. Torsion samples 84
III.3.3. Summary 90
III.4. Correlation between defect size and HCF strength 90
III.4.1. Defect measurement 90
III.4.2. Kitagawa-Takahashi diagram 92
III.5. Conclusions 95
Syntheses 97
Chapter IV. Preliminary investigations on the high cycle fatigue sensitivity to microstructure and defect 98
IV.1. Microstructure sensitive modeling framework for defective materials 99

IV.2. Explicit microstructure model and fatigue prediction approach 102
IV.2.1. Finite element model 102
IV.2.2. Material constitutive laws and fatigue approach 104
IV.3. Results 110
IV.3.1. Application and evaluation of non-local method based on experimental results 110
IV.3.2. Further investigation of the non-local method on the microstructure effect 118
IV.4. Conclusions 124
Synthesis 126
Chapter V. Numerical study of the effect of roughness and porosity on the HCF performance of AM 316L 127
V.1. Preparatory investigations on the modeling of SLM steel 316L 129
V.1.1. Crystallographic orientation & grain morphology 130
V.1.2. Surface roughness & Pores 136
V.2. Modeling configurations 141
V.2.1. Design of geometrical models 141
V.2.2. Constitutive models 144
V.2.3. Loading condition 148
V.2.4. Fatigue criteria 148
V.3. Fatigue simulations of smooth models 148
V.3.1. Discussion on the experimental reference for simulation 148
V.3.2. Statistical method for microstructural heterogeneity 149
V.3.3. Investigations on R* 155
V.4. Fatigue simulations using models with roughness and defects 159
V.4.1. Models with artificial semi-ellipsoidal defects 159
V.4.2. Models with roughness 162
V.4.3. Models containing artificial defect and roughness 169
V.5. Role of plasticity in fatigue simulation 172
V.5.1. Comparisons between elastic and plastic constitutive models in smooth models ... 172
V.5.2. Comparisons between elastic and plastic predictions in defective models 174
V.5.3. Summary 176

V.6. Conclusions 177

Syntheses 179

Conclusions and prospects 180
References 183
Appendix A. Experimental data of vertically fabricated SLM 316L high cycle fatigue tests 195
A.1. Staircase method 195

A.2. Tensile fatigue tests 196

A.3. Torsional fatigue tests 198

A.4. Bending fatigue tests 201

Appendix B. Mesh convergence test 205
Appendix C. Application of the neighbor layer method 207
C.1. Smooth models 207

C.2. Models with artificial semi-ellipsoidal defects 208

C.3. Roughness models 210

C.4. Combined models 211

Résumé substantiel 213
Chapitre I. Bibliographie 217
Chapitre II. Fabrication et caractérisation du matériau de l'étude 224
Chapitre III. Les expériences et analyses sur la tenue en fatigue 239
Chapitre IV. Etude préliminaire de l'effet de la microstructure et des défauts sur la tenue en fatigue 251
Chapitre V. Etude numérique de l'effet de la rugosité et de la porosité sur les performances en fatigue du 316L SLM 264

List of figures

Figure I-1: Comparison of AM processes in terms of deposition rate and precision of features 7
Figure I-2: Schematic illustrations of the SLM process (Patterson, Messimer and Farrington, 2017) ... 8
Figure I-3: Diagram of the various domains of fatigue and highlighting of the dispersion at low amplitudes of stress. (Guilhem, 2011)..... 10
Figure I-4: Customized removable partial dentures made from SLM SS 316L (Almufleh *et al.*, 2018).. 11
Figure I-5: (A-C) fatigue crack initiates from internal defect; (D-E) fatigue crack initiates from surface defect (Solberg *et al.*, 2019) in a SLM SS 316L under cyclic tension loading 14
Figure I-6: S-N plots of vertically built SLM 316L under loading at R=0.1 with different surface treatments 15
Figure I-7: Fracture surfaces of as-built sample [σ_a =350 MPa, 28161 cycles] (a) (b) (Elangeswaran *et al.*, 2019) 16
Figure I-8: Fracture surfaces of a machined sample [σ_a =350 MPa, 254980 cycles] (a) (b) (Elangeswaran *et al.*, 2019)..... 16
Figure I-9: LoF defects responsible for crack initiation and failure in machined specimens fabricated vertically (Shrestha, Simsiriwong and Shamsaei, 2019) 17
Figure I-10: S-N plots for vertically built SLM 316L under loading at R=-1 with different surface treatment..... 17
Figure I-11: S–N curves for machined SLM processed 316L specimens under different heat treatments (Leuders *et al.*, 2014) 19
Figure I-12: EBSD inverse pole figure (IPF) maps for (a) as-built 316L specimens, (b) 316L following heat treatment for 2 h at 650 °C and (c) HIP processing. Orientations in the IPF maps have been plotted with respect to building direction (BD). (Riemer *et al.*, 2014) 19
Figure I-13: S-N plots of DMLS 316L in bending fatigue at a frequency of 25 Hz with regards to building direction (Mower and Long, 2016) 21
Figure I-14: (a) S-N curves for differently oriented specimens; (b) Light optical micrographs and EBSD-mappings of SLM-H (a, d), SLM-45 (b, e) and SLM-V specimens (c, f). (Blinn *et al.*, 2019) 22
Figure I-15: Strain-life fatigue data along with Coffin-Manson fits for LB-PBF SS 316L specimens in (a) machined vertical, diagonal, and horizontal directions(Shrestha, Simsiriwong and Shamsaei, 2019) 23
Figure I-16: S-N curves of SS 316L samples with different laser powers (Zhang *et al.*, 2017) 24
Figure I-17: (a) Mechanical (b) and fatigue properties of SS 316L samples (Zhang *et al.*, 2017)..... 24

Figure I-18: (a) Variation of Maximum stress at failure (MPa) with internal porosity fraction (%); (b) Kitagawa diagram of all the samples tested (Andreau, Pessard, *et al.*, 2019) (A, B, C represent different scanning speeds)..... 25
Figure II-1: Particle size distribution of 316L powder Prismadd12..... 31
Figure II-2: Powder of steel 316L under microscope: (a) SEM (b) SE detector (topography) (c) with BSE detector (chemical contrast)..... 32
Figure II-3: Powder structure (after chemical attack)..... 32
Figure II-4: (a) SLM machine (3D system ® ProX 320) and (b) fabricated tray of specimens..... 34
Figure II-5: Geometries of specimens (dimensions in mm): (a) Characterization specimens (microstructure); (b) Tension specimens (cyclic behavior and fatigue); (c) Bending specimens (fatigue); (d) Torsion specimens (fatigue)..... 35
Figure II-6:The temperature-time curve of stress relief heat treatment..... 36
Figure II-7: (a) Example of a diffraction peak obtained after a counting time of 60 seconds in a given direction and (b) example of fitting by the $\sin 2(\psi)$ method..... 37
Figure II-8: Location of the residual stress measures on the torsion and bending samples..... 37
Figure II-9: Illustration of microstructure observation planes..... 39
Figure II-10: Optical microscope observation on lasing plane Z..... 40
Figure II-11: Optical microscope observations on plane X/Y..... 41
Figure II-12: SEM observations in the plane Z..... 42
Figure II-13: SEM observations in the plane X/Y (long chemical attack)..... 43
Figure II-14: dendritic cellular network in SLM SS 316L..... 44
Figure II-15: Observation positions with the EBSD technique..... 44
Figure II-16: Post-treated EBSD mapping of the Z-plane..... 45
Figure II-17: Post-treated EBSD mappings of the X/Y-plane..... 45
Figure II-18: (a) pole figures and (b) inverse pole figures representing the mean orientations of the grains observed in the mapping of Z-plane..... 46
Figure II-19: (a) EBSD Maps and (b) optical micrographs of SS 316L obtained by SLM (Andreau, Koutiri, *et al.*, 2019)..... 47
Figure II-20: Influence of the shape of the melt pools on the preferential orientation of the grains: (a) case of low energy density and (b) case of high energy density (Sun *et al.*, 2019)..... 47
Figure II-21: (a) Effect of heat input on surface roughness and (b) effect of powder diameter on surface roughness (DebRoy *et al.*, 2018)..... 49
Figure II-22: Surface roughness in sample No.15, Tray 1..... 49
Figure II-23: Surface and linear roughness in (a) bending specimen and (b) torsion specimen..... 50
Figure II-24: Tomography in Z-plane: (a) slice No.250 (b) superimposing all slices..... 52
Figure II-25: Size and spatial distribution of the defects for all studied specimen..... 53

Figure II-26: Histogram and cumulative percentage of porosity of measured samples: (a) Tray1 - S3 - Porosity 0.0035%; (b) Tray2 - S5 - Porosity 0.026%..... 53
Figure II-27: Defects observations by SEM : (a) un-melted powder, (b) lack of powder and (c) pore formed between the particles of powder. 54
Figure II-28: Measured micro-hardness in an SLM sample..... 55
Figure II-29: Machined used in tensile test (MTS 809) 56
Figure II-30: Comparison between extensometer and gauge extensometer in tension for the polished specimen..... 57
Figure II-31: Tension curves for the raw surface specimen (red) and for the polished surface specimen (blue). 57
Figure II-32: Estimated Young's modulus of (a) as-built sample and (b) total-polished sample 58
Figure II-33: S-N curve of 316L under tension loading in LCF domain..... 60
Figure II-34: Stress-strain curves under cyclic tension-compression at E=0.3%: (a) all cycles and (b) selected cycles. 61
Figure II-35: Stress-strain curves under cyclic tension-compression at E=0.45%: (a) all cycles and (b) selected cycles. 61
Figure II-36: Stress-strain curves under cyclic tension-compression at E=0.6%: (a) all cycles and (b) selected cycles. 61
Figure II-37: Stress-strain curves under cyclic tension-compression at E=0.75%: (a) all cycles and (b) selected cycles. 62
Figure II-38: Half-life cycles of different loadings 62
Figure II-39: Cyclic softening curves under different cyclic deformations 63
Figure III-1: Bending and torsional fatigue test machine (Rumul ® CrackTronic) 69
Figure III-2: Frequency evolution along a bending fatigue test carried out with a Rumul® CrackTronic machine. The experiment is stopped when the frequency drop reaches 0.1 Hz. 69
Figure III-3: Bending specimens after different preparations: (a) as-built and (b) simple-polished..... 71
Figure III-4: S-N curves for two surface state conditions (As-built and Simple-polished) in fully reversed uniaxial tension/compression 71
Figure III-5: S-N curves for three surface state conditions (As-built, Simple-polished and Total-polished) in fully reversed plane bending. The fatigue test results for machined specimens of wrought 316L steel are also given for comparison. 72
Figure III-6: S-N curves for three surface state conditions (As-built, Simple-polished and Total-polished) in fully reversed torsion..... 72
Figure III-7: SEM observations on fatigue crack initiation site(s): (a) single defect at one initiation site; (b) several defects at two initiation sites 77
Figure III-8: (a) Elongated shaped defect (b) and irregular shaped defect at fatigue crack initiation site 78

Figure III-9: Fracture surface of specimen P1-S5 (scenario of fatigue crack initiation and growth is not clear) 78
Figure III-10: Two independent fatigue crack initiation sites in specimen (P1-S16) 79
Figure III-11: Parallel adjacent defects observed in simple-polished specimens 80
Figure III-12: Defects observed on the as-built lateral surface of simple-polished bending specimens: (a) a combination of roughness and pores; (b) parallel adjacent defects 80
Figure III-13: Representative crack initiation site in as-built specimen: (a) in the middle of top surface; (b) in the edge of top surface 82
Figure III-14: Morphology of defects in as-built specimens: (a) open-form defect; (b) subsurface defect 82
Figure III-15: The three fracture modes 85
Figure III-16: Representative fatigue crack path under torsion loading 85
Figure III-17: Macroscopic crack path in total-polished torsion specimen: stage I (mode II) followed by stage II (mode I) 86
Figure III-18: Fracture surfaces of total-polished specimen under torsion loading 86
Figure III-19: Secondary crack in the total-polished specimen under torsion loading 87
Figure III-20: Example of the fatigue crack initiation and growth mechanism from defect under torsional loading. Two stages are clearly visible 87
Figure III-21: Fracture surface observation on the simple-polished torsional specimen 88
Figure III-22: Surface state of an as-built torsion specimen 88
Figure III-23: Crack path in an as-built torsional specimen 89
Figure III-24: Defects at the origin of failure in as-built torsion specimens: (a) a series of surface defects; (b) two clustering subsurface defects 89
Figure III-25: Different methods proposed to measure irregular defect(s) (HOURIA, 2015; Le *et al.*, 2018; El Khoukhi *et al.*, 2019; Romano, Miccoli and Beretta, 2019) 91
Figure III-26: Two different measurement techniques to assess the size of a cluster of adjacent defects 92
Figure III-27: Kitagawa diagram using the minimalist measurement methods with different parameters as effective defect size: (a) depth, (b) Feret diameter, (c) Murakami parameter, (d) modified Feret diameter 93
Figure III-28: Kitagawa diagram using the maximalist measurement methods with different parameters as effective defect size: (a) depth, (b) Feret diameter, (c) Murakami parameter, (d) modified Feret diameter 94
Figure IV-1: Example of finite element models used 103
Figure IV-2: Pole figures of (a) 100, (b) 111 orientation for the crystallographic orientations implanted in numerical models 104

Figure IV-3: Comparison of the maximal shear stress (a) between isotropic elasticity (Iso. E.) and cubic elasticity (Cub. E.). and (b) between cubic elasticity (Cub. E.) and cubic elasticity + crystal plasticity (Cub. E. + CP.) (Robert *et al.*, 2012)..... 106
Figure IV-4: Schematic illustrations of non-local methods: (a) critical radius method and (b) neighbor layer method..... 109
Figure IV-5: FE models containing semi-circular defects with radii of 5,15,30,60,120,200 µm respectively..... 110
Figure IV-6: Von Mises equivalent stress fields in numerical models with same microstructure configuration but different defect size: (a) 5µm; (b) 15µm; (c) 30µm; (d) 60µm; (e) 120µm; (f) 200 µm 111
Figure IV-7: Distribution of maximum local stress concentration factor in models with different microstructures but same defect size (defect size as legend) 112
Figure IV-8: Distributions of grain-average hydrostatic stress amplitude and shear stress amplitude in numerical models with same microstructure configuration but different defect size: (a) 5µm; (b) 15µm; (c) 30µm; (d) 60µm; (e) 120µm; (f) 200 µm..... 113
Figure IV-9: Results of the fatigue tests conducted on the 316L steel in uniaxial tension and torsion with a loading ratio R =-1 (Guerchais *et al.*, 2015)..... 114
Figure IV-10: Kitagawa-Takahashi diagrams of local fatigue indicating parameters..... 114
Figure IV-11: Normalized Kitagawa-Takahashi diagrams with the application of (a) critical radius Dang Van criterion;(b) neighbor layer Dang Van criterion;(c) critical radius Matake criterion; (d) neighbor layer Matake criterion; (e)critical radius Papadopoulos criterion; (f) neighbor layer Papadopoulos criterion 115
Figure IV-12: Fatigue limit intervals of 96 models containing the same defect but different microstructure from the criteria: Dang Van, Matake, Papadopoulos. (a) critical radius method (b) neighbor layer method..... 117
Figure IV-13: Fatigue limit intervals of 24 models containing the same defects and grain shapes but different grain orientations from the criterion: Dang Van. (a) critical radius method (b) neighbor layer method..... 118
Figure IV-14: Histograms of grain size for different grain morphology configurations: (a) Gaussian distributed Voronoi polygon (b) uniform distributed quadrangle (c) log-normal distributed Voronoi 1 (d) log-normal distributed Voronoi 2 119
Figure IV-15: Illustrations of different grain morphology configurations: (a) Gaussian distributed Voronoi polygon (b) uniform distributed quadrangle (c) log-normal distributed Voronoi 1 (d) log-normal distributed Voronoi 2 120
Figure IV-16: Fatigue limit intervals of 24 models containing same defects but different grain morphology from (a) critical radius Dang Van criterion;(b) neighbor layer Dang Van criterion;(c) critical

radius Matake criterion; (d) neighbor layer Matake criterion; (e)critical radius Papadopoulos criterion; (f) neighbor layer Papadopoulos criterion 121
Figure IV-17: Effective areas of critical radius method and neighbor layer method in different studied microstructures: (a) uniform distributed grains and (b) log-normal distributed grains 122
Figure IV-18: Illustrations of different grain size configurations: (a) 30 µm; (b)100 µm 122
Figure IV-19: Relationship between grain size and effective crack length (replot from (El Haddad, Smith and Topper, 1979)) 123
Figure IV-20: Effective defect sizes for different average grain size configurations of proposed realizations of non-local method and pre-fixed parameter values 124
Figure V-1: BC maps of SLM 316L: (a) bottom (b) top (c) middle part of the sample 131
Figure V-2: Ellipticity measurement of EBSD map (top area of the sample) 132
Figure V-3: Theoretical log-normal distribution and empirical distributions of grain size 133
Figure V-4: Comparison of theoretical log-normal distribution curve and probability density of grain size of generated models 133
Figure V-5: Calculated Young's moduli for 24 realistic textured grain orientations sets generated randomly 135
Figure V-6: Pole figures in direction 100, 110 and 111 of employed orientation sets 136
Figure V-7: Schematic illustration of several surface roughness parameters (adapted from (Tekçe *et al.*, 2018)) 137
Figure V-8: Selected roughness profiles 138
Figure V-9: Reconstructed pores detected by µCT 139
Figure V-10: Histogram and kernel density estimation curve of pores' sizes 139
Figure V-11: Schematic illustration of designing imitating LoF defect in the numerical model(*: adapted from (Mergulhão and Das Neves, 2018)) 140
Figure V-12: Illustrations of 5 tessellations involved in the numerical model 142
Figure V-13: Different types of defective models (zoom view of the local top surface) 143
Figure V-14: Comparison between the experimental responses of 316L steel under different imposed amplitudes and the predictions of the crystal plasticity model 148
Figure V-15: Von Mises stress distribution in a smooth polycrystalline model subjected to a tension loading of 100 MPa 150
Figure V-16: Scatter maps of hydrostatic stress and maximum shear stress (a) from every element or (b) from every grain in a polycrystal FE model 152
Figure V-17: Evolution of the median of the extreme value distributions of Dang Van FIP as a function of loading conditions. The black dots correspond to the median (probability of 0.5), the two limits of the interval correspond to a probability of 0:1 and 0:9 (i.e. 80% of the results are within this interval).(Hor *et al.*, 2014) 153

Figure V-18: GEV fitting for predicted fatigue limits using Dang Van criterion from different tessellated polycrystal models: (a) Quadrangle (b) Voronoi 154
Figure V-19: Scatter map of the two components in Dang Van criterion from the critical grains in 100 instantiations 155
Figure V-20: Dang Van stress distributions with respect to different non-local parameters in a smooth polycrystalline model subjected to a tension loading of 100 MPa 156
Figure V-21: PDF and CDF curves fitting the stochastic responses of FIP in polycrystalline models with different microstructural configurations using R*= 60 µm 156
Figure V-22: Scattered predicted fatigue limits from three fatigue criteria((a) Matake; (b) Dang Van; (c) Papadopoulos) regarding texture types and categorized by the tessellation type 158
Figure V-23: Distributions of the non-local fatigue indicating parameters (Dang Van (R*=60µm)) in non-textured and textured numerical models under tension loading of 100 MPa 161
Figure V-24: Non-local Dang Van stresses using different R* (15, 30, 45 and 60 µm) for a log-normal Voronoi-polygon-tessellated model with roughness 163
Figure V-25: Distributions of three non-local FIPs (Dang Van, Matake, Papadopoulos) with R*=60 µm in models with roughness under cyclic tension loading 164
Figure V-26: Histograms and fitted Weibull distribution curves of predicted fatigue limits using different non-local parameter values for stochastic configured polycrystalline models 165
Figure V-27: Medium values of predicted fatigue limits using different non-local FIPs with respect to different roughness profiles 166
Figure V-28: Distributions of non-local Dang Van stress and roughness profiles for model P3 and model P4 167
Figure V-29: Predicted fatigue limit of models containing surface roughness versus roughness characteristic parameters 168
Figure V-30: Distributions of FIP (non-local Dang Van stress with R* = 30 µm) of models with the same microstructure configurations (morphology and orientation of grain) but different defect(s): (a) surface roughness, (b) LoF defects, (c) surface roughness + LoF defects 170
Figure V-31: Predictions of fatigue limit from Dang Van criterion using different values of R* categorized by the tessellation type (2 log-normal distributed Voronoi tessellations:LN_V1, LN_V2 and 1 quadrangle tessellation: Q2) 171
Figure V-32: Distribution of plastic strain in a smooth polycrystal aggregate with isotropic texture after a cyclic tension loading at 232 MPa 172
Figure V-33: Distribution of the difference of von Mises stress between elastic constitutive model and plastic constitutive model in a smooth polycrystal aggregate with isotropic texture in the most stressed timestep in the last cycle of a cyclic tension loading at 232 MPa 173

Figure V-34: Distribution of the Dang Van stress (R*=60 µm) in smooth polycrystal aggregates using plastic and elastic constitutive models respectively with isotropic texture after a cyclic tension loading at 232 MPa 173
Figure V-35: Distribution of the Dang Van stress (R*=60 µm) in smooth polycrystal aggregates using plastic and elastic constitutive models respectively with realistic texture after a cyclic tension loading at 232 MPa 174
Figure V-36: Distribution of the Dang Van stress (R*=60 µm) in defective polycrystal aggregates using plastic and elastic constitutive models respectively with realistic texture after a cyclic tension loading at 150 MPa 175

Figure C-1: Comparisons of predicted fatigue limit intervals under tension loading using different N* values for non-local Dang Van criterion 208
Figure C-2: Distributions of the non-local fatigue indicating parameters (Dang Van (N*=4)) in non-textured and textured numerical models under tension loading of 100 MPa 209
Figure C-3: Non-local Dang Van stresses using different N* (1, 2, 3,4 and 5) from a log-normal Voronoi-polygon-tessellated model with roughness..... 210
Figure C-4: Predictions of fatigue limit from Dang Van criterion using the neighbor layer method . 211

List of tables

Table I-1: Chemical compositions of SS 316L 12
Table I-2: Mechanical properties of SLM SS 316L from 3D systems® 12
Table II-1: Nominal and measured chemical composition of 316L 31
Table II-2: SLM processing parameters for specimen's fabrication 33
Table II-3: The parameters of residual stress analysis 36
Table II-4: Surface residual stress values after stress releasing heat treatment for the studied specimens. 38
Table II-5: Surface and linear roughness parameters of measured samples. 50
Table II-6: Porosity of the samples measured 54
Table II-7: Macro-hardness of tested specimens 55
Table II-8: Manufacturer and literature data of the mechanical properties in uniaxial tension of SS 316L obtained by SLM. 59
Table II-9: Low cycle tension-compression fatigue tests 60
Table III-1: Fatigue strength values assessed with the staircase method for different surface state conditions and different loading modes 73
Table III-2: Positions of crack initiation sites in simple-polished specimens 79
Table III-3: Summary of fractography observations on all the tested samples 84
Table IV-1: Characteristics summary of the different configured model 104
Table IV-2: Parameters of the constitutive models 106
Table IV-3: Parameters of the fatigue criteria for a 316L steel 108
Table IV-4: Local stress concentration factor with respect to different defect radius 112
Table IV-5: Experimental results for defective steel 316L 116
Table V-1: Calculated Young's moduli and Poisson ratios for different sampling areas of EBSD specimen 134
Table V-2: Characteristic roughness parameters of the 5 selected profiles 138
Table V-3: Statistical information of detected pores 140
Table V-4: Configurations of the models employed in the simulations 142
Table V-5: Isotropic elastic constitutive model parameters for studied 316L steel with regards to the different texture configuration 144
Table V-6: Interaction matrix of FCC structure and the associated slip systems 146
Table V-7: Searched intervals of objective parameters 147
Table V-8: Identified parameters of the Méric&Cailletaud crystal plasticity constitutive model 147
Table V-9: Quantitative estimations of fatigue limit for different tessellated models 154

Table V-10: Median values of predicted fatigue limits from models with the same type of loading, tessellation and orientation using non-local criteria (R*=60 µm) 158
Table V-11: Median values of predicted fatigue limits from models with the same type of loading, tessellation and orientation using Dang Van criterion with different values of R*..... 159
Table V-12: Mean values of predicted fatigue limits from models containing geometrical defects with the same type of loading, tessellation and orientation using non-local Dang Van criterion (R*=60 µm) 162
Table V-13: Predictions from a crystal plasticity model and a purely elastic model under a cyclic tension loading at 150 MPa..... 175
Table V-14: Predictions from a crystal plasticity model and a purely elastic model under a cyclic tension loading at 90 MPa..... 176
Table V-15: Predictions from a crystal plasticity model and a purely elastic model under a cyclic tension loading at 120 MPa..... 176

Table A-1: Staircase method for as-built and simple-polished tensile specimens 196
Table A-2: Parameters identification of staircase method for as-built and simple-polished tensile specimens 196
Table A-3: Summary of all the tensile fatigue tests conducted..... 198
Table A-4: Staircase method for as-built, simple-polished, and total polished torsional specimens .. 198
Table A-5: Parameters identification of staircase method for as-built, simple-polished, and total polished torsional specimens 199
Table A-7: Staircase method for all bending specimens 201
Table A-8: Staircase method calculations for all bending specimens 202
Table A-9: Summary of all the bending fatigue tests conducted 203
Table B-1: Comparison of different mesh qualities 205
Table C-1: Mean values of predicted fatigue limits from models containing geometrical defects with same type of loading, tessellation and orientation using Neighbor layer Dang Van criterion 210

Résumé étendu

Ces travaux de thèse de doctorat s'inscrivent dans le cadre de l'étude de la Fatigue à Grand Nombre de Cycles (FGNC) de l'acier 316L obtenu par Fabrication Additive (FA). Ils comportent deux volets bien distincts mais complémentaires portant pour le premier sur une caractérisation expérimentale du comportement en fatigue et pour le second sur la modélisation par la méthode des éléments finis des effets de la microstructure, de la microgéométrie de surface et des défauts.

Le **Chapitre I** est consacré à une revue bibliographique relative aux aspects clés de l'étude. La technique de FA, en particulier le procédé SLM (*Selective Laser Melting*), la FGNC et l'acier inoxydable 316L sont passés en revue pour préciser le contexte des travaux.

Des résultats expérimentaux récents de la littérature sont présentés. De nombreux facteurs interviennent dans les conditions d'amorçage des fissures de fatigue au sein de l'acier 316L SLM SS (*Stainless Steel*). Le facteur le plus étudié est l'état de surface. Les pièces brutes de fabrication présentent un état de surface caractérisé par une forte rugosité, considérée comme très néfaste à la résistance en fatigue. Il est confirmé que les pièces brutes ont des mauvaises performances en fatigue tandis que l'usinage ou le polissage des pièces obtenues par FA permettent d'augmenter les caractéristiques mécaniques notamment en fatigue. En ce qui concerne l'effet des traitements thermiques, les avis divergent. La microstructure semble être notamment modifiée par le traitement HIP (*Hot Isostatic Pressing*) mais la résistance en fatigue dans le régime FGNC ne semble parfois pas être affectée. On constate que la direction de fabrication qui modifie la texture cristallographique influence également le comportement à la fatigue. Il faut néanmoins être conscient du fait que les résultats présentés dans les différentes publications disponibles ne correspondent pas nécessairement aux mêmes paramètres de procédé. Des recherches récentes démontrent par exemple que la densité laser utilisée peut entraîner des performances en fatigue très différentes.

D'après les éléments disponibles dans la littérature sur le 316L SLM, il ne fait aucun doute que les défauts associés à la surface ainsi que certains paramètres microstructuraux comme la texture possèdent un impact considérable sur la réponse en fatigue.

Les travaux proposés dans ce projet de thèse visent à conduire une étude approfondie de ces deux paramètres tant du point de vue expérimentale que de la simulation.

Le **Chapitre II** est consacré à la description des conditions expérimentales et de certaines des propriétés de l'acier SLM SS 316L étudié. La démarche adoptée consiste en une maîtrise complète des étapes de préparation, fabrication et caractérisation des échantillons obtenus par la technique de SLM.

On se penche à la fois sur la caractérisation de la poudre utilisée pour la fabrication mais également sur les caractéristiques microstructurales des pièces fabriquées. Les défauts inhérents au procédé de fabrication additive sont mesurés et analysés. En plus des identifications mentionnées, des essais mécaniques de traction monotone et cyclique ainsi que des tests de dureté sont conduits et analysés.

Il est important de préciser que toutes les éprouvettes sont fabriquées verticalement et que des mesures des contraintes résiduelles effectuées après le traitement thermique de détensionnement appliqué montrent que certaines contraintes résiduelles peuvent subsister.

Des observations microscopiques montrent la présence de défauts et la tomographie μCT met en évidence la présence de pores. On constate également que le matériau est fortement texturé, avec des grains d'austénite allongés le long de l'axe de fabrication. Des scans EBSD (*Electron BackScatter Diffraction*) permettent d'accéder au type de texture cristallographique en jeu. Des mesures de rugosité de surface sur les échantillons bruts montrent que le niveau de rugosité (*Rz*) peut dépasser 200 μm.

Des mesures de dureté montrent que la dureté du SLM SS 316L se situe dans la plage 220-250 HV, ce qui est cohérent avec les données du SS 316L corroyé. En traction monotone, les caractéristiques recueillies sont proches de celles obtenues pour le 316L corroyé en matière d'UTS et d'allongement à rupture. Le module de Young est néanmoins bien plus faible avec une valeur aux alentours de 150 GPa. Afin de caractériser le comportement à l'écrouissage cyclique, des tests en traction-compression sous chargement cyclique sont conduits à quatre niveaux de déformation totale imposés : ± 0,30%, ± 0,45%, ± 0,60%, ± 0,75%. On observe une phase de durcissement rapide puis un adoucissement plus lent.

Les résultats des tests de fatigue sont présentés et analysés au **Chapitre III**. Les essais sont effectués en traction, flexion et torsion. Pour chaque condition de chargement, différents échantillons avec différents états de surface sont utilisés pour mieux appréhender l'effet de l'état de surface sur les performances en fatigue à grand nombre de cycles. Pour mieux comprendre le mécanisme d'amorçage des fissures de fatigue, des analyses fractographiques sont effectuées. Les défauts de type « Lack of Fusion » sont toujours à l'origine de l'amorçage des fissures. Les tailles des défauts observés sont ensuite mesurées et mises en regard avec les limites de fatigue correspondantes.

Il est très important de préciser qu'aucune étape de lasage de contour n'est appliquée dans cette étude. Les valeurs de rugosité de surface atteintes sont néanmoins cohérentes avec des données de la littérature où un lasage final de contour est adopté. Quoiqu'il en soit, de nombreux défauts de type LoF (*Lack-of-Fusion*) sont observés sur les faciès de rupture à la surface ou en sous couche et sont à l'origine des fissures de fatigue.

L'effet du gradient de contrainte n'est pas observé dans la présente étude car les résultats des tests de fatigue en flexion et en traction donnent des résultats similaires.

Les résistances en fatigue observées sont globalement faibles (en comparaison des données de la littérature). Ces valeurs peuvent s'expliquer par l'absence de lasage de contour et par conséquent par la présence de nombreux défauts de type LoF.

En utilisant la théorie de Murakami, on montre que la diminution de la résistance à la fatigue est bien corrélée avec l'augmentation de la taille effective du défaut. Dans les zones d'amorçage, on constate souvent des chapelets de défauts de type LoF. Pour obtenir des résultats cohérents, il est nécessaire de tenir compte de l'ensemble des défauts dans la mesure de la taille du défaut qui intervient dans l'analyse en fatigue.

En raison de la présence en nombre des défauts de type LoF, il est difficile de connaître avec précision l'effet seul de la rugosité de surface sur les conditions d'amorçage des fissures de fatigue.

Le **Chapitre IV** porte sur la mise en place d'une démarche de simulation numérique visant à mieux comprendre les effets de défaut et de microstructure et ceci à travers une approche non locale. Les travaux présentés sont purement numériques et les résultats des prédictions sont comparés aux résultats expérimentaux de Guerchais (Guerchais *et al.*, 2015). Un modèle éléments finis de microstructure virtuelle explicite est construit et utilisé. Les modifications des critères de fatigue par l'introduction de deux méthodes non locales sont expliquées et évaluées pour explorer qualitativement le lien entre la distance critique et la taille du défaut ou la microstructure. Pour mieux appréhender la portée des méthodes non locales proposées, certaines analyses concernant la morphologie et la taille des grains sont menées.

A l'aide des modèles éléments finis mis en place, la réponse mécanique locale à l'échelle des grains est obtenue. Il ressort de l'analyse mécanique que la microstructure introduit une forte hétérogénéité.

On montre cependant qu'une approche purement locale ne peut refléter correctement l'effet Kitagawa-Takahashi. Des résultats très conservatifs sont obtenus.

En introduisant une méthode non locale, une prédiction satisfaisante en fatigue tenant compte explicitement à la fois des défauts et de la microstructure peut être atteinte. La dispersion des résultats due aux hétérogénéités de microstructure est montrée et discutée. En particulier, pour le défaut de taille moyenne, la grande dispersion montre la compétition entre le défaut et la microstructure locale.

Trois critères de fatigue multi-axiaux exprimés en contraintes sont utilisés et évalués, Matake, Dang Van et Papadopoulos. Les trois critères sont à même, associée à l'approche non locale, de traduire l'effet Kitagawa-Takahashi. Le critère de Matake fournit toujours la limite de fatigue la plus élevée. Ceci doit être dû à l'utilisation de la contrainte normale dans l'expression du critère, au contraire des deux autres formulations qui font appel à la contrainte hydrostatique.

Concernant les deux formulations possibles de la méthode non locale, la méthode de la couche voisine est plus sensible à la microstructure. Des diffusions plus fortes peuvent être observées dans les résultats de la méthode de la couche voisine par rapport à ceux de la méthode du rayon critique.

D'autres analyses portant sur la morphologie et la taille des grains montrent la différence entre la méthode du rayon critique et la méthode de la couche voisine. La sensibilité à la taille des grains dépend du modèle non local utilisé.

Le cadre d'une approche de modélisation et de simulation numérique sensible à la microstructure a été utilisé avec succès au chapitre 4 pour reproduire l'effet K-T dans le cas d'un SS 316L corroyé. L'objectif du C**hapitre V** est d'appliquer la même démarche pour mieux comprendre le comportement en fatigue du SLM SS 316L.

Pour construire un modèle éléments finis de microstructure explicite dédié au SLM SS 316L, il est important d'intégrer l'ensemble des informations relatives à la microstructure et aux défauts issu des caractérisations présentées aux chapitres 2 et 3. Les résultats des calculs éléments finis sont post-traités par les méthodes non locales et une méthode statistique est employée pour obtenir des prédictions de la tenue en fatigue.

Les effets de rugosité, des défauts de type LoF et de la microstructure sont discutés sur la base d'un grand nombre de simulations.

L'application d'un modèle de comportement en plasticité cristalline est présentée à la fin du chapitre pour confirmer que la plasticité a une influence négligeable sur les prédictions conduites à l'aide d'une approche non locale et d'un critère exprimé en contrainte.

Les simulations sont donc conduites à partir de modèles EF où des paramètres de texture cristallographique, de taille et forme de grain, de rugosité de surface réaliste, de défaut type LoF sont intégrés.

Parmi les nombreux résultats obtenus, on peut souligner que la morphologie des grains ne semble pas être un paramètre du premier ordre sur la réponse en fatigue. La texture cristallographique présente elle un effet bien plus marqué. Les quelques simulations conduites en présence d'un défaut de géométrie simplifiée laissent également à penser que les défauts de type LoF ont un impact très important sur le comportement en fatigue.

Introduction

Context

Endurance is always a major concern of the industry. Fatigue failures were firstly observed and investigated in the 19th century. Since then, continuous research has accumulated abundant data and results. But a comprehensive understanding of the fatigue phenomenon is not yet achieved as the fast evolution of technologies brings out more new materials and new products. In this decade, Additive Manufacturing (AM) techniques undergo rapid advancements. The mechanical behavior of AM parts, particularly the fatigue behavior, becomes a concern for future industrial application. The AM materials, however, have distinguished mechanical properties compared to that of the conventional ones. More efforts are needed to complement the understandings, especially about the influences of inherent imperfect surface state and microstructure which is strongly dependent on the fabrication process of AM materials on fatigue behavior.

The present study is a continuation of several former pieces of research completed in the lab LAMPA (*Laboratoire Angevin de Mécanique, Procédés et innovAtion*). Mainly based on the numerical modeling solution given by Camille Robert, the experimental and numerical research about the effect of the defect on fatigue strength of wrought austenitic stainless steel 316L carried out by Raphael Guerchais, and the statistical analysis of fatigue indicator parameters done by Anis Hor, as well as the other related findings cumulated by the research team of the lab, this study will focus on the free surface effect of high cycle fatigue behavior of AM steels by experimental and numerical methods. Particularly, since the studied material is from the AM technique, the effect of microstructure will be assessed as well.

This research project is financially supported by the China Scholarship Council (CSC). The experimental part is realized in the lab ICA (*Insititute Clément Ader*) and the numerical part is completed in the lab LAMPA.

Objectives

The work presented in this dissertation deals with the fatigue behavior of additive manufactured metallic materials, particularly, of austenitic steel 316L in the context of high cycle fatigue (HCF) regime. Compared to the conventionally fabricated materials, the additive manufactured materials in as-built condition are distinguished by two main features: imperfect surface state and heterogeneous microstructure. AM material has an inevitable poor surface state which mainly originates from the inherent defects during the fabrication process, for instance, surface roughness, lack-of-fusion (LoF) defect, and gas-penetrated pore. These defects in AM parts are small in size and have an order of magnitude close to that of several grains. The influence of small defects on fatigue behavior is supposed to be connected with the microstructure, while the microstructure in AM products is often different from

that in conventional fabricated products. The objective is more precisely to study the effect of the stress concentration induced by inherent small defects and of the stress heterogeneity from the anisotropy of microstructure as well as their competitions.

Scientific approach

The investigations on exploring the high cycle fatigue behavior of selective laser melted (SLM) steel 316L are realized in both experimental and numerical ways.

The specimens are fabricated from recycled powder to be in line with industrial products. Contouring is intentionally prevented to represent the worst application scenario. Part of the specimens is kept in as-built condition while others are polished. Comprehensive fatigue tests are conducted in three loading modes including tension, bending and torsion. Because fracture surface observations show that fatigue failures are mainly caused by the lack-of-fusion defect, critical defects are measured and correlated with fatigue strengths based on the theory of Murakami.

A quasi-realistic explicit microstructure sensitive finite element model is then built up. The roughness profile comes from profilometry measurement. The microstructure is derived from data collected by EBSD observation. Multiaxial fatigue criterion combining non-local method is used. Simulated results are post-treated by a proper statistical method.

The layout of the thesis

This thesis is divided into 5 chapters.

A literature review of various important points for the understanding and orientation of the study is presented in the first chapter. General information concerning the three crucial aspects, namely, an advanced fabrication technique: selective laser melting; an industrial application interest: high cycle fatigue; and a widely used metallic material: stainless steel 316L, are introduced. Recent investigations on the fatigue behavior of selective laser melting stainless steel 316L are reviewed in different aspects.

Material preparation and characterization are presented in the second chapter. The fabrication process is described in detail from the powder to the specimens regarding powder characterization, specimens designing, fabrication process parameters, heat treatment, and mechanical treatment. The optical microscope, Scanning Electron Microscope (SEM) and Electron BackScatter Diffraction (EBSD) is used to characterize the microstructure of fabricated specimens. Profilometry and X ray tomography are conducted to measure the inherent defect in the as-built material. Typical mechanical experiments as the hardness test, monotonic tensile test, and cyclic tensile test are carried out and discussed.

The third chapter summarizes all conducted fatigue experiments. Experimental preparation of the fatigue test is presented. Staircase method is used to estimate fatigue limit under different configurations of surface treatment, loading mode, and building direction. The results are analyzed and discussed. Fracture surface observations of all tested specimens display typical fatigue-provoking defect patterns

in different surface situations. Modified Murakami method is used to quantitatively evaluate the relation between fatigue limit and inherent defect size.

A preliminary numerical study on defective material and based on 2D numerical simulations of polycrystalline aggregates is reported in the fourth chapter. The non-local method is introduced to an explicit microstructure model to resolve the problem in fatigue prediction raised by the complex stress state containing stress concentration and stress heterogeneity. Two different non-local method implementations are compared under different conditions. Kitagawa-Takahashi effect is reproduced on the defective models by both the proposed realizations of the non-local method.

The fifth chapter is devoted to a study of numerical simulations on quasi-realistic explicit microstructures of 316L austenitic steel in different surface states. Problems encountered during the establishment of the numerical polycrystalline aggregate model are discussed. The non-equiaxed grains are characterized by log-normal distributed Voronoi polygons. The strongly textured microstructure is represented by crystallographic grains with preferential directions. Roughness and porosity are examined numerically to be added to the numerical models. A statistical method based on generalized extreme value distribution is used to describe the stochasticity of microstructural attributes. Identification of the parameters in the plastic constitutive model is presented. Data from experiments are processed to create statistically representative numerical models. Simulations of differently configured microstructure are analyzed and discussed.

This dissertation ends with a conclusion summarizing the main results obtained during this study. Research perspectives aimed at improving the numerical methodology are proposed.

Chapter I.

Literature research

I.1. Generality 6

I.1.1. Selective laser melting of additive manufacturing 6

I.1.2. High cycle fatigue 9

I.1.3. Stainless steel 316L 10

I.2. The state-of-the-art research about fatigue behavior of SLM SS 316L 12

I.2.1. Effect of surface finish 13

I.2.1.1. R=0.1 13

I.2.1.2. R=-1 15

I.2.1.3. Summary 18

I.2.2. Effect of heat treatment 18

I.2.3. Effect of building direction 21

I.2.4. Effect of processing parameters 23

I.2.5. Discussion 25

I.3. Summary 26

Syntheses 28

I.1. Generality

This research project is under the context of the high cycle fatigue behavior of additive manufactured products. In this section, we give brief introductions of additive manufacturing and fatigue phenomenon as well as the studied material – austenitic stainless steel (SS) 316L.

I.1.1. Selective laser melting of additive manufacturing

Additive Manufacturing (AM) refers to the fabrication process where the solid object is made from numerical model by adding material together in contrast to the material-removing traditional technique such as machining. In the past two decades, AM technology has achieved rapid development. A series of terms were used, such as "Rapid prototyping", "3D printing" and "Solid free-form fabrication", which describe the characteristics of the technology from different aspects. Additive manufacturing can intervene at any point in a product's life: pre-production (Rapid prototyping), large scale production (rapid manufacturing) or repair (reload) for its advantages over the conventional fabrication methods: flexibility without fixed tool requirement, the possibility of mass customization, short production times, and manufacture of very complex shapes. The material-adding processes are realized in various ways which are categorized in ISO/ASTM52900-15, namely: Binder Jetting; Directed Energy Deposition; Material Extrusion; Material Jetting; Powder Bed Fusion; Sheet Lamination; Vat Photopolymerization. And this technique is compatible with different kinds of materials, i.e., metal materials, non-metal materials, and medical biomaterials.

Lately, AM becomes a very promising technology for the manufacture of complex-shaped components used in the aeronautics and aerospace industry because of the progress made by the industrial manufacturers in metal-based fabrication. There has been an exponential growth of the interest on the AM applications for metals in the fields of research and industry in recent years. A remarkable industrial breakthrough was reported from SIEMENS. 3D-printed turbine blades were fabricated and survived full-load tests in 2017. A continuous 8000 hour run for one full year of operation was reported later in 2018.[1] With the successful application in the industrial domain, AM proves its value in "*l'industrie du futur*" (the future industry).

As a developing technology, AM still has its limitations. Poor surface state and dimensional precision are the most evident flaws. As-built products show a strong surface roughness and have inherent defects, for instance, lack-of-fusion powder, porosity, and inclusions, which influence mechanical properties eventually. In Figure I-1, different Metal AM processes are evaluated with regards to production

[1]https://3dprintingindustry.com/news/siemens-celebrates-8000-hour-run-of-3d-printed-turbine-burner-140140/

precision and deposition rate. However, by sacrificing the deposition rate, i.e. the production time, improved precision is achieved by several techniques, particularly Powder Bed Fusion processes.

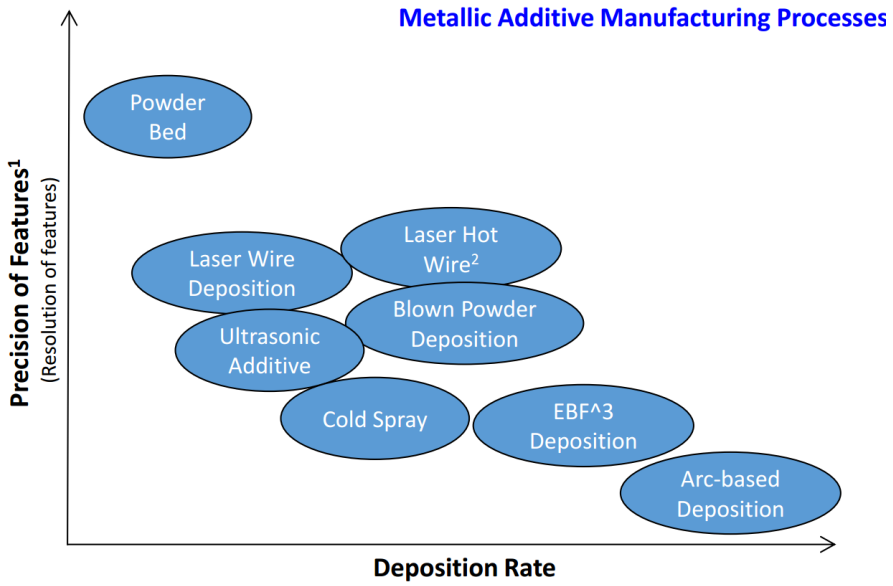

[1] Precision refers to the as-built state and does not encompass hybrid techniques and/or interim machining operations that would increase resolution. There are also a lot of other factors not considered in this chart including heat inputs to limit overall distortion.
[2] Technology still under full development

Figure I-1: Comparison of AM processes in terms of deposition rate and precision of features

The commonly studied techniques for AM of metals are Selective Laser Melting (SLM), Electron Beam Melting (EBM), both classified as Powder Bed Fusion processes, and Laser Metal Deposition (LMD), categorized as a Direct Energy Deposition process (Herzog *et al.*, 2016). The AM technique involved in this project is SLM which is originated in the 1990s at the Fraunhofer Institute ILT in Aachen, Germany and was classified as Laser Sintering. It grew exponentially in the field of metal component manufacturing (Meiners, Wissenbach and Gasser, 1996). By 2005, commercial laser sintering systems appeared, incrementally fusing layers of metal powder and thus obtaining solid objects (J. P. Kruth *et al.*, 2005). The appearance of these systems marked the birth of a new branch of technology - the rapid manufacture of parts.

The first selective laser sintering systems used powders with a polymer coating. Parts obtained by this process had low densities and required post-heat treatment under pressure to reach near-maximal densities (Shellabear and Nyrhilä, 2004). Parallel innovations have made it possible to use uncoated metal powders in Direct Selective Laser Sintering (DSLS) (Agarwala *et al.*, 1995). This concept served as a basis for the processes referred to today as Direct Metal Laser Sintering (DMLS), which is technically a particular embodiment of SLS (Selective Laser Sintering) (J. Kruth *et al.*, 2005). It should be emphasized that SLM systems rely on the melting of powders and initially used only pure metals. Nevertheless, there is a significant difference between SLM and SLS: while the former fully melts the powder, the latter heats it to a specific point where the powder grains can fuse; thus, SLS cannot achieve the near full density which characterizes the SLM products, and it usually requires postprocessing, such

as heat treatment and material infiltration. But although the difference between the SLM and SLS systems is clearly stated, the distinction between the two processes has become blurred because the new SLS systems are operated at sufficient powers to fuse powders; this is why, in practice, SLM and DMLS are used interchangeably.

The SLM building process starts with laying a thin layer of metal powder on a substrate plate in a building chamber. Once the powder is laid, the laser is used to melt and fuse selected areas according to the processed data. Once the laser scanning is completed, the building platform is lowered, the next layer of powder is deposited on top and the laser scans a new layer. The process is then repeated for successive layers of powder until the required components are completely built.

The process is represented in Figure I-2.

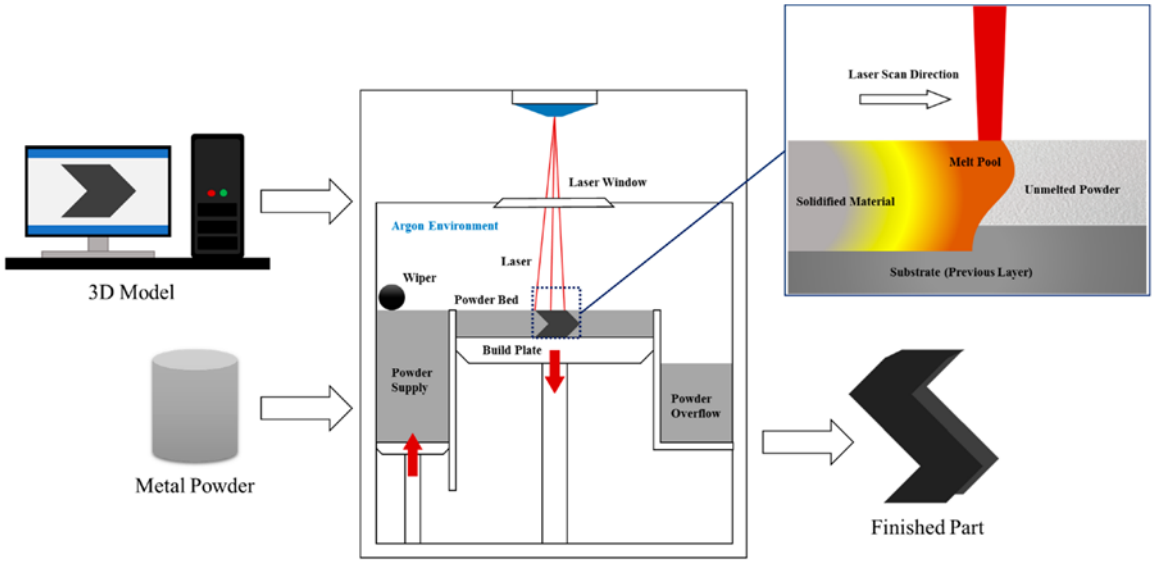

Figure I-2: Schematic illustrations of the SLM process (Patterson, Messimer and Farrington, 2017)

With this technique, a high energy density laser is used to melt and fuse metallic parts, in an inert gas atmosphere. Since the powder is fully melted, it is possible to have low porosity and good control over crystal structure, acting on the production parameters (such as laser power, scanning speed, hatch spacing, and layer thickness). Several physical phenomena have to be taken into account, such as the absorption of laser irradiation by the powder material, the balling phenomenon, that disrupt the formation of continuous melts, or the thermal fluctuation experienced by the material during the process, that causes residual stress on the components built, and can therefore lead to crack formation and delamination. However, small localized heating and rapid cooling in SLM reduce the pick-up of interstitial elements. Previous studies have shown good results in terms of relative density, especially under high laser power and low scanning speed, and strength (UTS, YS) of the manufactured pieces, compared to parts produced by casting or other AM techniques (Tolosa *et al.*, 2010).

Although SLM is by far the best solution among AM metal processes in terms of surface quality, the as-built surface of SLM products is not satisfying. One purpose of the present work is to study the influence of surface roughness and porosity in the 316L steel fabricated by SLM on its fatigue behavior.

I.1.2. High cycle fatigue

Fatigue failure has always been a concern for engineers for centuries. Fatigue failure has the characteristics of locality, and sensitivity to the environment and defects. Therefore, fatigue damage is often not easy to detect in time and easily causes accidents. The most representative description of the fatigue phenomenon is "Material can be induced to fail by many repetitions of stresses, all of which are lower than the static strength. The stress amplitudes are decisive for the destruction of the cohesion of the material.", known as "Wohler laws" (Schütz, 1996).

Typical mechanical properties of materials (such as yield stress and ultimate tensile strength) are identified by static experiments. These mechanical properties do not fully reflect the characteristics of the material under the loading of cyclic alternating stress. Therefore, if a part or structure that works under an alternating loading is still designed according to static loading, sudden failures often occur during use. There are many obvious essential differences between fatigue failure and traditional static failure:

(1) Static failure is a failure under a maximum load: Fatigue failure is a failure under repeated loads. It does not occur in a short period of time, but it takes a certain period of time, or even a long time, to fail.

(2) When the static stress is less than the yield limit or strength limit, static failure does not occur; while the alternating stress is far less than the static strength limit, or even less than the yield limit, fatigue failure may occur.

(3) Static failure usually has obvious plastic deformation. Fatigue failure usually does not have significant external plastic deformation signs, even for ductile metallic materials. Just like the brittle failure, it is not easy to detect in advance, which indicates that Fatigue failure is even more dangerous.

Three Fatigue regimes can be distinguished (shown in Figure I-3), depending on the number of cycles to failure.

Low cycle fatigue (LCF) is a situation where the stress is high enough to generate plastic deformation and fail within a low number of cycles ($N_f < 10^4$-10^5).

High cycle fatigue (HCF) corresponds to the low-stress situation which is below the macroscopic yield stress and the rupture happens in 10^6-10^7 cycles.

Very high cycle fatigue (VHCF) concerns the situation of a long service life as well as often a high loading frequency. Fatigue limit declines further after 10^7 cycles. An infinite life does not seem to exist for metallic materials (Pyttel, Schwerdt and Berger, 2011).

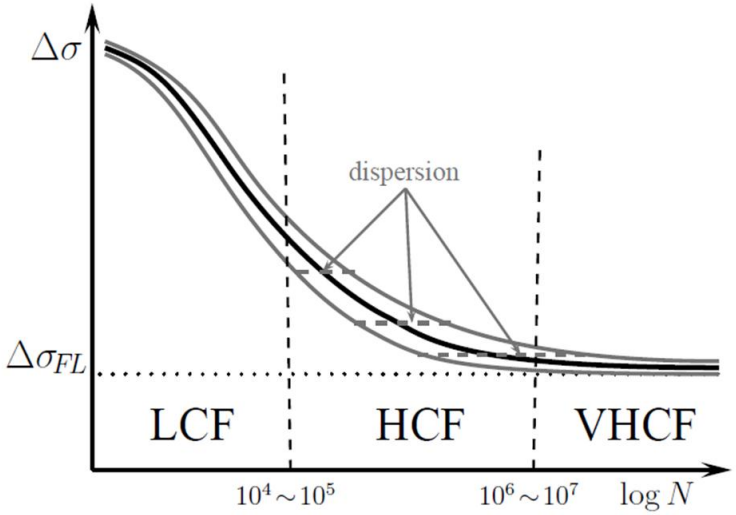

Figure I-3: Diagram of the various domains of fatigue and highlighting of the dispersion at low amplitudes of stress. (Guilhem, 2011)

Today, a large number of aeronautical and aerospace components, such as engine components and turbine blades, are often subject to cyclic loads of very high frequencies that exceed, for their lifetime, one million cycles. Damage to parts under this type of loading is very often referred to as HCF.

HCF is a type of fatigue that involves small deformations and a large number of cycles to lead to failure. The total stress is composed of average stress and alternating stress. The average stress is caused by the residual stresses, the loads induced during assembly or by a highly heterogeneous temperature distribution. The alternating stress is mechanical or thermal stress of any frequency. HCF implies lower stresses with respect to the yield stress. Usually, there is no plastic deformation at the macroscopic scale in the HCF regime. That is to say, the main macroscopic deformation in HCF is the elastic deformation. In HCF regime, the fatigue crack preferably initiates at the surface and the crack initiation phase represents a greater proportion of the total lifetime. A large dispersion of the results is noted in this area. This is mainly due to the peculiarities of the microstructure of the material, among which the grain orientation configurations and the presence of impurities or/and flaws.

In the present study, we focus on the HCF regime with number of cycles to failure such as $N_f > 10^6$ to 10^7.

I.1.3. Stainless steel 316L

SS316 is an austenitic chromium-nickel stainless steel containing a deliberate amount of molybdenum which increases general corrosion resistance and especially improves its pitting resistance

to chloride ion solutions. SS 316L is the extra-low carbon version of SS316 that minimizes harmful carbide precipitation during welding. Because of its combination of good mechanical properties at high temperatures, excellent corrosion resistance, and good machinability, this steel is used as a general-purpose material with excellent mechanical and corrosion properties. Its chloride resistance makes this specific grade of stainless steel suitable for marine applications. SS 316L is also the preferred material for use in hydrogen atmospheres or for hydrogen piping/cooling applications. Furthermore, 316L retains good mechanical properties at sub-zero and even cryogenic temperatures and is suitable for structural components in low-temperature applications.

For the Additive Manufactured (AM) SS 316L, its applications are often limited in high value-added scenarios because of the expensive cost of fabricating process, e.g.: medical and dental applications (Figure I-4), heat exchangers, lightweight structures, etc. (Yap *et al.*, 2015)

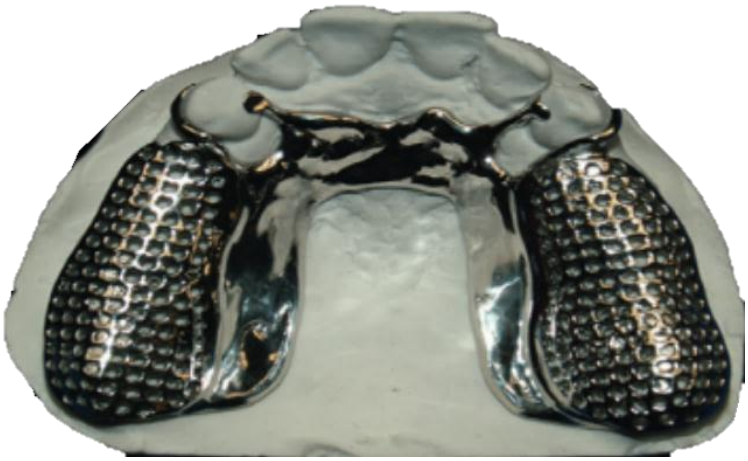

Figure I-4: Customized removable partial dentures made from SLM SS 316L (Almufleh *et al.*, 2018)

Generally, higher porosity is encountered in AM parts due to incomplete fusion, if compared to wrought material. AM SS 316L has achieved significant success with near full density, reasonable tensile properties and fatigue crack growth behavior (Lou *et al.*, 2017).

According to ASTM A240 (ASTM International, 2018), chemical compositions in SS 316L should meet certain standards. In terms of AM, the chemical compositions of manufactured material have slight differences. The values from the ASTM standard and from AM machine provider 3D systems are listed in Table I-1. The differences are denoted by using italic form.

Moreover, because of the distinguished fabrication process, the material properties from AM parts are different from conventional ones. Regarding this study, the mechanical properties of SLM SS 316L from 3D Systems® are listed in Table I-2. As stated by the producer, the specimens tested were manufactured with standard parameters on a ProX DMP 320 machine using the process parameter of Config B.

Table I-1: Chemical compositions of SS 316L

Element	% of weight	
	<<ASTM>>	<<3D SYSTEMS>>
Iron	Balance	Balance
Carbon	≤0.03	≤0.030
Manganese	≤2.0	≤2.00
Silicon	*≤0.75*	*≤1.00*
Phosphorus	≤0.045	≤0.045
Sulfur	≤0.03	≤0.030
Chromium	*16.0-18.0*	*16.50-18.50*
Molybdenum	*2.0-3.0*	*2.00-2.50*
Nickel	*10.0-14.0*	*10.00-13.00*
Nitrogen	*≤0.1*	*≤0.11*

Table I-2: Mechanical properties of SLM SS 316L from 3D systems®

Measurement	**Condition**	**Stress relief**	**Full anneal**
Mechanical properties			
Young's modulus (Gpa)			
Horizontal direction		180 ± 15	180 ± 15
Ultimate tensile strength (MPa)	ASTM E8M		
Horizontal direction		660 ± 20	610 ± 30
Vertical direction		570 ± 30	540 ± 30
Yield strength Rp0.2% (MPa)	ASTM E8M		
Horizontal direction		530 ± 20	370 ± 30
Vertical direction		440 ± 20	320 ± 20
Elongation at break (%)	ASTM E8M		
Horizontal direction		39 ± 5	51 ± 5
Vertical direction		49 ± 5	66 ± 5
Hardness, Rockwell B (HRB)	ASTM E18	90 ± 6	83 ± 4
Physical properties			
Density (g/cm^3)		8	
Surface Quality			
surface roughness			
Vertical direction (Z) (µm)		5-10	

I.2. The state-of-the-art research about fatigue behavior of SLM SS 316L

One of the most concerned topics in the field of the durability of additive manufacturing metallic materials is the complexity of predicting fatigue failure. For the AM materials, the microstructure is often different from its conventional counterpart although they share the same chemical composition. The process parameter and post-processing treatment have great influences on AM materials' fatigue

performance as well as their mechanical properties. Specifically, products from SLM may exhibit a specific microstructure and contain multiple defects such as pores or lack-of-fusion. Their irregular shapes and pronounced sharpness result in a detrimental effect on the fatigue performance of the part.

The research on the fatigue performances of SLM SS 316L can be traced back to 2013, to the best of the author's knowledge. In the following section, emphasis will be placed on the influence of surface roughness.

I.2.1. Effect of surface finish

As-built AM products without post-machining can preserve the very feature making AM technique different and promising from traditional subtractive manufacturing. But the fatigue performance of as-built products is always poorer compared to that of conventional fabricated products (Yadollahi and Shamsaei, 2017). Higher surface roughness is one of the reasons for the poor fatigue performance of SLM steels compared to conventionally manufactured steels. The staircase effect of the SLM process, partially melted particles stuck on the surface, and unstable melt pool aggravate the surface roughness of SLM steels (Afkhami *et al.*, 2019). Therefore, in order to improve the fatigue characteristics of the SLM steel, their surface roughness can be smoothed by surface treatment. For example, conventional surface treatment procedures (such as turning) create compressive residual stresses and remove superficial defects from the material. They also compress near-surface defects by plastic deformation and reduce their negative effects on mechanical properties.

The loading ratio R is often set to 0.1 or -1 in the literature. The fatigue strength, which usually refers to stress amplitude, is different under a loading ratio of 0.1 or -1. There exist several correction methods as Goodman model (Goodman, 1899), Gerber model (Gerber, 1874) and Walker model (Walker, 1970). But the fatigue test results are not transformed in this literature research and are treated separately by the loading ratio.

I.2.1.1. *R=0.1*

Spierings et al. (Spierings, Starr and Wegener, 2013) conducted fatigue experiments of vertically built SLM processed SS 316L specimens using different surface treatments, i.e. as-built, machining and polishing that generate surface roughness (Ra) equals to 10.0, 0.4 and 0.1 µm respectively. The fatigue testing was performed at R=0.1 using a 50 Hz sinusoidal tensile load to a maximum of 10^7 cycles. The surface state has an effect on the fatigue limit and the as-built specimens show a poorer performance. Spierings et al. also indicated that the results of polished specimens were in a wider scatter band compared to others. This is probably due to remaining defects after the surface treatments. Still, the influence of mechanical surface treatment was considered small for this case in their conclusion

probably explained by the sphere powder particles did not bring strong stress concentration at the surface and other effects as anisotropy as well as dynamic behavior might be involved.

Solberg et al. (Solberg *et al.*, 2019) tested 13 tensile samples under load control with a ratio of 0.1 at a frequency of 10 Hz. Three contours and internal hatching are used as scanning strategies during fabrication. The run-out threshold was set to $2*10^6$ cycles. From fractography, specimens failed from defects in the surface region at low load levels in the HCF regime, while the specimens failed from internal defects at the higher load levels as shown in Figure I-5.

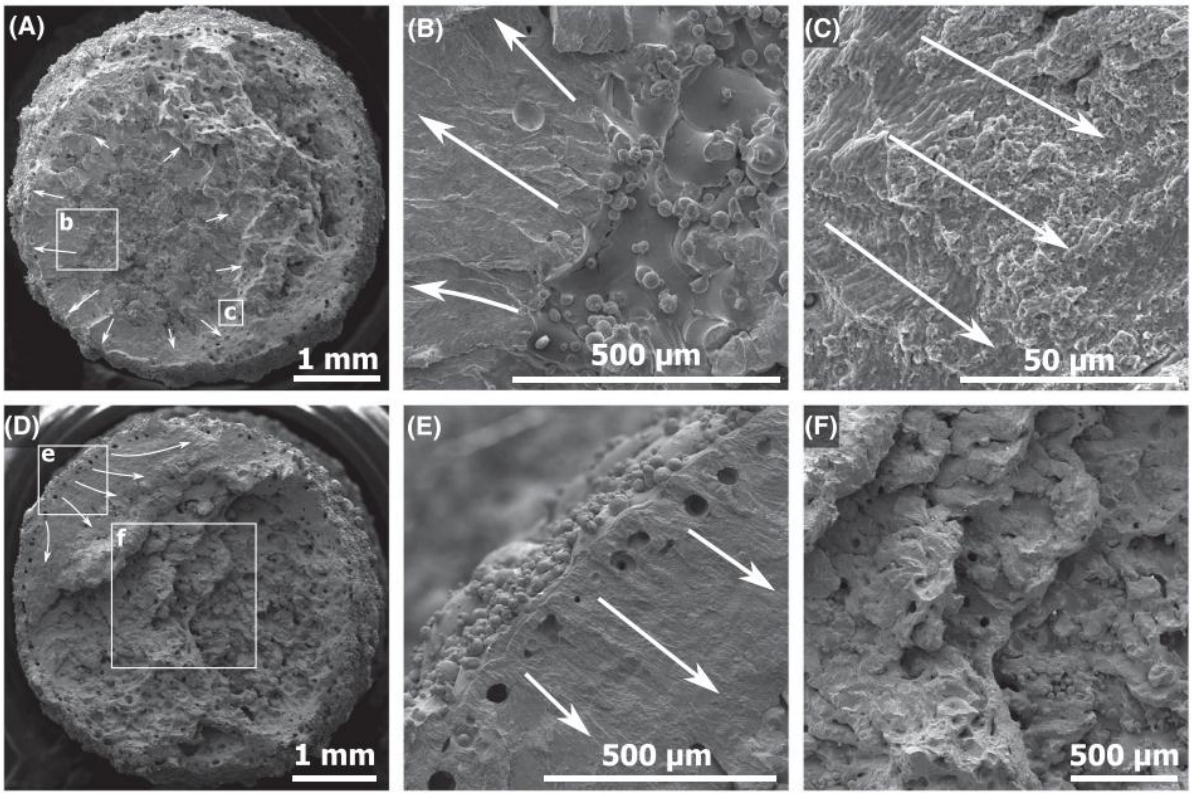

Figure I-5: (A-C) fatigue crack initiates from internal defect; (D-E) fatigue crack initiates from surface defect (Solberg *et al.*, 2019) in a SLM SS 316L under cyclic tension loading

Besides the enumerated previous investigations, Davies et al. (Davies, 2017) conducted 7 HCF tests of vertically built SLM SS 316L specimens machined and polished using tensile load at R=0.1 and frequency of 30 Hz.

The results of all the above-mentioned fatigue tests are plotted in Figure I-6. The machined specimens yield good fatigue strengths that are comparable with conventional wrought 316L. But the as-built specimens are poor in terms of their fatigue limit. The batch of polished specimens exhibit similar behaviors with the ones from machined specimens. Apparently, the mechanical treatment can somehow affect the fatigue behavior of AM steels.

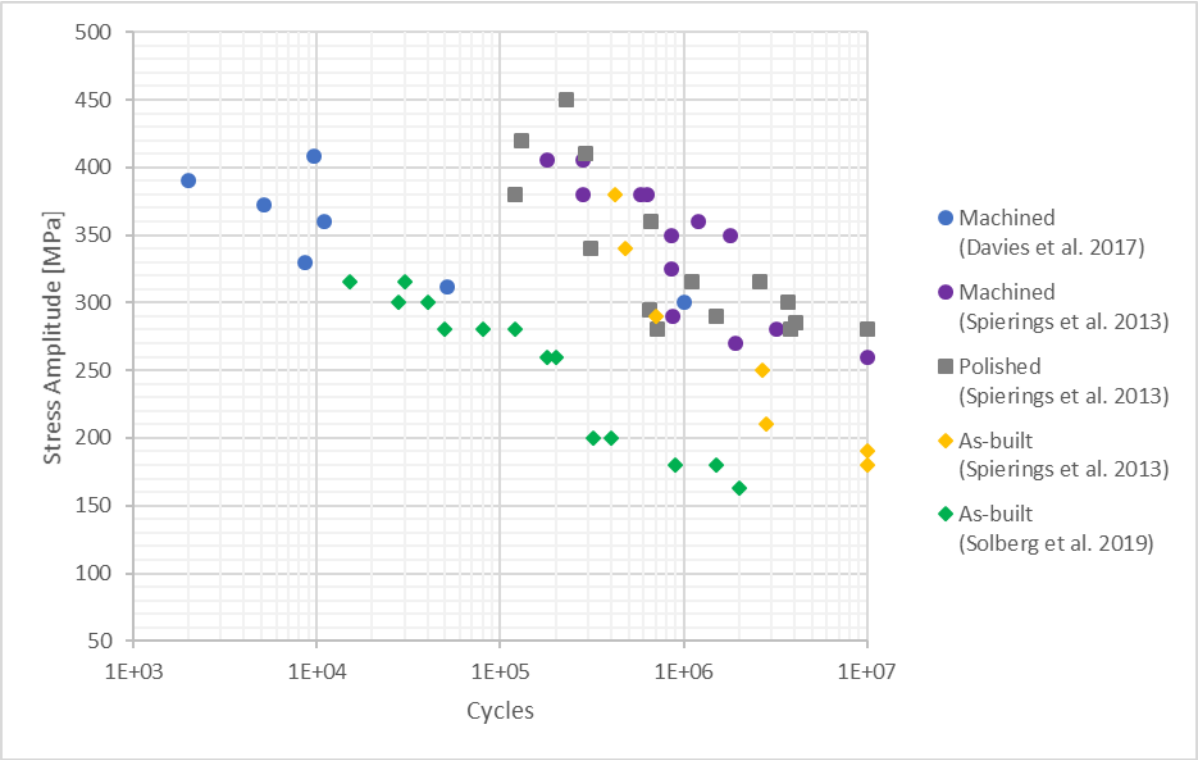

Figure I-6: S-N plots of vertically built SLM 316L under loading at R=0.1 with different surface treatments

I.2.1.2. *R=-1*

Uhlmann et al. (Uhlmann *et al.*, 2017) performed rotating bending tests at a stress ratio of -1 with vertically built SLM SS 316L specimens in 3 different surface states: as-built, vibratory finished and turned. At $2*10^6$ cycles, the as-built specimens yielded a fatigue limit at about 100MPa and the vibratory finished ones showed an increase in fatigue limit at about 140 MPa. The turned samples had the best fatigue performance with an endurance limit of about 200 MPa. Considering the roughness measured that the as-built specimens had a roughness with highest *Ra* and *Rz*, *Ra* for both the vibratory finished specimens and the turned specimens were similar while the *Rz* was higher for the former than the latter, the results of the fatigue tests correlated with the surface roughness. The SEM analysis showed, for all three types of samples, that the fatigue failure initiated at the binding defects at or slightly under the surface. The local stress raiser can be inner defects, surface roughness features or possible compressive residual stresses.

Elangeswaran et al. (Elangeswaran *et al.*, 2019) conducted tensile tests (loading ratio R=-1) as per ASTM E8M norms at a strain rate of 0.5%/min in the elastic domain and 40%/min in the plastic domain at 60Hz. Measured roughness parameter *Ra* is 0.5 ± 0.06 µm and 7.2 ± 1.3 µm for the machined surface condition and non-machined samples, respectively. The fracture surface of an as-built specimen displays multiple cracks initiating from the surface and propagating towards the core (Figure I-7) while the

machined sample does not present observable unfused powder particles and seems to have only one initiated crack (Figure I-8).

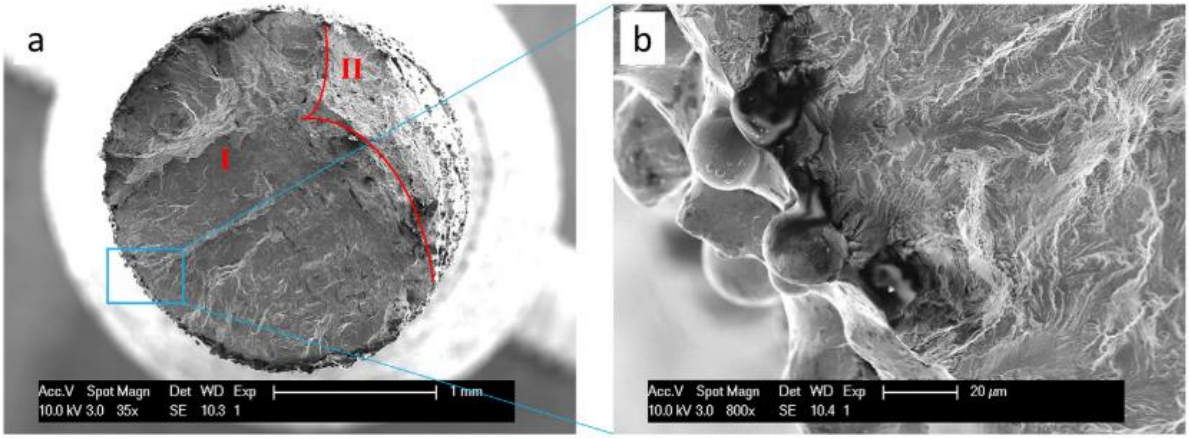

Figure I-7: Fracture surfaces of as-built sample [σ_a =350 MPa, 28161 cycles] (a) (b) (Elangeswaran *et al.*, 2019)

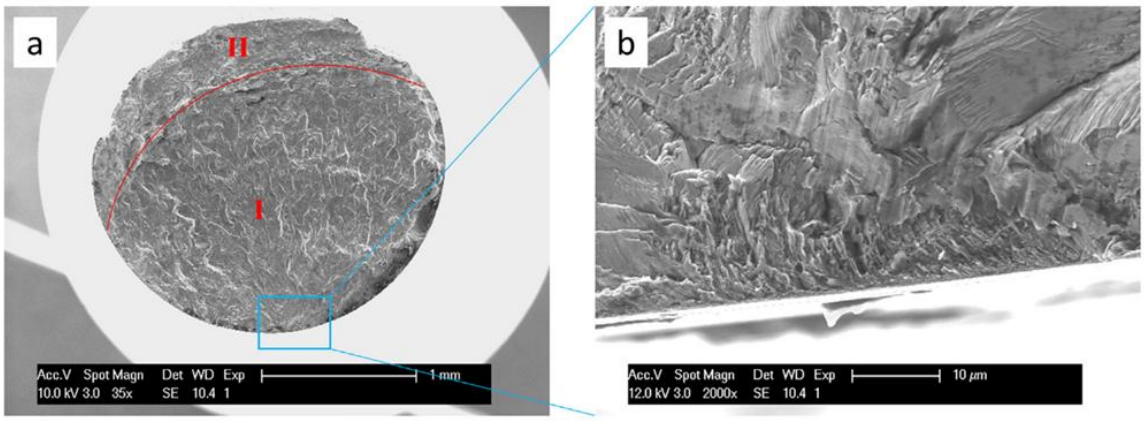

Figure I-8: Fracture surfaces of a machined sample [σ_a =350 MPa, 254980 cycles] (a) (b) (Elangeswaran *et al.*, 2019)

Shrestha et al. (Shrestha, Simsiriwong and Shamsaei, 2019) conducted strain-controlled fully-reversed tests with a ratio of -1 on both machined and as-built specimens following ASTM Standard E606. Loading frequencies between 0.65 and 2.5 Hz, depending on the strain amplitude, were used to minimize the effect of strain rate. These frequencies are lower compared to that of Elangeswaran et al. (Elangeswaran *et al.*, 2019). The measured *Ra* for as-built specimens is about 21 µm. By comparing the results from as-built and machined samples, it is found that surface finish did not have much effect on the fatigue behavior of 316L SS specimens due to the presence of larger internal lack-of-fusion defects. This conclusion is in contrast to previous findings as machining can improve fatigue performance. However, from the microscope observation, evident Lack-of-Fusion (LoF) defects were seen in these samples (shown in Figure I-9). In addition, the loading cycles in this research are all within 10^6 which are lower than others.

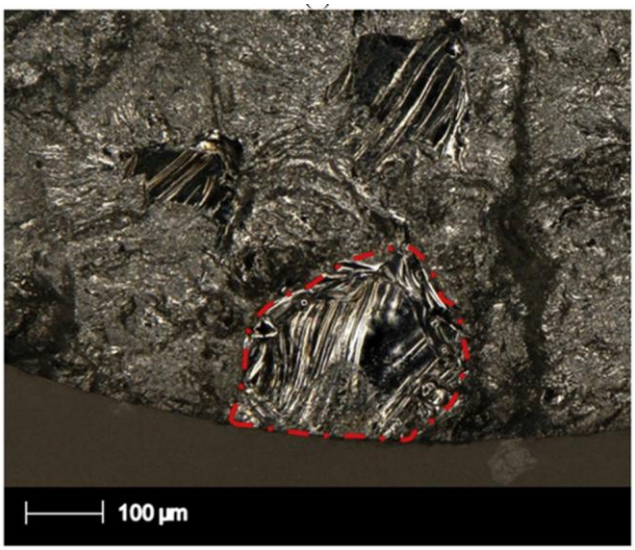

Figure I-9: LoF defects responsible for crack initiation and failure in machined specimens fabricated vertically (Shrestha, Simsiriwong and Shamsaei, 2019)

The results of the above-mentioned fatigue tests are plotted in Figure I-10. Still, we can observe that the mechanical treatment to the surface of specimen can improve the fatigue performance.

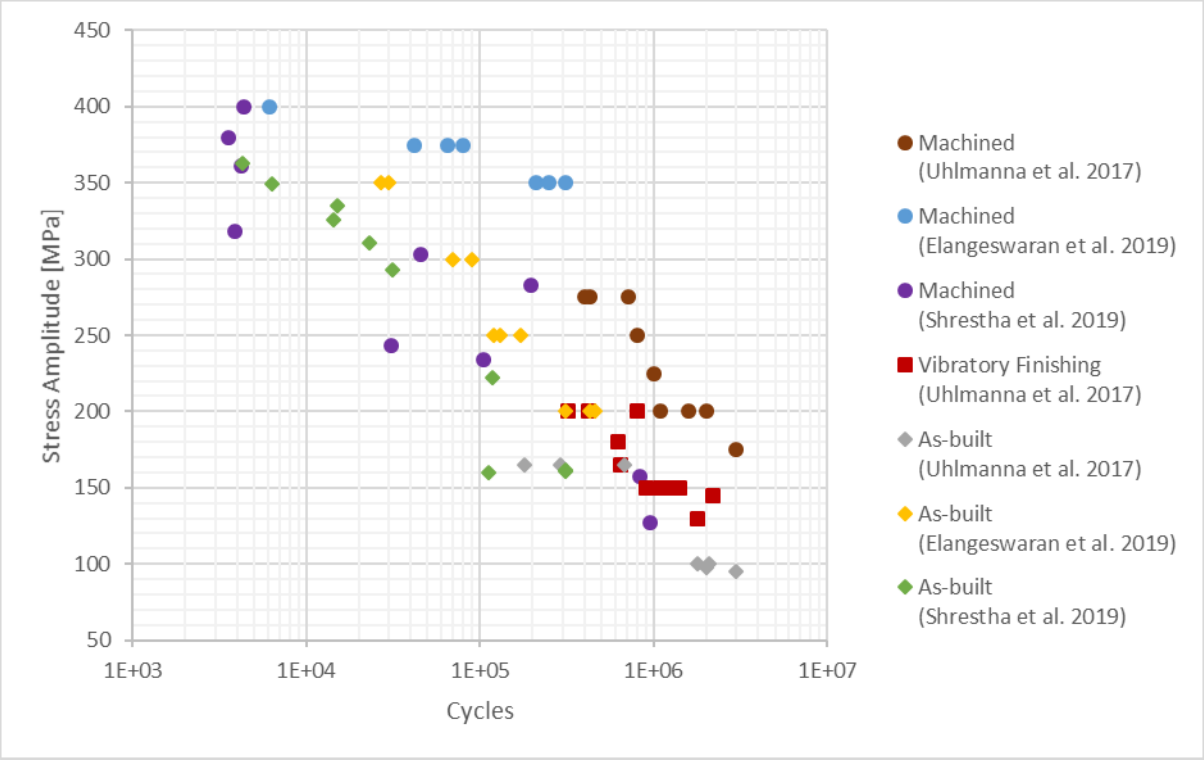

Figure I-10: S-N plots for vertically built SLM 316L under loading at R=-1 with different surface treatment

I.2.1.3. *Summary*

Surface finish has been long known to influence at the first order the fatigue properties. The as-built surface roughness can be optimized via the laser contour parameters (Yang *et al.*, 2019), the part position, orientation (Chen *et al.*, 2018), and powder size distribution (Spierings, Herres and Levy, 2011). The occurrence of porosity or un-melted particles in powder bed fusion parts, especially at or near the surface, has also been shown to reduce fatigue strength.

But post-manufacturing processes, such as machining and polishing, may not always be feasible for AM parts, for instance, in the remote manufacturing scenario or for complex-shaped products. Moreover, it is time-consuming and increases the global cost of additively manufactured parts. In some medical applications, parts having rougher surfaces are more prone to assist cohesion between the patient's bone/tissue and AM orthopedic implants than the smooth parts (Dewidar, Khalil and Lim, 2007) (Liu, Chu and Ding, 2004). Therefore, it is necessary to characterize the effect of surface roughness on the fatigue performance of laser-based AM parts.

From the enumerated literature, as could be expected, mechanical surface treatment improves the fatigue properties of SLM steels. However, this improvement is only observed in the HCF limits of SLM steels. This result is predictable because the behavior in HCF is more dependent on the surface quality of defects and materials than in LCF (Afkhami *et al.*, 2019). Apart from the research from Uhlmann et al. (Uhlmann *et al.*, 2017), all mentioned studies use machining as the treatment to eliminate surface roughness. As a ductile material, 316L is easily plastically deformed by surface machining whilst strong residual stress can be introduced. It is hence difficult to decouple the effects of the different factors due to the surface finishing process.

I.2.2. Effect of heat treatment

The mechanism of the effect of heat treatment on fatigue behavior of 316L is the change in the grain structure which affects the microstructure and monotonic properties (Bryson, 2005). The commonly used heat treatments are annealing and hot isostatic pressing (HIP).

Riemer et al. (Riemer *et al.*, 2014) reported their HCF tests of SLM processed SS 316L to investigate the effect of post-processing, especially the microstructural features from different heat treatments. The sinusoidal loading was at a stress ratio of R=-1 and a frequency of 40 Hz. The run-out was defined by a number of $2*10^6$ cycles. Three batches of specimens were used and were subjected to different heat treatments: as-built; heated at 650 °C for 2h; HIPed. The results were plotted in the following S-N plots (Figure I-11). The results showed that all the machined specimens regardless of their heat treatment method had similar fatigue strengths compared to conventional ones which were in the range of 267 to 317 MPa. But changes of the microstructure can be clearly observed by EBSD (shown in Figure I-12).

Furthermore, he tested as-built specimens and found a fatigue limit of 108 MPa. As Riemer et al. pointed out, the experimental results of AM materials can hardly be compared directly due to different processing and post-processing operations which can lead to different microstructural properties. The tendency that machining can improve the fatigue performance of SLM SS 316L from both the researches of Spiering et al. (Spierings, Starr and Wegener, 2013) and Riemer et al. (Riemer *et al.*, 2014) can be observed.

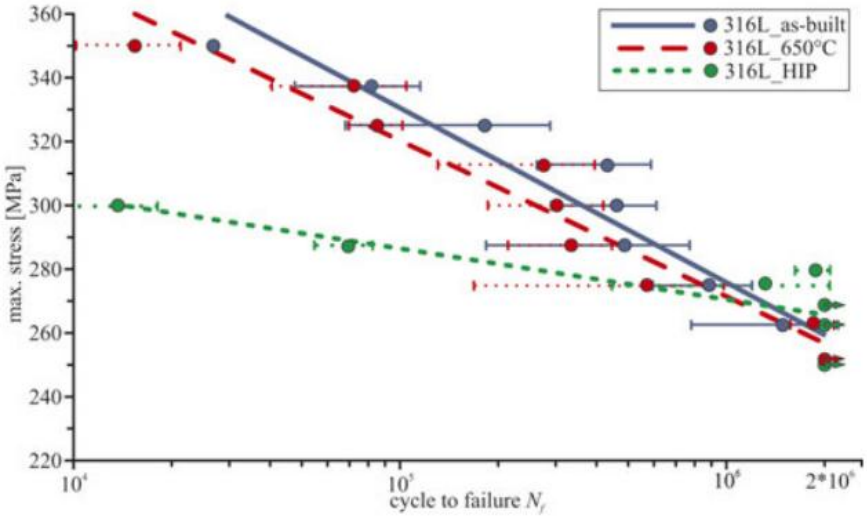

Figure I-11: S–N curves for machined SLM processed 316L specimens under different heat treatments (Leuders *et al.*, 2014)

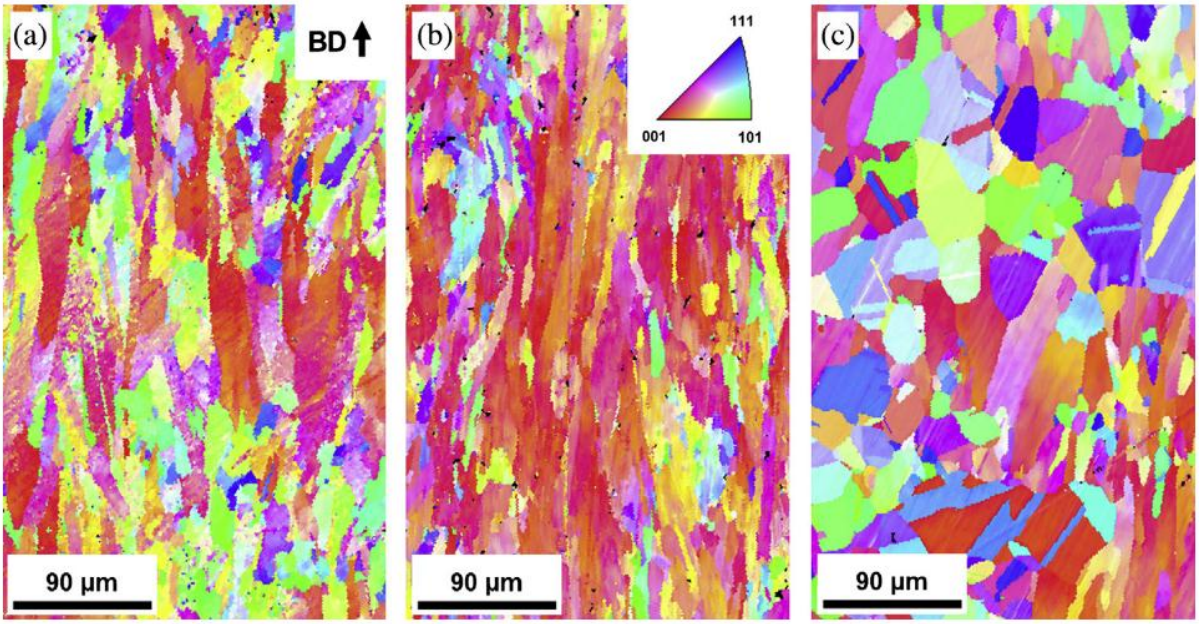

Figure I-12: EBSD inverse pole figure (IPF) maps for (a) as-built 316L specimens, (b) 316L following heat treatment for 2 h at 650 °C and (c) HIP processing. Orientations in the IPF maps have been plotted with respect to building direction (BD). (Riemer *et al.*, 2014)

Leuders et al. (Leuders *et al.*, 2014) compared additional similar tests but of Ti-alloy to the results of Riemer et al. (Riemer *et al.*, 2014) so as to reveal the role of ductility. 316L is a highly ductile material while TiAl6V4 ductility is lower. Results showed that the behavior of TiAl6V4 under cyclic loading is dominated by the process-induced pores and the fatigue behavior of 316L is strongly affected by its monotonic strength. For the SLM SS 316L, its high ductility makes it insensitive to micrometer-sized pores in the LCF range while small pores contribute mainly to the crack initiation in the HCF range.

Mower and Long (Mower and Long, 2016) also investigated the mechanical behavior and fatigue behavior of the SLM SS 316L in terms of the effect of heat treatment. Particularly, most of the specimens used were kept in the as-built surface state without post-machining to preserve this very feature making AM technique different and promising. 5 batches of specimens were tested under bending loading at a ratio of -1 and a frequency of 25 Hz as follows: wrought and machined, horizontal, vertical and HIP, and 2 vertical as-built. The results are plotted in Figure I-13.

The vertical as-built specimen subjected to a stress of 110MPa failed at about 10^6 cycles which is in good accordance with the fatigue limit of 108MPa to a lifetime of $2*10^6$ for the as-built SLM SS 316L in the research of Riemer et al. (Riemer *et al.*, 2014). HIP did not change significantly low cycle behavior governed by large defects. This analysis is in line with the finding of Leuders et al. (Leuders *et al.*, 2014). But a strong improvement of high cycle fatigue strength for as-built (un-machined) specimens can be seen. The explanation is that HIP reduces the prevalence of smaller-sized defects which distribute largely on or near the as-built surfaces. As for all the specimens of Riemer et al. (Riemer *et al.*, 2014), machining eliminated most of small defects near the surface.

From Figure I-13, the effect of building direction is revealed and will be discussed in the following section.

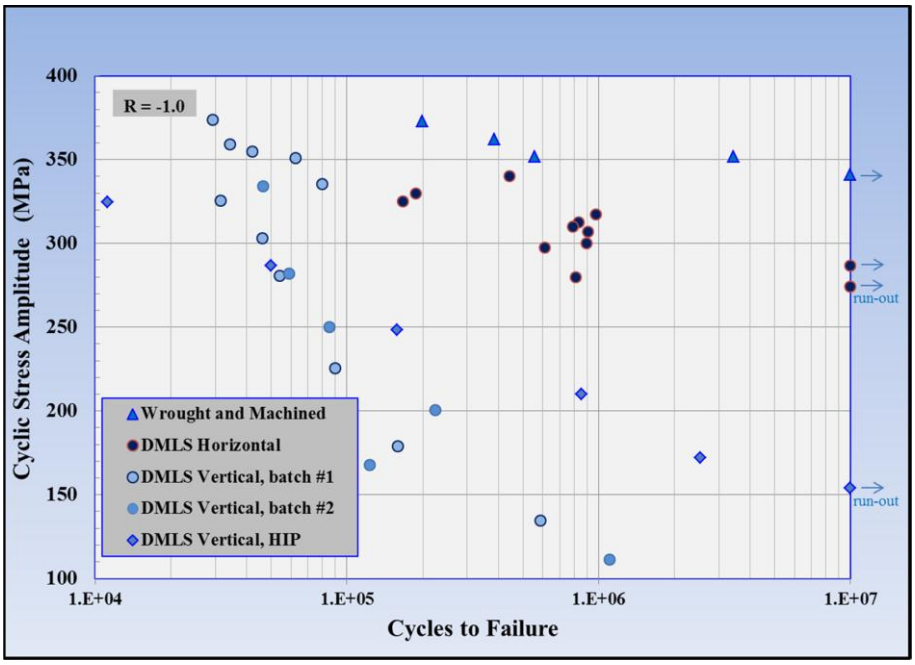

Figure I-13: S-N plots of DMLS 316L in bending fatigue at a frequency of 25 Hz with regards to building direction (Mower and Long, 2016)

I.2.3. Effect of building direction

The effect of building direction should be taken into consideration because the AM materials usually have grains preferentially oriented in the building directions even after heat-treatment.

In the research of Mower and Long (Mower and Long, 2016), the horizontally built specimens had 3 times better performance compared to the vertically built ones while all the specimens were in the as-built surface state (see Figure I-13). From the observations of fracture faces, the horizontally built or vertically built samples fractured because of surface or subsurface defects.

Liverani et al. (Liverani *et al.*, 2017) tested the SLM SS 316L specimens using 2 different building direction of 90° and 45° under rotating bending loading at a load ratio of -1. The threshold for "run-out" was set to $3*10^5$. The specimens were machined. Fatigue limits of the samples at $3*10^5$ cycles were found to be 295 MPa and 365 MPa for 90° built and 45° built respectively. The trend that the fatigue strength for vertical building direction is weaker compared to the fatigue strength for 45° building direction is consistent with the trend reported by Mower and Long (Mower and Long, 2016). The measured UTS for samples built in 45° and 90° were approximately 640 MPa and 570 MPa. Hence, the relationship between the ultimate tensile strength and fatigue behavior was displayed. Fractographic analyses showed that fatigue crack nucleated from pores and binding defects for both vertical and 45° built samples.

A very different S-N curve from Blinn et al. (Blinn *et al.*, 2019) is shown in Figure I-14 (a). The results were from SLM SS 316L samples built in three directions: horizontal, 45° inclined and vertical.

All specimens were turned and polished to keep only the properties of the additively manufactured material volume. No heat treatment was mentioned. The loading was tension-compression with a ratio of -1 at a frequency of 2Hz. It is observed that the vertically built specimens exhibit a better fatigue strength compared to the 45° inclined built and horizontally built specimens. As is seen from the fractography observations, crack initiation at lower stress amplitudes occurs at microstructural defects, i.e. pores. In Figure I-14(b), the microstructure of the tested samples is shown. Besides the different layer orientations, no significant differences in the microstructure of differently oriented specimens can be observed. The microstructure is not as textured as in other results from the literature (e.g. Figure I-12) possibly due to different processing parameters, different powder characteristics, and different manufacturing machines. Because of the different microstructure obtained, it is not surprising to have contradictory results.

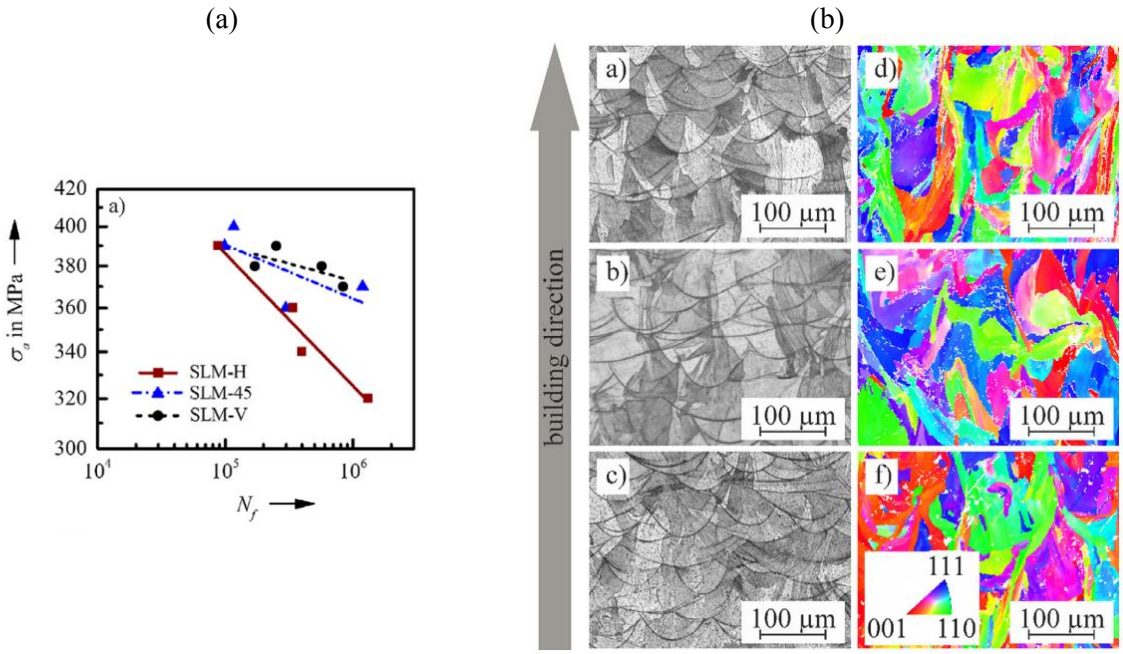

Figure I-14: (a) S-N curves for differently oriented specimens; (b) Light optical micrographs and EBSD-mappings of SLM-H (a, d), SLM-45 (b, e) and SLM-V specimens (c, f). (Blinn *et al.*, 2019)

Still, Figure I-15 shows a dissimilar outcome from Shrestha et al. (Shrestha, Simsiriwong and Shamsaei, 2019). The horizontally built specimens possessed the highest fatigue resistance, while the least fatigue strength was obtained for diagonally built specimens. An explanation from the authors indicates that the different building direction leads to the different projected area of defect in the loading direction. On the other hand, diagonal specimens experience a longer interlayer time interval since a higher amount of material is melted and solidified per layer along with the need for fabrication of support structures. The longer interlayer time interval leads to higher cooling rates, which may result in larger manufacturing-induced LoF defects.

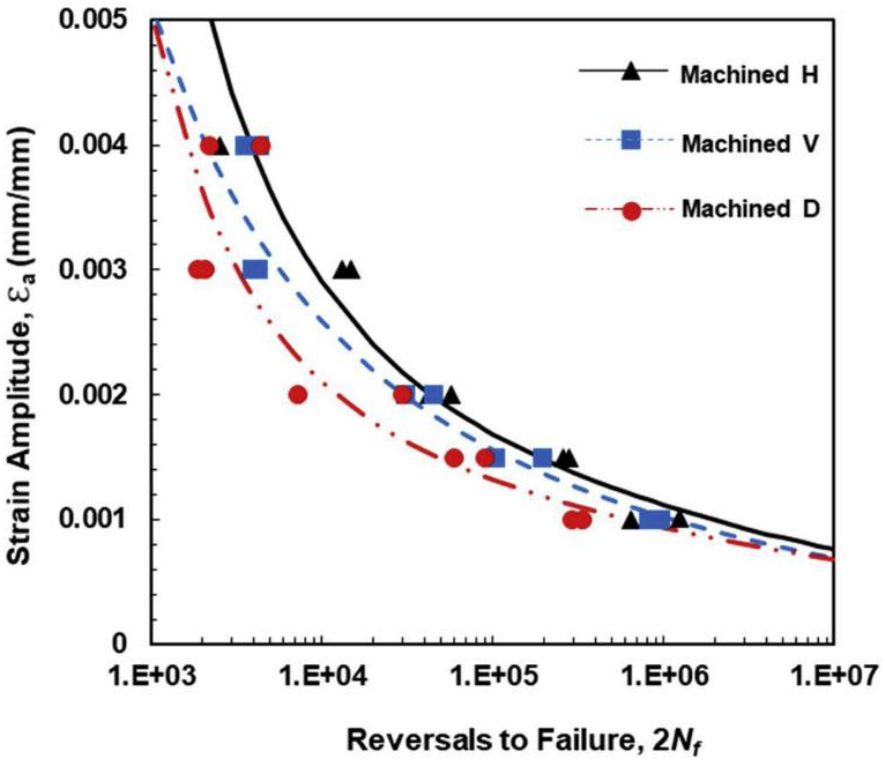

Figure I-15: Strain-life fatigue data along with Coffin-Manson fits for LB-PBF SS 316L specimens in (a) machined vertical, diagonal, and horizontal directions(Shrestha, Simsiriwong and Shamsaei, 2019)

The effect of building direction on the fatigue behavior of SLM SS 316L is still in debate. This finding brings out another concerned aspect of fatigue investigation on the AM materials: the processing parameters that are discussed in the following section.

I.2.4. Effect of processing parameters

Processing parameters can strongly change the AM material properties (Cherry *et al.*, 2014; Ahmadi *et al.*, 2016; Lackey, 2016; Liverani *et al.*, 2017; Suryawanshi, Prashanth and Ramamurty, 2017). However, there is no standard for choosing parameters of SLM processing which leads to the current situation that the process parameters are hardly identical in different literature.

The main challenge for laser powder bed fusion techniques is usually to combine satisfactory as-built surface finish and minimum internal porosity rate. The first criterion is addressed via the optimization of the SLM process itself. The internal porosity rate depends mostly on the laser hatching parameters, e.g. powder, speed, and scanning strategy. Fabricating at higher speed also lowers the local temperatures and thermal gradients of part, which reduces the residual stresses and thus the need for subsequent thermal treatments.

Although many pieces of research studied mechanical properties in terms of process parameters, few concerned fatigue behaviors. Zhang et al. (Zhang *et al.*, 2017) reported fatigue tests under sinusoidal tension loading at R=0.1 of SLM SS 316L made with different laser power: 50%, 70%, 100%, 130%,

150% from the optimized setting P0. All the samples were cut from horizontally built blocks by EDM wire cutting and machined subsequently. No heat-treatment was applied because the residual stress was considered inconsequential to the fatigue properties by the authors. The case when the number of cycles reached 10^6 was considered as a run-out. All results were plotted in the following Figure I-16. Only the 0.5P0 batch of specimens showed a notable diminution in fatigue strength. The high cycle fatigue properties of the specimens showed some similarities with their UTS, as shown in Figure I-17. Fractography analysis showed the driven fracture mechanism was most of the time the porosity for the 0.5P0 and 1.5P0 and microstructure for the other batches.

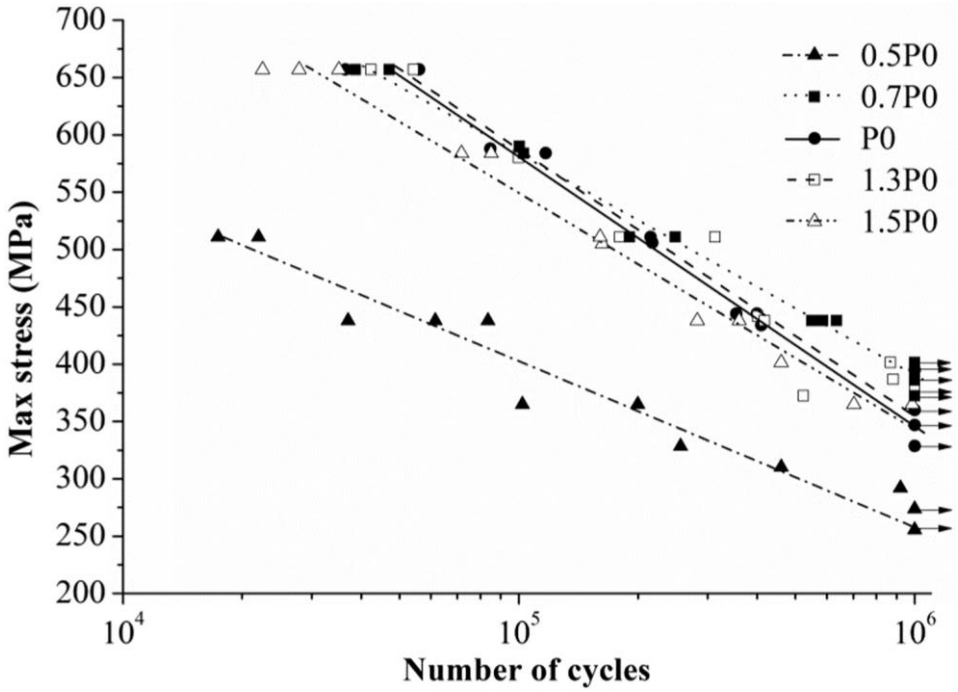

Figure I-16: S-N curves of SS 316L samples with different laser powers (Zhang *et al.*, 2017)

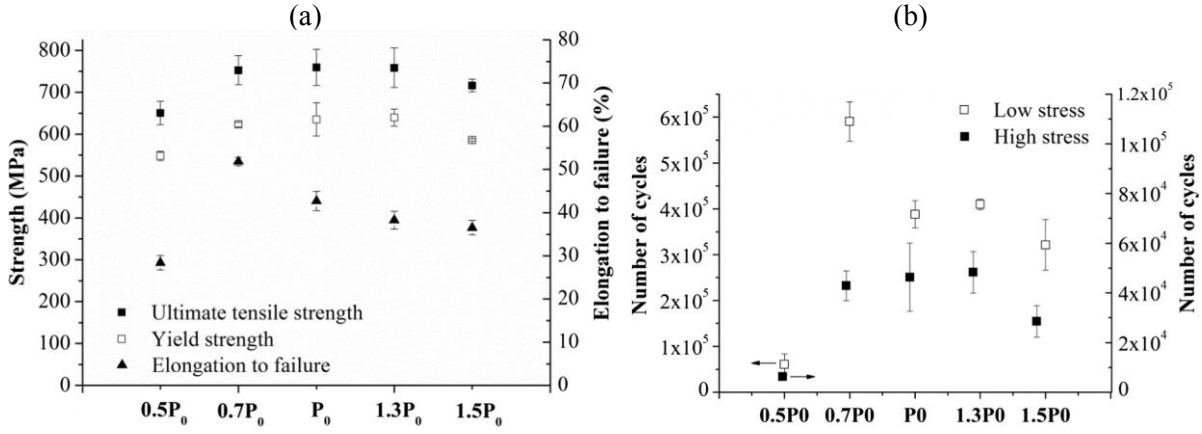

Figure I-17: (a) Mechanical (b) and fatigue properties of SS 316L samples (Zhang *et al.*, 2017)

Andreau et al. investigated the influence of contour and hatching zones on HCF properties of 316L (Andreau, Pessard, *et al.*, 2019). The samples used were fabricated vertically using optimized contour parameters and were polished using 2000 grit paper until mirror-like surfaces were obtained. Several

samples were turned to remove the contour for comparison. Different hatching zones were realized by varying the scanning speed whilst the other parameters (power, diameter, hatch spacing) were kept identical. A higher scanning speed usually results in a higher porosity rate. Tensile fatigue tests were conducted at a ratio of 0.1 and a frequency of 65 Hz. Samples that did not fail after 10^6 Hz were considered run-out. It is found that the 316L samples fabricated at conventional parameters or 25% higher speed showed similar fatigue properties (shown in Figure I-18 a). In addition, if compared to other research (see Figure I-6), the reported loading levels at failure are similar to that of machined samples in literature. We can conclude that the HCF properties were mostly influenced by the contour in the first hundreds of microns from the surface. Besides, a Kitagawa diagram is shown in Figure I-18 b. The fatigue strengths of samples tested are plotted over the corresponding critical defects measured. This finding confirms that the global fatigue properties of samples are mostly driven by the critical defects dimensions.

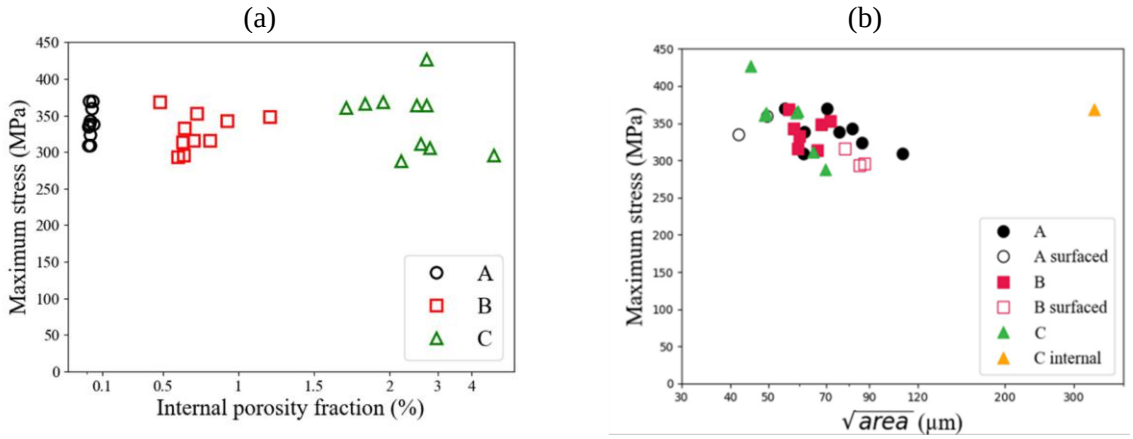

Figure I-18: (a) Variation of Maximum stress at failure (MPa) with internal porosity fraction (%); (b) Kitagawa diagram of all the samples tested (Andreau, Pessard, *et al.*, 2019) (A, B, C represent different scanning speeds)

Although the presence of pores in additively manufactured parts and their influence on mechanical properties is a highly discussed topic in the literature, their harmfulness can be greatly impacted by their position and the density close to the surface of a sample. Productivity rates could be greatly increased by combining optimized fabrication parameters close to the surface of a part with faster parametrizations in the bulk.

I.2.5. Discussion

For the as-built parts made of SLM 316L, defects and microstructure which are directly related to the building parameters are the main sources of fatigue crack initiation.

The fatigue process is very sensitive to surface conditions. Since fatigue cracks occur mainly on free surfaces, surface conditions have a considerable effect on fatigue strength. Specimens obtained by SLM

contain many defects that are inherent to the process and are impossible to eliminate even with the best process parameters monitoring. Samples in the as-built state from SLM manufacturing always show very poor fatigue performances.

Microstructure also plays a role in the fatigue properties, but to a lesser extent. The grain orientation versus the solicitation direction and the grain morphology can both impact the low cycle fatigue life and the fatigue crack growth behavior. In the high cycle fatigue domain, the effect of the microstructure seems to be less pronounced due to the presence of pores that control the fatigue strength. HIP only closes internal pores. Hence, no significant difference seems to be found in the context of HCF. Annealing treatments, that reduce porosity as well as modify the microstructure, can affect the fatigue properties. But for 316L, some results of the literature show superior mechanical performances in as-built parts than in heat-treated ones. Moreover, the porosity of SLM 316L is often lower than 0.1% which means further effort to reduce porosity seems to be unnecessary.

There have been contrary reports on the effect of layer orientation on the fatigue behavior of SLM SS 316L. The anisotropy in the fatigue behavior is primarily dependent on the types of defects found responsible for crack initiation and failure. As the stress concentrations resulting from LoF defects depend on their orientation with regard to the loading direction, specimens fabricated in different orientations are likely to show different fatigue behavior. On the other hand, stress concentrations resulting from the spherical pores may not depend on their orientation with respect to the loading direction, which can result in a more isotropic fatigue response.

I.3. Summary

As a complicated and much-studied phenomenon, fatigue relates to a broad range of aspects. This project is framed in the high cycle fatigue phenomenon of additive manufactured steel 316L. Generalities regarding the key aspects: AM technique, in particular the SLM technique, High cycle fatigue, and Stainless steel 316L are reviewed to complement the subject's context.

Recent related experimental results are presented. Many factors are involved in the fatigue crack initiation in SLM SS 316L. The most investigated factor is the surface finish state. It is known that the as-built parts have a notable and inevitable rough surface state which is believed to be detrimental to the fatigue strength. It is confirmed that the as-built parts have poor performances while machining or polishing can increase the endurance limit. The effects of different heat treatments lead to some controversy. Heat treatment is often considered as a common method to improve materials' performance. For the machined specimens, annealing does not necessarily change the high cycle fatigue performance or the polycrystalline microstructure. The microstructure is changed by HIP but the fatigue limit in the HCF regime seems sometimes to be unaffected. Building direction which changes the texture

of produced specimens is found to influence fatigue behavior. Nevertheless, the effects of different affecting factors can be hardly decoupled from results of the literature since the process parameters are not always the same. Recent research demonstrates that the laser density used during fabrication may result in different fatigue performances.

With these preliminary understandings of the fatigue behavior of the SLM SS 316L, specific investigations concerning many aspects, e.g. surface state, microstructure, building direction, etc. are needed. In the context of the current PhD study, we have to make choices. The surface roughness and the defects are always considered to be detrimental to fatigue performance. But the exact role played by the microstructure has not yet been actively investigated and still remains an open question.

Even though the current project contains an important experimental part, it turns out that an additional comprehensive numerical study is essential to answer some of the questions regarding the coupling effects of surface roughness, defects and microstructure on the fatigue strength of SLM 316L.

Syntheses

- General information of the research context is provided: SLM technique, fatigue phenomenon, and properties of the studied material, SS 316L.

- Recent research of SLM SS316L in the fatigue domain is comprehensively reviewed in different aspects: the effect of surface finish, the effect of heat treatment, the effect of building direction and the effect of processing parameters.

- Surface treatment, e.g. machining, turning, and polishing, can improve the fatigue performance of AM material.

- Heat treatment does not necessarily increase the fatigue limit for SLM parts at least for the machined specimen. Its effect on as-built parts is in debate.

- It is often assumed that the vertically fabricated specimen has the poorest fatigue strength. But both support and opposition can be found in the literature.

- Processing parameters have a great influence on the fabricated part's microstructure which results in scatter in fatigue behavior.

Chapter II.

Material preparation and characterization

II.1. Specimens elaboration 30

II.1.1. Powder characterization 30

II.1.2. Fabrication of specimens 33

II.1.3. Heat treatment 35

II.2. Microstructural characterization 38

II.2.1. Macrostructure of the SLM SS 316L 39

II.2.2. Microstructure of the SLM SS 316L 41

II.2.3. Grain morphology and Crystallographic texture 44

II.3. Inherent defect characterization 48

II.3.1. Surface state characterization 48

II.3.2. Porosity characterization 51

II.4. Mechanical behavior 54

II.4.1. Hardness 54

II.4.2. Monotonic tensile test 55

II.4.3. Cyclic tensile test 59

II.5. Conclusions 63

Syntheses 65

In this chapter, the material properties of the austenitic stainless steel fabricated by selective laser melting, SLM SS 316L, are studied. The experimental efforts made concerning material preparation, fabrication and characterization are described comprehensively.

In the first section, the preparation of specimens that are mainly fatigue test specimens along with several microstructure-testing specimens are explained from the powder characterization to the post-treatment of fabricated parts. In the second section, as the microstructure of AM material often varies and is highly dependent on the process parameters, different types of microstructure characterization are carried out and the results are discussed. In the third section, the inherent defects resulting from the additive manufacturing SLM process are measured and analyzed. The role played by those defects is analyzed with regard to fatigue strength. Typical mechanical tests, i.e. monotonic and cyclic tension loading tests, together with hardness tests are presented in the fourth section and a comparison with data from the literature is proposed.

II.1. Specimens elaboration

The specimens used in this study were produced by the company PRISMADD (currently Weare Group), the manufacturing and post-treatment protocol is the one applied by the company to industrial parts made of 316L steel. This protocol consists in using a (new or recycled) powder volume N times until the oxygen rate becomes greater than 1000 ppm. The manufacturing parameters are also optimized by the company to minimize the porosity rate. A stress relieving heat treatment (in air) is then carried out before the parts are removed from the production tray by wire Electric Discharge Machining (EDM). This section is devoted to a description and an analysis of this protocol. The powder properties are first presented, then the manufacturing and post-processing parameters are detailed. The residual surface stresses after heat treatment are measured and analyzed.

II.1.1. Powder characterization

The precision and the quality of additive manufactured products are strongly influenced by the powder quality. Among the numerous characteristic parameters, the particle size is the most important one. The powder used in this study is an austenitic stainless steel 316L powder of industrial grade. It is a 12-times sieved (recycled) powder (with an oxygen rate less than 1000 ppm) seen by Weare Group as appropriate for providing quality AM parts. An analysis of the recycled powder chemical composition was performed. The nominal (normalized) and the actual (used) chemical composition of SS 316L is given in Table II-1. The chemical composition of the studied 316L powder is close to the nominal one.

Table II-1: Nominal and measured chemical composition of 316L

element	C	Mn	P	S	Si	Cr	Ni	Mo	N	Fe
%m (nominal)	<0.03	<2	<0.045	<0.03	<0.75	16-18	10-14	2-3	<0.1	balance
%m (measured)	/	/	/	/	/	15.87	10.86	1.46	/	71.8

Laser granulometry analysis was realized on two powder samples to make sure the repeatability (sample A and B whose distributions are displayed in Figure II-1). The particle size is described by D10-D90 where D10 is the equivalent volumetric diameter at cumulative probability of 10% and D90 is the equivalent volumetric diameter at cumulative probability of 90%. D50 (equivalent volumetric diameter at cumulative probability of 50% called also average equivalent diameter) can be used to compare between two powder distributions. The particle size in the delivery state (before recycling) is 5-25 µm, as can be seen in Figure II-1.

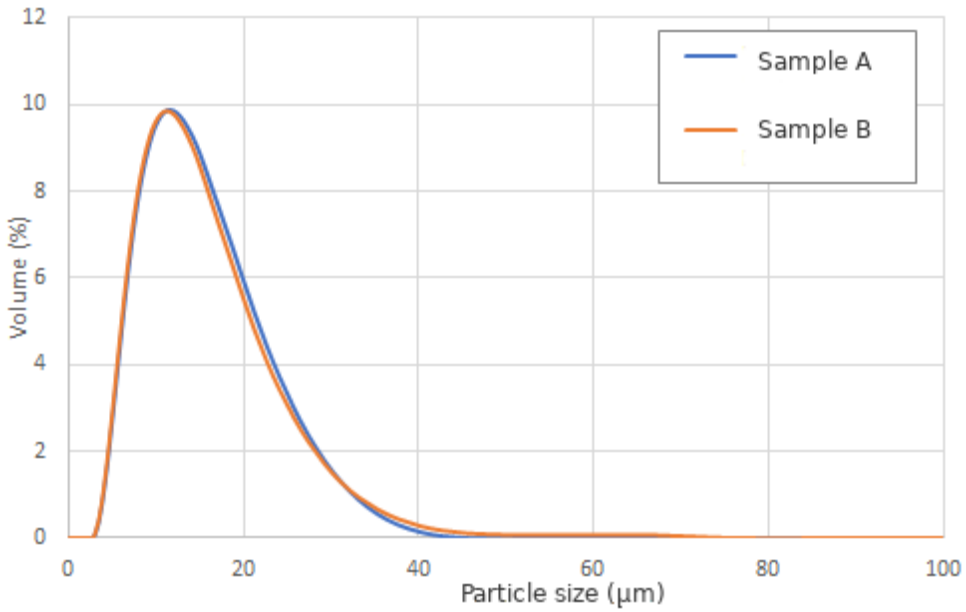

Figure II-1: Particle size distribution of 316L powder Prismadd12

From the microscopic observations shown in Figure II-2 , the particles appear to be predominantly spherical but sometimes show asymmetrical satellite-like shape. The satellite-like particle is formed when one particle sticks to a larger one during solidification. The powder recycling can lead to the presence of oxidized particles which are a source of internal imperfection.

(a)

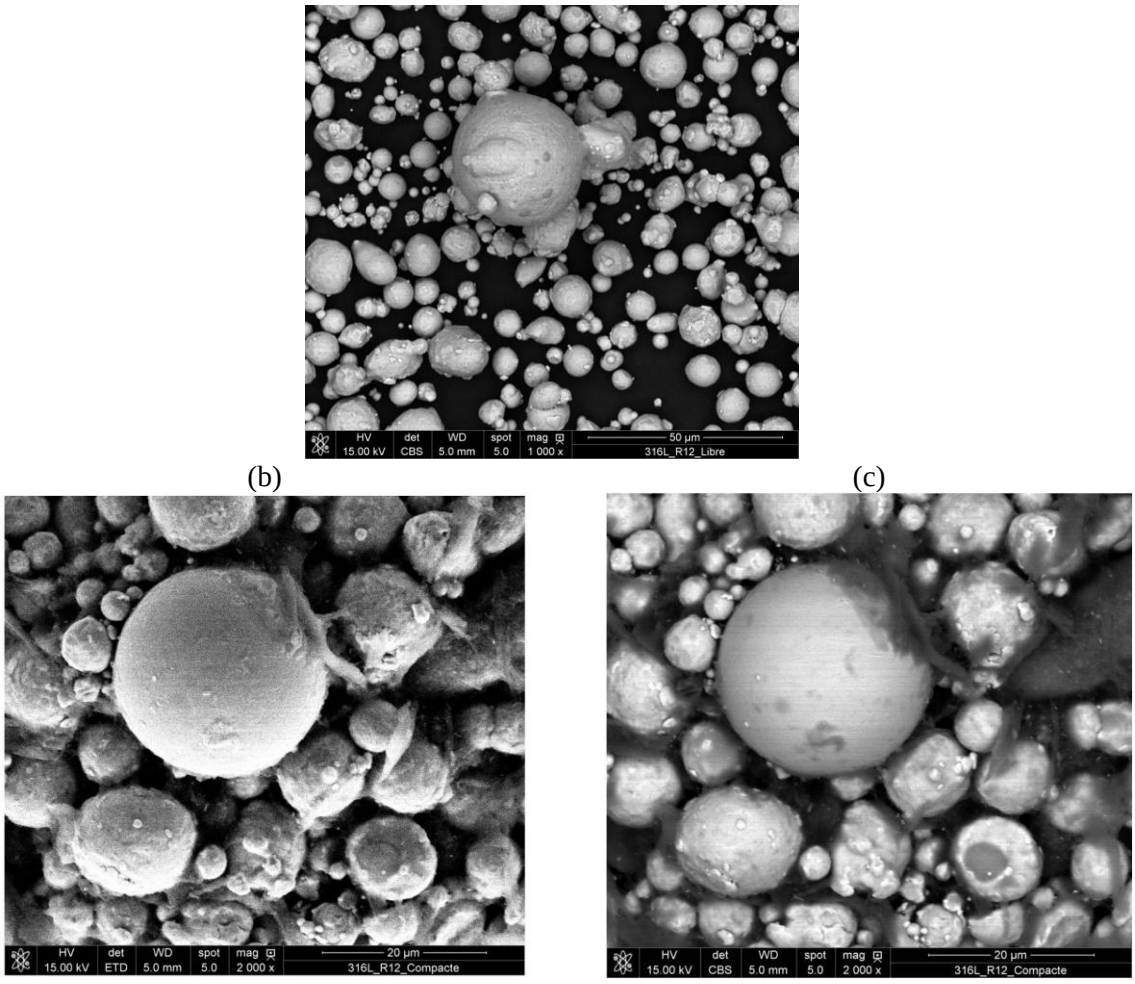

Figure II-2: Powder of steel 316L under microscope: (a) SEM (b) SE detector (topography) (c) with BSE detector (chemical contrast)

The microstructure of a powder particle can be observed after chemical attack. The SEM observation (see Figure II-3) shows the powder is almost single phase and has a fine microstructure with an average grain size of less than 4 µm.

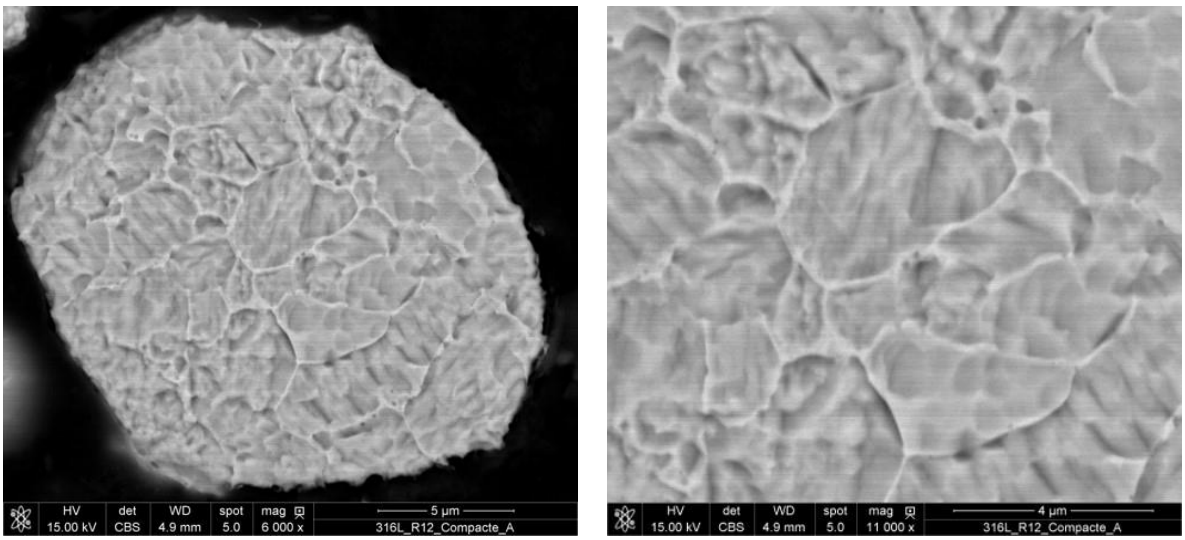

Figure II-3: Powder structure (after chemical attack)

II.1.2. Fabrication of specimens

Two trays of around 80 specimens were manufactured with the same process parameters by the Weare Group. The SLM machine ProX DMP 320 (see Figure II-4a) was used with optimal parameters for SS 316L (listed in Table II-2). The powder melting and fusion was achieved by a laser with a spot size of 70 µm and with a power of 275 Watts. The laser scanning speed was 700 mm / s and the jumping speed 5000 mm / s. The hatch spacing was set to 70 µm and the layer thickness to 30 µm. The scanning strategy was hexagons, also known as random islands, with a recovery distance of 10 µm. Contouring was not applied here. Generally, the specimens used in the literature often experience contouring since it is a default configuration for most of the SLM machines. More exactly, this process step can improve the surface state. In our study, as we try to focus on the surface state effect, the choice is made to skip this step and hence to work with high roughness for the as-built configuration.

Table II-2: SLM processing parameters for specimen's fabrication

Machine	Energetic parameters					Scanning strategy	
ProX DMP 320	Laser spot size (µm)	Scanning speed (mm/s)	Power (W)	Hatch spacing (µm)	Layer thickness (µm)	Laser trajectory	Contouring
	70	700	275	70	30	random island	No

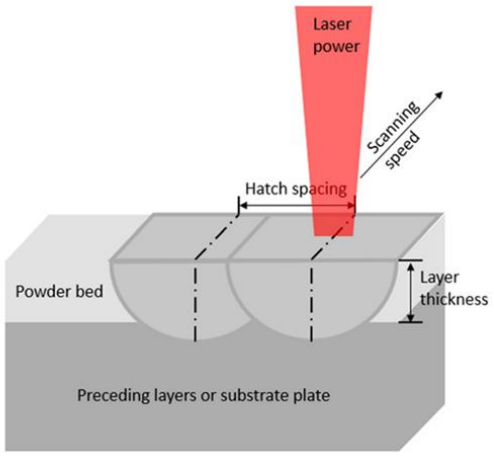

SLM process parameters: laser power, scanning speed, hatch spacing, and layer thickness (Yap *et al.*, 2015)

(a) (b)

Figure II-4: (a) SLM machine (3D system ® ProX 320) and (b) fabricated tray of specimens

All the specimens with the geometry shown in Figure II-5 were vertically built, i.e. the axis oriented along the vertical direction. Two identical trays were fabricated, each tray contained (Figure II-4b):

- 30 specimens for bending fatigue test,
- 30 specimens for torsion fatigue test,
- 5 specimens for traction test and,
- 15 cylinder specimens of length 10 mm and of 3 different diameters (2; 4 and 8mm) for microstructure and defect characterization.

All the specimens have been numbered (Figure II-4b) in order to track a possible effect of the location on the different properties.

(a) Characterization specimens (microstructure)

cylinder specimens of length 10 mm and of 3 different diameters (2; 4 and 8mm)

(b) Tension specimens (cyclic behavior and fatigue)

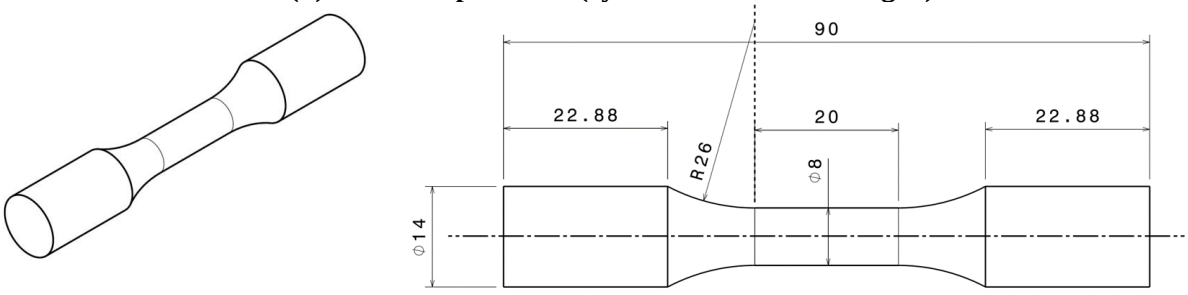

(c) Bending specimens (fatigue)

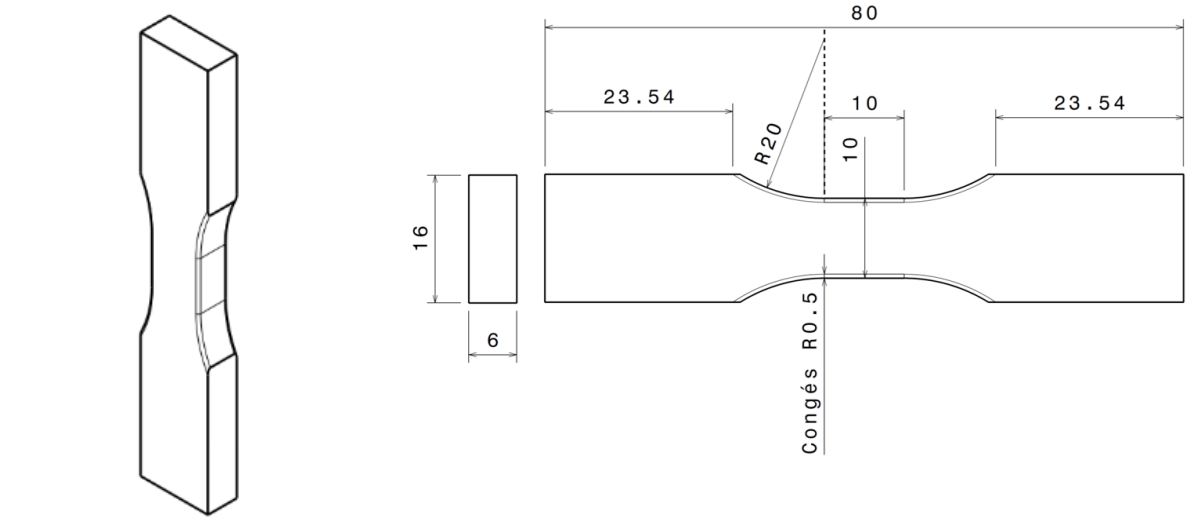

(d) Torsion specimens (fatigue)

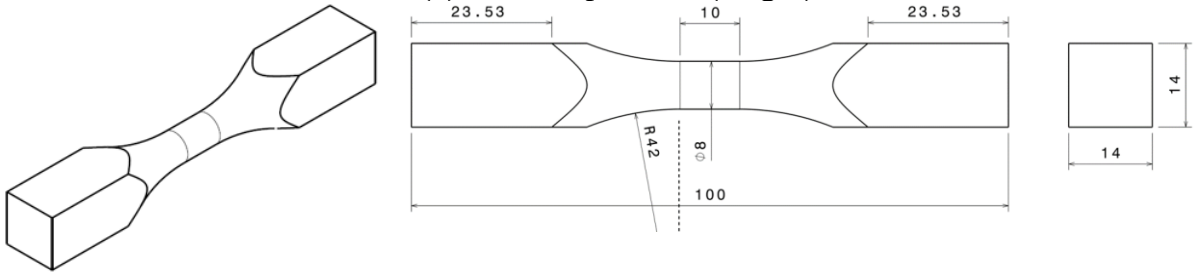

Figure II-5: Geometries of specimens (dimensions in mm): (a) Characterization specimens (microstructure); (b) Tension specimens (cyclic behavior and fatigue); (c) Bending specimens (fatigue); (d) Torsion specimens (fatigue)

II.1.3. Heat treatment

A stress relieving treatment recommended and used by Weare Group was carried out on the assembly before the separation of the specimens from the tray (substrate plate). This treatment aim is to reduce or remove the residual stresses without modifying the mechanical properties of SS 316L. It consists in a temperature holding of 620 °C during 90 minutes followed by a natural cooling during 800 minutes until the temperature drops to 180 °C (Figure II-6). This treatment is conducted in the air atmosphere without environment control. Then, wire electrical discharge machining is used to cut off the samples from the trays. Even though some results in the literature (Leuders *et al.*, 2014; Riemer *et al.*, 2014; Zhang *et al.*, 2019) point out that the residual stress state does not affect the mechanical properties of SS316L in particulars fatigue performance, this heat treatment was applied in this study.

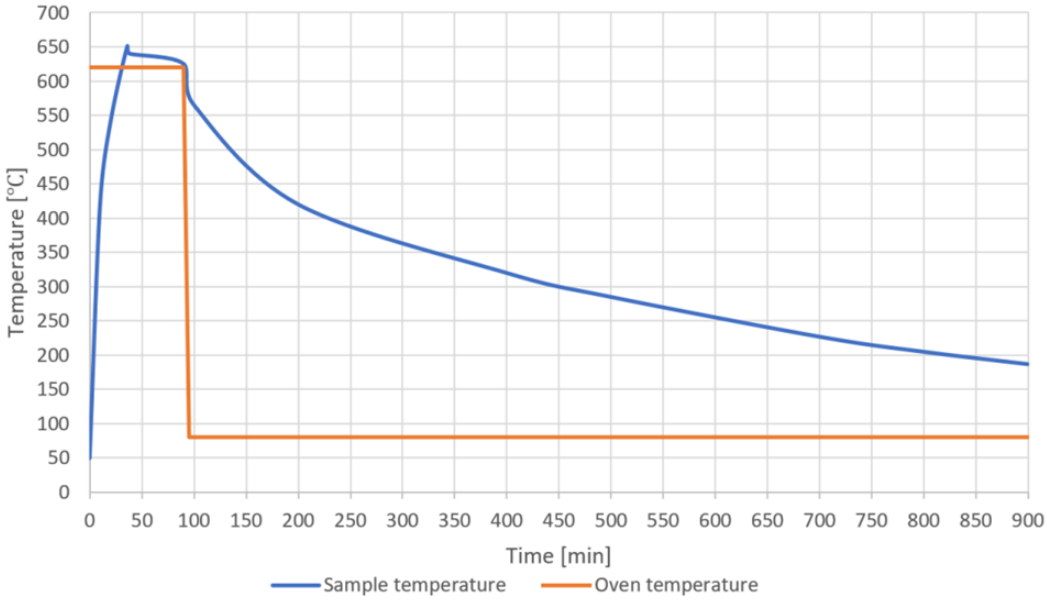

Figure II-6:The temperature-time curve of stress relief heat treatment

The surface residual stresses resulting from the SLM process were analyzed after the stress releasing heat treatment by X-ray diffraction method. The surfaces of 3 torsion and 3 bending samples in different tray locations were chosen to perform this analysis. The measurements are conducted in:

- the direction parallel to the building (manufacturing) direction designated by "direction 1" (longitudinal direction of the bending specimens and along the axis of revolution for the torsion specimens).
- the transverse direction, orthogonal to direction 1 (designated by “direction 2”)

A collimator is used to obtain a beam diameter of 2 mm. The parameters of the analysis are summarized in Table II-3. An example of the diffraction peaks obtained is illustrated in Figure II-7a. This peak is then analyzed after a fitting procedure using a Lorentzian function. The $\sin^2(\psi)$ method is applied (Figure II-7b) to obtain the value of the normal and the shear stresses according to the studied direction and plane.

Table II-3: The parameters of residual stress analysis

Anode:	Mn Kalpha	Diffraction angle (2θ):	152°
Filter:	Chromium	{h k l} plane:	{3 1 1} (Fe(γ))
Counting time:	60 seconds	Anisotropy coefficient (ARX):	1,79
Number of directions:	19	U	20 kV
		I	1 mA

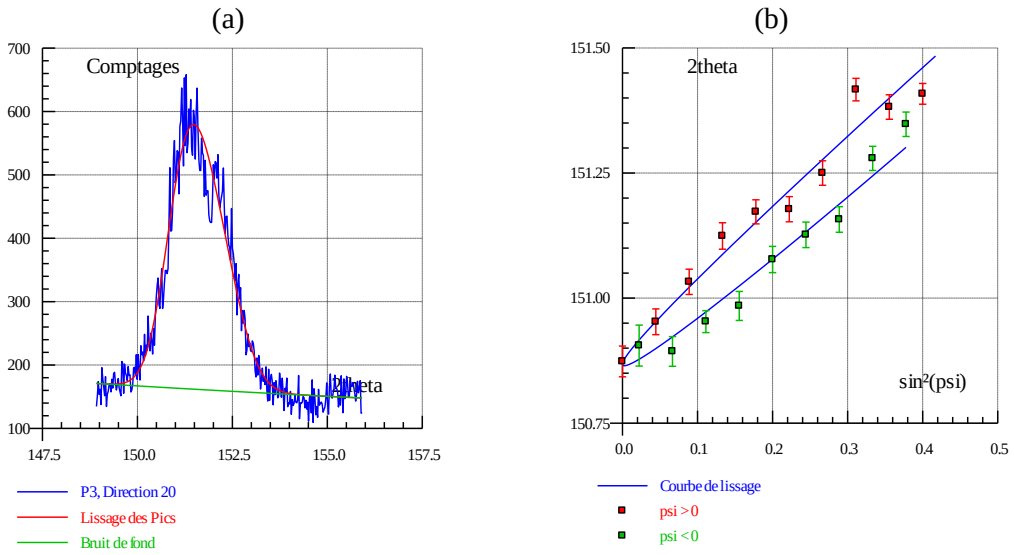

Figure II-7: (a) Example of a diffraction peak obtained after a counting time of 60 seconds in a given direction and (b) example of fitting by the $\sin^2(\psi)$ method.

The measures were made on the four faces (indexed by A, B, C and D in Figure II-8) of the upper and lower heads of the 3 torsion specimens (specimen 6, 13 and 18) and on the gauge length (indexed by face A, face B, profile A and profile B in Figure II-8) of the bending specimens (specimen 2, 16 and 27).

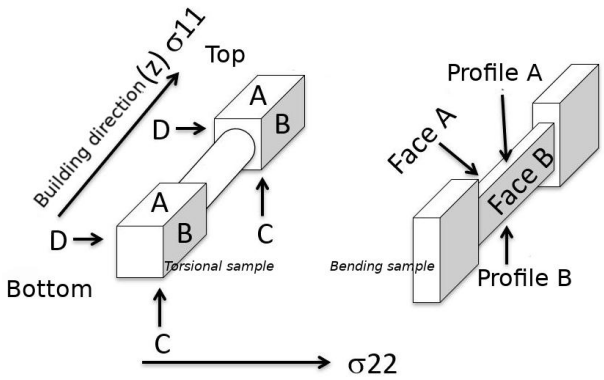

Figure II-8: Location of the residual stress measures on the torsion and bending samples

The different results collected are listed in Table II-4. It is observed that:

- The heat treatment did not relieve completely the residual stresses, but they are rather low. The σ_{11} component was in a range 100-200 MPa while the σ_{22} component varied from 50 to 100 MPa.
- The shear stress is zero everywhere.
- The residual stresses do not seem to depend on the measure position on the specimen or the sample position on the tray.

Table II-4: Surface residual stress values after stress releasing heat treatment for the studied specimens.

		σ11 [MPa]	$I_{\sigma 11}$ (±) [MPa]	σ22 [MPa]	$I_{\sigma 22}$ (±) [MPa]	τ12 [MPa]	$I_{\tau 12}$ (±) [MPa]
Bending specimen 2	Face A	130	12	63	14	0	2
	Face B	164	20	100	14	5	2
	Profile A	142	14	71	20	1	2
	Profile B	117	17	74	18	0	2
Bending specimen 16	Face A	174	16	100	14	-6	3
	Face B	189	9	55	8	8	2
	Profile A	117	14	51	15	-3	2
	Profile B	182	24	62	13	-4	1
Bending specimen 27	Face A	103	16	44	9	4	2
	Face B	72	11	64	14	8	2
	Profile A	100	20	73	10	5	3
	Profile B	145	14	56	15	5	2
Torsional specimen 6	A top	127	29			7	5
	B top	170	16			12	3
	C top	97	9			4	1
	D top	70	21			3	3
	A bottom	137	11			-2	2
	B bottom	170	9			0	2
	C bottom	100	14			-3	2
	D bottom	91	9			0	2
Torsional specimen 13	A top	132	12			4	2
	B top	196	16			7	3
	C top	119	18			10	3
	D top	86	12			3	2
	A bottom	172	20			-5	3
	B bottom	164	15			-5	2
	C bottom	114	15			2	2
	D bottom	93	15			-5	2
Torsional specimen 18	A top	90	18	50	8	2	1
	B top	144	21	67	15	4	2
	C top	181	16	97	14	0	2
	D top	159	15	65	14	5	2
	A bottom	105	13	54	11	3	2
	B bottom	154	21	74	14	2	2
	C bottom	200	15	83	10	6	2
	D bottom	127	15	52	12	0	2

II.2. Microstructural characterization

The microstructures generated by SLM can be observed at two scales. We distinguish:

- The macrostructure generated by the passage of the laser spot and leading to fusion pools.
- The microstructure composed by grain crossing several melt pools and whose morphology and crystallographic texture are highly dependent on the cooling kinetics.

The observations were carried out on two planes (Figure II-9): (i) Z-plane also called manufacturing or lasing plane, this is the plane perpendicular to the manufacturing axis Z, it contains the history of a single layer; (ii) X/Y-plane, this is the plane perpendicular to X or Y and parallel to the Z axis. This

plane is constructed layer by layer during manufacturing and therefore contains the thermal history of all layers.

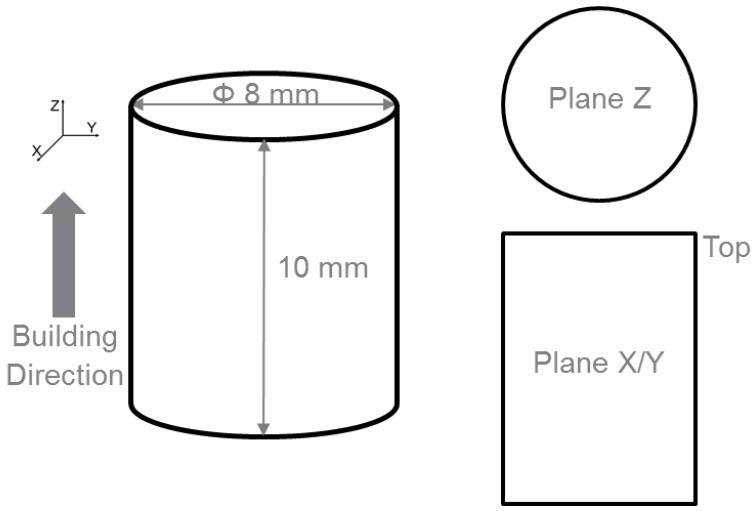

Figure II-9: Illustration of microstructure observation planes.

II.2.1. Macrostructure of the SLM SS 316L

The macroscopic structure of the Z-plane can be seen in Figure II-10. Using optical macroscopy, it is possible to distinguish weld beads corresponding to the main direction of the laser displacement. In this plane, the section of the grains is austenitic quadrangular. The optimized technique of 3D printing of metals consists of separating the manufacturing plane into several zones, generally of rectangular shapes. Once the laser finishes one zone it passes to the next one and can carry out the welding in the direction perpendicular to the preceding zone. This optimization reduces the residual stress in the final sample. The laser path is visible when changing directions (see "Laser spots" in Figure II-10).

With respect to the X/Y-planes (see Figure II-11), we can see ellipses, characteristic of the SLM process since they represent a section of the melt pools which appear during the passage of the laser. The macrostructure resembles fish scales. The observation of these planes makes it possible to clearly distinguish the interfaces between the layers, as well as, to see the elongated shape of austenitic grains crossing several layers. We can also observe the grains that are formed during the manufacturing process. Their growth direction roughly coincides with the Z-axis of the specimen.

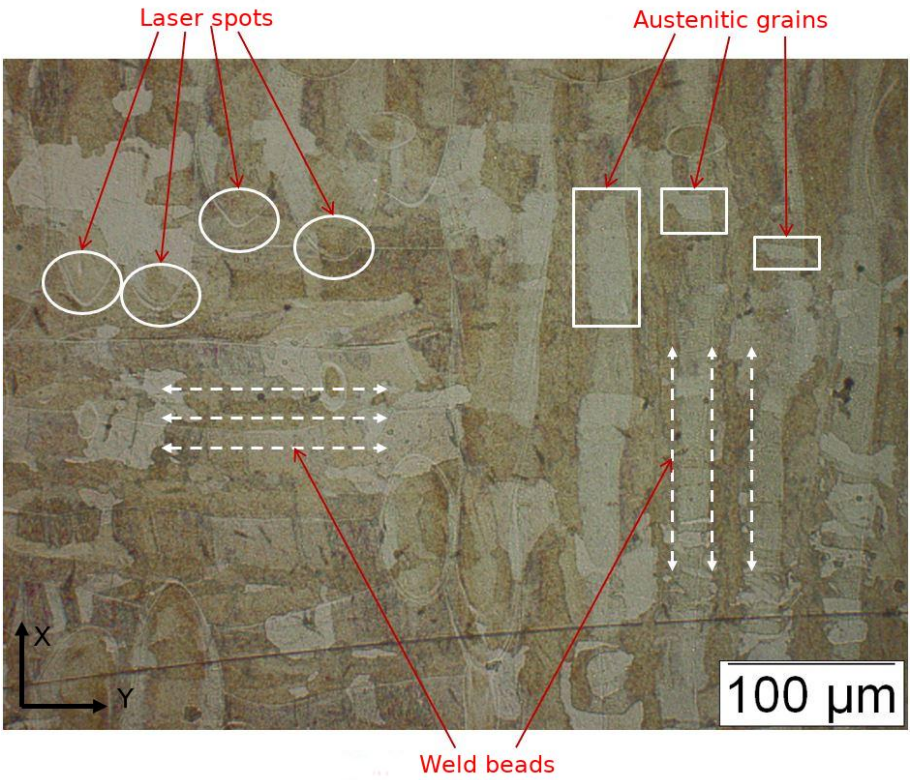

Figure II-10: Optical microscope observation on lasing plane Z

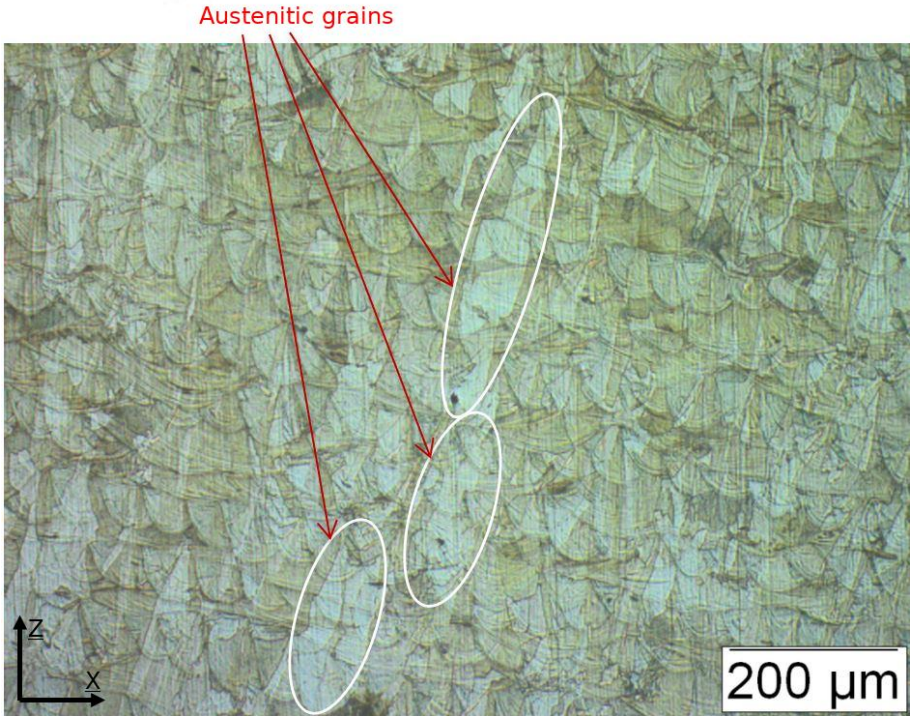

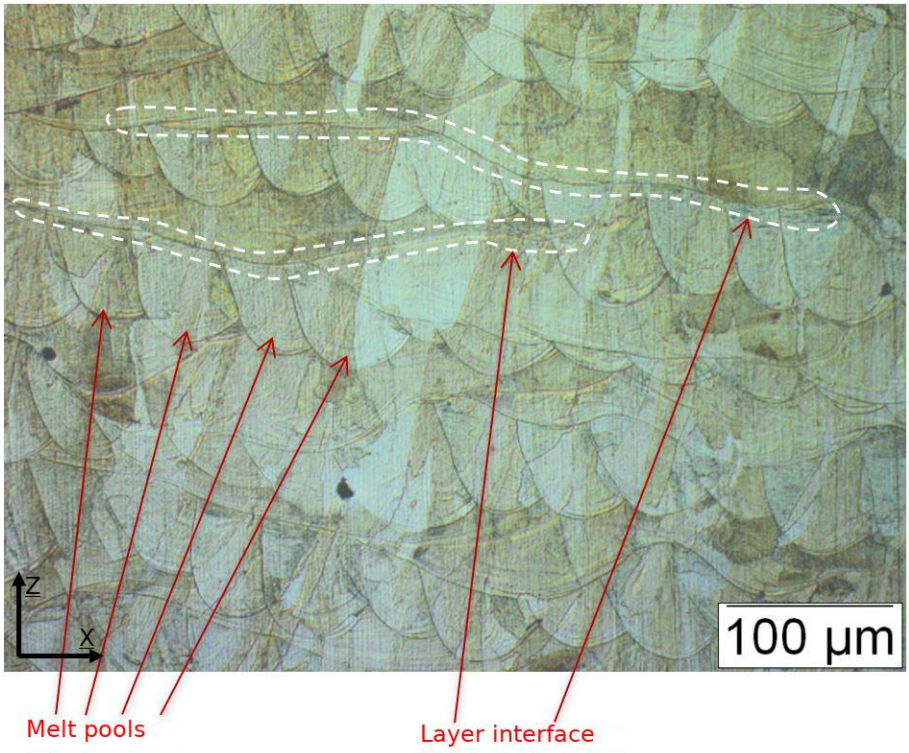

Figure II-11: Optical microscope observations on plane X/Y

II.2.2. Microstructure of the SLM SS 316L

By means of a chemical attack with aqua regia, we can reveal the grains of austenite. For the micrograph taken on the surface perpendicular to the building direction, a 10-seconds chemical attack was conducted. While for the lateral micrographs, the chemical attack lasted 40 seconds.

The microscopic structure in the Z plane of the specimen is shown in Figure II-12. At this scale, it becomes possible to observe the dendritic structure of the austenitic grains.

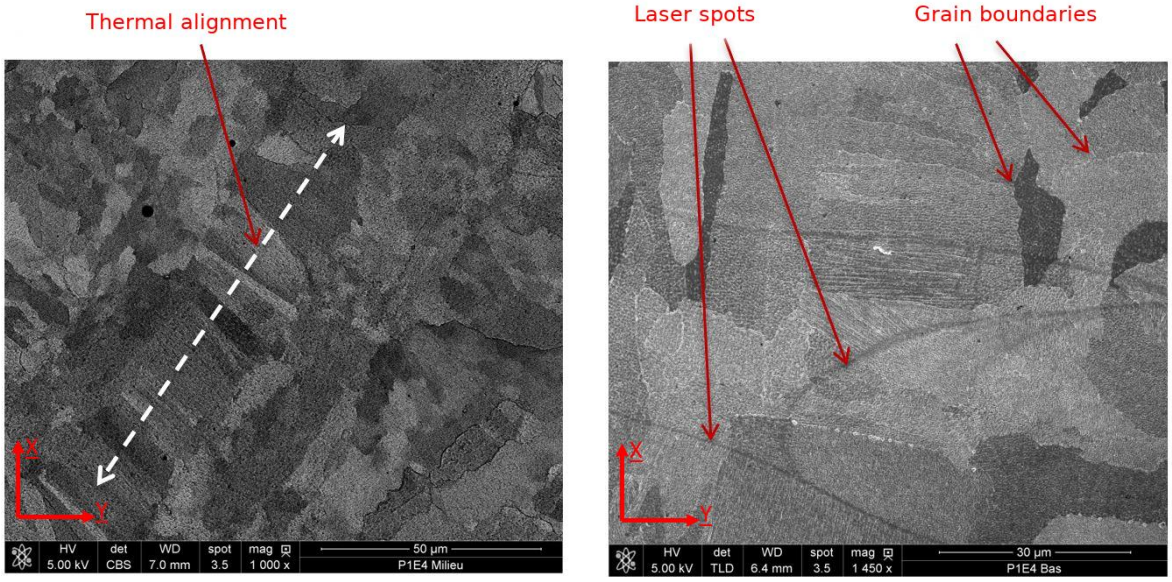

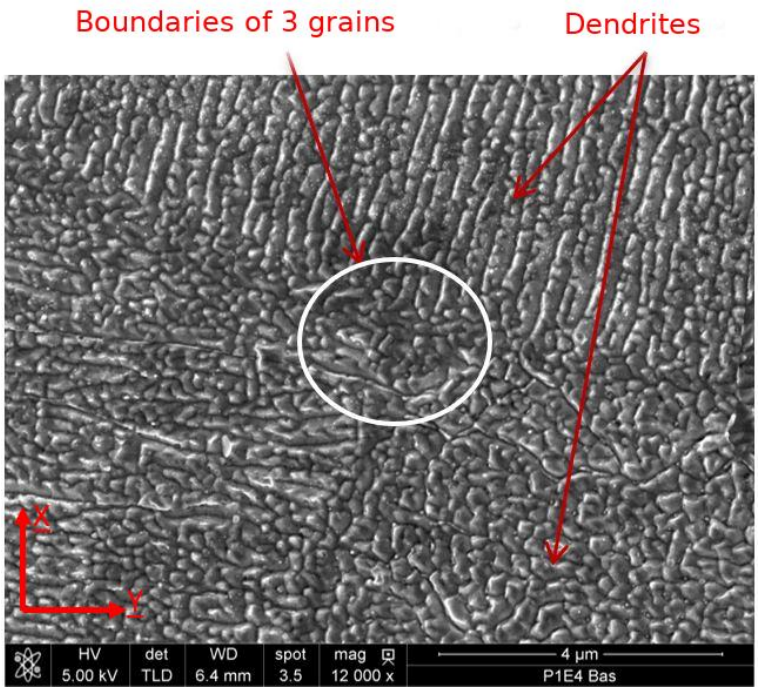

Figure II-12: SEM observations in the plane Z

The Figure II-13 illustrates the microstructure in the X/Y-planes. We can observe the columnar grains oriented along the Z-axis and passing through several layers. Figure II-13 b-d clearly shows the crossing of the melt pools by the grains. This aspect can only be seen on a side section. Conventionally, the preferred direction of growth in FCC materials is the <100> direction. It is oriented according to the maximum local thermal gradient. In SLM, despite the high cooling rates (≈10^6 K / s), this preferred direction of growth is respected. We thus find, in all the studies, a grain growth along <100> perpendicular to the solidification front formed by the melt pools.

On a finer scale, we can see bundles of dendrites passing through melt pools. This type of structure is obtained during the very rapid solidification of the melt pools.

(a) (b)

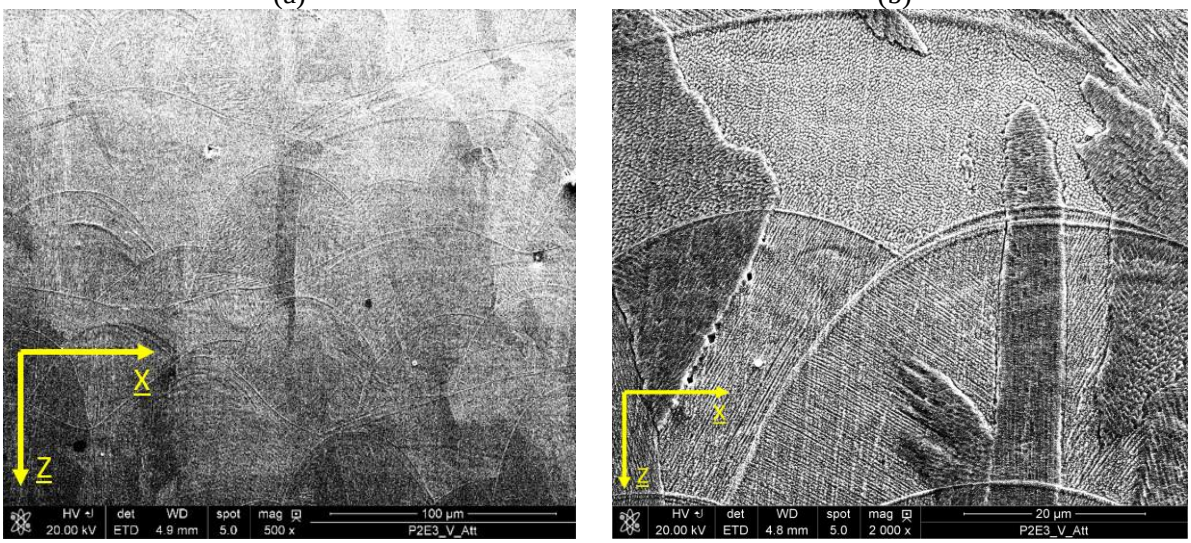

(c) (d)

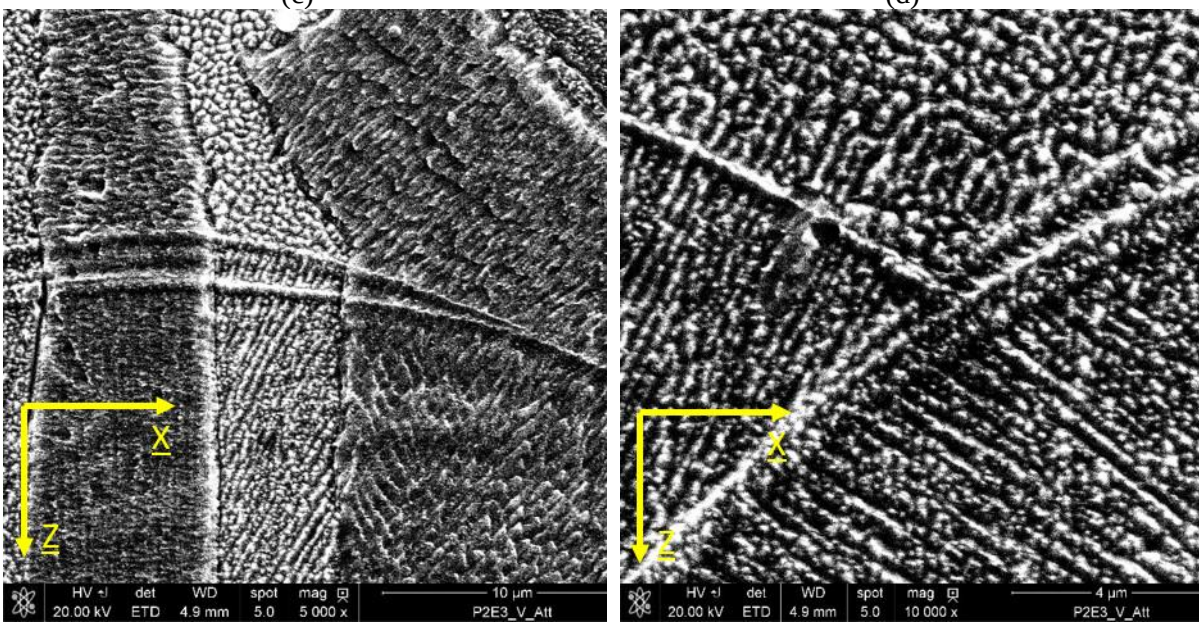

Figure II-13: SEM observations in the plane X/Y (long chemical attack)

The above observations show there is an alignment of the austenitic grains. This alignment is of thermal origin. The growth is epitaxial since the grains tend to grow along the thermal gradient, i.e. according to the direction of construction.

For both planes, by increasing the magnification, we begin to see the dendritic cellular network (Figure II-14), which is at the origin of the grains and the orientation of which creates the difference in colors on the images. Figure II-14 (a) shows that dendrites aligned in the same direction. The different directions that dendrites can take when moving from one grain to another is shown in Figure II-14b. We note the presence of nanoscale spherical particles between the dendrites (Figure II-14 (c)). The grains are columnar, pass through the melt pools and consist of dendrites resulting from rapid solidification after the laser passage.

(a) (b)

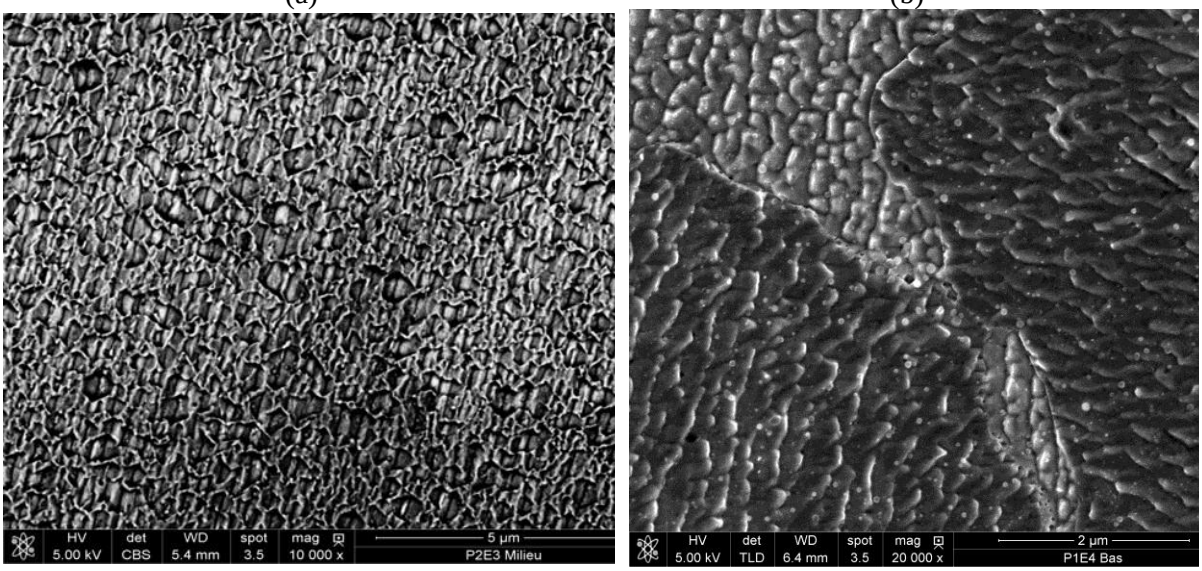

(c)

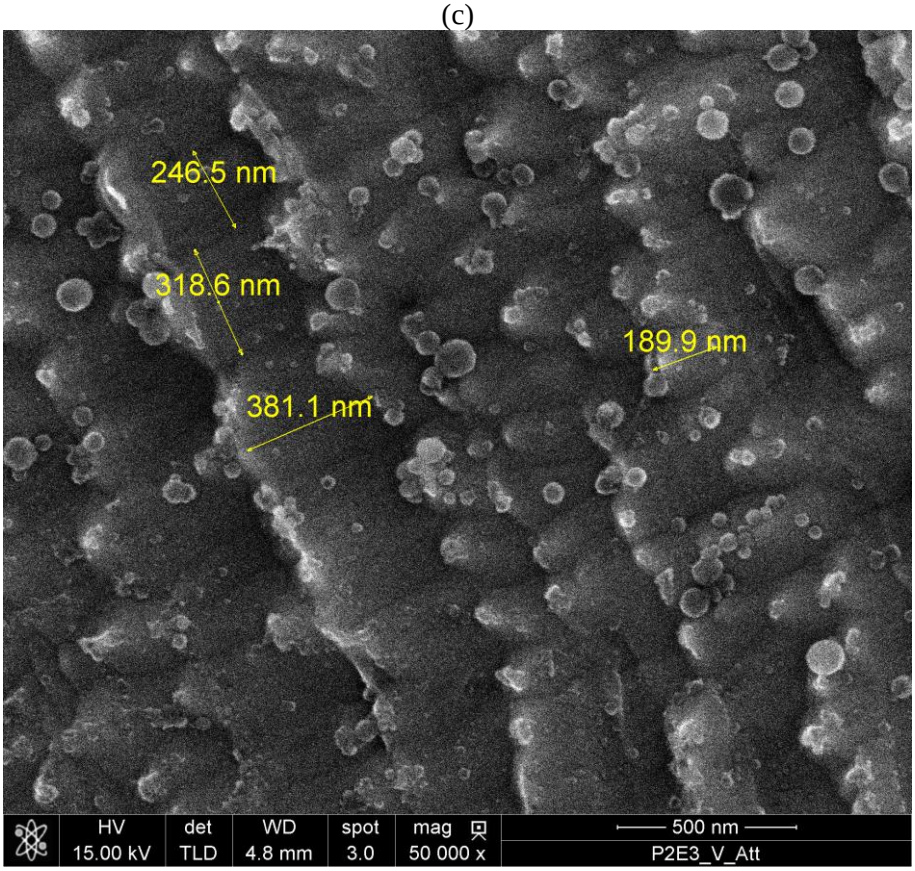

Figure II-14: dendritic cellular network in SLM SS 316L

II.2.3. Grain morphology and Crystallographic texture

To get a better knowledge of the microstructure, Electron Back Scatter Diffraction (EBSD) was used to observe the grain morphology and orientation. This analysis was carried out on a cylinder with a diameter of 8 mm and a height of 10 mm (see Figure II-15). The Z-plane was observed in the center of the specimen. While the X/Y-plane was observed in the bottom (corresponding to the first layers produced), in the middle and in the top (corresponding to the last layers produced).

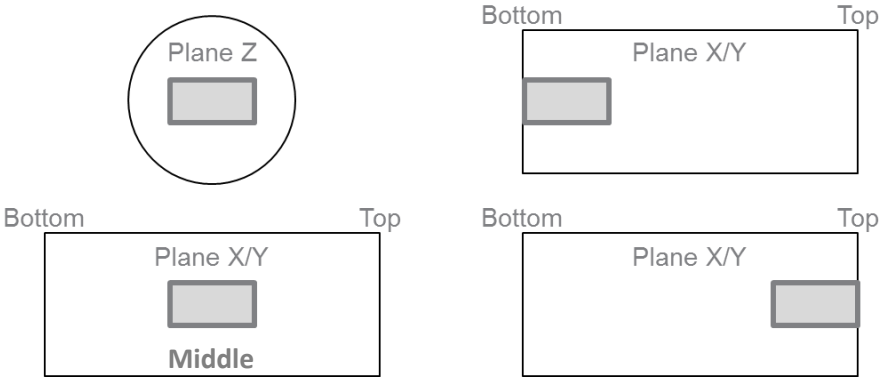

Figure II-15: Observation positions with the EBSD technique

The post-treatment of the results was performed by using the MTEX libraries. This post-treatment leads to EBSD mapping (with reconstituted grains) (Figure II-16 and Figure II-17), pole figures (Figure II-18a), and inverse pole figures (Figure II-18b). Based on this mapping, it is possible to reconstitute the grains by fixing the criterion of misorientation between two neighboring grains. In this study, this value of misorientation was taken equal to 6°.

The grain size is not homogeneous in the observed samples. Elongated columnar grains that cross several layers are visible. In Addition, no twin is present. The dislocation cells may be trapped in the dendritic structure leading to this absence.

With the exception of the grains in contact with the support and the grains of the extreme surface (where the cooling kinetics are different), all the other grains have a relatively identical morphology and size over the entire length of the cylinder. There is therefore no microstructure gradient along the sample.

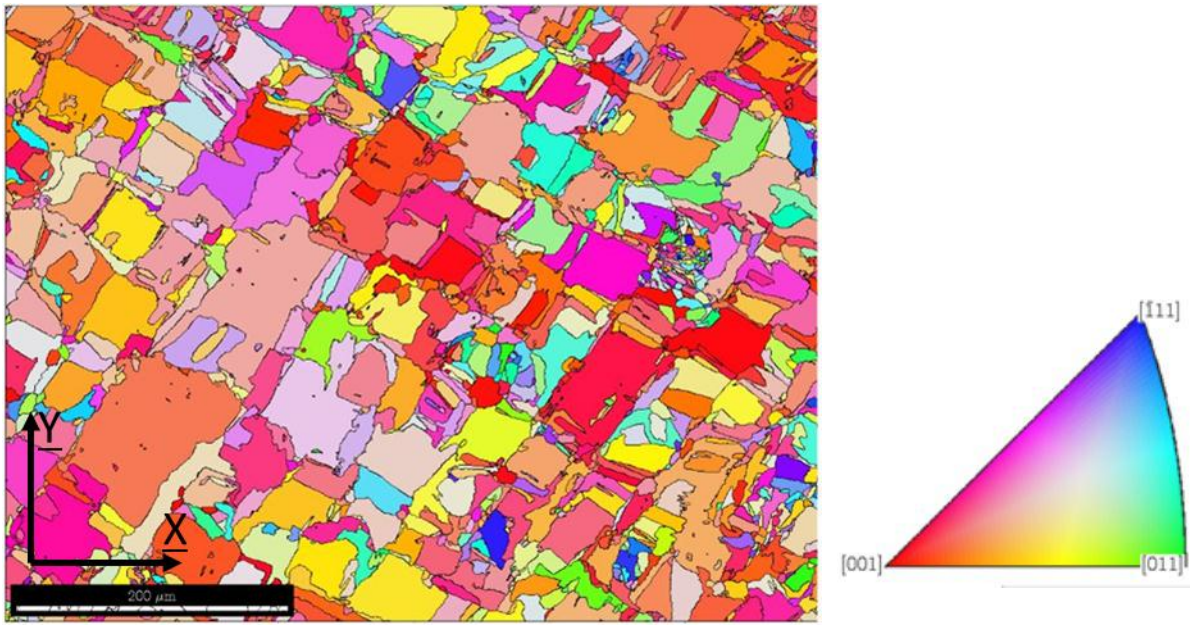

Figure II-16: Post-treated EBSD mapping of the Z-plane

(a) bottom (b) middle (c) top

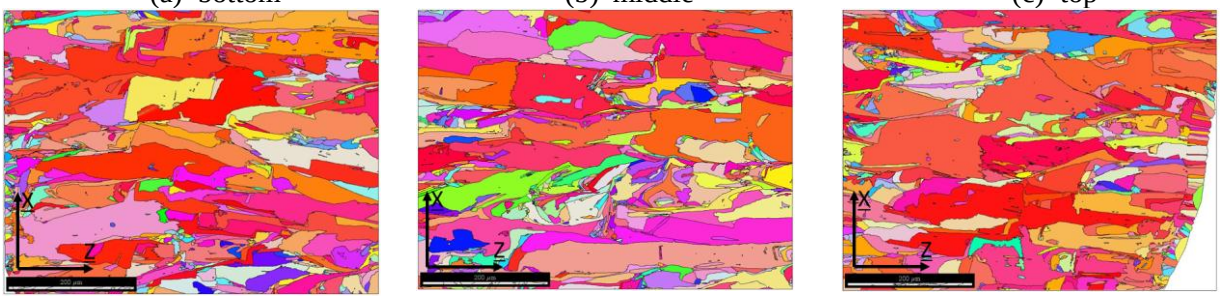

Figure II-17: Post-treated EBSD mappings of the X/Y-plane

Pole figures and inverse pole figures demonstrate the textured microstructure of this material due to the additive manufacturing process. We can see a very marked preferential orientation of type <100>

(the axis <100> of the crystal mainly coincides with the manufacturing axis Z), which resembles the directed solidification of single crystals.

(a) pole figures of the Z-plane mapping (grains)

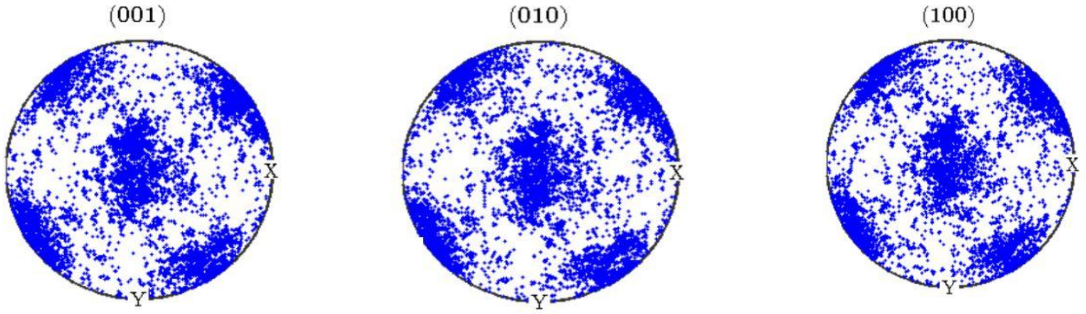

(b) inverse pole figures of the Z-plane mapping (grains)

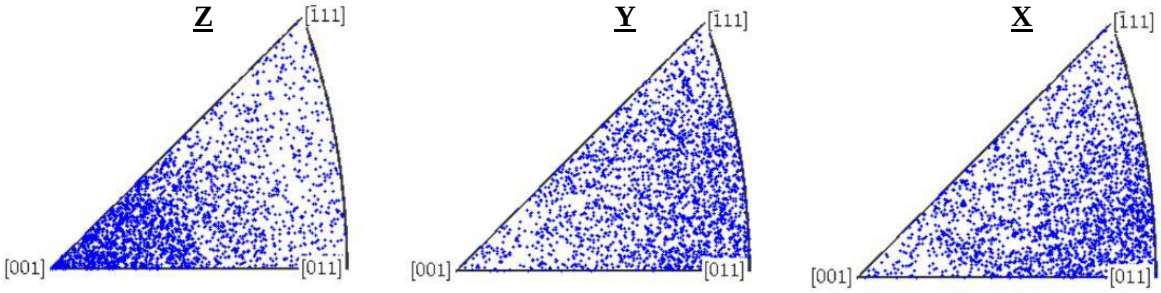

Figure II-18: (a) pole figures and (b) inverse pole figures representing the mean orientations of the grains observed in the mapping of Z-plane.

This texture has been widely observed in the literature regarding the SLM process. Other grain morphologies and textures have also been observed by modifying the process parameters. In fact, the linear energy, defined as being the ratio between the laser power and the laser scanning speed, modifies both the melt pool shape and the crystallographic grain growth. Choo et al. (Choo *et al.*, 2019) studied the effect of laser power on the texture formed during the manufacture of 316L steel cylinders by SLM. In their study the laser power varies from 380 W to 200 W while keeping the other parameters constant (v = 300 mm/s, diameter = 0.207 mm, layer thickness = 60 µm, hatch spacing = 100 µm). A 90° rotation of the pattern (zig-zag) is performed between each layer. Changing the power while keeping the other parameters constant is the same as changing the energy density provided by the laser. At high power (380 W), a strong texture (100) is observed along Z (Choo *et al.*, 2019). It corresponds to the direction of preferential solidification of FCC materials. At an intermediate power (260 W), the texture (110) is the majority. Finally, at low power (200 W), the overall orientation of the grains is random.

This change in texture is hence function of power and the shape of the melt pools plays an important role. As a matter of fact, whatever the power, the grains (100) grow according to the thermal gradient, and therefore radially in the melt. At 380W, the melt pools are flat and wide, the grains therefore grow vertically. For intermediate power values, the melt pools are less flat. The radial growth of the grains (100) associated with the covering of the weld beads therefore generates an overall texture (110) along

Z. This is the principle of the chevron growth between weld beads explained by Andreau et al. (Andreau, Koutiri, *et al.*, 2019) and reported in Figure II-19. Finally, at low power, the melt pools remain round but no longer overlap enough to generate epitaxial growth, so the texture is more isotropic.

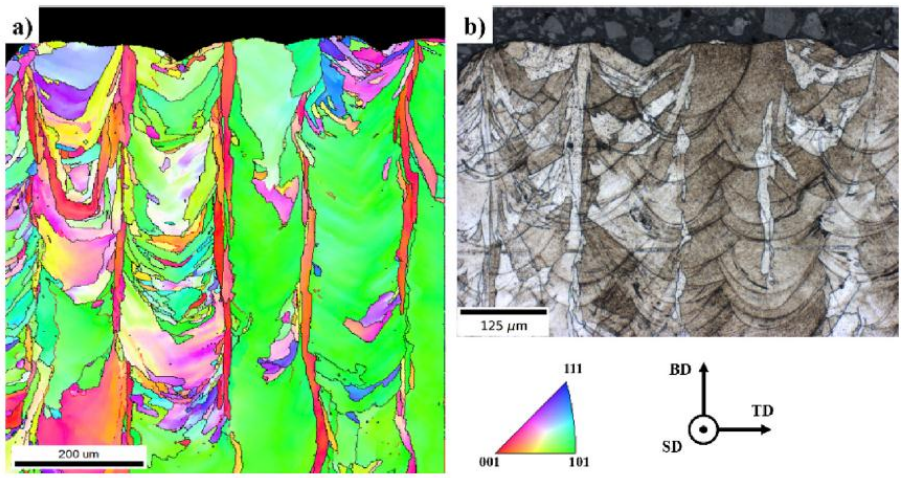

Figure II-19: (a) EBSD Maps and (b) optical micrographs of SS 316L obtained by SLM (Andreau, Koutiri, *et al.*, 2019)

Sun et al. (Sun *et al.*, 2019) studied a higher power domain. They find that, at very high power, the melt pools are very deep and fine while at medium power the melt pools are less deep and wider. This results in differences in shape of the solidification front, which directly impacts the direction of grain growth. (Figure II-20).

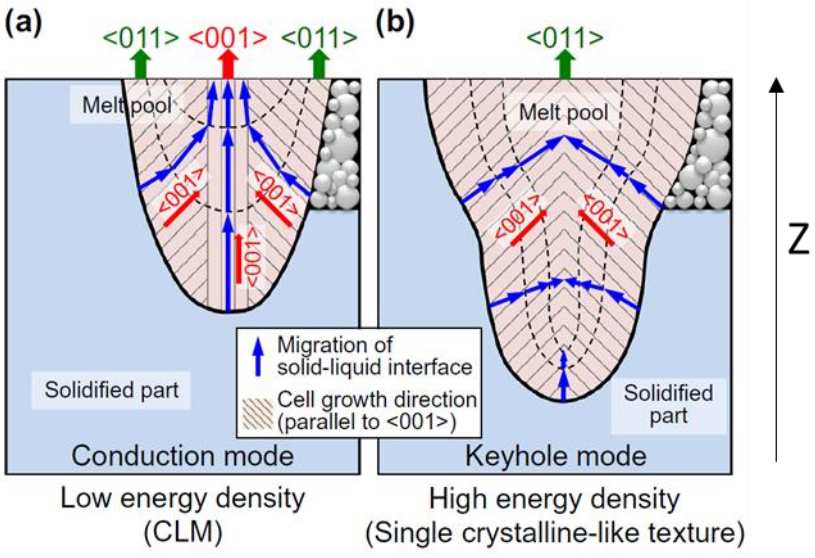

Figure II-20: Influence of the shape of the melt pools on the preferential orientation of the grains: (a) case of low energy density and (b) case of high energy density (Sun *et al.*, 2019).

At very high power, the pool is in a keyhole regime, so it is excessively deep and thin at its end. This particular form allows the growth of the planes <110>//Z as explained by Figure II-20. For medium

powers, the shape of the solidification front allows the epitaxial growth of grains <100>//Z from the bottom of the melt.

The preferential orientation of the grains has a significant impact on their elastoplastic behavior. It has been shown that grains oriented <100> // Z deform by plastic sliding while those oriented according to <110> // Z essentially deform by micro / nano-twinning. This results in a much better ductility and resistance of the materials with the orientation <110> // Z predominant (TWIP effect). Several lamellar crystallographic composites are studied in order to combine the beneficial effects of each of the orientations (Sun *et al.*, 2019). This kind of microstructure was also obtained by Andreau et al.(Andreau, Koutiri, *et al.*, 2019).

II.3. Inherent defect characterization

In this section we are interested in characterizing and quantifying the surface and volume defects generated by SLM. First, the surfaces of several rectangular and cylindrical samples were characterized using ALICONA optical roughness system. Then the volume defects were quantified using the X-ray µCT tomography technique.

II.3.1. Surface state characterization

The surface quality is not only an aesthetic issue, but also a key factor for the success of SLM. The SLM parts in the as-built condition exhibit high surface roughness. This is mainly attributed to the stair stepping effect of this process. Figure II-21 shows the dependency of surface roughness on the heat input (DebRoy *et al.*, 2018). Independently from the alloy, the plot confirms that surface roughness can be reduced by increasing the heat input. Yet, extremely high heat input can lead to defect appearance because of high thermal stresses. Adding to that, the powder grades influence the surface roughness as shown in Figure II-21b. Large particles induce higher surface roughness as compared to thinner counterparts. It is shown that SLM part built with thin particles lead to smoother surface.

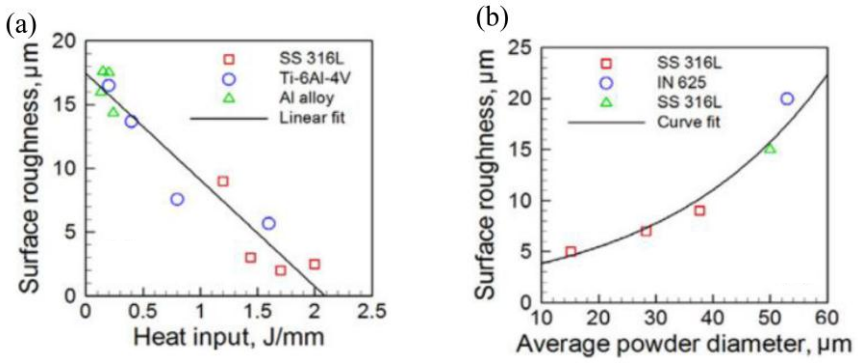

Figure II-21: (a) Effect of heat input on surface roughness and (b) effect of powder diameter on surface roughness (DebRoy *et al.*, 2018)

In this work, the surface and the linear roughness of HCF specimens were studied. The objective is to analyze the effect of the specimen location on the as-built surface roughness. Figure II-22 gives an example of the roughness amplitude for an as-built specimen.

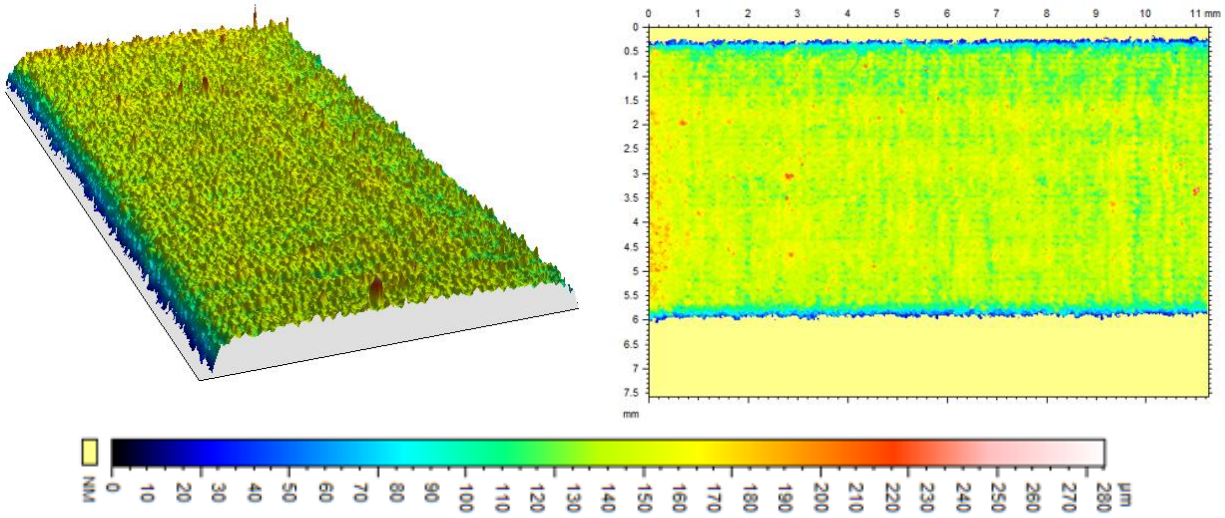

Figure II-22: Surface roughness in sample No.15, Tray 1

For each tray, the roughness is studied on 3 bending specimens (2 measurements by specimen corresponding to 2 faces) and 3 torsion specimens (1 measurement by specimen). Typical results for each type of specimen are presented (Figure II-23).

(a) Bending specimen

a1) Surface roughness (ISO 25178)

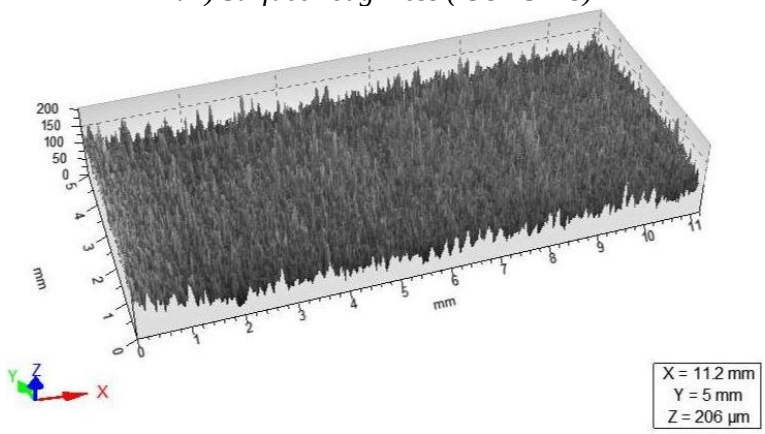

a2) Linear roughness (ISO 4287)

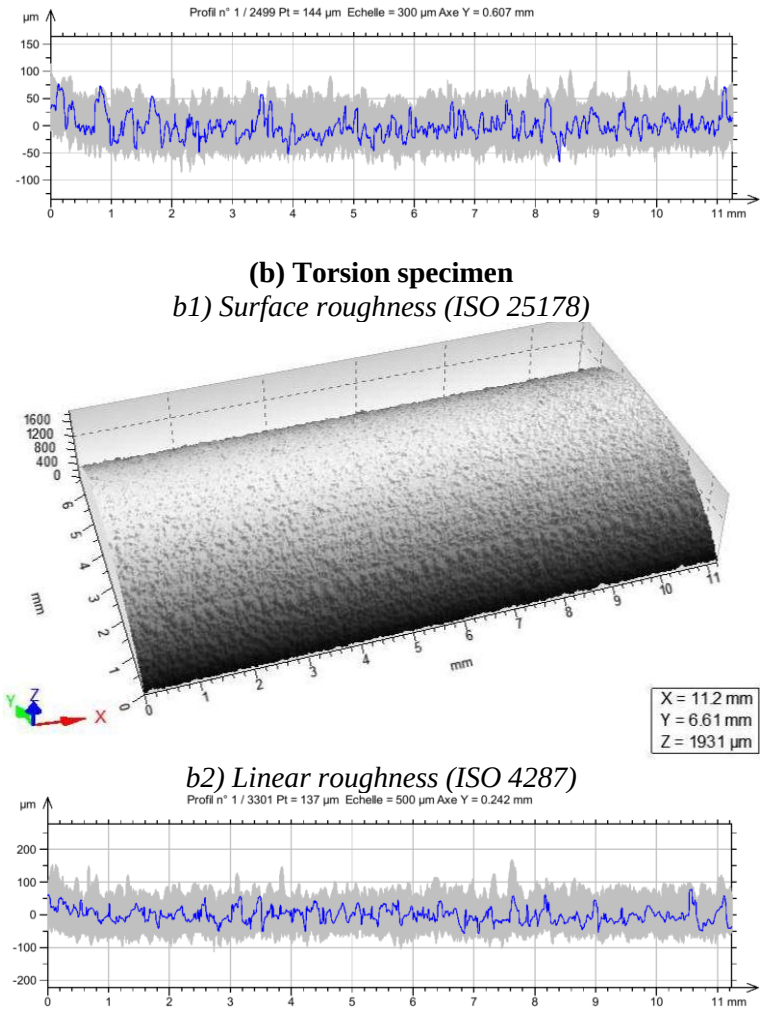

(b) Torsion specimen

b1) Surface roughness (ISO 25178)

b2) Linear roughness (ISO 4287)

Figure II-23: Surface and linear roughness in (a) bending specimen and (b) torsion specimen

Several surface and linear roughness indicators were calculated using the ISO 25178 (for surface roughness) and the ISO 4287 (for linear roughness) standards. These parameters are illustrated in Table II-5 for the investigated specimens. This analysis shows that the surface and linear roughness of the specimens was almost identical regardless of its location on the manufacturing tray.

Table II-5: Surface and linear roughness parameters of measured samples.

Specimen	Reference	Sa [µm]	Sq [µm]	Sz [µm]	Ra [µm]	Rq [µm]	Rz [µm]
Bending specimen (rectangular)	Tray 1, sample 1, face A	8.01	10.3	97.7	7.23	9.35	53.9
	Tray 1, sample 1, face B	13.3	17.0	141	12.7	16.3	88.8
	Tray 1, sample 15, face A	9.18	12.0	119	7.85	10.1	55.8
	Tray 1, sample 15, face B	12.3	16.4	174	11.8	15.4	88.4
	Tray 1, sample 30, face A	12.5	16.3	164	12.1	15.7	89.6
	Tray 1, sample 30, face B	12.8	16.4	140	11.9	15.3	82.8
	Tray 2, sample 1, face A	12.2	15.7	156	11.7	15.0	81.3
	Tray 2, sample 1, face B	8.37	10.7	116	8.19	10.5	57.9
	Tray 2, sample 15, face A	8.82	11.4	147	8.53	11.1	62.6
	Tray 2, sample 15, face B	12.4	16.3	169	11.9	15.5	89.3
	Tray 2, sample 30, face A	13.0	18.7	150	11.8	15.0	81.8
	Tray 2, sample 30, face B	12.5	16.3	148	12.4	16.1	91.6

Torsion specimen (cylindrical)	Tray 1, sample 1	15.4	19.4	168	13.5	17.2	92.2
	Tray 1, sample 13	11.3	14.5	134	13.5	17.1	91.2
	Tray 1, sample 25	11.2	14.8	160	13.1	17.1	97.1
	Tray 2, sample 1	12.5	16.0	135	14.8	18.6	96.2
	Tray 2, sample 13	10.2	13.2	159	13.0	16.6	89.3
	Tray 2, sample 25	11.0	14.0	132	12.9	16.7	91.1

Sa: Arithmetical mean height of the surface *Ra: Arithmetical mean height of the profile*
Sq: Root mean square height of the surface *Rq: Root mean square height of the profile*
Sz: Maximum height of the surface *Rz: Maximum height of the profile*

It is noted that the linear roughness of the as-built specimen is relatively large: *Ra*= 7 ~ 15 µm. The sampling data recorded herewith will be used to build a model with realistic roughness in the numerical investigation shown in Chapter V.

There are several methods to improve the surface quality of SLM components such as:

- Mechanical methods: abrasive sandblasting and machining;
- Chemical processes: acid etching and oxidation;
- Thermal processes: plasma spray and re-melting technique.

Several studies have proven that machining can decrease surface roughness leading to higher fatigue life. In fact, machining removes the stress concentration effect of the surface roughness providing longer life for the machined surfaces. The major drawback of this method is that it cannot be used for parts with complex geometries. Alternatively, laser re-melting may be a solution to improve surface quality. It requires high production time. The Laser Surface Re-melting (LSR) technique needs less production time as compared to laser re-melting of individual cross sections. Applying LSR may have a side effect on the flatness of the top surface. In fact, an elevated ridge of the solidified material can appear at the edges because the laser beam pushes the molten material to the part contour (Kruth *et al.*, 2010). The edge-effect problem can be solved by choosing the appropriate set of parameters or by leaving the right time interval between the laser melting scan and the re-melting scan.

In the literature, contradictory fatigue results are reported for as-built and machined or polished specimens. This is mainly attributed to differences in crack initiation mechanism, defect types and locations and material type and ductility (Yadollahi and Shamsaei, 2017). In the as-built condition, cracks are generally induced by surface discontinuities, whereas machined or polished specimens exhibit crack initiation from surface roughness and internal defects.

II.3.2. Porosity characterization

µCT tomography was performed on 6 samples of 4 mm diameter and 10 mm length. Figure II-24 shows the image of a section distant from the edge in the Z plane, as well as an image with all the sections in this plane superimposed. The device capacity, the sample size and the acquisition parameters make it possible to view only defects greater than 8 µm (corresponding to the size of one pixel). Defects of diameter less than 8 µm cannot be detected by this method. Despite this limitation, this technique is considered sufficient because defects below this threshold have no effect on fatigue strength.

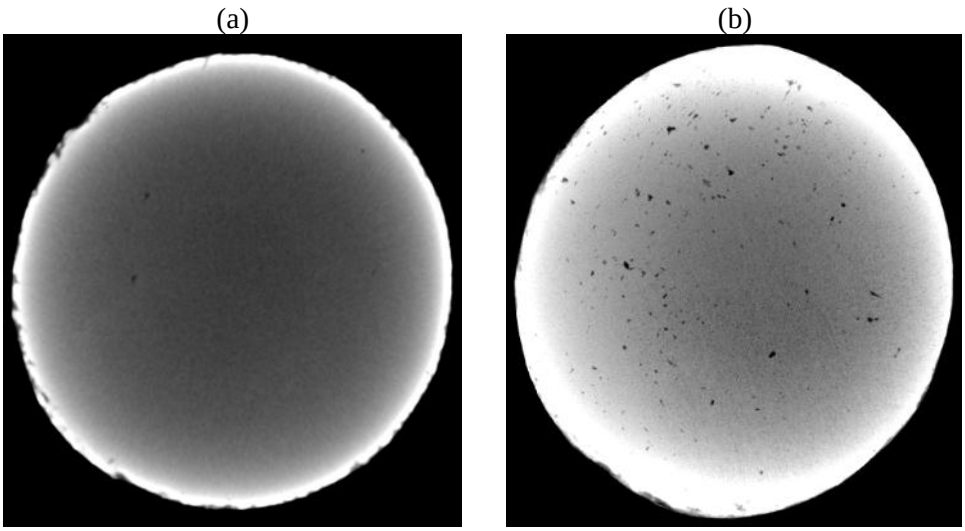

Figure II-24: Tomography in Z-plane: (a) slice No.250 (b) superimposing all slices

By taking the images in the other planes, it is possible to reconstruct the 3D model of the defects. This treatment was carried out using the *imageJ* and *slicing 4D* softwares. The size (in pixel) and the spatial distribution of the defects observed for all studied specimen are shown in Figure II-25. It will be seen that for all the samples the defects have an equivalent diameter of less than 4 pixel (30 μm) and they are distributed randomly in the volume.

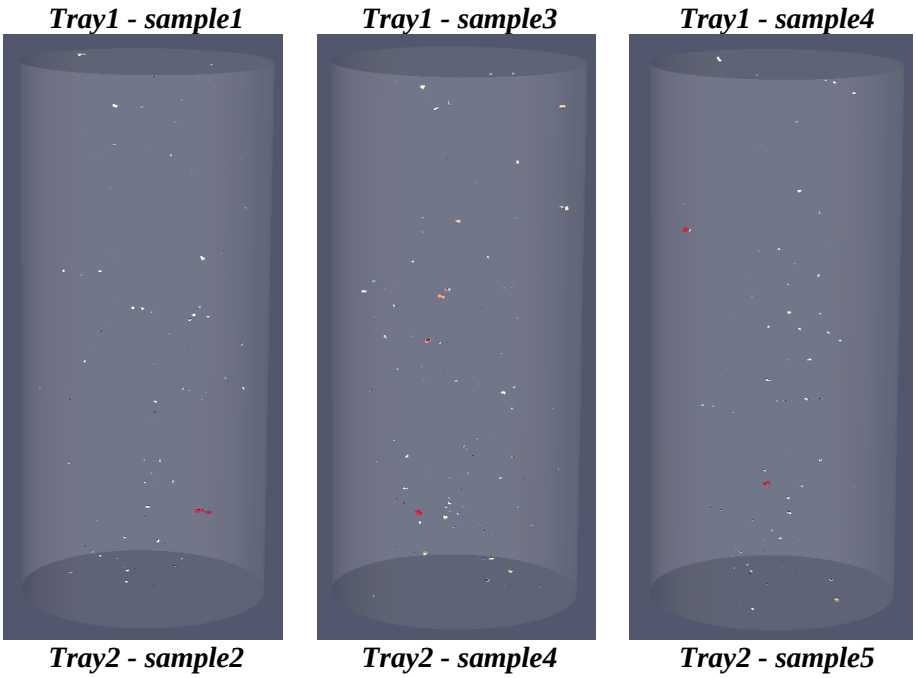

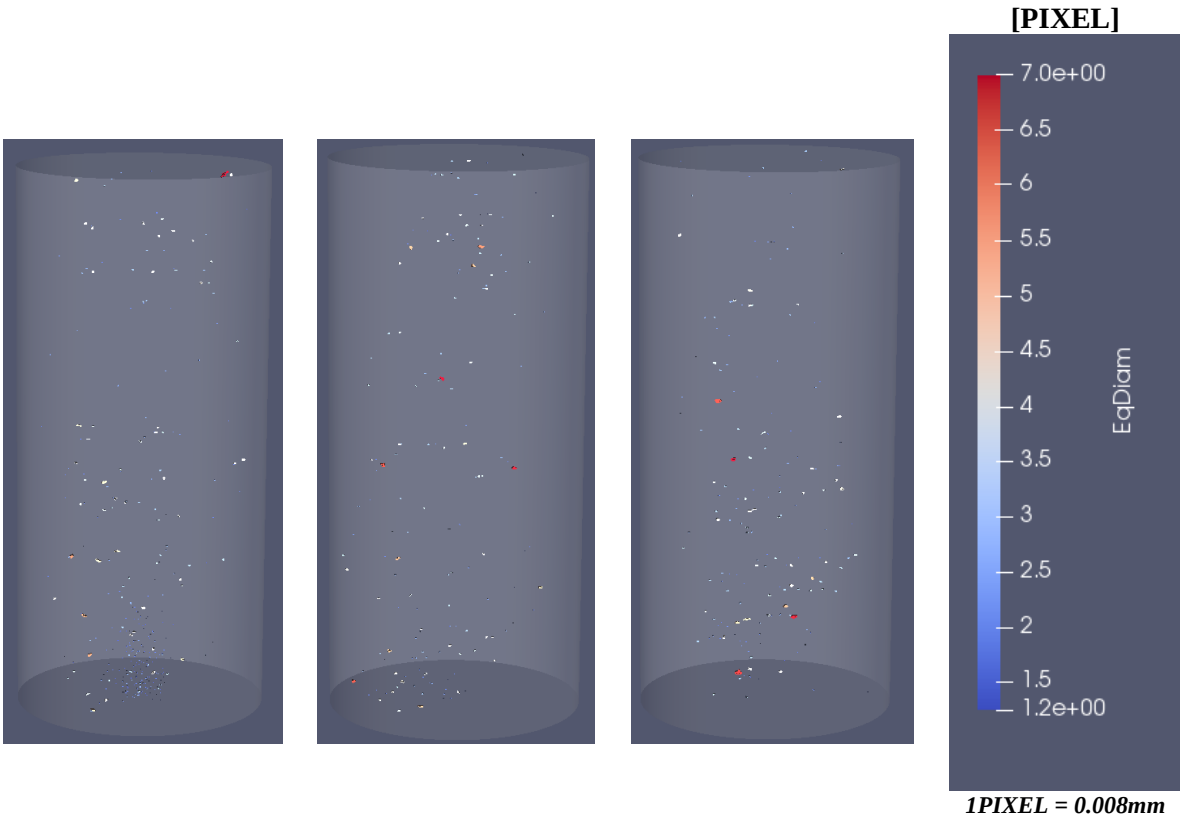

Figure II-25: Size and spatial distribution of the defects for all studied specimen

A quantitative study was carried out on the size, number and spatial distribution of these defects. Figure II-26 shows the distribution of these defects for the two least porous (0.0035%) and most porous (0.026%) samples among the 6 samples studied. It will be noted that, in both cases, 90% of the defects have a volume less than 65.10^{-6} mm^3 (i.e. equivalent diameter less than 30 µm). In each sample, a small number (less than 8) of defects has a volume greater than 10^{-4} mm^3 (i.e. equivalent diameter greater than 50 µm).

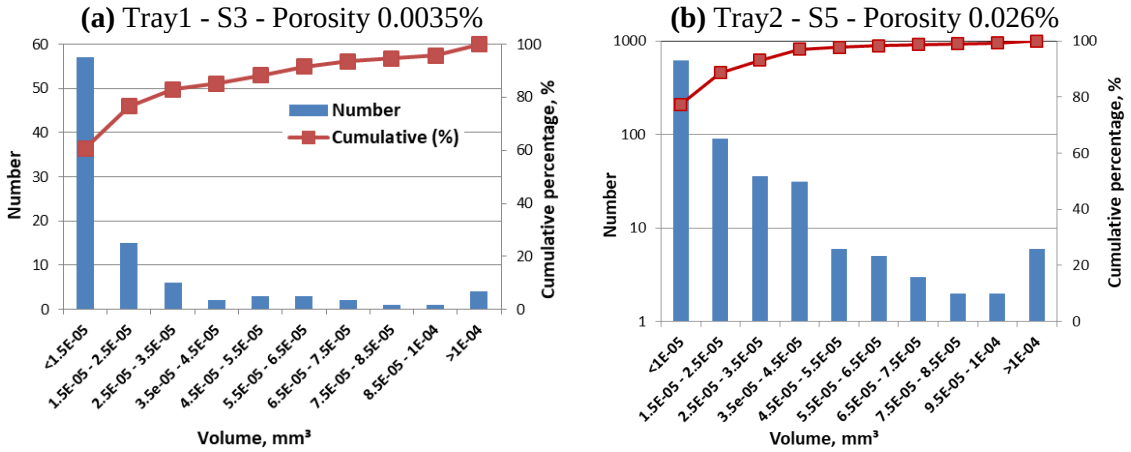

Figure II-26: Histogram and cumulative percentage of porosity of measured samples: (a) Tray1 - S3 - Porosity 0.0035%; (b) Tray2 - S5 - Porosity 0.026%

Finally, Table II-6 illustrates the porosity of the samples belonging to Tray 1 and Tray 2. From the results of this analysis, we can conclude that the mean porosity level is generally less than 0.04%.

Table II-6: Porosity of the samples measured

Samples	Tray1 (Radius = 1,8mm)			Tray 2 (Radius = 1,8mm)		
	Sample1	Sample2	Sample3	Sample4	Sample5	Sample6
Studied Height(mm)		6,8068			6,8080	
Total cross section(mm^2)		10,1787			10,1787	
Total volume(mm3)		69,2853			69,2971	
Total void volume(mm^3)	0,0051	0,0244	0,0244	0,0244	0,0019	0,1286
Porosity (%)	0,0074	0,0352	0,0352	0,0352	0,0027	0,1856

To better characterize those volume defects, a destructive analysis (cutting and polishing) was carried out on several samples. From SEM images, the defects seem to be of three types:

- a particle of un-melted powder (Figure II-27a)

- a lack of powder (Figure II-27b)

- a pore formed between the particles of powder (Figure II-27c)

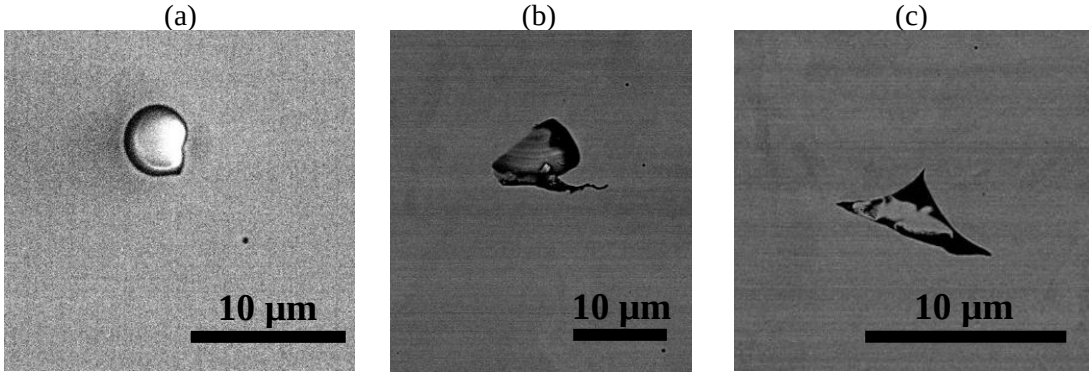

Figure II-27: Defects observations by SEM : (a) un-melted powder, (b) lack of powder and (c) pore formed between the particles of powder.

II.4. Mechanical behavior

II.4.1. Hardness

The micro-hardness of the material is measured on a cylindrical sample in three different directions (see Figure II-28). Note that there is no hardness gradient from the surface to the core of the sample. The results of the macro-hardness measurements in the X / Y plane are shown in Table II-7. It can be

seen that there is almost no difference between the Z plane and the X / Y plane and between one specimen to another. The hardness values are comparable to those found in the literature (Kruth *et al.*, 2010)**.** Indeed, Tucho et al. (Tucho *et al.*, 2018) studied the influence of laser power, scanning speed, layer thickness and hatching distance parameters on Vickers hardness. They have shown that the hardness lies in the range of 185 to 282 HV.

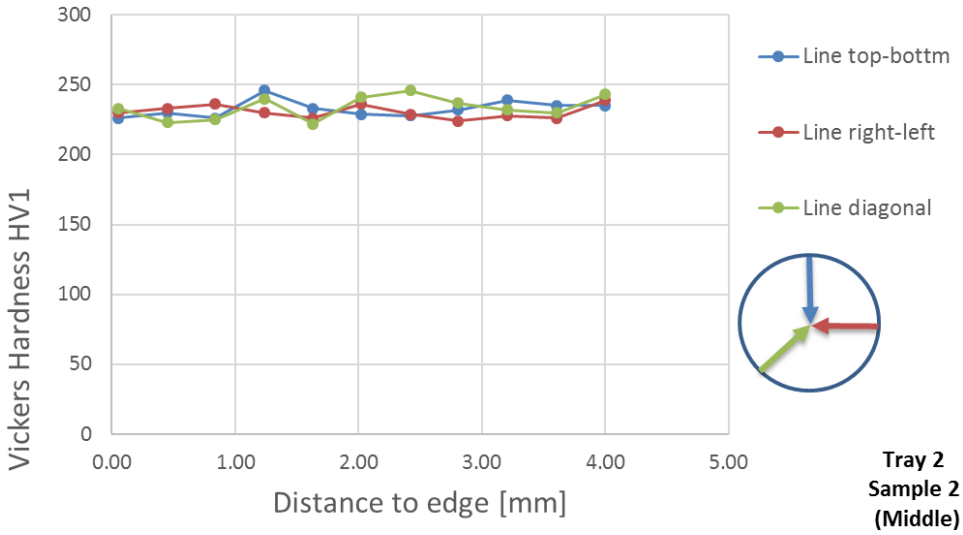

Figure II-28: Measured micro-hardness in an SLM sample

Table II-7: Macro-hardness of tested specimens

Sample	Average of Macro-hardness (Hv)
Tray2, sample 4 (middle)	224
Tray2, sample 4 (top)	223
Tray 2, sample 3 (middle)	231
Tray 2, sample 3 (bottom)	229
Tray 2, sample 3 (top)	222

II.4.2. Monotonic tensile test

Two specimens with different surface preparations, as-built and total-polished, were used for analyzing the mechanical properties. The machine used MTS-809 is shown in Figure II-29.

Figure II-29: Machined used in tensile test (MTS 809)

Each sample was subjected to monotonous tension until it broke. Clamping pressure was set to 50 bar. No slippage or crushing was observed on the sample heads. The tests were strain controlled with a deformation rate $10^{-3}s^{-1}$. An extensometer with an initial length of 12.5 mm was used for both specimens. The total-polished specimen was instrumented with an HBM 1-LY41-3/350 unidirectional strain gauge while the surface state of the as-built specimen was too rough to paste a gauge. All data was retrieved at the same time base by a universal HBM MX440B acquisition box. Precision of the extensometer was checked by comparing it with the gauge. From Figure II-30, we can see that the two curves are similar. The stress-strain curves of as-built and total-polished specimens are plotted in Figure II-31. Due to the limitation of the extensometer's range, the extensometer was reset to zero once the measured strain reached 15%. The reinitiating of extensometer was repeated 4 times to reach an elongation of the specimen at about 60%.

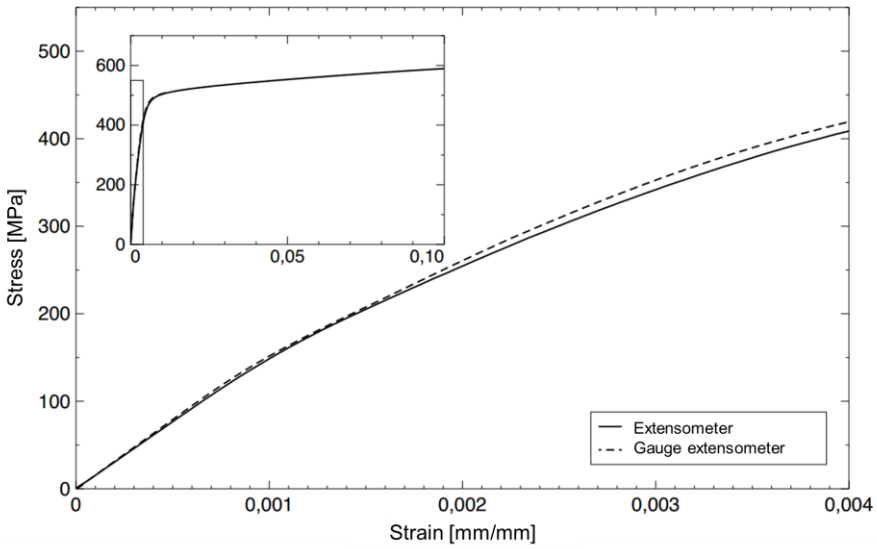

Figure II-30: Comparison between extensometer and gauge extensometer in tension for the polished specimen

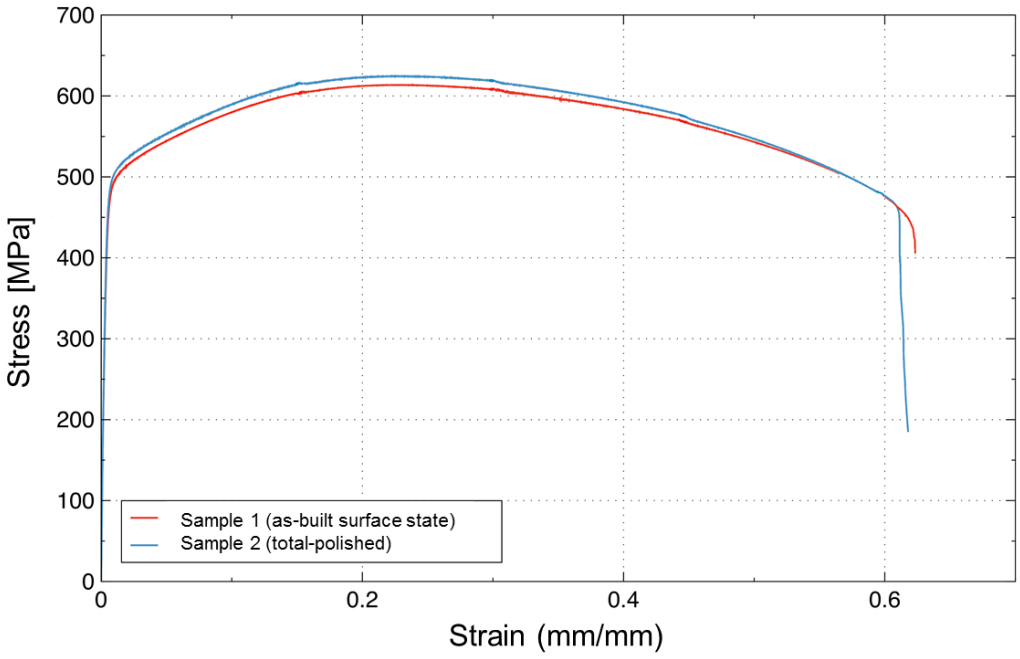

Figure II-31: Tension curves for the raw surface specimen (red) and for the polished surface specimen (blue).

The estimated Young's modulus is found to be 150 GPa. We will show, in Chapter V, that the crystallographic texture is responsible for this low value.

(a)

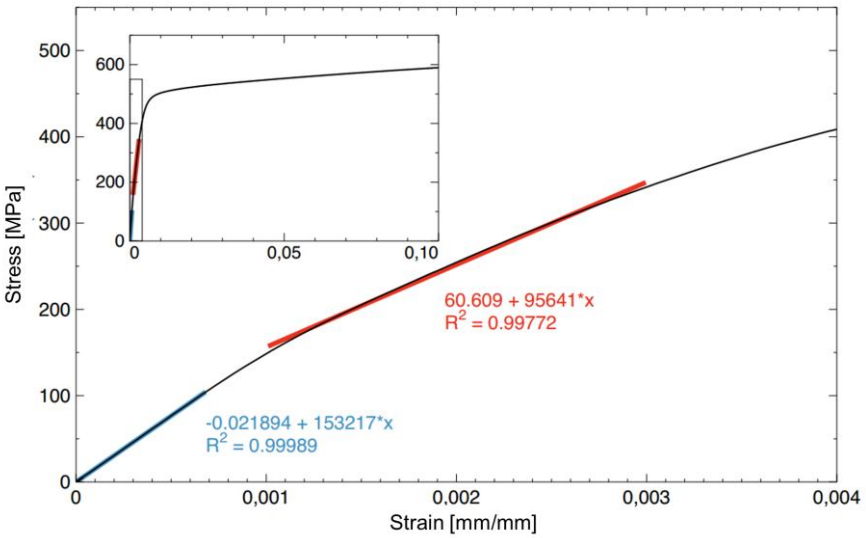

(b)

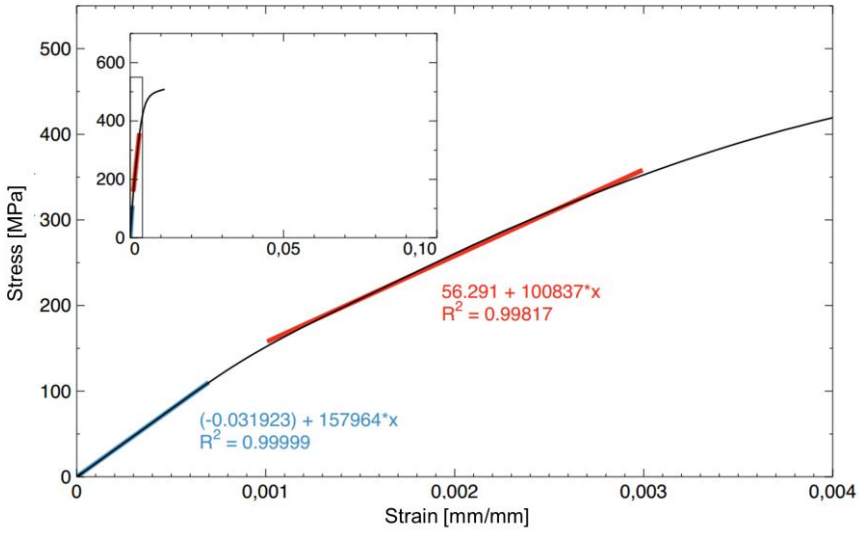

Figure II-32: Estimated Young's modulus of (a) as-built sample and (b) total-polished sample

As shown in Table II-8 gathering data from the literature, a large range of mechanical properties is found and can be attributed to the variety of the manufacturing parameters used. Note that only data from manufactured vertically components are collected (except for ASM Handbook which is the reference value for forged 316L). The significant increase (35 to 100%) in the yield strength (YS) of 316L steel obtained by SLM, compared to that obtained conventionally, could be explained by the multi-scale structuring of the microstructure, in particular the presence of cellular dislocation substructures. The latter would induce a hardening of the material by the Hall-Petch effect according to certain authors (Zhong *et al.*, 2016), Recently, this hypothesis is verified by Bahl et al. (Bahl *et al.*, 2019) as well as by Li et al (Li *et al.*, 2019). The latter report respectively that the relation of Hall Petch cannot be applied in such a simple way.

The maximum stress values (UTS) remain in the same order of magnitude (but often in the upper range) but it is known that the defects are more numerous in the materials obtained by SLM (in particular porosities).

The special feature of SLM SS 316L is its high YS/UTS ratio (Table II-8). Indeed, it is generally between 0.7 and 0.9 whereas it is conventionally between 0.4 and 0.5. This is all the more interesting since, for conventional materials, an increase in this ratio generally leads to a reduction in the elongation at break. However, for the 316L steel obtained by SLM, the strain to failure remains generally the same or is even better. This high value of YS / UTS ratio is probably associated with the hardening induced by the SLM process. During manufacture, due to the high thermal gradients, constraints arise at the grain scale which implies the creation of numerous dislocations, themselves being at the origin of the work hardening.

The Young's modulus of 316L obtained by SLM is generally lower than the one of wrought 316L. Several explanations exist in the literature. Some authors link this drop to the crystalline anisotropy of the material. In this study, this assumption seems reasonable and some simulations will be carried out in Chapter V to check it.

Finally, the 316L steel produced for this study has mechanical tensile properties comparable to the literature. A slight increase in strain to failure is observed (60% against maximum 54% in the literature).

Table II-8: Manufacturer and literature data of the mechanical properties in uniaxial tension of SS 316L obtained by SLM.

	UTS (MPa)	YS (MPa)	YS/UTS	A%	E (GPa)
HT - Present study	**610 - 630**	**450 - 470**	**0.74**	**60**	**150 - 157**
As built- manufacturers data EOS (PILLOT, 2016)	540 ± 55	470 ± 90	0.87	50 ± 20	180
As built- SLM Solutions (PILLOT, 2016)	654 ± 49	550 ± 39	0.84	35 ± 4	169 ± 31
As built- Tolosa 2010 (Tolosa *et al.*, 2010)	570 - 590	530 - 560	0.94	42 - 45	
As built- Kuznetzov 2016 (Kuznetsov *et al.*, 2016)]	685 - 708	567 - 582	0.83	34 - 35	
As built- Liverani 2017 (Liverani *et al.*, 2017)	540 - 570	420 - 500	0.84	40 - 70	
As built- Riemer 2014 (Riemer *et al.*, 2014)	565	462	0.82	54	
As built- Bahl 2019 (Bahl *et al.*, 2019)	565 ± 10	480 ± 20	0.85	44 ± 5	
As built- Spierings 2011 (Spierings, Starr and Wegener, 2013)	760	640	0.84	30	
As built- Salman 2019 (Salman *et al.*, 2019)	1016 ± 8	550 ± 10	0.54	50	
Forged, ASM Handbook (1993)	*620*	*310*	*0.5*	*30*	*205*

II.4.3. Cyclic tensile test

To characterize the mechanical cyclic behavior of 316L steel, another series of tests was conducted using the same machine as for the monotonic tensile tests. These tests were carried out on the as-built specimens and were strain controlled with a loading ratio R = -1 and 400 measurement points per cycle.

The strain rate was $10^{-3}s^{-1}$. Table II-9 characterizes the imposed strain levels, the number of cycles before failure and the average softening per 100 cycles calculated for the linear part of the softening curves (see Figure II-39). The endurance curve corresponding to these tests is presented in (Figure II-33).

Table II-9: Low cycle tension-compression fatigue tests

Sample Name	Strain (%)	Rupture (cycles)	Δσ per 100 cycles (MPa)
Tray 2, sample 5	±0.30	81815	0.02
Tray 1, sample 1	±0.45	10931	0.24
Tray 2, sample 2	±0.60	5390	0.67
Tray 1, sample 4	±0.75	2767	1.49

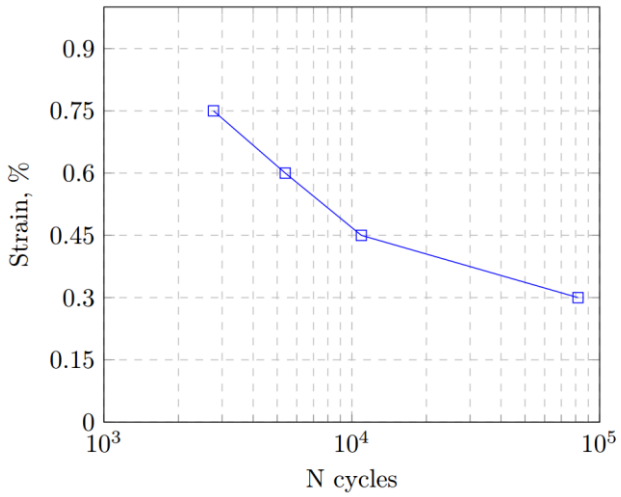

Figure II-33: S-N curve of 316L under tension loading in LCF domain

Results are post-processed using MATLAB software. The purpose of the post-treatment was to obtain the hysteresis curves and the softening curves, as well as to determine the moment of rupture. There were two criteria for determining this moment and both were based on softening.

According to the first, the specimen is considered broken if the tangent to the softening curve starts to rotate clockwise and the change of the inclination to a period of 10 cycles is greater than 1, the value found empirically. The second criterion is based on the maximum stress drop. At the moment when the fall begins to exceed 0.5 MPa at the interval of 10 cycles, the rupture is observed. The values obtained from the two criteria are close. Their average was used as the final value corresponding to the break. It should be noted that to use these criteria it was necessary to filter the data of the softening curve so that it was smooth and monotonous. For this, a second-order low-pass filter of Butterworth type was used, with the cut-off frequency of π /100.

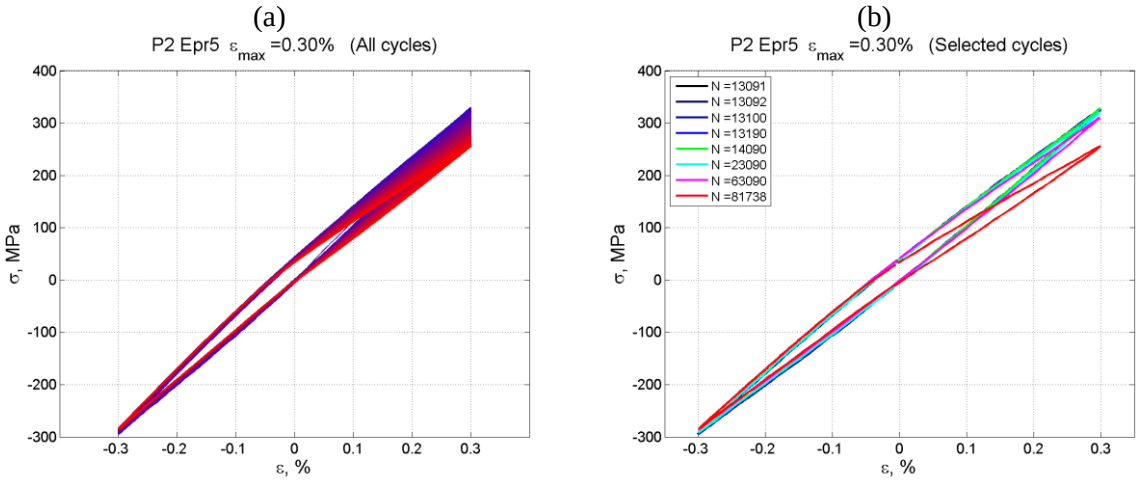

Figure II-34: Stress-strain curves under cyclic tension-compression at E=0.3%: (a) all cycles and (b) selected cycles.

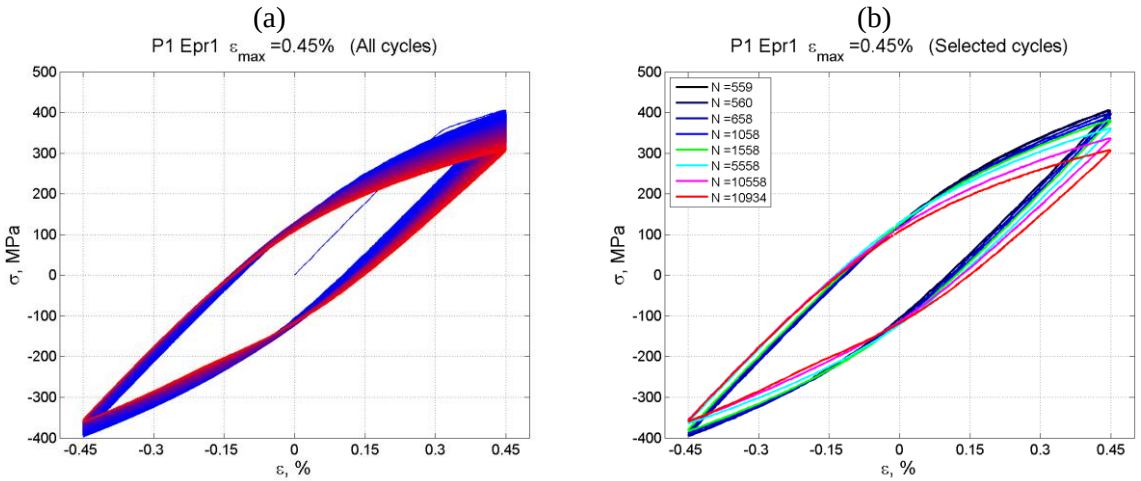

Figure II-35: Stress-strain curves under cyclic tension-compression at E=0.45%: (a) all cycles and (b) selected cycles.

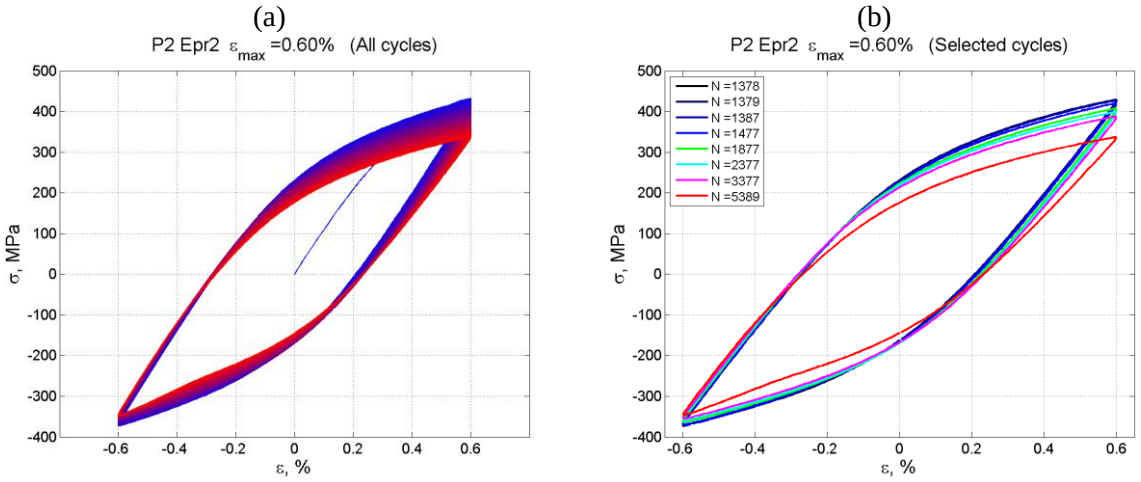

Figure II-36: Stress-strain curves under cyclic tension-compression at E=0.6%: (a) all cycles and (b) selected cycles.

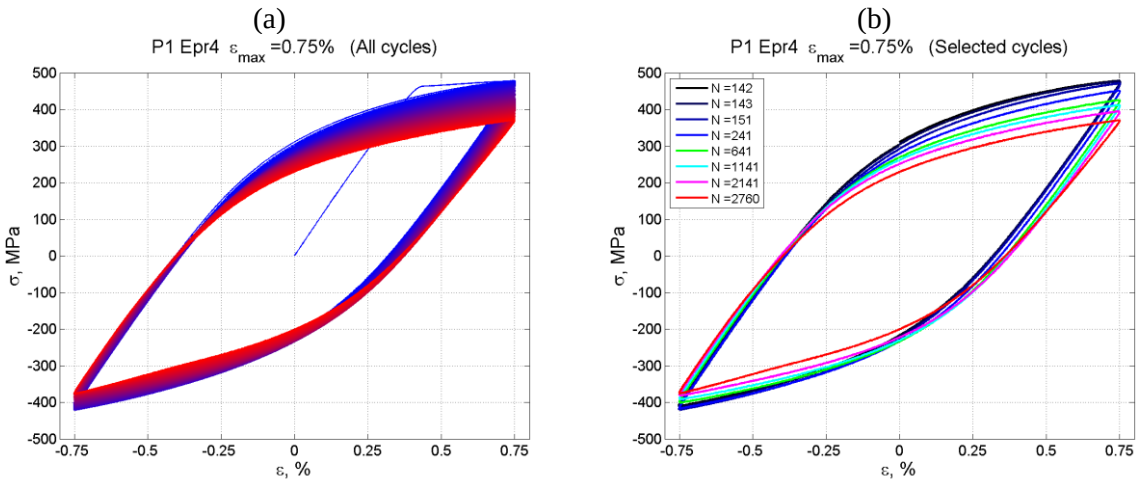

Figure II-37: Stress-strain curves under cyclic tension-compression at E=0.75%: (a) all cycles and (b) selected cycles.

Figure II-34-37 show that with an increase in imposed deformation, the hysteresis curves become more and more open, which is related to the plastic deformation of the specimen. In addition, it can be emphasized that the softening phenomenon is much greater in tension than in compression. It is also interesting to look at the stabilized half-life cycles, and then compare them on the same graph (Figure II-38):

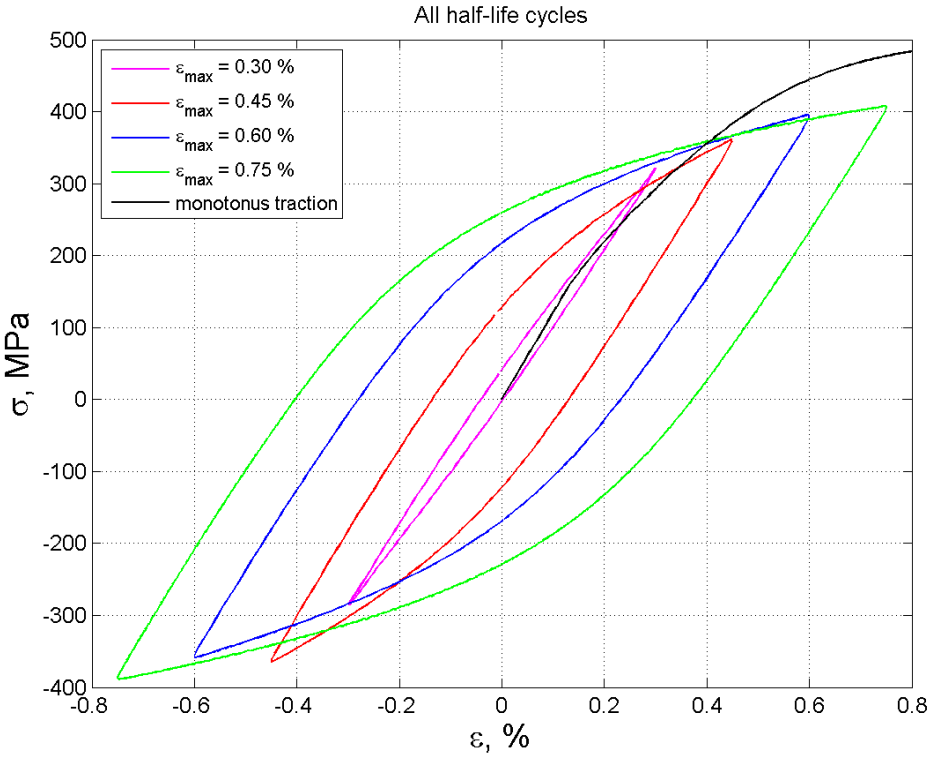

Figure II-38: Half-life cycles of different loadings

The softening of the material during the tests can be observed on the softening curves, plotted for each level of deformation and compared in Figure II-39.

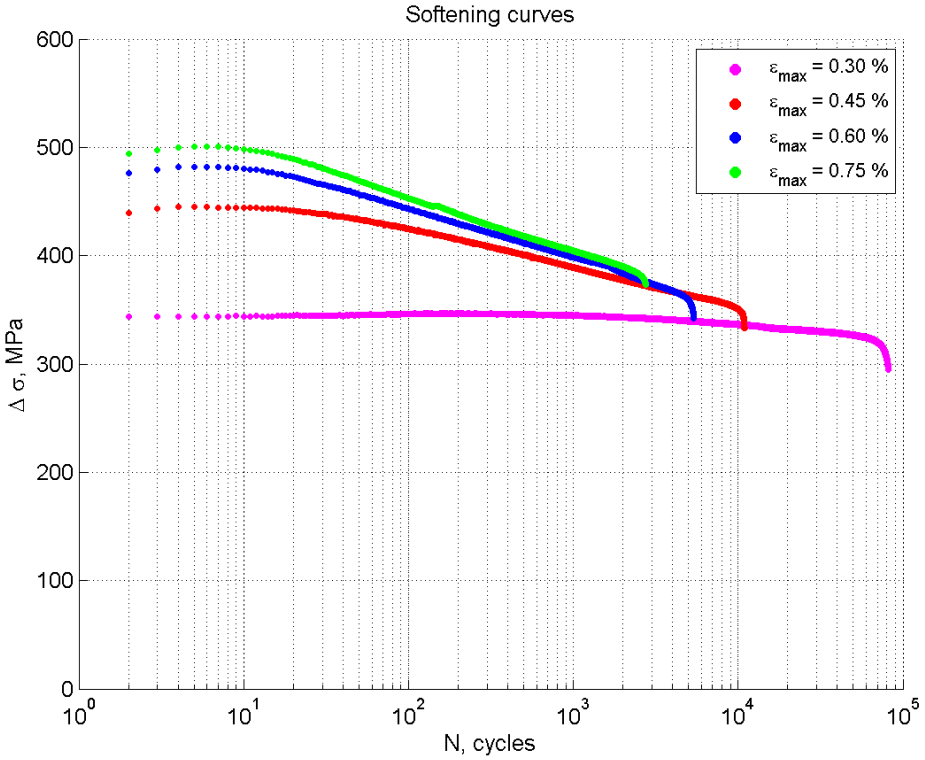

Figure II-39: Cyclic softening curves under different cyclic deformations

In low cycle fatigue, it is not unusual to observe a cyclic softening. This behavior is also seen on wrought 316L steel (Mu *et al.*, 2013; Guerchais, 2014). However, it is interesting to note an asymmetry between tension and compression for our steel obtained by SLM. The softening is indeed much more pronounced in tension than in compression.

II.5. Conclusions

It is well known that the AM material properties are very dependent on the manufacturing parameters. The analysis of the powder can for instance give information on the origin of the imperfections in the final products. The specimens of the present study were manufactured vertically. Their resistance is supposed to be lower in that case. Residual stress measurements made after the heat treatment shows that stress relieving heat treatment could not completely eliminate residual stresses. In some parts they reached 200 MPa.

Microscopic observations showed the presence of surface defects, and µCT tomography highlighted the presence of pores. According to the analysis of the macro-and microstructure, we see that the material is strongly textured, with grains of austenite elongated along the manufacturing axis. These observations were confirmed by EBSD which made it possible to characterize more precisely the structure of the material at the grain level as well as to quantify their different characteristics. Surface

roughness measurements on the raw specimens showed that in some places the roughness level *Rz* could exceed 200 μm.

The results of the hardness measurements show that the hardness of SLM SS 316L is in the range of 220 to 250 HV which is consistent with conventionally fabricated SS 316L. The monotonic tensile tests show that the AM specimen is similar to conventional ones in terms of UTS and elongation rate. But the estimated Young's modulus value is around 150 MPa which is lower than the nominal value of wrought 316L. LCF tests are carried out in tension-compression. Four strain levels are applied: ± 0.30%, ± 0.45%, ± 0.60%, ± 0.75%. For each level, the hysteresis curves and the softening curves are drawn and analyzed. As the imposed strain increases, the hysteresis curve becomes more open and the softening more pronounced. For instance, the softening at ε= ± 0.30% does not exceed 0.02 MPa per 100 cycles, while that for the test piece ε= ± 0.70% is 1.49 MPa.

Syntheses

Design process	Original material	Recycled 316L powder (size 5 - 25 µm)
	Fabrication process	Vertically built SLM with optimal processing parameters No contouring step
	Heat treatment	Annealing (620°C for 90 min)
Microstructure	Phase	Austenitic, absence of twinning, dislocations in cells
	Grain morphology	Elongated grains according to the direction of fabrication and passing through several layers (melt pools)
	Texture	Strongly textured
	Porosity	Less than 0.04% with 90% of defects of equivalent diameter less than 30 µm
Surface	Roughness	Very rough (*Ra* greater than 10 µm)
	Residual stress	Longitudinal, in tension (~ 100 MPa), no shear stress
Mechanical performance	Hardness	225 Hv (no microstructure gradient)
	Elastic performance	Young's modulus less than 200 GPa (elastic anisotropy)
	Cyclic performance	Continuous cyclic softening

Chapter III.

Fatigue experiments and analysis

III.1. Experimental fatigue test set-ups and conditions 68

III.1.1. Tensile fatigue tests 68

III.1.2. Bending and torsional fatigue tests 68

III.1.3. Surface preparation 70

III.2. Fatigue strength results and analysis 71

III.2.1. S-N curves 71

III.2.2. Effect of the surface state 73

III.2.3. Effect of loading type 73

III.2.4. Discussion 74

III.3. Fractographic analysis 76

III.3.1. Bending samples 76

III.3.1.1. Total-polished specimens 76

III.3.1.2. Simple-polished specimens 78

III.3.1.3. As-built specimens 81

III.3.1.4. Summary 83

III.3.2. Torsion samples 84

III.3.2.1. Total-polished specimens 85

III.3.2.2. Simple-polished specimens 88

III.3.2.3. As-built specimens 88

III.3.3. Summary 90

III.4. Correlation between defect size and HCF strength 90

III.4.1. Defect measurement 90

III.4.2. Kitagawa-Takahashi diagram 92

III.5. Conclusions 95

Syntheses 97

The results of the fatigue tests are detailed and discussed in this chapter. The experiments are carried out under tensile, bending and torsional loading modes. For each loading condition, different surface preparation techniques (machining, polishing) are applied to investigate the effect of surface state on high cycle fatigue performance. As surface defects and roughness are likely to affect the fatigue response of SLM 316L, fractographic analysis is performed on each failure surface and the mechanism of fatigue crack initiation is identified. Defect size is then measured and correlated with the corresponding fatigue strength.

III.1. Experimental fatigue test set-ups and conditions

III.1.1. Tensile fatigue tests

The tensile fatigue tests are conducted in ambient air and temperature on a biaxial servo-hydraulic testing system, MTS® 809 (Figure II-29). The same machine was used for the monotonic tensile tests. The experiments are carried out under stress control at a load ratio R = -1 and a frequency of 15 Hz.

The target stress σ being defined, the cylindrical specimens of diameter D are subjected to the load F:

$$F = \frac{\sigma}{\frac{\pi D^2}{4}} \qquad (III.1)$$

The staircase method (appendix A.1) is applied to get the fatigue strength. The first specimen is subjected to a stress corresponding to the expected average fatigue strength. If the specimen survives $2*10^6$ cycles, it is discarded and the next specimen is subjected to a stress that is one increment above the previous applied level, i.e. after a survivor the applied stress level is increased by one increment. The increment corresponds to the expected value of the standard deviation. When a specimen fails prior to reaching $2*10^6$ cycles, the obtained number of cycles is noted, and the next specimen is subjected to a stress that is one increment below the previous applied level

III.1.2. Bending and torsional fatigue tests

A table resonant testing machine, Rumul® CrackTronic, is used (Figure III-1) to apply the bending and torsion loading modes.

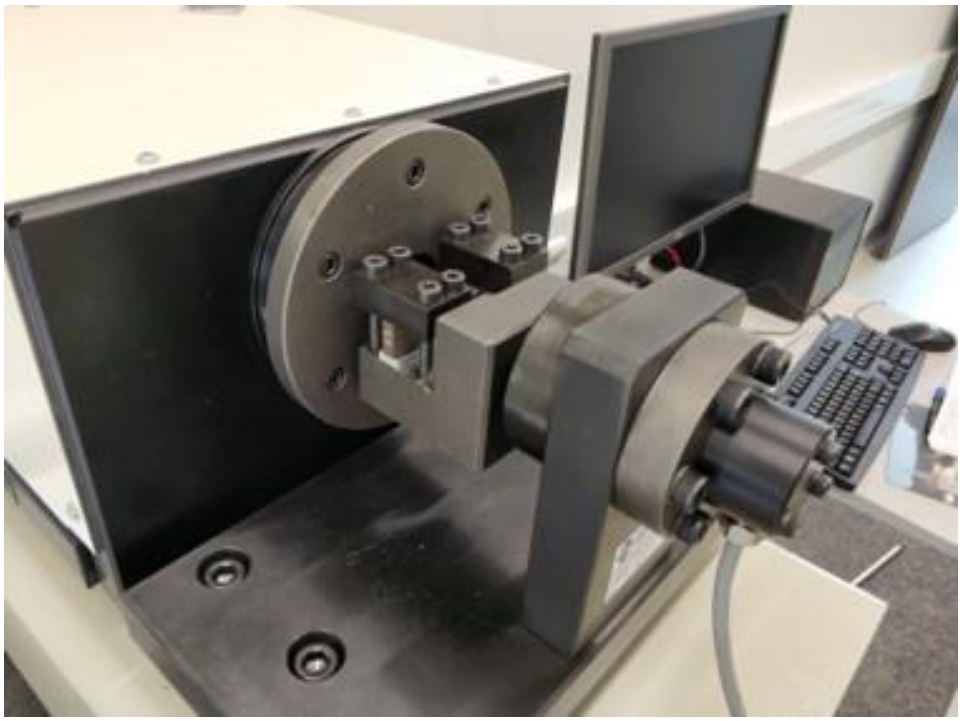

Figure III-1: Bending and torsional fatigue test machine (Rumul ® CrackTronic)

Unlike servohydraulic fatigue set-ups, the Rumul® CrackTronic uses an electromagnetic driven resonator, built as a rotary oscillator, to create an appropriate bending or torsion moment. Independent to the dynamic drive, a static moment is possible to be applied to the specimen via a torsion rod. The test frequency is not controlled but depends on the specimen stiffness. In our experiments, the values reached were f = 96~98 Hz for the as built specimens and f = 94~96 Hz for the polished specimens. The resonant system allows crack initiation to be detected. For all our experiments, the tests are stopped and the number of cycles is recorded for a frequency drop of 0.1Hz. The corresponding detected crack is usually of a few millimeters long. A typical frequency curve is shown (Figure III-2).

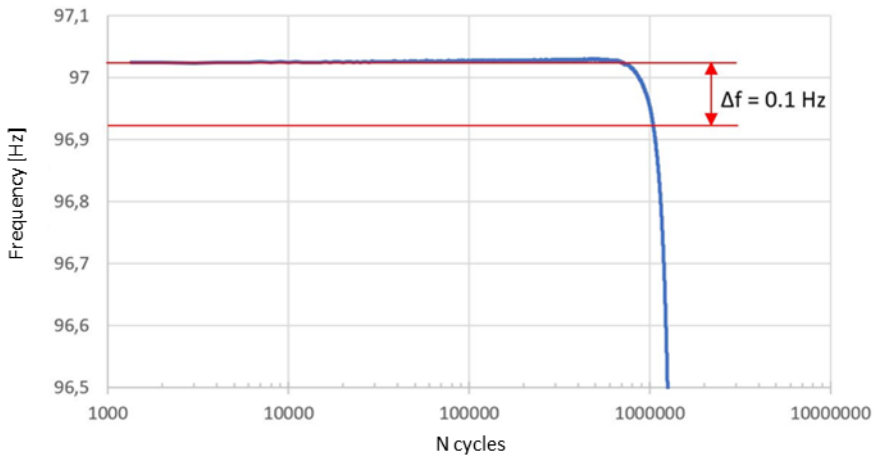

Figure III-2: Frequency evolution along a bending fatigue test carried out with a Rumul® CrackTronic machine. The experiment is stopped when the frequency drop reaches 0.1 Hz.

As for the tensile fatigue tests, the bending and torsional fatigue tests are stress-controlled. The corresponding moments are calculated as follows.

The bending moment writes

$$M_b = \frac{\sigma J}{y} \qquad (III.2)$$

where *J* is the second moment of area for a rectangular section and *y* is the perpendicular distance to the neutral axis:

$$J = \frac{bh^3}{12} \qquad (III.3)$$

with *b* and *h* the dimensions of the rectangular section.

Knowing the specimen diameter, the torque to set the torsional stress value was calculated with:

$$M_t = \frac{2\tau I_G}{d} \qquad (III.4)$$

where I_G is the second moment of area for a circular section:

$$I_G = \frac{\pi D^2}{32} \qquad (III.5)$$

III.1.3. Surface preparation

As the mechanical behavior of SLM components is greatly dependent upon the surface state, it seems natural to investigate the fatigue strength in the as-built condition. Let us recall that for AM components of complex shape, machining is not always achievable. Machining, which is usually applied in the literature to eliminate surface irregularities, is not used in this study. We try, as far as possible, to avoid the introduction of local plastic deformation and residual stresses at the surface of our specimens. Mechanical polishing is expected to be the most adapted technique to remove the surface irregularities

Three different surface state conditions are hence investigated: as-built (AB), simple-polished (SP) and total-polished (TP). An as-built bending fatigue test specimen is shown in Figure III-3a. For the SP case, we remove only the surface roughness on the free surface (shown in Figure III-3b). The thickness of the removed layer is approximately 50 μm. For the TP case, we polish the whole surface of the specimen to remove the surface roughness. Then, we continue the polishing until 250 μm is removed. The TP specimen has a near-perfect surface state assimilated to a machined specimen.

The hand polishing process is detailed as follows. Successive polishing is carried out with silicon carbide abrasive papers of different FEPA granulometry: P100, P280, P600, P1200, 1200/4000. Each specimen requires 2 to 3 hours of polishing. Approximately 50% of the time is spent on the first paper, 20-25% on the second, and so on. With the last paper, a few minutes of polishing are enough to get a

mirror surface. The last step of mechanical polishing is carried out using a felt sheet on which is sprayed a diamond solution having a particle size of 10 µm. This last polishing lasts less than 10 minutes per specimen.

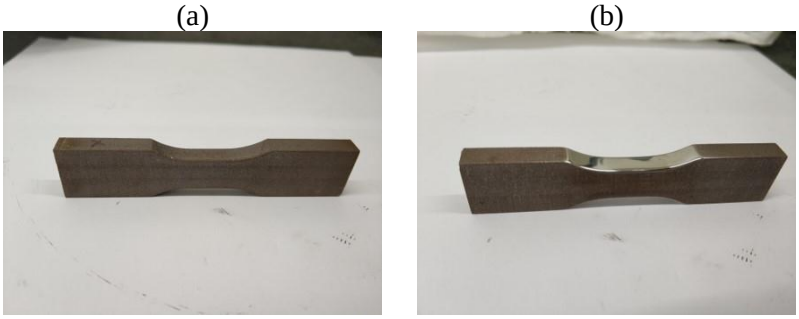

Figure III-3: Bending specimens after different preparations: (a) as-built and (b) simple-polished

III.2. Fatigue strength results and analysis

III.2.1. S-N curves

All the fatigue results are detailed in the Appendix A. The S-N curves for the three loading modes and the three surface state conditions are shown on Figure III-4, Figure III-5 and Figure III-6. The average fatigue strengths calculated by the staircase method are listed in Table III-1.

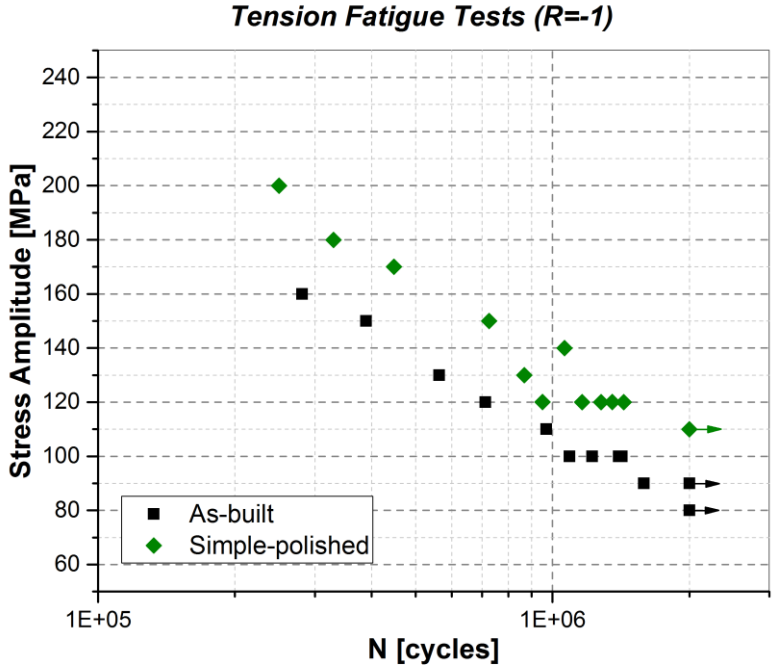

Figure III-4: S-N curves for two surface state conditions (As-built and Simple-polished) in fully reversed uniaxial tension/compression

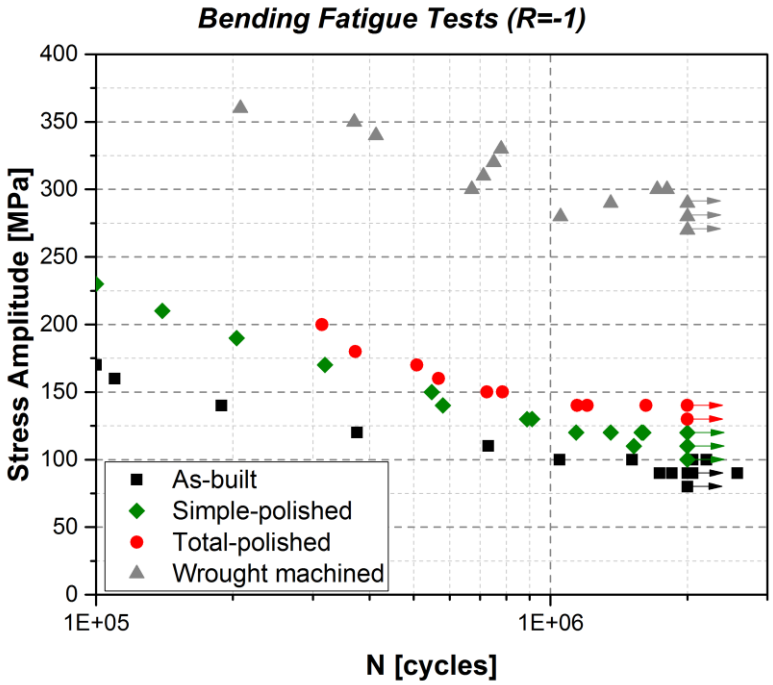

Figure III-5: S-N curves for three surface state conditions (As-built, Simple-polished and Total-polished) in fully reversed plane bending. The fatigue test results for machined specimens of wrought 316L steel are also given for comparison.

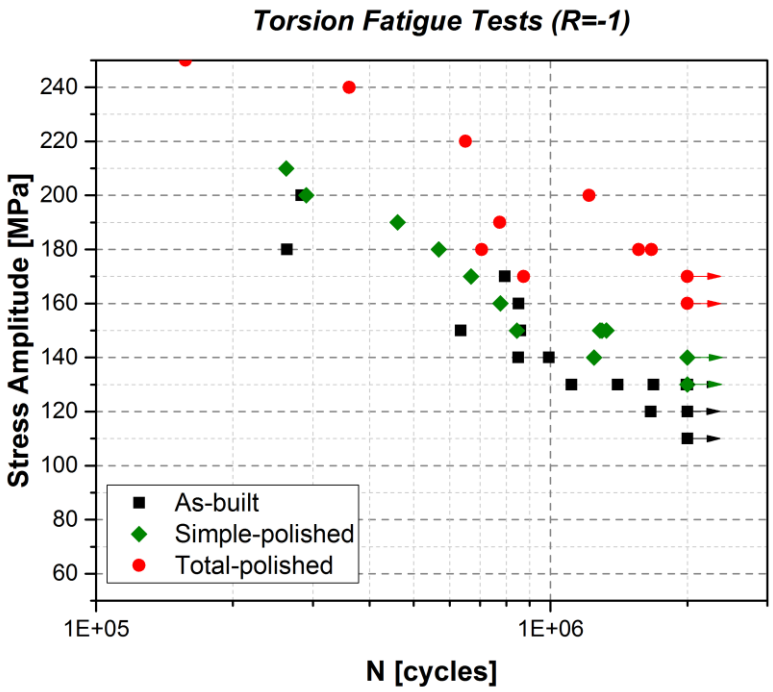

Figure III-6: S-N curves for three surface state conditions (As-built, Simple-polished and Total-polished) in fully reversed torsion

Table III-1: Fatigue strength values assessed with the staircase method for different surface state conditions and different loading modes

	Loading condition		
Surface finish	Tension	Bending	Torsion
As-built	92.5	90	127
Simple-polished	115 (24% ↑)	116(29% ↑)	143(12% ↑)
Total-polished	-	138(53% ↑)	172(35% ↑)

Unit: MPa

III.2.2. Effect of the surface state

In the current study, two mechanical surface treatments named simple polishing and total polishing are applied in the gauge length. The simple polishing is the process where the specimen is polished until the mirror surface state is achieved. Correspondingly, total-polished specimens are the simple- polished specimens subjected to additional polishing.

For the tension loading condition, two sets of specimens are used to study the effect of surface roughness: as-built specimens and simple-polished specimens. Simple polishing clearly increases the average fatigue strength from 92.5 MPa to 115 MPa, i.e., a 24% increase. Likewise, fatigue tests under bending loading show a 29% increase of the fatigue strength for simple-polished specimens compared to the as-built specimens. Results from the torsion loading are slightly different. The as-built specimens show an average fatigue strength of 127 MPa while the simple-polished results lead to a value of 143 MPa. The difference is thus 12% and is apparently lower than the one from the other two loading modes. Hence, eliminating the surface roughness improves the fatigue strength of SLM SS 316L. The improvement is more emphasized under tension or bending loading modes.

For the bending and torsion fatigue tests, besides the as-built and simple-polished specimens, a set of total-polished specimens is added. As previously pointed out, a contouring step is intentionally not applied during the fabrication of all the specimens. The difference observed between the simple-polished specimens and the total-polished specimens is an indicator of the effect of contouring. The fatigue strength has been further improved after the additional polishing. To understand the origin of the differences between the results from the different batches, a better knowledge of the failure mechanisms occurring in simple-polished and total-polished specimens is essential and some fractographic analyses will be carried out later in the document.

III.2.3. Effect of loading type

No evident difference is found between the tension and bending fatigue tests. Previous research often reports that the bending fatigue limit is higher than the tension fatigue strength due to the beneficial stress gradient effect (Wentzel and Huang, 2015). In the current study, the fatigue strength under tension

and bending are remarkably lower than the common strength of wrought 316L. The stress gradient effect is not detectable and might be masked by other phenomena.

The experimental investigation also reveals that the SLM SS 316L has a higher average fatigue strength under torsion than under bending or tension. This observation should be put in perspective, as our fatigue data are highly scattered and the number of tests per condition is maybe not enough. That being said, if we assume that the average fatigue strengths under torsion and tension are close, it does mean that the alloy shows a brittle type behavior, as alloys containing defects (cast iron, cast aluminum alloys ...) most of the time do (Le *et al.*, 2018; El Khoukhi *et al.*, 2019). Some fractographic observations should help explain this macroscopic behavior.

III.2.4. Discussion

A major finding of this experimental investigation is that the fatigue strength of the SLM 316L is lower than the one of wrought316L regardless of the surface state condition. Even if the surface of the specimen is mirror polished, the fatigue strength at $2*10^6$cycles under bending or tension loading modes only improved by around 25% (from about 90 MPa to 115MPa). A further polishing for bending specimens increases fatigue performance. The fatigue reaches around 140 MPa. Much lower than the wrought 316L fatigue strength of 288 MPa at $2*10^6$ cycles under bending loading. This fatigue limit is in line with previous research in the literature (Puchi-Cabrera *et al.*, 2004; Roland *et al.*, 2006; Guerchais *et al.*, 2014). All the fatigue experiments have been conducted in the same way. The significant difference between the fatigue strength of SLM 316L and wrought 316L is this worth noting.

As described in the previous chapter, monotonic and cyclic mechanical tests have been conducted for the SLM material. It is found that the current fabricated 316L has no significant difference in terms of mechanical behavior compared to other SLM fabricated 316L in literature. Besides the yield strength and ultimate tensile strength, the hardness measured for the fabricated samples is in line with the nominal values of the 316L. Therefore, the poor fatigue performance observed in this study cannot be ascribed to its mechanical properties.

About the heat treatment, all the specimens tested have been annealed. The original intention of the annealing process is to reduce the residual stress. Despite the lack of an investigation on the heat treatment effect in this study, we think that the annealing process is not the reason for the unsatisfactory fatigue strength observed.

Regarding the powder, let us recall it can be recycled up to 12 times which is not that usual in the literature. There exist several investigations on the effect of recycled powder in SLM for different materials. Generally, the microstructure and mechanical behavior of the AM materials using recycled powder as well as the chemical composition are similar to that of virgin powder which is consistent with our experimental findings (O'Leary *et al.*, 2015; Strondl *et al.*, 2015; Asgari *et al.*, 2017). Additionally,

it is reported that the recycled powder may even reduce the surface roughness in certain scenarios thanks to fewer surface dendrites on the recycled powder surface (Gorji *et al.*, 2019). Nevertheless, there is no direct comparison regarding fatigue behavior for the recycled powder and the virgin powder of 316L in literature. And, in the framework of this study, the role of recycled powder is presumed to be negligible. Even though we did not arrange experiments using new-powder-fabricated samples for comparison, we believe that the recycled powder is not responsible for the low fatigue strength observed. A further experimental investigation might be of value to check this.

With regard to the fabrication process, the company in charge of the fabrication used optimized process parameters. But no optimization is specified in terms of fatigue behavior. The fabrication process has many parameters which can be connected to the fatigue behavior. We may only provide some conjectures hereby. Laser density and scanning speed influence the porosity rate of the fabricated part. As it is verified that our samples have almost full density, we may assume that these two parameters are not the primary reasons for the poor fatigue strength. Different scanning strategies will result in different melt pool layout which is also a source of anisotropy. According to the work of Konečná et al. about Inconel 718 (Konečná *et al.*, 2016), the fatigue crack paths do not correspond to melt pool tracks or particular building layers. It is supposed that the scanning strategy is not the reason either. The texture of the fabricated part is affected by the scan rotation and scanning strategies. Even though it is widely accepted that <001> texture of cubic material evolves favorably due to epitaxial growth during solidification, there are cases where non-textured microstructure is observed (Suryawanshi, Prashanth and Ramamurty, 2017) (see Figure I-14, for example). The microstructure in this study is found to be strongly textured. Thus, the strong textured state of the microstructure is considered as a potential reason for the low fatigue strength observed.

The defects due to the SLM process probably play the dominant role on the fatigue strength drop.

Concerning the as-built specimens, due to its poor surface state, it is reasonable to attribute the bad fatigue performance to the surface defects. Similar values of fatigue limit for as-built SLM SS 316L have been reported in the literature that is discussed in Chapter I (Mower and Long, 2016; Uhlmann *et al.*, 2017). For example, in the experiments of Mower and Long, the as-built samples have a fatigue strength lower than 100 MPa under cyclic bending loading with a ratio of -1 at $2*10^6$ cycles.

Regarding the simple-polished specimens, polishing the surface eliminates the roughness and likely the related surface defects. The fatigue strength is then improved.

About the total-polished specimens, we expected this batch of specimens to be defect-free and then to recover the fatigue strength level given in the literature. To this regard, the obtained results were disappointing.

In the work of Shrestha et al. (Shrestha, Simsiriwong and Shamsaei, 2019), it is though mentioned that two machined specimens failed after 10^6 cycles (under strain-controlled tension loading) with

equivalent stress amplitudes of 127 MPa and 157MPa respectively. The poor fatigue strength observed is assumed to be due to large LoF defects beneath the surface.

Following this conclusion, we have to check to what extent the defects at the origin of fatigue failure can explain our results. It is expected that the fractographic analysis can offer more information about the fatigue behavior of the SLM 316L. The fracture surfaces of every tested specimen are observed using SEM. Details are presented in the following section.

III.3. Fractographic analysis

Observations on the fracture surfaces reveal where and why the fatigue crack initiates. From the previous analysis about the endurance limit, it is known that the fatigue performance of SLM 316L is weaker compared to conventional wrought 316L. Further investigation, i.e. fractographic analysis, is conducted to explore the mechanism of fatigue failure in SLM 316L. All bending specimens and torsion specimens are inspected. Tension specimens are not exploitable because the fracture surfaces were damaged during the cyclic tension-compression load at a load level R = -1.

III.3.1. Bending samples

III.3.1.1. *Total-polished specimens*

10 total-polished specimens were used to get an estimate of the average fatigue strength. All the fracture surfaces are observed using SEM. At most two initiation sites are observed for all of the 10 cases. For each sample, one single fatigue crack can be found on the fracture surface. The fracture surfaces show similar features. In general, a large cowrie pattern area with river shape fatigue striations emerging from one or two points can be seen. The fatigue crack initiation sites are always located on the free surface. Regarding the position(s) of crack initiation(s), there exist two kinds of configurations: single site and multiple sites (mostly 2 sites, in this study). In terms of the situation of crack initiation, 2 categories are used: single defect at initiation site and several adjacent defects at initiation sites, as shown in Figure III-7.

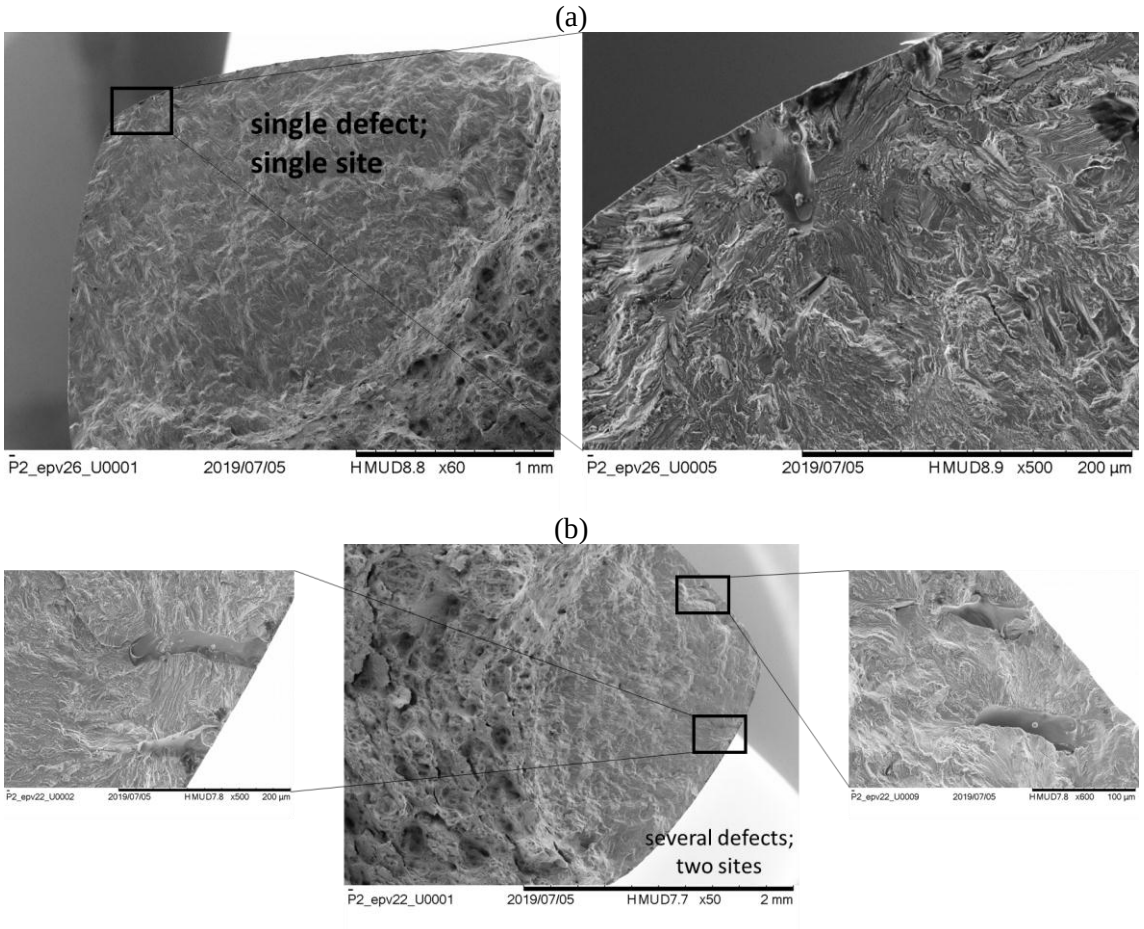

Figure III-7: SEM observations on fatigue crack initiation site(s): (a) single defect at one initiation site; (b) several defects at two initiation sites

Among all the defects observed, two representative defect shapes can be distinguished (see Figure III-8). Most of the time, the observed defect presents an elongated shape while irregular shape can be seen occasionally (P2-S2, P2-S28). The elongated defect can be considered approximately as an ellipse with an ellipticity ratio of about 3 to 5. It is always the major axis of the elliptical defect that penetrates the solid part. Hence, the defect is even more harmful under the perpendicular loading and leads to a strong stress concentration as well as a strong stress gradient. The size of the fatigue-controlling defect varies. The defect responsible for fatigue crack initiation has an area ranging from 2800 to 10000 µm².

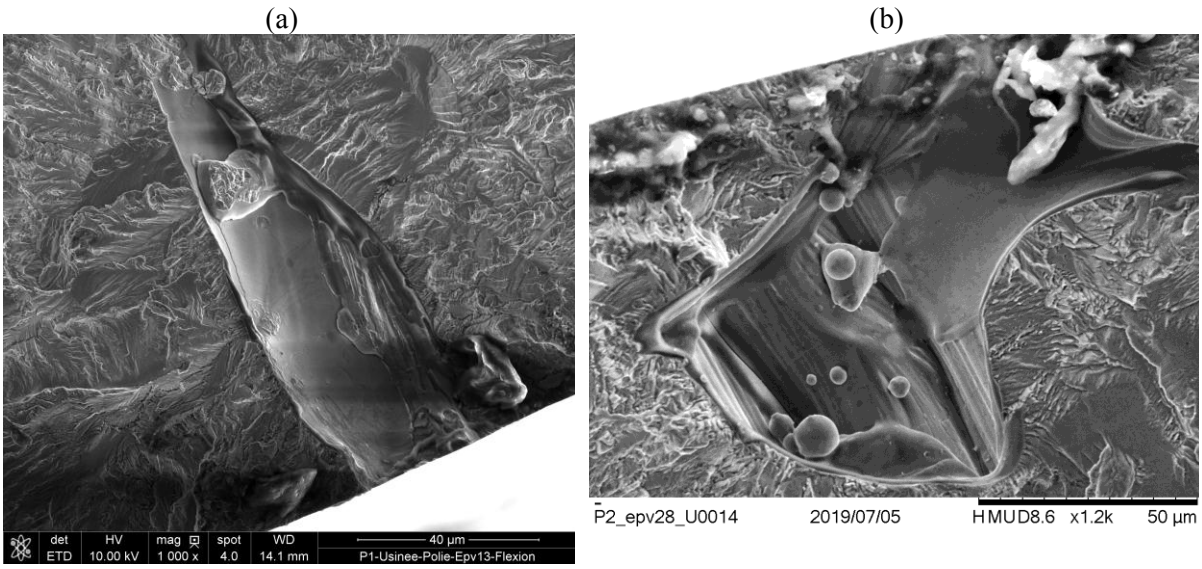

Figure III-8: (a) Elongated shaped defect (b) and irregular shaped defect at fatigue crack initiation site

III.3.1.2. *Simple-polished specimens*

14 simple-polished specimens are subjected to bending fatigue loading. The fractographic analysis shows that 13 out of 14 specimens have evident fatigue cracks. Cowrie pattern areas can be found in this kind of specimen. The unusual fracture surface is observed in one certain specimen (P1-S5). The scenario of crack initiation and growth cannot be defined (Figure III-9). The other 13 specimens lead to conventional fatigue failures.

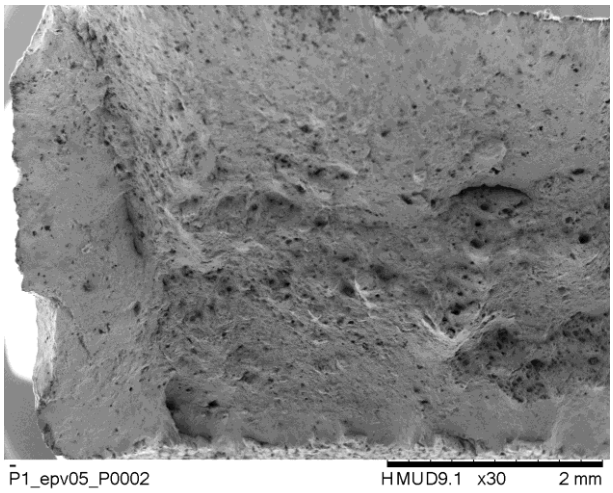

Figure III-9: Fracture surface of specimen P1-S5 (scenario of fatigue crack initiation and growth is not clear)

Unlike the total-polished specimens, several cracks can be observed. 9 out of 13 specimens present only one fatigue crack while the remaining 4 present clearly 2 independent fatigue cracks. A representative picture for 2 independent fatigue cracks in one specimen is shown in Figure III-10. In the above discussion about total-polished specimens, we mention a configuration that a fatigue crack can

possibly initiate from several sites. There is a possibility that all the initial defects contribute to the crack formation while it is also possible that the subsidiary defects can only cause non-propagated cracks and later the cracks are activated due to principal defects. But it is clear that the multiple cracks form solely and do not interact with each other. Even without the presence of other cracks, one crack can lead to fatigue failure. Hence, we will treat the multiple cracks in one specimen as several isolated cracks. A total of 17 cracks are observed and measured.

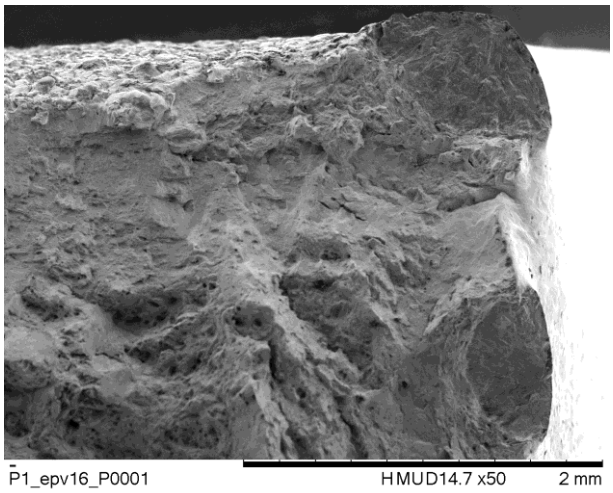

Figure III-10: Two independent fatigue crack initiation sites in specimen (P1-S16)

Another difference between simple-polished specimens and total-polished specimens is that the presence of defect increases significantly.

For the simple-polished specimens, the upper and lower surfaces where the stress level reaches its maximum value are polished to eliminate surface roughness. The left and right sides where the stress level is lower because of the stress gradient of bending loading are left as built. The positions of cracks are listed in Table III-2. A great majority of cracks initiates from the rough surface. However, stress level and surface state compete for control of fatigue failure as several cracks are found on the simple-polished surface of the specimen. More high-magnification observations are conducted to check the fatigue crack initiation mechanism.

Table III-2: Positions of crack initiation sites in simple-polished specimens

Crack initiation position	Sample number
As-built surface (10+3)	P1-S3; P1-S9; P1-S11; P1-S13(C1, C2); P1-S15; P1-S20(C1, C2); P1-S21; P1-S23(C1, C2); P1-S24; P1-S26
Simple-polished surface (3+1)	P1-S6; P1-S16(C1, C2); P1-S27

For the cracks on the simple-polished surface, although it is not the most frequent scenario, an interesting observation of the simple-polished surface is found about the defect morphology. As shown in Figure III-11, several parallel adjacent defects with similar morphology are seen. The shape of the

defect is close to the defect observed in the total-polished specimen. It is expected that this defect is due to the fabrication process. Compared to other researches in which the "contouring" is usually included, this pattern of defects arrangement is never reported, even for as-built products. The clusters of LoF defects play the predominant role compared to the lateral surface roughness in those cases. In the total-polished specimens, we observed adjacent LoF defects but not as clustered as those of the simple-polished specimens. The explanation can be that those LoF defect clusters exist mostly on or near the surfaces. So, we can get rid of them by removing a thick layer of material on the surface.

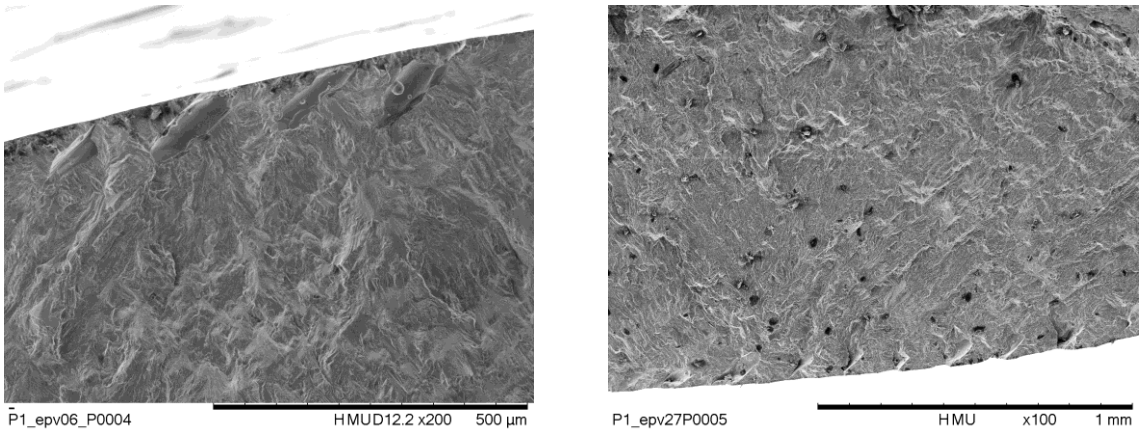

Figure III-11: Parallel adjacent defects observed in simple-polished specimens

Most of the cracks are found on the unpolished surface. Although the loading level is lower compared to the top surface, the defects on the lateral surface have a larger size and interact with the surface roughness. A representative inherent defect of the as-built part is shown in Figure III-12. These defects have often a size of several hundred micrometers. Parallel adjacent surface defects can be seen in the as-built surface as well. They may be similar of the adjacent defects seen in the polished surface which play a dominant role over surface roughness in fatigue failure.

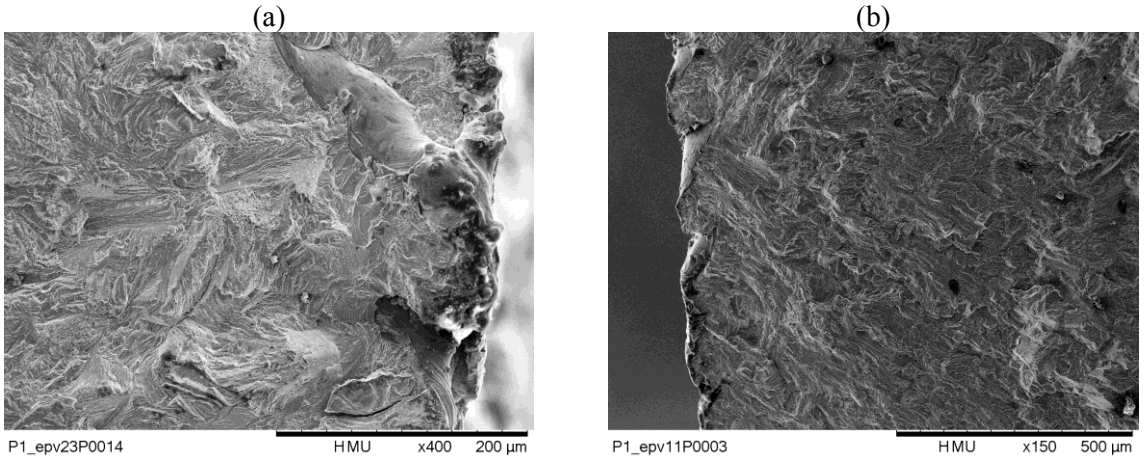

Figure III-12: Defects observed on the as-built lateral surface of simple-polished bending specimens: (a) a combination of roughness and pores; (b) parallel adjacent defects

III.3.1.3. *As-built specimens*

15 as-built specimens are used in the bending fatigue tests. 2 as-built specimens do not present clearly fatigue crack type failure. For the remaining 13 specimens, we locate 15 independent fatigue cracks. Among these 15 cracks, 5 initiated from the lateral side where the stress level is lower than the top surface. Since all the specimens are vertically built, the four longitudinal surfaces can be considered identical in terms of surface state

The as-built specimens keep all inherent defects. The photos (Figure III-13) typically show the main mechanism of fatigue failure for as-built specimens. Several defects are found in the vicinity of the initiation site. Those defects acting simultaneously or successively are likely to be all responsible for the fatigue failure. A series of parallel defects distributed on the top surface are seen on Figure III-13 a). From the bottom picture (Figure III-13 b), in the edge of the specimen, both roughness defects and lack-of-fusion pores make the surface state extremely poor.

(a)

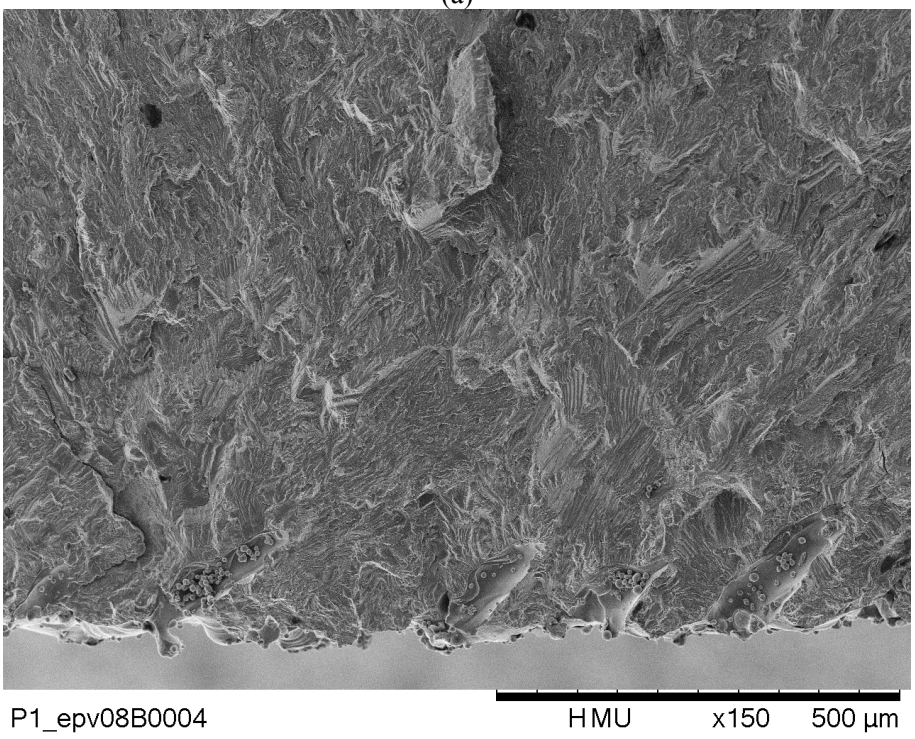

(b)

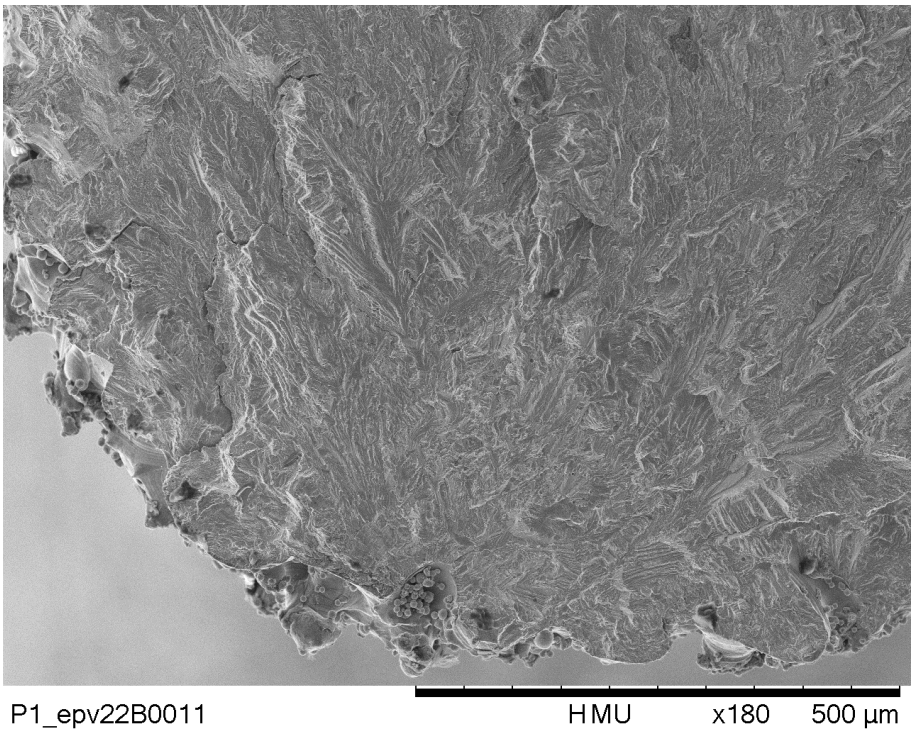

Figure III-13: Representative crack initiation site in as-built specimen: (a) in the middle of top surface; (b) in the edge of top surface

In terms of morphology, the defects found in the as-built specimens are of the same kind as those observed in the as-built surface of the simple-polished specimens as shown in Figure III-14. The inclined elongated LoF defect is often the critical defect. The defects are often a combination of lack-of-fusion and surface imperfectness which is caused by surface tension or precision of laser projection. For the defect in Figure III-14 (a), its open-form makes it detectable under profilometry, while in Figure III-14 (b), the defect is subsurface and cannot be measured by a surface scan.

(a) (b)

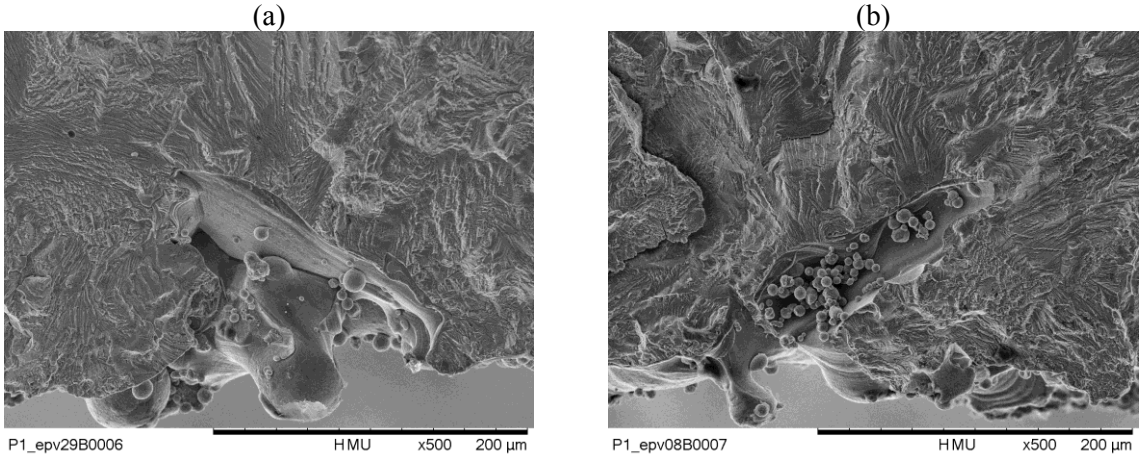

Figure III-14: Morphology of defects in as-built specimens: (a) open-form defect; (b) subsurface defect

III.3.1.4. *Summary*

The cracks observed here mainly initiate from LoF defects. The porosity measured in this study is less than 0.1%. It is consistent with the previous observations where no gas pore can be seen.

The LoF defect is usually flat and undetectable under μCT. But the elongated morphology plus the deep penetration of LoF defect are very harmful in terms of fatigue. For the as-built specimen, LoF defects combined with surface roughness strongly decreases fatigue performance. Simple polishing which removes a thin layer of the surface can only get rid of roughness. A cluster of adjacent LoF defects can still be seen. Nevertheless, a stronger polishing removing a layer of 250 μm seems to be insufficient to eliminate all the LoF defects. The LoF defects at crack initiation site seems though fewer in total-polished specimens. We can deduce that the distribution of LoF defects is highly concentrated on the surface. Under a certain depth, the presence of the LoF defect decreases.

For most of the total-polished specimens, we can find only one unique fatigue crack while multi-cracks are observed for as-built and simple-polished specimens. A closer look at the crack shows several crack initiation sites. All the initiation sites are found on the surface or subsurface.

The above-mentioned observations are summarized in Table III-3.

Table III-3: Summary of fractography observations on all the tested samples

Specimen number		Total polished 10		Simple polished 14		As-built 15	
Fatigue failure / (undefined type failure)		10 / (0)		13 / (1)		13 / (2)	
Single crack	Multiple cracks*	10	None	9	4(2)	11	2(2)
Fatigue crack observed		10		17		15	
As-built surface	Polished surface	None	10	13	4	15	None
Single site	Multiple sites†	8	2(2)	15	2(2)	Uncountable	
Initiation site		12		19			
Single defect	adjacent defects#	6	5(2);1(3)	11	3(2);1(3); 1(4); 1(5);1(8)		
Inherent defect observed		19		36			
Elongated defect	Irregular defect	15	4	19	17		

Note:
*: Number of specimens with multiple cracks (number of cracks)
†: Number of cracks having multiple sites (number of sites)
#: Number of sites having adjacent defects (number of defects)

III.3.2. Torsion samples

In the classical fracture mechanics theory, the propagation of crack is categorized by three modes: opening mode, sliding mode and tearing mode. Schematic illustrations are shown in Figure III-15. For wrought metallic material, a typical torsion fracture mechanism is shown in Figure III-16. After initiation, a mode II crack growth is observed in the first stage. The crack path is on the plane of maximum shear stress. From a critical crack length, the crack path changes and mode I becomes predominant (stage II). The crack propagates in two perpendicular planes experiencing the maximum normal stress.

Regarding AM materials, very few results are reported in the literature about the fatigue crack growth features under torsion loading. To the authors' best knowledge, there is no result on SLM 316L. The aim of the present investigation on torsion failure surfaces is to clearly explain the role of defects on crack initiation and growth and to check if the stage I (mode II) and stage II (mode I) are observed.

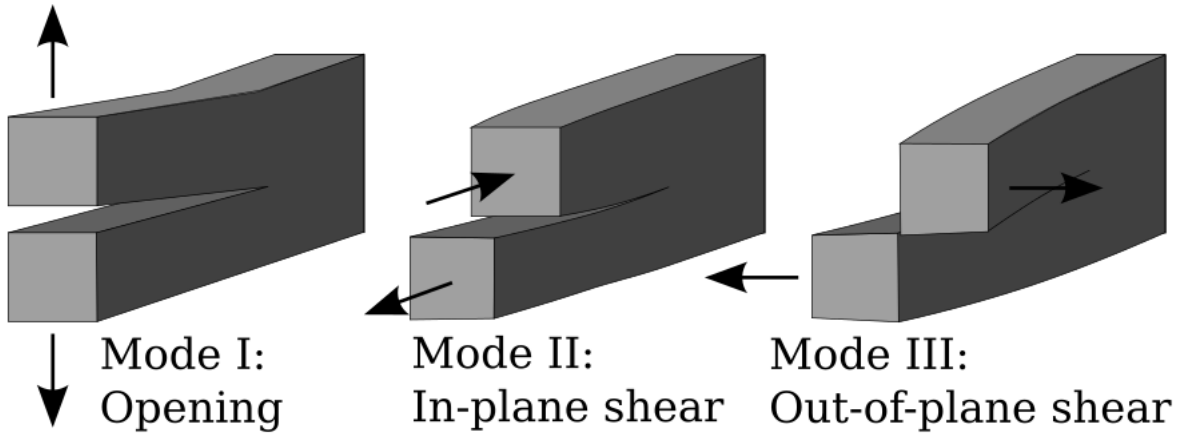

Figure III-15: The three fracture modes

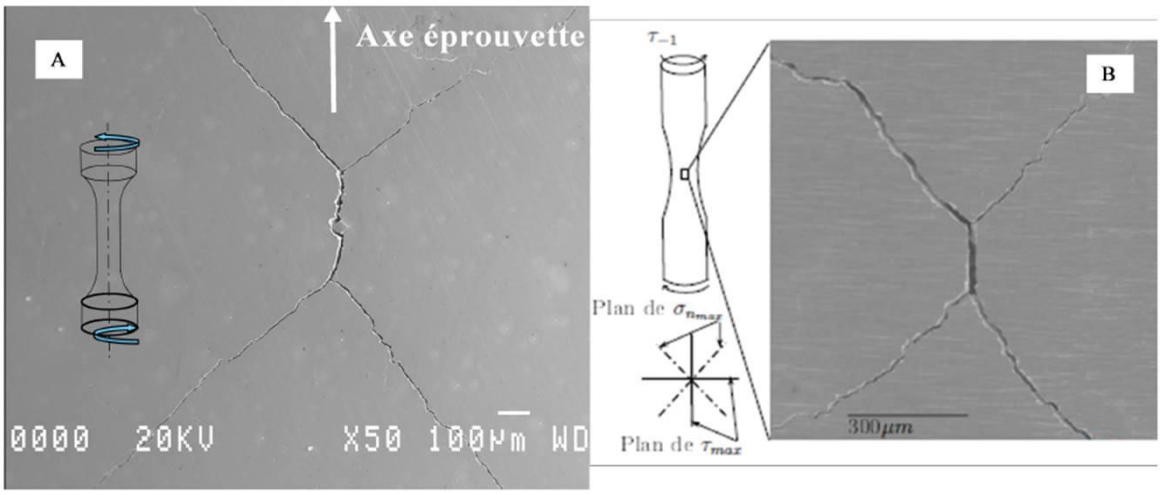

Figure III-16: Representative fatigue crack path under torsion loading

III.3.2.1. *Total-polished specimens*

Some observations on the free surface of the gauge length are conducted for the total-polished specimens after failure. It can be seen that the specimen breaks into two parts because of mode I cracks perpendicular to the maximum normal stress planes. The normal to the fracture surface and the axial direction of the specimen make a 45° angle. Besides the two cracks which go through the entire section, one smaller crack oriented 90° to the specimen axis is visible in the central initiation area. It is then clear that the observed mode I cracks originate from a mode II crack as can be seen in Figure III-17. As the mode II crack is small, SEM observations are carried out to better illustrate the first stage of crack initiation and propagation.

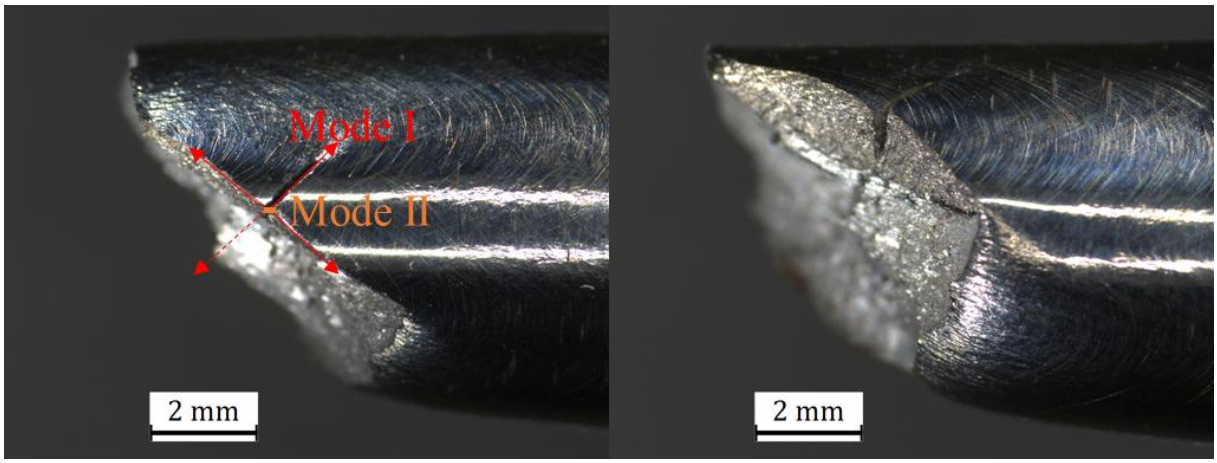

Figure III-17: Macroscopic crack path in total-polished torsion specimen: stage I (mode II) followed by stage II (mode I)

Form Figure III-18, we can see that a LoF defect is responsible for the crack initiation. This defect lies in the subsurface of the specimen and is not eliminated by polishing. Two perpendicular cracks form from both sides of the defect. The size of this LoF defect is similar to the measurements made in the bending specimens. A photo from the same specimen of a secondary crack is shown in Figure III-19. It is observed that crack initiates in shear mode and expands along the maximum normal stress planes.

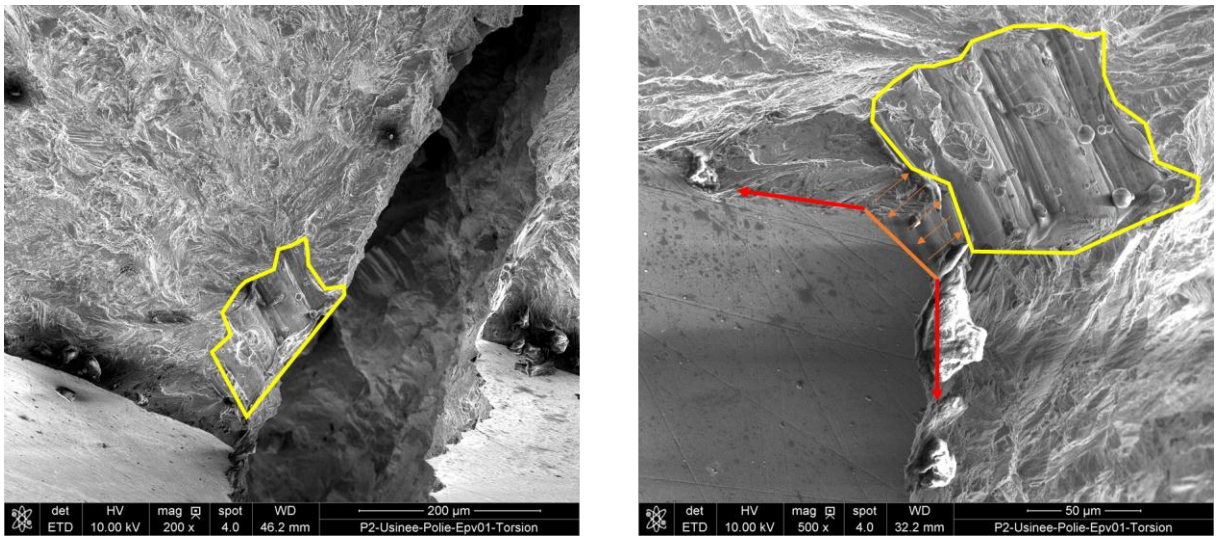

Figure III-18: Fracture surfaces of total-polished specimen under torsion loading

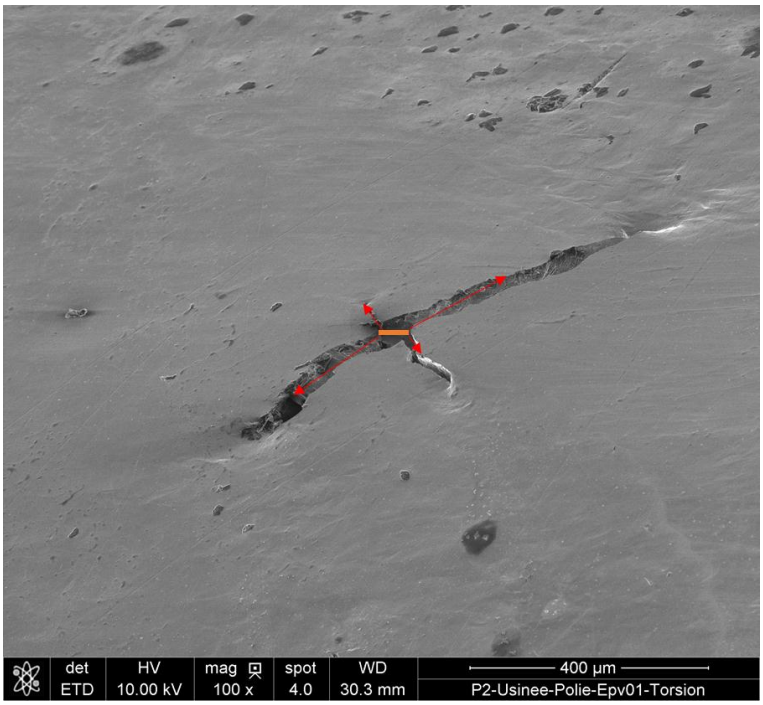

Figure III-19: Secondary crack in the total-polished specimen under torsion loading

As mentioned before, the polishing procedure completely removes the surface roughness. But surface defects, in particular LoF defect, are still present. For the great majority of total-polished specimens, the LoF defect can be found at the initiation site of fatigue crack (see Figure III-20). The crack path is seen clearly on the free surface. The shift from shear stress plane to normal stress plane confirms the proposed fatigue failure mechanism.

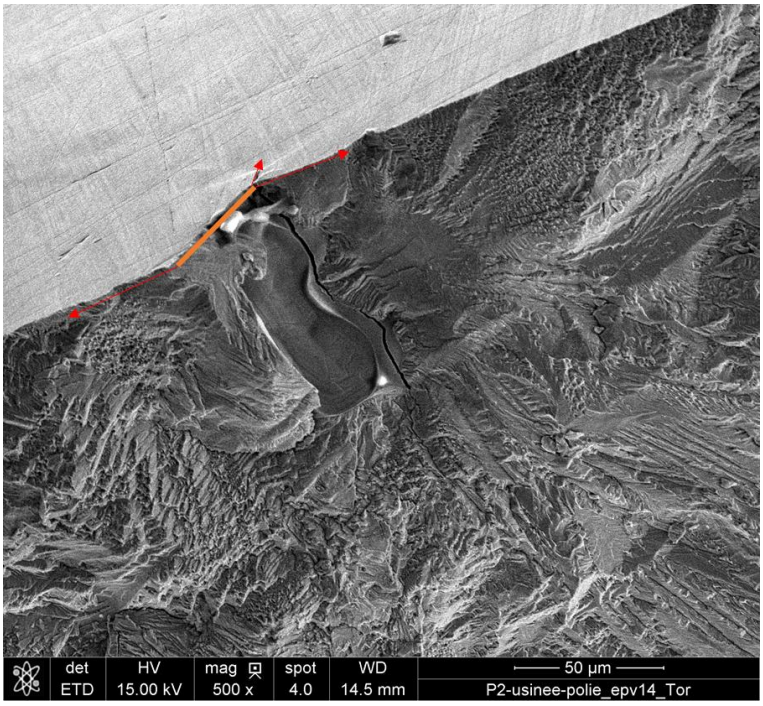

Figure III-20: Example of the fatigue crack initiation and growth mechanism from defect under torsional loading. Two stages are clearly visible.

III.3.2.2. *Simple-polished specimens*

The crack path in the simple-polished specimen is not as typical as the one in the total-polished specimen. Generally, the main crack still follows the maximum normal stress plane. The presence of surface defects seems to affect the crack propagation path. The local stress concentration can hence result in a change of maximum normal stress plane orientation and lead to a tortuous crack path.

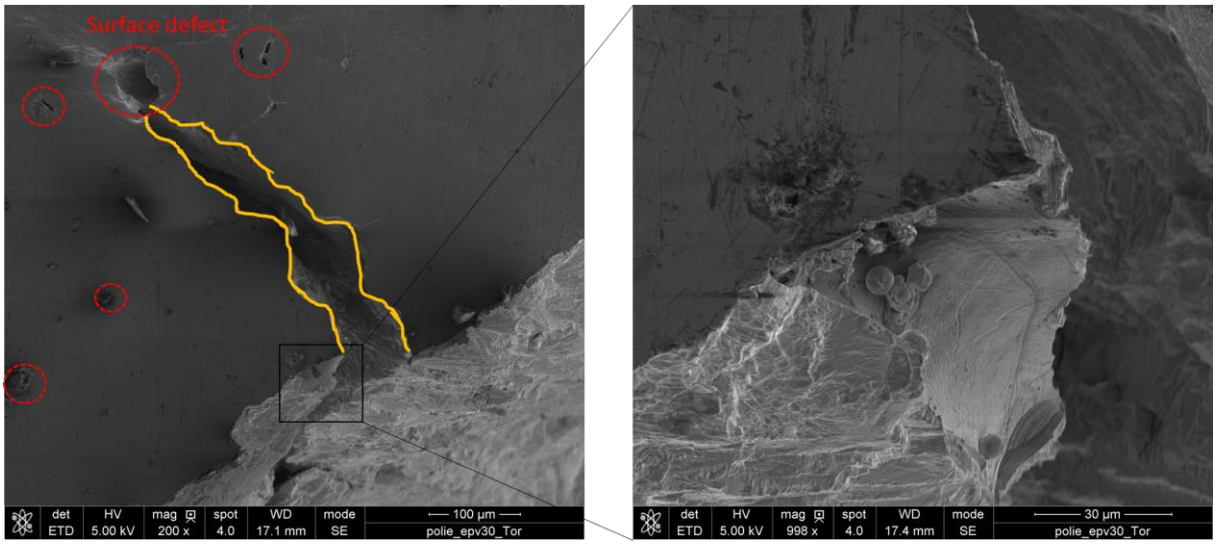

Figure III-21: Fracture surface observation on the simple-polished torsional specimen

III.3.2.3. *As-built specimens*

It is difficult to distinguish the role of roughness and pores in the fatigue initiation for as-built specimens. Figure III-22 shows the surface state of the as-built specimen.

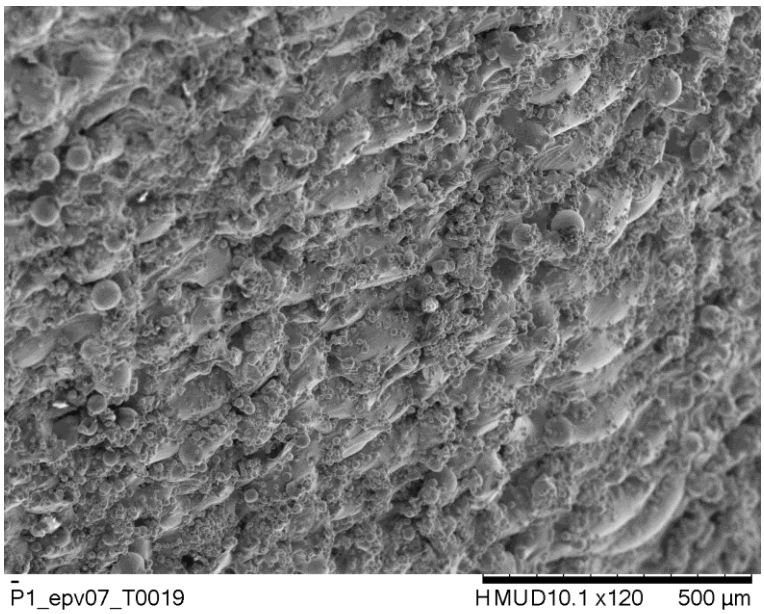

Figure III-22: Surface state of an as-built torsion specimen

As for as-built specimens, the normal to the fracture plane is oriented 45° to the specimen axis, meaning the mode I is predominant. A series of large LoF defects are present at the initiation site (see Figure III-23). Figure III-24 a) illustrates that defects exist everywhere on the crack path. A horizontal mode II crack grows among adjacent LoF defects which makes it difficult to see. Nevertheless, the non-coplanar fracture surfaces indicate the existence of this mode II horizontal crack. On the right, the picture shows that two neighboring defects initiate one fatigue crack. Because of the rough surface state, surface defects are everywhere. The critical defect's presence is much more frequent compared to the one of polished specimens. Moreover, the size of the defect is larger and clustering defects are often seen.

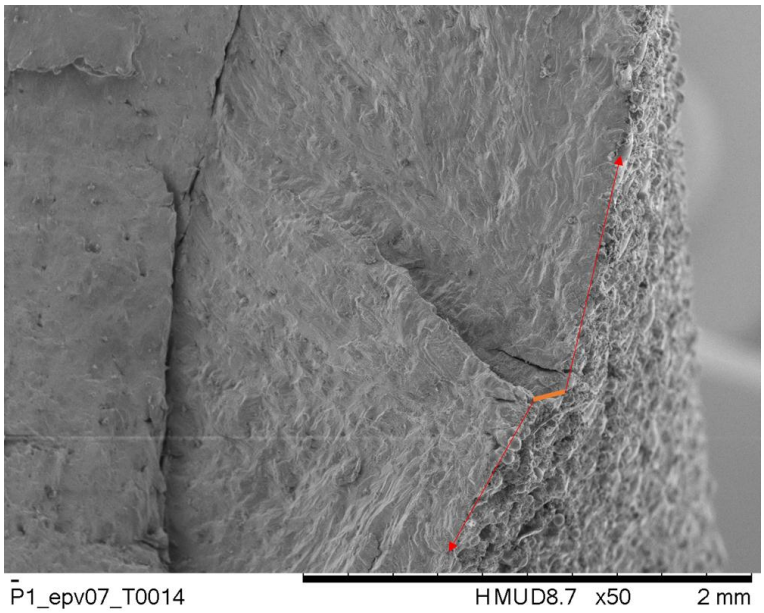

Figure III-23: Crack path in an as-built torsional specimen

(a) (b)

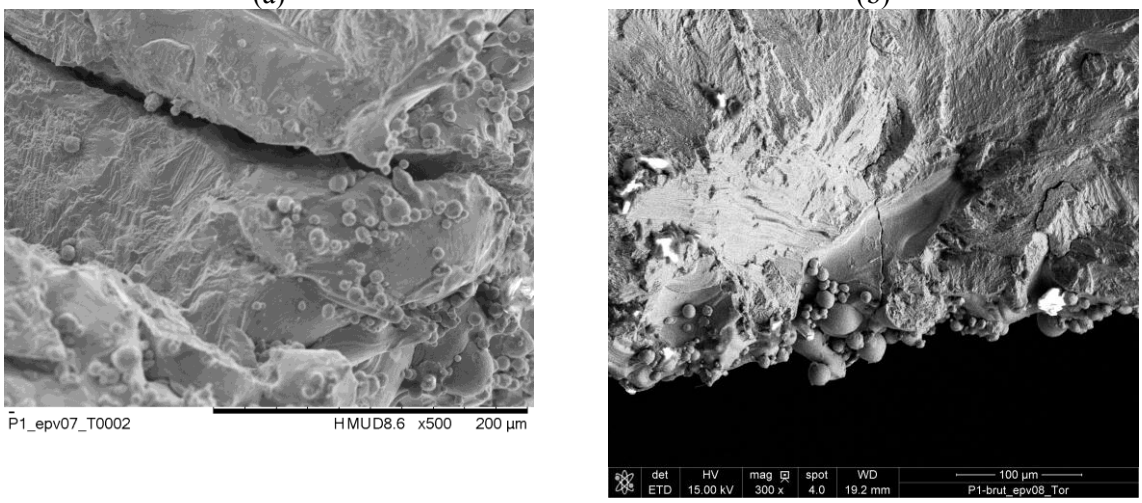

Figure III-24: Defects at the origin of failure in as-built torsion specimens: (a) a series of surface defects; (b) two clustering subsurface defects

III.3.3. Summary

Fractography analysis helps us to explore the mechanism of fatigue crack initiation and propagation.

For the bending and torsion samples, the crack initiation sites are always found to be LoF defects. The origin of the lack-of-fusion pores in the contour layer is unclear but could be attributed to the combination of several phenomena. To begin with, a lack of sufficient bead overlap between the starting and ending point of one circular contour can occur. Additionally, an interaction between the laser and contaminants such as spatter or nanoparticles in specific laser trajectories could induce heterogeneities in the melt pool shape, and thus impact the melt pool overlap. Especially, the defects are flat with often an elongated shape.

Another issue is that the torsional fatigue limit is a bit higher than the bending fatigue limit. From the fracture surface observations, we know the mechanism of fatigue failure is still shear stress driven in the first stage. This could explain this result.

The fatigue test results clearly showed that the experimental fatigue strength is lower than expected. This can be partially explained by the previous fractographic observations. Indeed, even in the total-polished specimen, large LoF defects can be found. For the other surface state conditions (AB, SP), clusters of defects are responsible for fatigue failure. These clusters of adjacent sharp defects are likely to be very detrimental to the fatigue strength and could explain the differences observed with the literature data.

III.4. Correlation between defect size and HCF strength

III.4.1. Defect measurement

In AM materials, porosity is mainly composed of gas and lack-of-fusion pores. Gas pores are usually of spherical shape and show a size less than 100 μm. Lack-of-fusion defects are often elongated and non-spherical. The irregular shape of LoF defect makes it difficult to choose a representative parameter to describe its geometry. Different measurement methods are proposed in the literature. Schematic illustrations are presented in Figure III-25. According to the original definition of the Murakami parameter (Murakami, 2002), the considered area should be a smooth contour wrapping the irregular defect outline. Romano et al. (Romano, Miccoli and Beretta, 2019) measure the actual area of LoF defect and use an equivalent circle to replace the defect. Le (Le *et al.*, 2018) uses Feret diameter as well as the Murakami parameter which is the square root of the area projected onto the plane of maximum normal stress. El Khoukhi (El Khoukhi *et al.*, 2019) chooses the depth of defect as the description parameter. Nevertheless, none of the above methods can deal with several defects at the crack initiation site. Iben Houria (HOURIA, 2015) proposed an alternative way to consider two defects at one crack initiation

site. If the two defects are close to each other, they are treated as one big defect. A rectangle is used to encompass the two defects and its $\sqrt{Area}$ is considered as the effective defect size.

Murakami

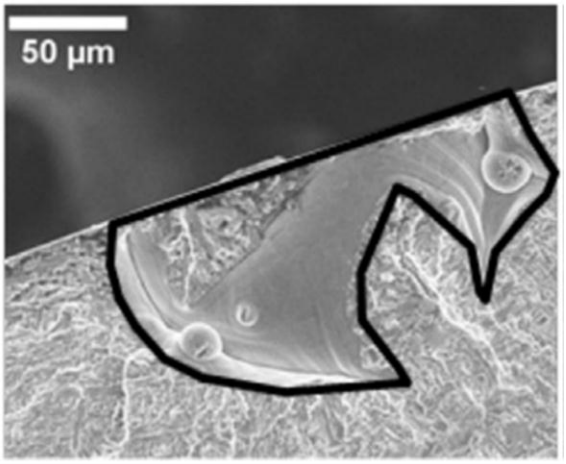

Le et al.

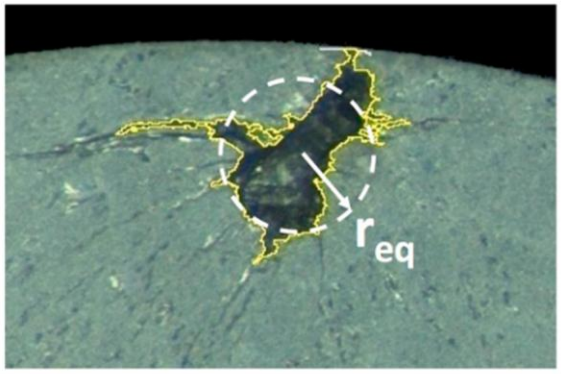

Romano and Beretta

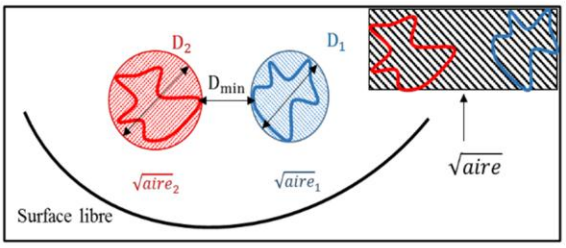

Iben Houria

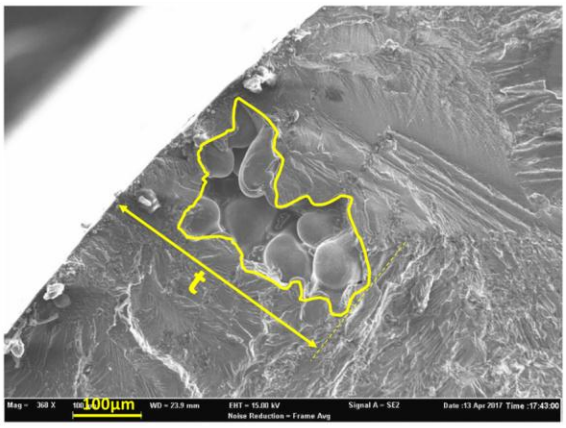

El khoukhi et al.

Figure III-25: Different methods proposed to measure irregular defect(s) (HOURIA, 2015; Le *et al.*, 2018; El Khoukhi *et al.*, 2019; Romano, Miccoli and Beretta, 2019)

In our observations of fracture surface, several defects are frequently encountered in the crack initiation zone, especially for the as-built condition.

In order to have a better understanding of the impact of the defects observed in our experiments, we will propose a practical treatment by modifying the previously mentioned methods. A convex hull is used as an effective zone containing the defect(s). The original description of the effective area is "a smooth contour", according to Murakami himself. However, the choice of one smooth contour is highly dependent on the operator. By using a convex hull, the measurement will be consistent without the influence of artificial factors. Another advantage of the convex hull is the Feret diameter will keep unchanged as the original defect shape.

Regarding the adjacent defects, two measurement techniques are proposed and used. Either the largest defect size or the area occupied by all the defects are considered. The following pictures (Figure III-26) show examples of these two distinct measurements.

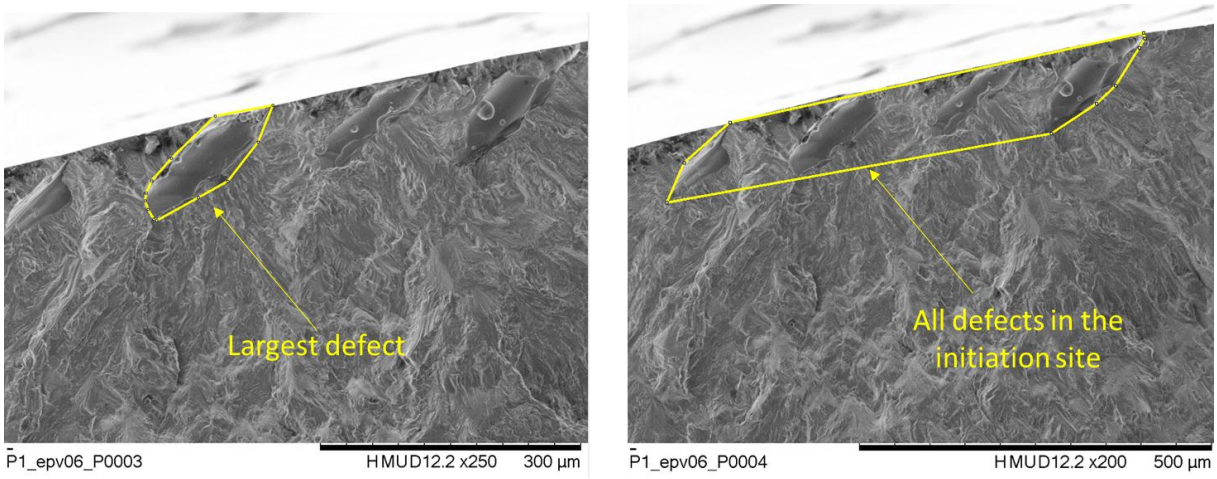

Figure III-26: Two different measurement techniques to assess the size of a cluster of adjacent defects

Considering the complexity of LoF defect shape, we will make use of several parameters to describe the critical defects. Murakami parameter, Feret diameter as well as defect depth will be used to identify the relation between fatigue performance and critical defect size. In addition, we define a new parameter called "Modified Feret diameter" which is the square root of the product of maximum Feret diameter and minimum Feret diameter. The product of maximum Feret diameter and minimum Feret diameter is equivalent to the area of the unique minimum rectangle which encompasses the defects. This parameter is considered by far the most regular description of the irregular defect (s).

III.4.2. Kitagawa-Takahashi diagram

All the observations made on the bending specimen failure surfaces can be used to build a Kitagawa diagram. The run-out and the failed specimens are distinguished together with the surface state conditions. Total-polished results are represented by red marks; simple-polished results are indicated by green marks and as-built results correspond to blue marks. For the run-out cases, dot shape marks are used. And cross shape marks denote those failed cases.

When the size of the biggest defect is used (minimalist measurement approach), it can be seen that none of the size parameters can clearly take into account the surface state effect (Figure III-27). Using the depth of the critical defect, the two polished batches cannot be distinguished. Considering the other three parameters, defects in total-polished specimens are always smaller compared to the other two batches. The simple-polished specimens and the as-built specimens have similar outcomes. The explanation is that the largest defect found at the initiation site in these two batches is similar. In conclusion, the minimalist measurement approach is not the best choice to describe the situation in the current study where several defects act simultaneously in the crack initiation zone.

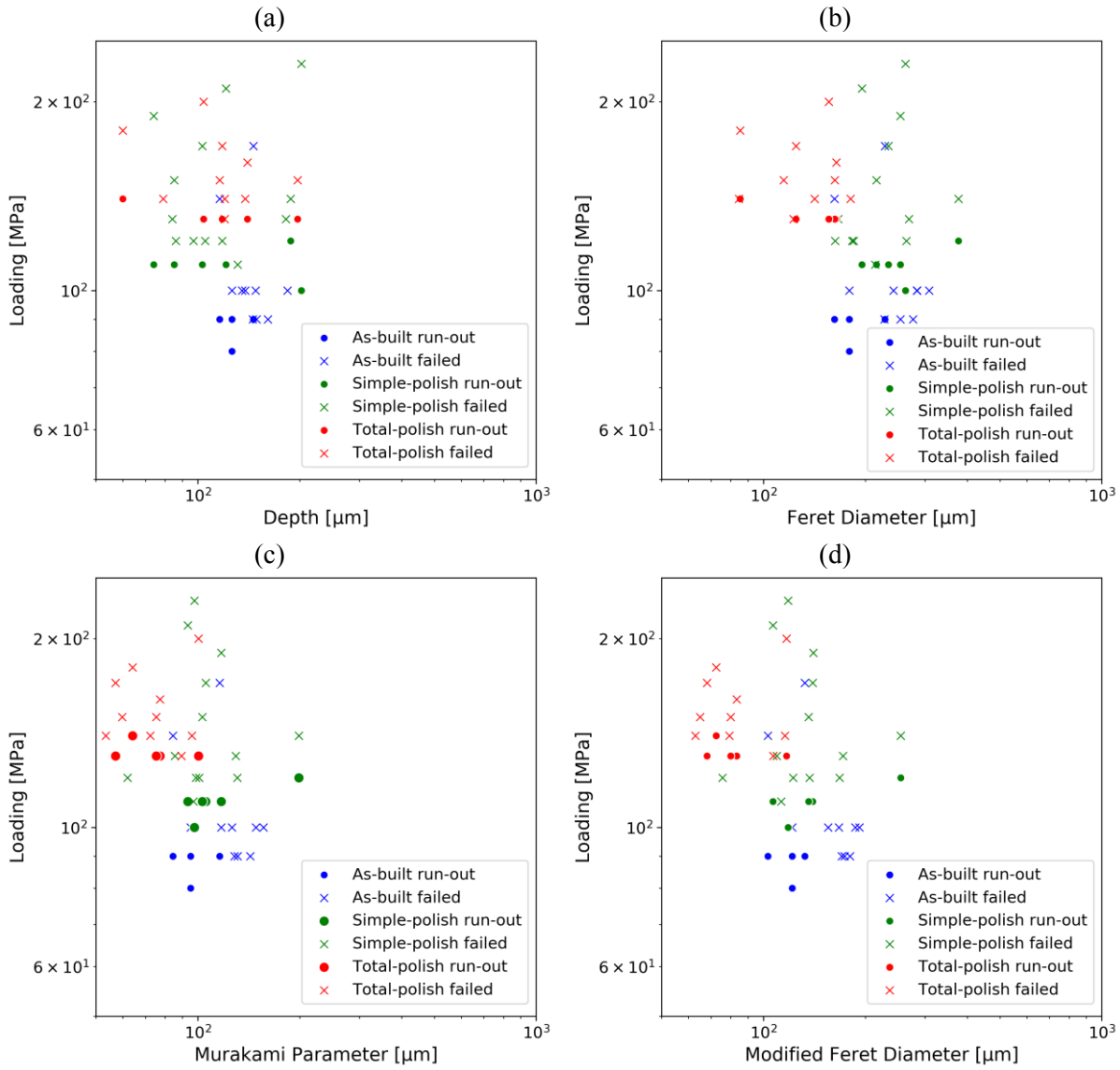

Figure III-27: Kitagawa diagram using the minimalist measurement methods with different parameters as effective defect size: (a) depth, (b) Feret diameter, (c) Murakami parameter, (d) modified Feret diameter

If now, the total area occupied by several adjacent defects is used as the measure of the defect size at initiation (maximalist measurement approach), the situation is quite different. Figure III-28 shows a pretty good correlation between the fatigue strength and the defect size for all the size parameters, except for the depth. Let us recall that the Murakami power law (Eq. III.6) often gives good correlation between defect size and fatigue strength:

$$\sigma_w = 1.43(H_v + 120) * \sqrt{Area}^{-\frac{1}{6}} \qquad (III.6)$$

A similar power law expression ($y=a*x^b$) is used to fit our results with the application of least square method. It should be noted that a is a material parameter which is dependent on the material's hardness and b is a parameter describing the relationship between ΔK_{th} and defect size. Considering that

Murakami has conducted a series of experiments for various materials and defect types and indicated -1/6 is a universal value for the exponent, we add a reference fitting line of which the parameter b is fixed at -1/6 for comparisons.

Using depth as the defect-describing parameter seems to be unfruitful. When using Feret diameter, a fitted slope of approximately -0.18, which is in good agreement with Murakami exponent, is found. Murakami parameter and modified Feret parameter yield similar results, with a slope of –0.26. The maximalist measurement approach is hence found to adequately reflect the detrimental impact of the size of several adjacent defects on the fatigue strength. From Figure III-28, it is also clearly observed that the biggest critical defects are present in the as-built specimens, while the total-polished case leads to the smallest defect size.

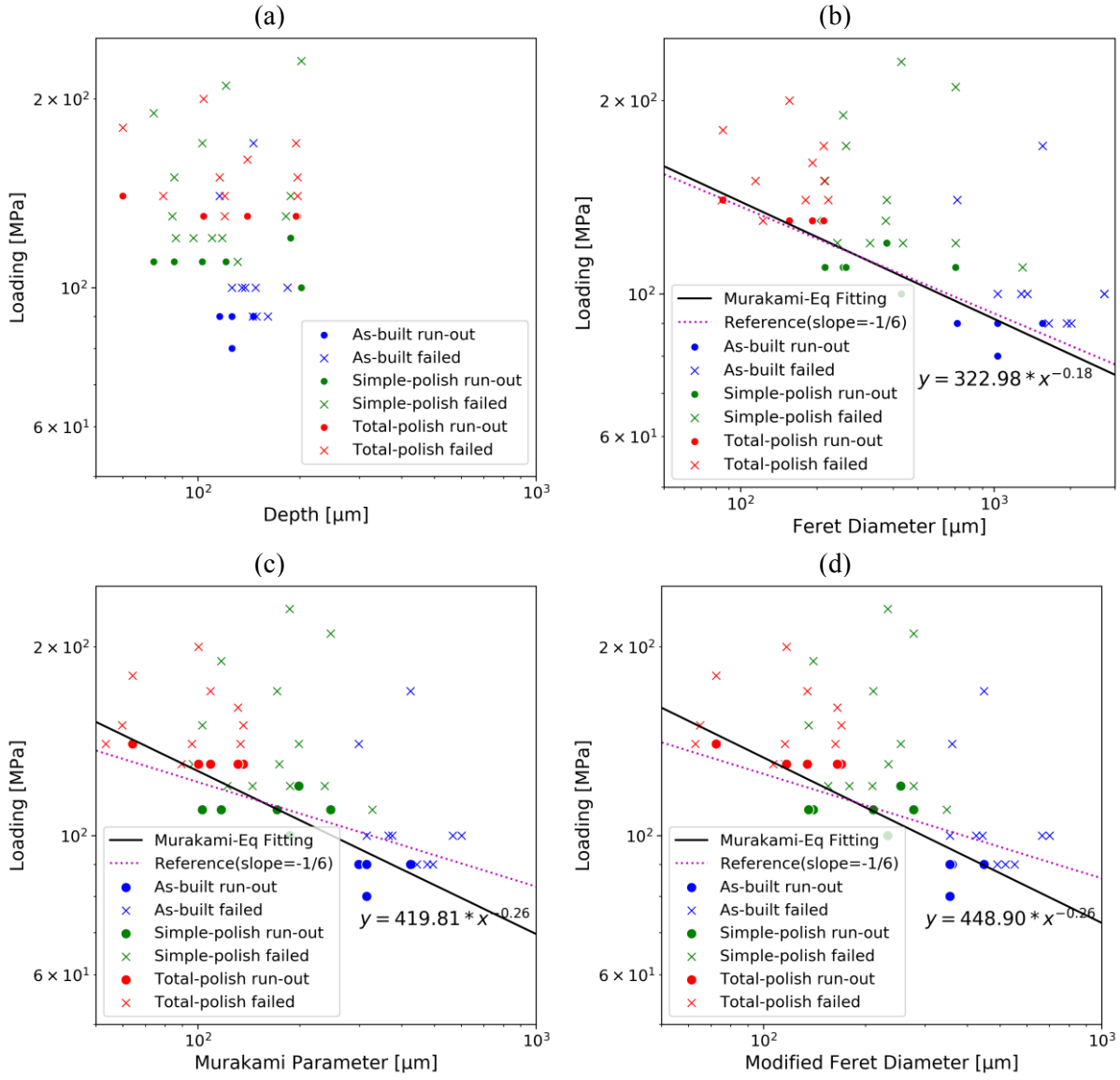

Figure III-28: Kitagawa diagram using the maximalist measurement methods with different parameters as effective defect size: (a) depth, (b) Feret diameter, (c) Murakami parameter, (d) modified Feret diameter

In the light of that the Murakami power law has been successfully used in describing the fatigue behavior of defective material, the above findings enlighten us that, leaving aside the distinguishing features of AM, e.g. the microstructure, internal pores…, the fatigue performances of AM steels can still be controlled by the surface/subsurface defects as of the conventional steels.

III.5. Conclusions

Despite the absence of the contouring step in our process, the surface roughness of our specimens are consistent with the literature data, unlike our fatigue strength levels which are much lower except for the as-built case. The main difference seems to come from the presence of a lot of subsurface LoF defects that are known to significantly affect the fatigue behavior.

The effect of the stress gradient is not observed in the current investigation since the bending fatigue tests and tension fatigue tests yield similar results. The apparent absence of gradient effect is maybe due to the presence of numerous, large and sharp defects. We attribute the overall poor fatigue strength to the inherent defects, in particular, the surface or subsurface LoF defects.

The fatigue crack initiation and growth under torsion loading show a stage I (mode II) followed by a stage II (mode I). LoF defects are observed at the crack initiation site and can lead to tortuous crack path.

Following Murakami approach, it is found that the bending fatigue strength decrease correlates well with the increase of an effective defect size. In the case of several adjacent defects present in the initiation zone, a modified measurement method is then proposed and the related maximalist approach is found to adequately model the effect of the different surface state conditions investigated.

Due to the presence of large internal LoF defects, the effects of surface roughness on initiating fatigue cracks were minor in this study. Surface quality has a minor effect on the fatigue behavior of SLM SS 316L specimens whilst the inherent LoF defect originated from the fabrication seems to be the main controlling parameter.

Results from Chapter II clearly demonstrated that the SLM SS 316L have similar mechanical properties as wrought SS 316L. Hardness, UTS, strain to failure, cyclic behavior are close. The microstructure features are though very different with a strong morphological and crystallographic texture. Chapter III has stressed the importance of LoF defects originated from the fabrication process. But the low Young's modulus suggests the textured microstructure has also an influence on the mechanical properties. To better assess the respective effects of microstructure and surface defects, additional experimental data would then be required. Another experimental campaign was not planned in the context of this PhD thesis. We hence turn to the use of numerical tools and we will try in the next

two chapters to get a better understanding of the main controlling parameters in fatigue of SLM materials.

Syntheses

- The fatigue limits have been estimated using the staircase method for SLM SS 316L in tension, bending and torsion loading modes respectively.

- The effect of the stress gradient is not observed in the conducted experiments.

- Polishing the surface improves the fatigue strength of SLM SS 316L.

- The fatigue cracks always initiate from inherent LoF defect(s) in SLM SS 316L.

- Several adjacent LoF defects are often observed on the fracture surface. It is concluded that these clusters of defects act conjointly and can be considered as one large defect in terms of fatigue prediction.

Chapter IV.

Preliminary investigations on the high cycle fatigue sensitivity to microstructure and defect

IV.1. Microstructure sensitive modeling framework for defective materials 99

IV.2. Explicit microstructure model and fatigue prediction approach 102

IV.2.1. Finite element model 102

IV.2.2. Material constitutive laws and fatigue approach 104

IV.2.2.1. Crystal cubic elasticity 104

IV.2.2.2. Fatigue criteria 106

IV.2.2.2.1. Matake criterion 107

IV.2.2.2.2. Dang van criterion 107

IV.2.2.2.3. Papadopoulos criterion 108

IV.2.2.3. Non-local method 108

IV.3. Results 110

IV.3.1. Application and evaluation of non-local method based on experimental results 110

IV.3.1.1. Mechanical analysis 110

IV.3.1.2. Fatigue analysis 113

IV.3.2. Further investigation of the non-local method on the microstructure effect 118

IV.3.2.1. Effect of grain morphology 118

IV.3.2.2. Effect of grain size 122

IV.4. Conclusions 124

Synthesis 126

The main aim of the present study in the numerical aspect is to enrich the fatigue modeling of defective materials by investigating the effect of defects under the framework of microstructure sensitive modeling. In this chapter, we focus on the parametric study of non-local method in its application to the microstructure sensitive modeling. The work presented here is purely numerical and the results are compared to the experimental results from Guerchais et al. (Guerchais *et al.*, 2015). An explicit virtual microstructure finite element model is built up and used. Modifications of fatigue criteria by introducing non-local methods are explained and evaluated to qualitatively explore the connection between critical distance and the defect size or the microstructure. To better reveal the value of the non-local method, further investigations concerning grain morphology and grain size are conducted. It is expected that the proposed realizations of the non-local method are compatible with general simulation scenarios.

IV.1. Microstructure sensitive modeling framework for defective materials

The numerical simulation of metallic polycrystalline aggregates has developed quickly in the past decades (McDowell and Dunne, 2010; Schwartz, Fandeur and Rey, 2013; Briffod, Shiraiwa and Enoki, 2017). Its application to the fatigue predictions is more and more valued for the efficiency and cost-saving as the fatigue experiments are very time consuming and require massive efforts on the devices' setting up and specimens' preparation. In the high cycle fatigue regime, it is well known that the strength is highly influenced by the defects, especially the ones on (or close to) the free surface (Nadot *et al.*, 1999). The defects in the metallic materials are frequently encountered due to the manufacturing process or the material nature, e.g. shrinkage pores in cast aluminum alloys with large grain size (Le *et al.*, 2018), gas pore or lack-of-fusion defects and fine microstructure for materials from the additive manufacturing process (Le *et al.*, 2019). More investigations on artificially induced defects (Billaudeau, Nadot and Bezine, 2004) or surface irregularities (Abroug *et al.*, 2018) are reported too. Even though anisotropy and stochasticity of microstructure can be displayed by advancing experimental instruments such as SEM, EBSD and AFM, sometimes definitive conclusions from experiments are hardly achievable due to the restrictions as sample number, fabrication reproducibility, etc. Since fatigue is a local phenomenon, microstructure impacts obviously the initiation and propagation of fatigue crack from

inherent defect by acting as the main source of scatter in fatigue test results. Vincent et al. found that the critical defect size has a connection with characteristic microstructural dimension other than actual physical length for different steels (Vincent *et al.*, 2016). But the converse conclusion is reported by Bracquart et al. for aluminum alloy (Bracquart *et al.*, 2018). When dealing with the issue of microstructure/defect competition in fatigue, a simulation would be reliable if the microstructure is explicitly taken into consideration.

The effect of defect size on reducing the high cycle fatigue performance of a material is often schematically shown by the Kitagawa-Takahashi (K-T) diagram (Kitagawa and Takahashi, 1976). El Haddad et al. (El Haddad, Smith and Topper, 1979) proposed a single curve for all defect sizes by using the short crack correction. Two main mechanisms are presented by the two lines. The horizontal line represents that, within a certain range, the defect size does not change the high cycle fatigue limit while the other line indicates that the fatigue limit drops linearly on the log-log scale as the defect size increases. Based on the good prediction of Linear Elastic Fracture Mechanics on fatigue performance of specimen having a long crack, the second line can generally be related to the stress intensity threshold. In the *K-T* diagram, the non-damaging cracks do not affect fatigue performance, as well as the long cracks, lead to a strong decrease of fatigue limit. From the perspective of industrial application, it is of great importance to explore the transition region where the short crack has an influence but does not play the dominant role.

Microstructural features such as grain boundaries and crystallographic orientations play important roles in the fatigue damage process (Guilhem *et al.*, 2010). For a crack with the length on the order of several grains, the microstructure governs its propagation which cannot be predicted by LEFM using macroscopic variables (Lukáš and Kunz, 1994). A framework of explicit microstructure sensitive modeling is for instance proposed by McDowell et al. (McDowell, 2007) to estimate fatigue behavior from microstructural perspectives. The introduction of defects and microstructure to the numerical model can bring a great amount of stress heterogeneity, i.e. local stress concentration and local stress gradient. Stress concentration will affect strongly the local mechanical response which causes dislocation or deformation leading to fatigue failure. Theoretical stress concentration factor K_t defined

by the ratio of the local maximum stress and the nominal stress is commonly used to characterize the stress concentration in the vicinity of the defect. In terms of fatigue behavior, another parameter K_f which is the ratio of fatigue strength of a smooth specimen to that of a notched specimen presents more clearly the influence brought by a stress concentrator (Yao, Xia and Gu, 1995). However, K_f is always less than K_t because of the effect of stress gradient and size. For defective materials, the critical point at the notch root always over-emphasizes the effect of stress concentration which leads to an underestimation of fatigue performance. Additionally, the extreme value from finite element model is highly dependent on the mesh size without further treatment.

In order to investigate the effect of defect and microstructure as well as their competition, the non-local method is implemented under the framework of microstructure sensitive modeling in this study. The concept used is the critical distance theory (Qylafku *et al.*, 1999). The idea of the critical distance theory is assuming there is a small zone with the size of several grains in which the grains affect each other mutually leading to fatigue initiation. This method has been successfully applied in several pieces of research on the fatigue performance of defective materials. But in the applications, the definition of the critical distance is somehow vague. Taylor gives an explicit expression of the critical distance parameter L (Taylor, 1999) which is a function of material's threshold ΔK_{th} and fatigue limit σ_0. This model works well in the life assessment as it can give the prediction of fatigue life within the same order of the experimental observation (Bellett *et al.*, 2005). But considering the microstructure, the result is not that satisfactory since the parameters are macroscopic and cannot represent what happens locally. Even if we calibrate these parameters locally in the hot spot, a local calibration for a non-local method seems to be unreasonable. A more frequently encountered treatment is to give a suitable L_{cr} without further explanation (Vayssette *et al.*, 2019). Besides the concept of L_{cr}, an alternative realization using microscopic parameters (layer depth) was proposed and tested (Guerchais, Morel and Saintier, 2017).

However, from the concept of the critical distance theory, the non-local parameter should have a connection with the critical defect size and the microstructure. Inspired by the findings of Vincent et al. (Vincent *et al.*, 2016) that the critical defect size is relative to the microstructural attributes, two different realizations of the non-local method are proposed and evaluated in this study. One is the critical radius

method which doesn't make explicit reference to microstructure. Another one is the neighbor layer method characterized via microstructural attributes.

Based on the explicit microstructure sensitive modeling framework, Robert et al. tested both elastic and plastic material behavior models under different types of loading to simulate the meso-mechanical response in the polycrystalline aggregate (Robert *et al.*, 2012). The predominant role of elastic anisotropy on simulations in the HCF regime, which is in agreement with the finding of Sauzay (Sauzay, 2007), authorizes the simplification of neglecting crystal plasticity in HCF prediction for some materials. Hor et al. (Hor *et al.*, 2014) evaluated several multi-axial stress-based fatigue criteria statistically at the grain scale of polycrystalline aggregate. Guerchais et al. (Guerchais, Morel and Saintier, 2017) firstly introduced the neighbor layer method in his investigation of the effect of defects. Though the predictions from his probabilistic and non-local determinant criteria are in line with the experimental findings, the identification of parameters is not explained which remains unclear in the simulation perspective. The current study will be an extension of previous researches dealing with microstructure sensitive modeling.

IV.2. Explicit microstructure model and fatigue prediction approach

IV.2.1. Finite element model

The objective numerical model is an explicit microstructure sensitive model which contains the quasi-realistic forms of grains and the organized distribution of grain orientations. A frequently used and realistic way of generating the microstructure of polycrystalline is to use Voronoi polyhedral to tessellate the microstructure (Robert and Mareau, 2015). The conceived model should be three-dimensional. But for the models containing defects that can be of tens of the grain size, the three-dimensional models are not feasible considering the computation expense. For instance, a 316L steel having a mean grain size of 15 μm will be divided into more than 200000 grains even if the studied volume is set to only 1 mm^3. The 2D model is acceptable for its approximated results and a lower expense of computational resources. The simulations in this study are performed by a two-dimensional square-shaped domain partitioned by convex polygons (Quey, Dawson and Barbe, 2011). Three batches of models are built up and are summarized in Table IV-1. The models in the first batch have the same average grain size corresponding to the cited experimental research which serves as the reference results. In the second batch, equiaxed and non-equiaxed grain distribution are used and compared. The equiaxed case is represented by a normal distribution of grain size which is in good agreement with the

conventional fabricated steel and the non-equiaxed cases are described by the uniform distribution or the log-normal distribution. More grain sizes are examined by the models of the third batch. The loading type is tension-compression fatigue loading with a ratio R=-1. The left end of the FE model is pinned while the bottom is restrained from vertical displacement. The loading is applied to the right end. The top surface is considered as the free surface. Several illustrations are presented in Figure IV-1.

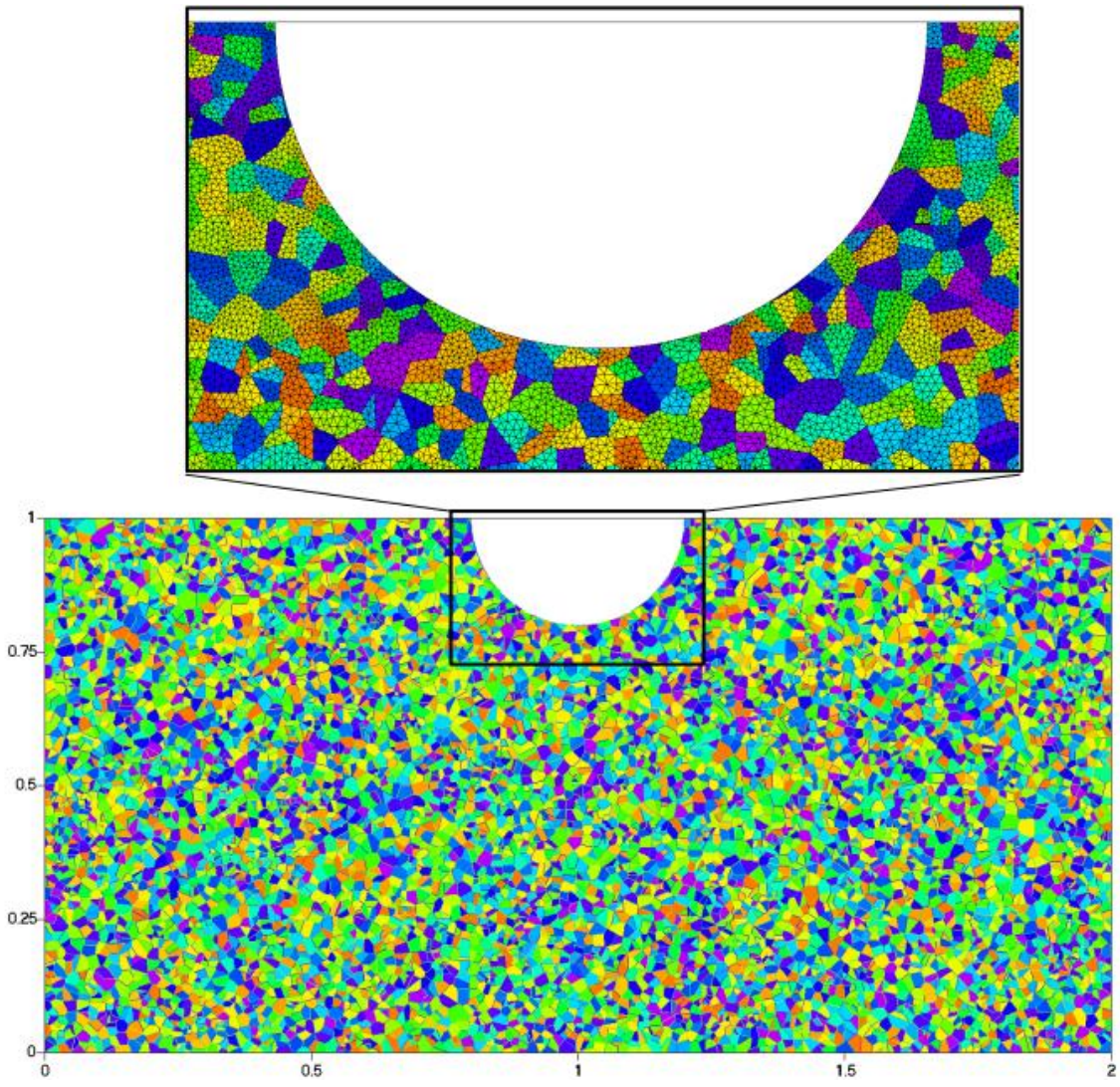

Figure IV-1: Example of finite element models used

For the benchmark model, which has a 2*1 mm^2 studied area with an average grain size of 15 µm, approximate 9000 grains are used to discretize the space. The mesh generator Gmsh (Geuzaine and Remacle, 2009) is used. The reduced 3-ordered triangular element is employed in the mesh. Previous research about the numerical methods for the modeling of polycrystalline materials points out that the yielded results change with an increasing mesh resolution (Robert and Mareau, 2015). The convergence is not always achieved in the finite element model, but the error is assumed to be insignificant with a fine mesh. Convergence tests of the non-local responses, which are presented in the appendix D, are performed to choose an appropriate mesh size. The characterized lengths of 2 µm in the vicinity of the

defect and 5 µm in the rest part are applied. i.e. the grains near the defect are each discretized on average with 50 elements while 10 elements for the remote grains. The model has approximately two million degrees of freedom. The finite element model is two-dimensional, but the slip direction is in a three-dimensional space. The generalized plane strain hypothesis is used to take the deformation in the third direction into account. Isotropic texture is used in this model, which means this crystallographic aggregate can be considered as having no preferential orientations (see Figure IV-2).

Figure IV-2: Pole figures of (a) 100, (b) 111 orientation for the crystallographic orientations implanted in numerical models

Table IV-1: Characteristics summary of the different configured model

	Model Configurations				Number of simulations
	Defect size	Grain morphology	Grain orientation	Grain size	
Batch1	6 values 5,15,30,60,120,200 µm	4 kinds Voronoi tessellations*4	24 sets Isotropic*24	1 15 µm	576
Batch2	6 values 5,15,30,60,120,200 µm	4 kinds Uniform tessellation, Voronoi tessellation, Log-normal Voronoi tessellation *2	24 sets Isotropic*24	1 15 µm	576
Batch3	3 values 15,60,200 µm	4 kinds Voronoi tessellations*4	12 sets Isotropic*12	2 30,100 µm	288

IV.2.2. Material constitutive laws and fatigue approach

IV.2.2.1. *Crystal cubic elasticity*

The anisotropy of metallic polycrystalline aggregates is due to its microstructure. The anisotropy of the material has two main sources that are the elastic anisotropy and the plastic deformation in the slip systems. To better describe the contribution to the anisotropy of elastic part and plastic part, Figure IV-3 presents an investigation on the mechanical response in polycrystal copper which shows an anisotropy factor of 3.26 (Robert *et al.*, 2012). In all the loading types, the cubic elastic model produces highly

scattered results (gray scattered points in Figure IV-3a) compared to that of the isotropic elastic model (black straight line in Figure IV-3b). Even though the addition of crystal plasticity part to the cubic elastic model can slightly reduce the maximum shear stress in the highest value range, the results with or without crystal plasticity are still in quite good agreement as the distribution fits well the regression line. Even though the mechanism of fatigue is still linked to plastic deformation, the crack initiation is mostly local slip-driven, as is pointed out by Gao et al.(Gao *et al.*, 2007). More specifically, inherent surface defect, for instance, pores induce the slip dislocation and stress concentration(Jiang *et al.*, 2018). Nevertheless, the aim of the numerical model is to use mechanical quantities to indicate fatigue initiation. Since stress concentration actives the slip dislocation, stress can be considered a relevant indicator of fatigue initiation. In terms of simulated mechanical responses under the HCF regime, especially the calculated stresses, the crystal plasticity part has limited influence. For the sake of simplicity, the constitutive model is characterized by crystal cubic elasticity in this study. The accuracy loss due to the missing of crystal plasticity is expected not to affect the main tendencies observed in our simulations.

Material used is the austenitic stainless steel 316L. On one hand, austenitic steel shows a Face-centered cubic (FCC) crystal structure having limited slip systems number (12 slip systems) compared to other microstructures which reduce the computation time. On another hand, austenitic steel has been widely used for several decades. Abundant related researches can be found in the literature. The anisotropic elasticity material constitutive law contains 3 independent coefficients describing the crystal stiffness tensor C_{1111}, C_{1122} and C_{1212}. The anisotropic factor has a value of 3.64 which is close to the value 3.26 of the copper studied by Robert et al. (Robert *et al.*, 2012). Teklu et al. (Teklu *et al.*, 2004) calibrated these values for the Fe-18Cr-14Ni steel which are listed in Table IV-2. They are in good agreement with the parameters for the pure ɣ-Fe (Huntington, 1958). All the grains share the same parameters while each of them has a different crystallographic orientation. Isotropic elasticity characterized by Young's modulus and Poisson's ratio is used to describe macroscopic homogeneity. The cubic elastic model is homogenized to make sure that it is equivalent to the isotropic elastic model for the isotropic textured situation at the macroscopic scale.

(a) Effect of cubic elasticity

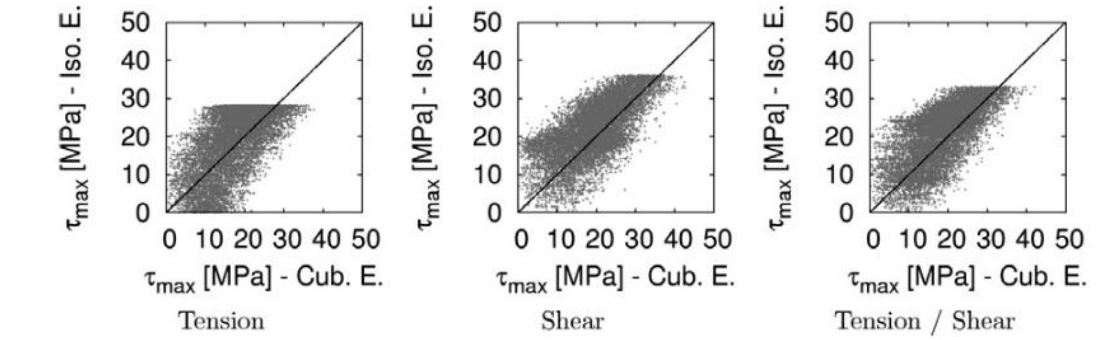

(b) Effect of crystal plasticity

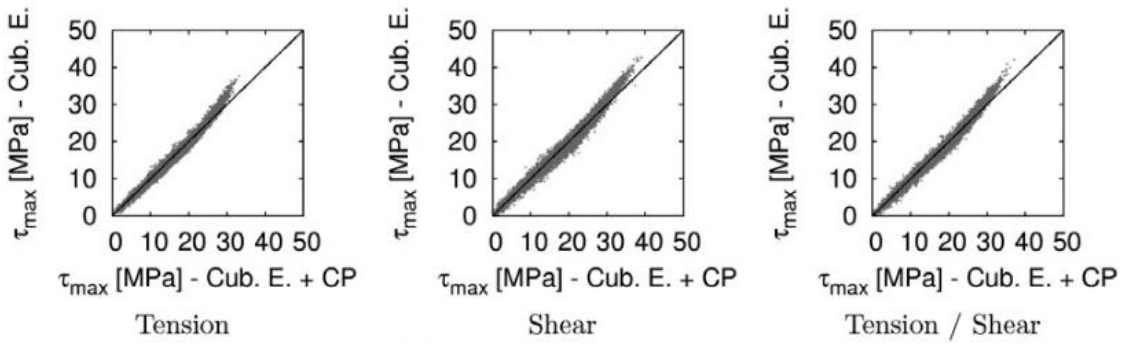

Figure IV-3: Comparison of the maximal shear stress (a) between isotropic elasticity (Iso. E.) and cubic elasticity (Cub. E.). and (b) between cubic elasticity (Cub. E.) and cubic elasticity + crystal plasticity (Cub. E. + CP.) (Robert *et al.*, 2012)

Table IV-2: Parameters of the constitutive models

isotropic elasticity		cubic elasticity			
E (GPa)	ν	C_{1111} (GPa)	C_{1122} (GPa)	C_{1212} (GPa)	anisotropic factor $2*C_{1212}/(C_{1111}-C_{1122})$
194	0.284	197	125	122	3.64

IV.2.2.2. *Fatigue criteria*

As will be shown in the next part, the local stress state at the scale of the grains is most of the time multiaxial even if the macroscopic applied loading is a uniaxial one. To deal with these multiaxial states of stress and their effects on fatigue crack initiation, it is proposed to make use of multiaxial stress criteria detailed hereafter.

To reflect the oriented nature of fatigue crack initiation, stress critical plane criteria have been proposed by many authors in the literature [33]. They aim at reducing a multiaxial stress state to an equivalent uniaxial one and very often combine normal and shear stress parameters on a critical plane.

Three representative stress-based criteria are used in this study: Matake [34], Dang Van [35], Papadopoulos [36].

IV.2.2.2.1. Matake criterion

From many observations in the literature dealing with the fatigue of metallic materials, shear is the overwhelming mechanism of fatigue initiation. Matake proposed a criterion assuming that fatigue damage of material is due to the maximum shear stress amplitude $\tau_{a,max}$ along with the normal stress $\sigma_{n,max}$ in the plane of maximum shear stress.

The criterion is formulated as follows:

$$\tau_{a,max} + \alpha_{mat}\sigma_{n,max} \leqslant \beta_{mat} \qquad (IV.1)$$

α_{mat} and β_{mat} are material parameters identified from tension and torsion fatigue limit (s-1 and t-1) by following equations:

$$\alpha_{mat} = 2\frac{t_{-1}}{s_{-1}} - 1\,;\beta_{mat} = t_{-1} \qquad (IV.2)$$

IV.2.2.2.2. Dang van criterion

The Dang Van criterion is widely used for its multi-scale approach. He proposed that there are two parameters involved in the fatigue process, namely the microscopic shear stress in grain area and the microscopic hydrostatic stress, both assessed in the elastic shakedown state. The former is responsible for crack nucleation along with slip bands and the later influences the crack opening process. The criterion is mathematically formulated as follows:

$$\max_{t}\left\{\max_{\underline{n}}\left[\left\|\underline{\hat{t}}(n,t)\right\| + \alpha_{dv}\hat{\sigma}_{hyd}(t)\right]\right\} \leq \beta_{dv} \qquad (IV.3)$$

In which, $\underline{\hat{t}}$ denotes resolved shear stress and $\hat{\sigma}_{hyd}$ denotes hydro-static stress. As the cyclic loading changes with time, both $\underline{\hat{t}}$ and $\hat{\sigma}_{hyd}$ are time-dependent and are expressed in time functions. $\underline{n}$ is the slip systems in a grain. α_{dv} and β_{dv} are material parameters identified from tension and torsion fatigue limit (s_{-1} and t_{-1}) by following equations:

$$\alpha_{dv} = \frac{t_{-1} - \frac{s_{-1}}{2}}{\frac{s_{-1}}{3}}\,;\beta_{dv} = t_{-1} \qquad (IV.4)$$

IV.2.2.2.3. Papadopoulos criterion

In the case of the specimen subjected to a load below the fatigue limit, small cracks are often observed and do not propagate. Generalized shear stress amplitude ($T_{s,a}$) and the maximum value of normal stress (Σ_n) are combined to predict the fatigue failure in the Papadopoulos criterion.

Instead of using the maximum value of resolved shear stress and normal stress, Papadopoulos chose the integral values of shear stress and normal stress along all the slip systems and slip planes. The criterion is given in the following equations:

$$\sqrt{\langle T_{s,a}^2 \rangle} + \alpha_{pap} \max_t [\langle \Sigma_n(t) \rangle] \leq \beta_{pap}$$
$$\sqrt{\langle T_{s,a}^2 \rangle} = \sqrt{5} \sqrt{\frac{1}{8\pi^2} \int_{\phi=0}^{2\pi} \int_{\theta=0}^{2\pi} \int_{\chi=0}^{2\pi} T_{s,a}^2 \, d\chi sin(\theta) d\theta d\phi} \qquad (IV.5)$$
$$\langle \Sigma_n(t) \rangle = \frac{1}{8\pi^2} \int_{\phi=0}^{2\pi} \int_{\theta=0}^{2\pi} \int_{\chi=0}^{2\pi} \Sigma_n(t) d\chi sin(\theta) d\theta d\phi$$

Where α_{pap} and β_{pap} are material parameters identified from tension and torsion fatigue limit (s_{-1} and t_{-1}) by the following equations:

$$\alpha_{pap} = \frac{3t_{-1}}{s_{-1}} - \sqrt{3}; \beta_{pap} = t_{-1} \qquad (IV.6)$$

The values of parameters mentioned above in these criteria are listed in Table IV-3.

Table IV-3: Parameters of the fatigue criteria for a 316L steel

α_{mat}	β_{mat} (MPa)	α_{dv}	β_{dv} (MPa)	α_{pap}	β_{pap} (MPa)
0.269	147.5	0.403	147.5	0.171	147.5

IV.2.2.3. *Non-local method*

In this research, the non-local method is based on the well-established "critical distance" theory. It supposed that there exists an effective zone in which the grains affect each other mutually and lead to plastic deformation during the fatigue crack initiation (Taylor, 1999). Regarding its application to the numerical simulations there exists different ways to apply this theory, i.e. point method, line method, area method and volume method (Bellett *et al.*, 2005). In terms of the area method, which is used in this study, the determinant criterion mentioned above is adapted to the following form:

$$\left(\int_S \sigma_{FIP} \, dS \right) / S \leqslant \beta \qquad (IV.7)$$

in which, σ_{FIP}, S and β are fatigue indicating parameter, the effective zone, and the fatigue limit, respectively.

The critical distance is often determined by the effective crack length l_0 introduced by El Haddad or an empirically derived value. Successful applications were reported (El May *et al.*, 2015; Krzyżak, Robak and Łagoda, 2017) on the homogeneous models. It is expected that the critical zone has some connections with the microstructure. Particularly, the explicit microstructure modeling contains the sources of scatter e.g. the crystallographic orientations, the grain size, the grain morphology which is omitted in the homogeneous models.

Two types of non-local approaches are examined in this paper: the critical radius method and the neighbor layer method. The sensitivity of the parameters to the microstructure features are evaluated. Two non-local parameters are proposed: R^* and N^*, which denotes the radius of this effective zone or the depth of neighbor layers respectively. These two different implementations of the non-local method stand for two different fatigue initiation mechanisms: critical radius method emphasizes an effective area within a certain range without explicit consideration of actual microstructure configuration; neighbor layer method shows the interaction among adjacent grains and characterized by microstructural features as grain shape and grain size. Two schematic diagrams are shown in Figure IV-4. The critical zones for the two methods are defined in Eq. (*IV.8*). In the literature, the non-local method is often applied locally, i.e. only the most stressed element or grain is chosen as the critical spot to which the non-local treatment is applied. The implementation of the non-local method in this study is a global treatment over the whole model. So, the extreme value can be obtained not only at the singular point of defect edge but also at several potential positions in the vicinity of defect which corresponds to the experimental finding.

$$V_{e0} = \{element | dist(element, e0) \leq R^*, element \in FEmodel\}$$
$$V_{g0} = \{grain | neighbor(grain, g0) \leq N^*, grain \in FEmodel\} \quad (IV.8)$$

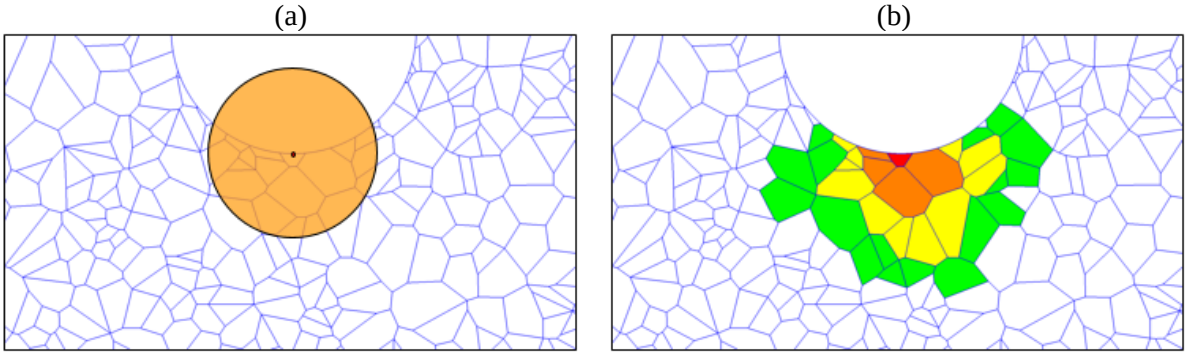

Figure IV-4: Schematic illustrations of non-local methods: (a) critical radius method and (b) neighbor layer method

Identification and calibration of the non-local parameters can be laborious and are not the point of this research. We make a compromise on the accuracy of results by only trying several possible values. For the N^*, 2,3,5,9 and 13 are tested representing the first layers, the first two layers, etc. This neighbor layer parameter is assumed to be of the same order of magnitude as the grain size. For the R^*, five

different values are tested in the following analysis, 15 µm, 30 µm, 60 µm,120 µm and 180 µm representing one, two, four, eight and twelve times of grain size, respectively.

IV.3. Results

IV.3.1. Application and evaluation of non-local method based on experimental results

The evaluation is based on 576 circular defected models with equiaxed morphology and 15µm average grain size. These 576 models contain 6 different sizes denoted by the radii of circular defects: 5, 15, 30, 60, 120, 200 µm, respectively (shown in Figure IV-5). For each defect, 4 different realizations of grain shapes combined with 24 grain orientations are applied. Among the 6 defect sizes, the 5 and 15 µm defects represent the defect within the range of one or two grains. The 30 and 60 µm defects represent the defects' sizes on the order of several grains. The 120 and 200 µm defects represent the defects pass through a lot of grains.

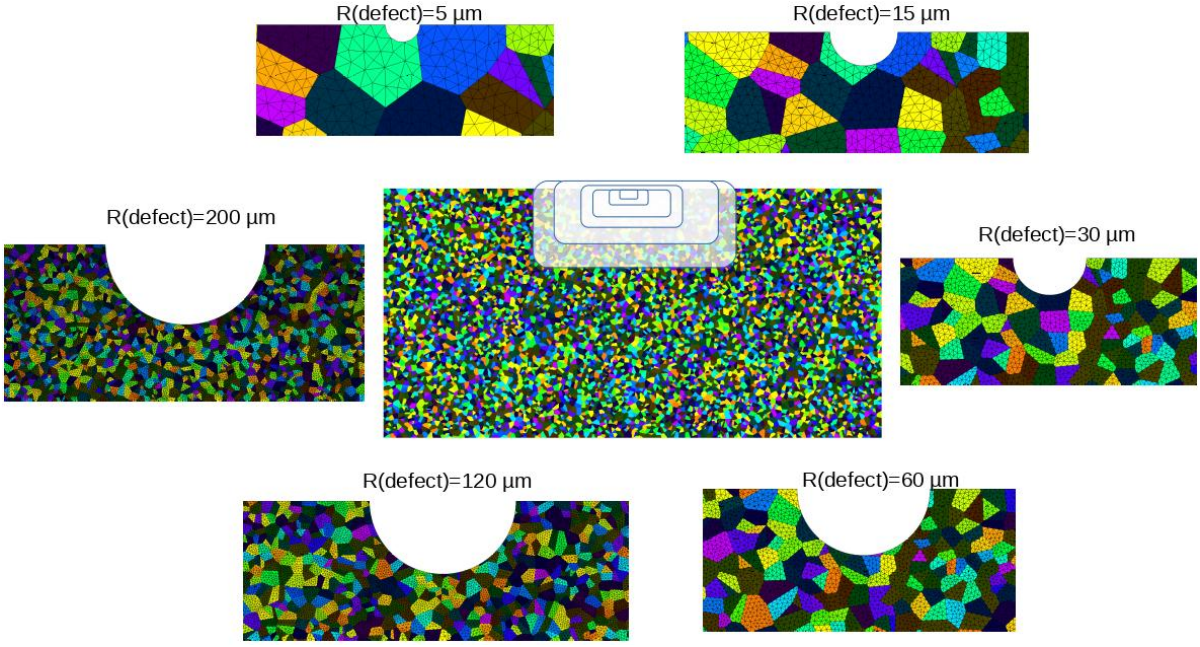

Figure IV-5: FE models containing semi-circular defects with radii of 5,15,30,60,120,200 µm respectively

IV.3.1.1. *Mechanical analysis*

The Von Mises equivalent stress fields for 6 finite element models with the same microstructures but different defect sizes are plotted in Figure IV-6. The defects range from 5 to 200 µm as introduced before. As far as the microstructure is concerned, the stress distribution of loaded polycrystalline is strongly heterogeneous. Even in the remote area to the defect, a strong loaded grain can have equivalent stress several times over that from an adjacent grain for their different crystallographic orientations.

Moreover, the position of the most stressed element changes due to microstructure. This heterogeneity also has an influence on the stress concentration factor. The local stress concentration factors from critical elements of all polycrystalline models are calculated and categorized by the defect size into 6 groups. Each group contains 96 different microstructure realizations. To present the scatter of calculated *Kt*, histograms, as well as distribution curves, are plotted in Figure IV-7. Average values and standard deviations for each group of models with the same defect are listed in Table IV-4. Refined meshes for models with small defects are used to better capture the local stress concentration. For the isotropic models, the yielded K_t from models with different defects is close to each other which makes the results from models containing explicit microstructure comparable. The calculated K_t from polycrystal models is always higher compared to that from isotropic models because of the interaction among neighboring grains. For the models containing small defects (5 μm and 15 μm), the defect may exist within one certain grain while larger defect passes through several grains which increases the influence of heterogeneity from grain boundary. Therefore, the K_t from polycrystal models with small defects are smaller.

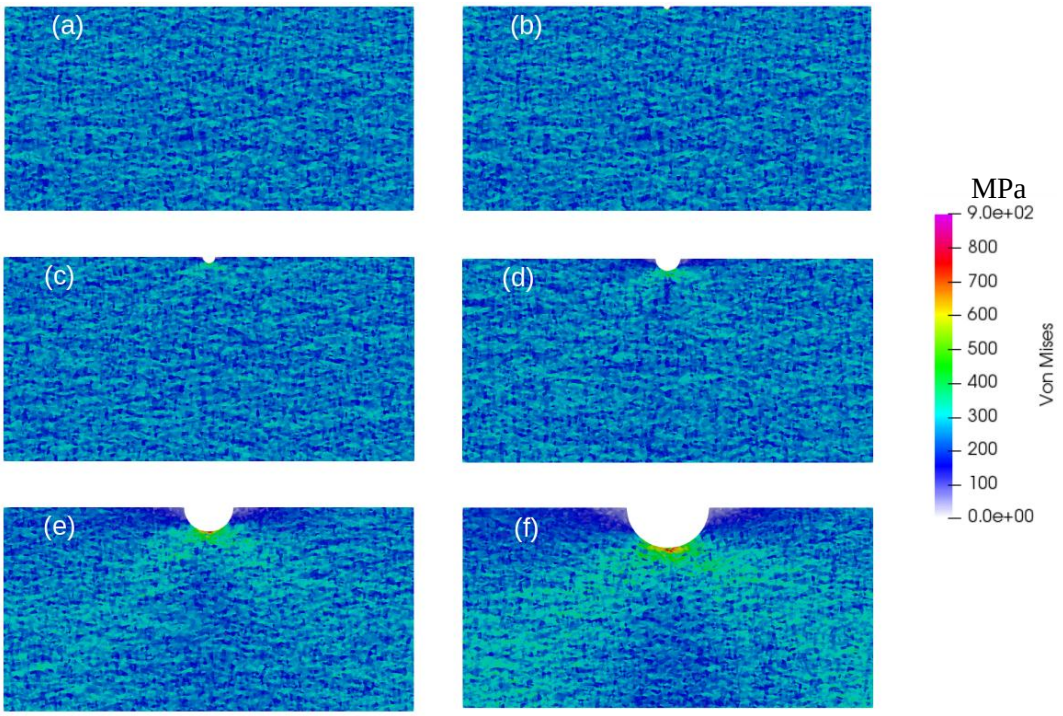

Figure IV-6: Von Mises equivalent stress fields in numerical models with same microstructure configuration but different defect size: (a) 5μm; (b) 15μm; (c) 30μm; (d) 60μm; (e) 120μm; (f) 200 μm

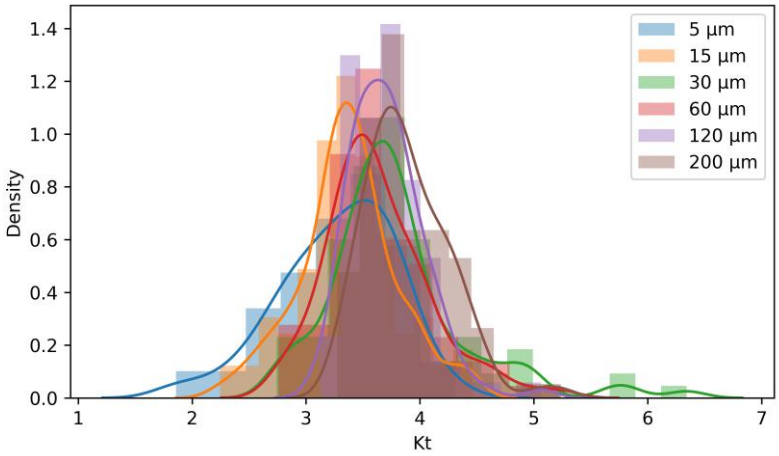

Figure IV-7: Distribution of maximum local stress concentration factor in models with different microstructures but same defect size (defect size as legend)

Table IV-4: Local stress concentration factor with respect to different defect radius

Defect Radius (µm)	5	15	30	60	120	200
Kt (isotropic model)	2.78	2.81	2.81	2.81	2.78	2.85
Kt (polycrystal models)	3.28 +/- 0.50	3.37 +/- 0.43	3.79 +/- 0.62	3.63 +/- 0.46	3.70 +/- 0.32	3.88 +/- 0.37

The mesoscopic quantities, namely the average shear stress amplitude in a grain ($\tau_{a,g}$) and the average hydrostatic stress amplitude in a grain ($\sigma_{h,a,g}$), are significant to characterize the fatigue initiation. The bivariate distributions of these two quantities are plotted for the models with different defect sizes in Figure IV-8. Regarding the distribution of hydrostatic stress amplitude, the general appearance looks like a quasi-normal distribution while for the distribution of shear stress amplitude, the general appearance is a skewed distribution. The stress state for each grain can be quite complex. Some grains are in uni-axial stress state while others are in multi-axial stress state. Even for the macroscopic tension loading, there are grains subjected to compression loading locally. As the defect size increases, the distributions of both shear stress amplitude and hydrostatic stress amplitude show stronger dispersion. But a linear tendency can be observed between the shear stress and hydro-static stress, especially for the extreme value. In terms of the extreme values, the maximum values in large defect models can be two times larger than those of small defect models. The change of extreme value in the critical grain exaggerates the effect of defects on the fatigue behavior.

The mechanical analysis offers some validity to the hypothesis in the critical distance theory that the fatigue crack is not only due to one or several most stressed grain(s). Crack initiation is the mutual effect of a series of grains.

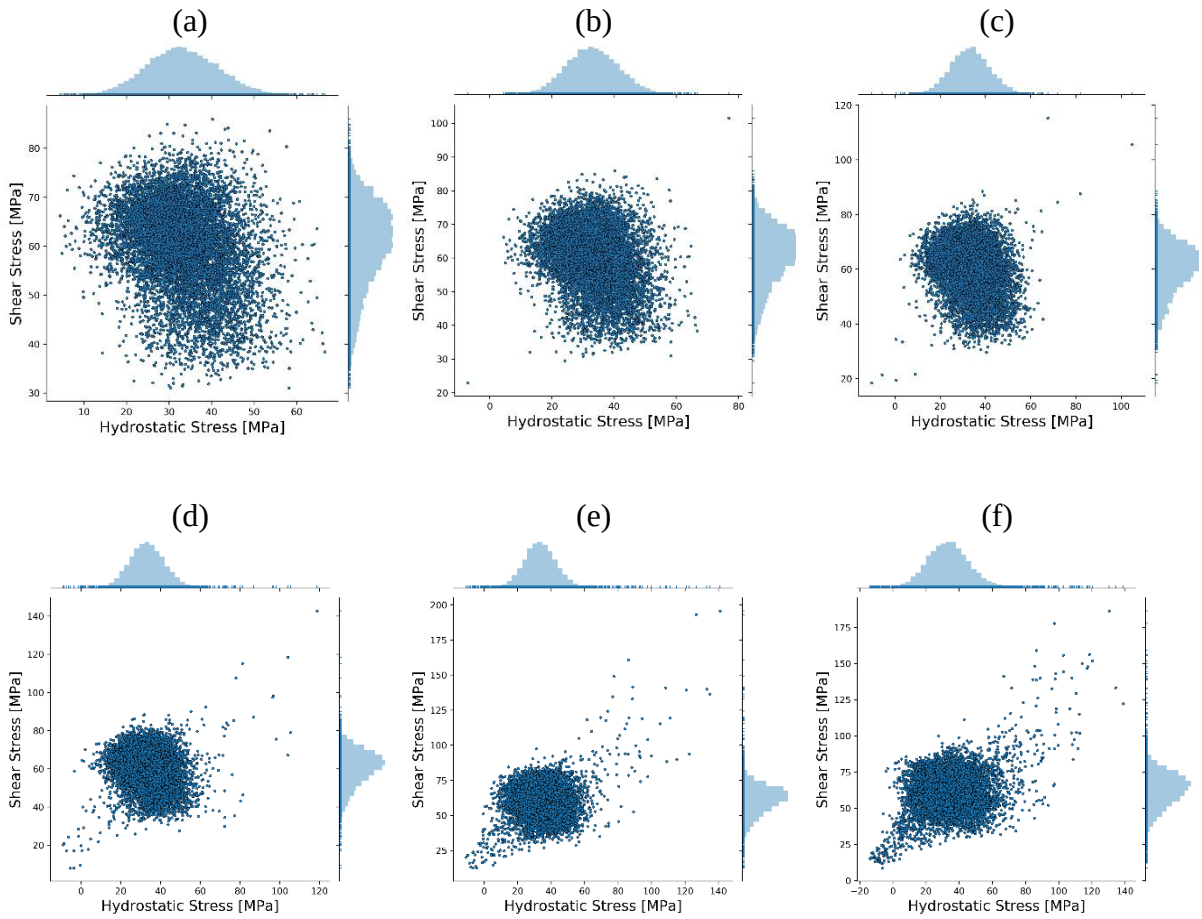

Figure IV-8: Distributions of grain-average hydrostatic stress amplitude and shear stress amplitude in numerical models with same microstructure configuration but different defect size: (a) 5µm; (b) 15µm; (c) 30µm; (d) 60µm; (e) 120µm; (f) 200 µm

IV.3.1.2. *Fatigue analysis*

Experimental research on the effect of defect has been conducted previously in authors' laboratory (Guerchais *et al.*, 2015). The results of uni-axial tension and torsion fatigue tests with respect to different semi-spherical defected specimens are shown in Figure IV-9.

These experimental results reveal that the HCF behavior of 316L has a tolerance of small defect for that the fatigue limit does not change greatly for a specimen with a defect inferior to several tens of µm. Moreover, scatter was observed from the test. For specimens with same defect size, their fatigue strengths may differ due to other influential factors as defect shape, microstructure, etc.

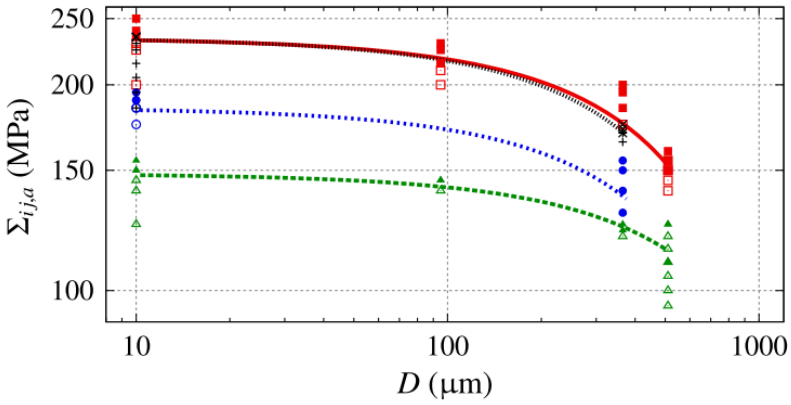

Loading condition	Tension	Torsion	Tension-torsion $\varphi_{\theta z} = 0°$	Tension-torsion $\varphi_{\theta z} = 90°$
Unbroken	□	△	⊙	+
Broken	■	▲	●	×

Figure IV-9: Results of the fatigue tests conducted on the 316L steel in uniaxial tension and torsion with a loading ratio R =-1 (Guerchais *et al.*, 2015)

The Kitagawa-Takahashi diagrams are plotted for different non-local methods. The predicted fatigue limits of each non-local parameters are normalized by the average prediction for the models containing 5 µm defect. This normalization is based on the experimental observation that non-propagating small defect has no influence on the fatigue behavior. The geometry parameter $\sqrt{Area}$ is chose to describe the defect size. In order to connect the two-dimensional simulations and the experimental results of three-dimensional semi-spherical defects, the artificial defects in 2D models are considered as notches in 3D models. The method proposed by Murakami (Murakami, 2002) to estimate the effective area for a very shallow circumferential notch and for roughness is adopted. In this way, the semi-circular defect in the studied model has an equivalent Murakami parameter calculated by the following equation:

$$\sqrt{Area} = \sqrt{10}\, r \qquad (IV.9)$$

In which, r denotes the 2D defect radius.

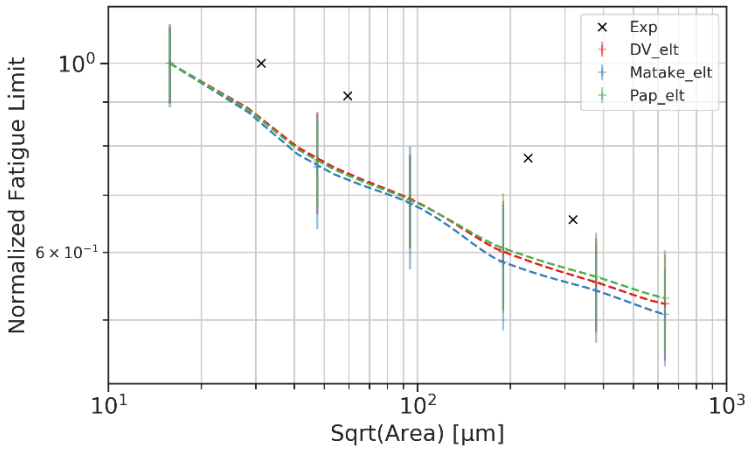

Figure IV-10: Kitagawa-Takahashi diagrams of local fatigue indicating parameters

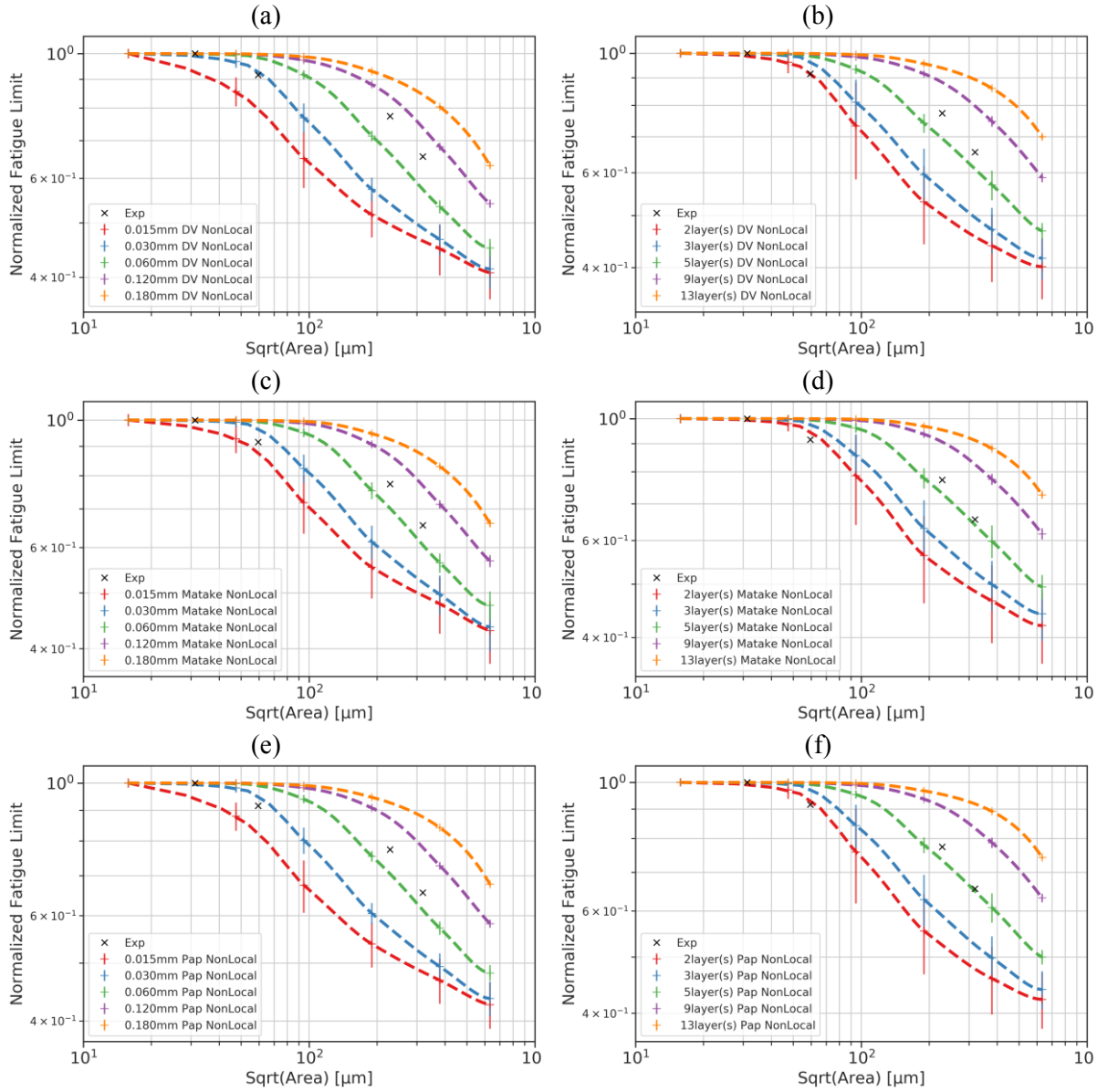

Figure IV-11: Normalized Kitagawa-Takahashi diagrams with the application of (a) critical radius Dang Van criterion;(b) neighbor layer Dang Van criterion;(c) critical radius Matake criterion; (d) neighbor layer Matake criterion; (e)critical radius Papadopoulos criterion; (f) neighbor layer Papadopoulos criterion

Figure IV-10 shows the predictions of the "local method" for which the extreme values are from the most solicited elements. Error bars are used to represent the average value +/- 1 standard deviation of the scattered normalized fatigue limits of models with different microstructures. To eliminate the dependency on the element size of the local integral point, a convergence test has been conducted. For the current microstructure, each grain is discretized by approximate 60 three-ordered elements. For notched/defected models, it can be seen that the predictions are always too conservative because of the sensitivity to the stress concentration.

The non-local methods show good tolerance for the small defects, presented in Figure IV-11. For a certain size of the defect, the larger non-local parameters yield the higher predicted fatigue limits. As the values of non-local parameters increase, the sizes of error bars decrease. Changes in the standard deviation demonstrate the different sensitivities to the microstructure of different values of non-local parameters. All three criteria yield similar predictions. From a qualitative perspective, the application of non-local methods gives a good description of the trend of the defect size effect on the high cycle fatigue behavior. From a quantitative perspective, the values of non-local parameters can be evaluated by comparing it to the experimental data. The data are presented in Table IV-5 and are plotted in the Kitagawa-Takahashi diagrams. At first glance, none of the 10 chosen parameters can perfectly fit the experimental data. The small parameters (i.e. R^*=0.030 mm or N^*=3) work well for the small defects but the predictions drop quickly when the defect size increases. The intermediate values (R^*=0.060 mm or N^*=5) can yield good predictions for the large defect size but they overestimate the performance of the small defect. The large parameters always overestimate the fatigue limit for the defects in this range. We may suppose that the non-local parameters have a connection with the defect size. But the fatigue experiments for defective material, especially for the material having small defects can be hardly achievable because the error of artificial defect size can usually be +/- 20µm. Besides, the scatter in HCF experimental results can be a concern that the accurate fatigue limit can hardly be obtained. Because of these limitations of experiments, we cannot determine whether the non-local parameter is a material constant which only depends on the kind of material or not. Considering that our main objective is to propose a numerical method to evaluate the effect of common defects which usually range within several hundreds of micrometers, we may say that when the N* equals to 5 or the R^* equals 0.060 mm, the predictions are acceptable.

Table IV-5: Experimental results for defective steel 316L

Equivalent Murakami parameter $\sqrt{Area}$ [µm]	31	60	229	320
Experimental fatigue limit Σ_0 [MPa]	232.5	212.5	180	152.5

We use the box-and-whisker plot to better present the dispersion in the fatigue predictions of different criteria (Figure IV-12). The box indicates the first and third quartiles by its upper and lower bound. The band inside the box represents the median value. Values with 1.5 interquartile range (IQR) of the lower quartile or of the upper quartile are considered maximum and minimum values shown by the ends of whisker. The black diamond marker represents the out-of-range value. Each box in the figures represents the distribution of the predicted fatigue limits from 96 models containing 4 different sets of grain position and morphology and 24 different crystallographic orientations. All three criteria show sensitivity to the microstructure. Among the three criteria, the Matake criterion is apt to yield higher predictions compared to the other two. Apart from the shear stress which is considered as the principal cause of fatigue failure, the Matake criterion uses the maximum normal stress, while the other two use

the maximum hydro-static stress, as the subsidiary factor. The difference between Dang Van criterion and Papadopoulos criterion is the way to calculate resolved shear stress as Dang Van uses the maximum shear stress from all the slip systems, while Papadopoulos integrates the shear stress on the slip systems. There are only minor differences in these tested criteria, and we cannot judge which criterion can be the best because of the restriction of our limited simulation configurations. The application of fatigue criterion should be based on the mechanism involved in the fatigue failure. Overall, all three criteria are compatible with the multi-axial stress state. By comparing the predictions of the neighbor layers method and the critical radius method, we can see that the neighbor layers method is more sensitive to the microstructure while the latter can still present the effect of microstructure. For the defects which are of several grains size, stronger dispersion can be seen which indicates the competition between the defect and the microstructure. The explicit microstructure modeling coupled with the non-local fatigue analysis method can explain well the experimental observation on metallic polycrystalline aggregate's high cycle fatigue behavior where the main source of scatter comes from the microscopic features.

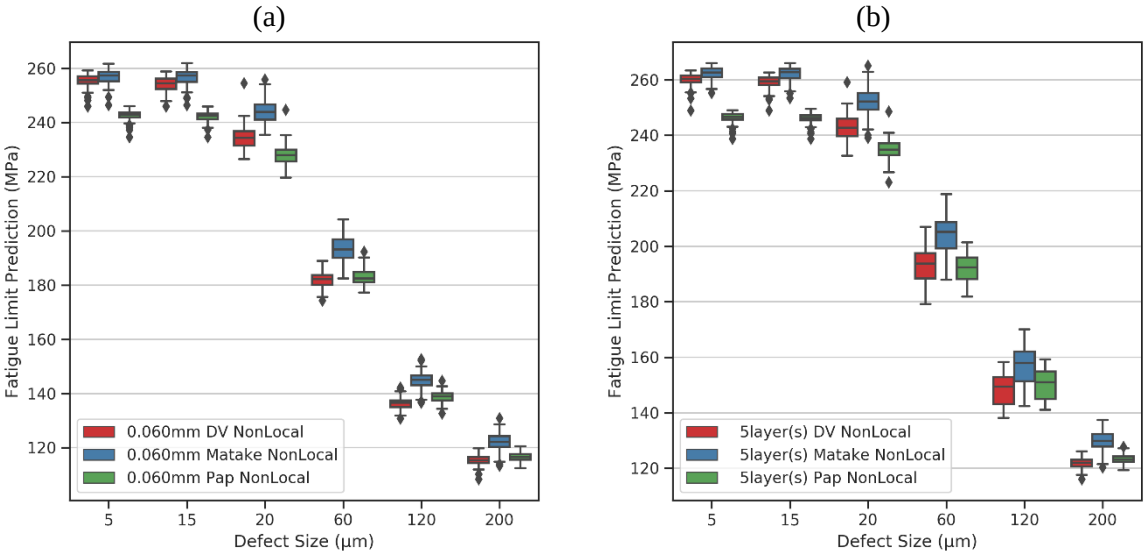

Figure IV-12: Fatigue limit intervals of 96 models containing the same defect but different microstructure from the criteria: Dang Van, Matake, Papadopoulos. (a) critical radius method (b) neighbor layer method

Two microscopic parameters are considered in the explicit microstructure sensitive model. In Figure IV-13, these two parameters are presented separately. Each box represents the twenty-four predictions from Dang Van criterion of different crystallographic orientations. The concatenated four boxes stand for the four different grain positions respectively. The effect of grain orientation can be observed in the results of both methods. Different grain orientations can result in a difference of 20 MPa of the fatigue limit. As mentioned before, the grain morphology is equiaxed in the numerical model. It is expected the neighbor layer method and the critical radius method would have similar outputs for the same grain arrangement. Surprisingly, the neighbor layer method is sensitive to the grain position and morphology

while the critical radius method gives similar predictions regardless of grain position and morphology. This comparison shows different application scenarios of the two methods. A further study about the grain morphology's effect on the two methods is presented in the following section.

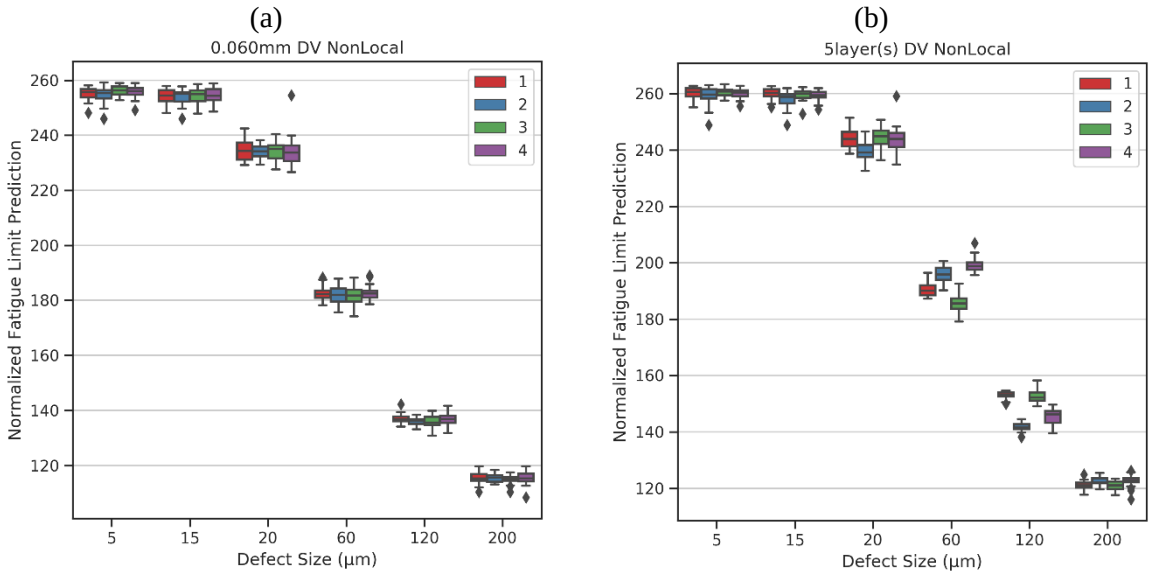

Figure IV-13: Fatigue limit intervals of 24 models containing the same defects and grain shapes but different grain orientations from the criterion: Dang Van. (a) critical radius method (b) neighbor layer method

IV.3.2. Further investigation of the non-local method on the microstructure effect

Several characteristic features are often used to describe the microstructure of polycrystalline, i.e. grain morphology, grain size, and grain texture. These microstructural parameters are usually determined by the fabrication process and affect both the mechanical and fatigue responses. To expand the application of the proposed non-local methods, it is of great value to study the effect of microstructural parameters. Considering the conventional fabricated metallic materials are often isotropic textured, only the effects of grain morphology and of grain size are investigated in the present study.

IV.3.2.1. *Effect of grain morphology*

In the previous polycrystalline FE models which served as the benchmark, Voronoi polygon tessellation is employed for its simple implementation and quasi-reality as many other pieces of research did (Guilhem *et al.*, 2010). Theoretically, the distribution of Voronoi polygons' equivalent size fits the Gaussian distribution, which is an approximation of many experimental observations on EBSD cartography of metallic polycrystalline aggregates (Baudoin *et al.*, 2016). The average grain size 15 μm is used as position parameter (μ) for Gaussian distribution while the shape parameter (σ) is 35% of the

grain size. A histogram representing the distribution of the Voronoi polygon tessellated models is shown in Figure IV-14. To explore the effect of grain morphology on the proposed non-local methods, more different configurations are implemented for comparison. The quadrangle tessellated model (shown in Figure IV-14b and Figure IV-15b) is chosen as the simplest description where all the grains are identical in size and form. This tessellation is the most efficient modeling method although it loses some fidelity of microstructure. Additionally, the manufacturing process affects the sizes and shapes of grains. Log-normal distribution was adopted in previous report (Toth *et al.*, 2013) to describe the grain size distributions obtained by full re-crystallization or additive manufacturing. As our objective is to test the non-local methods' compatibility with different kinds of microstructure but not to reproduce the experimental results, two log-normal distributions (Figure IV-14c, Figure IV-14d, Figure IV-15c, Figure IV-15d) with different artificial parameters are used in the following simulations. Both have an average grain size of 15 μm. But the latter is more deviated distributed which leads to the appearance of more small grains.

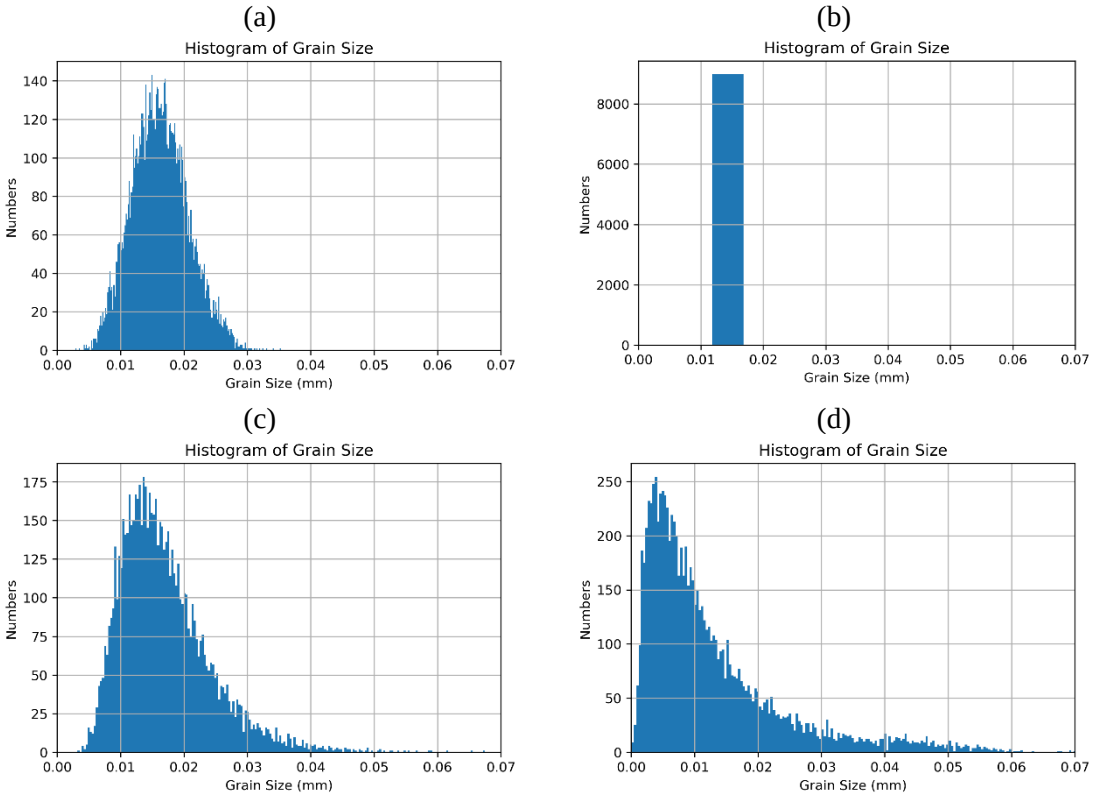

Figure IV-14: Histograms of grain size for different grain morphology configurations: (a) Gaussian distributed Voronoi polygon (b) uniform distributed quadrangle (c) log-normal distributed Voronoi 1 (d) log-normal distributed Voronoi 2

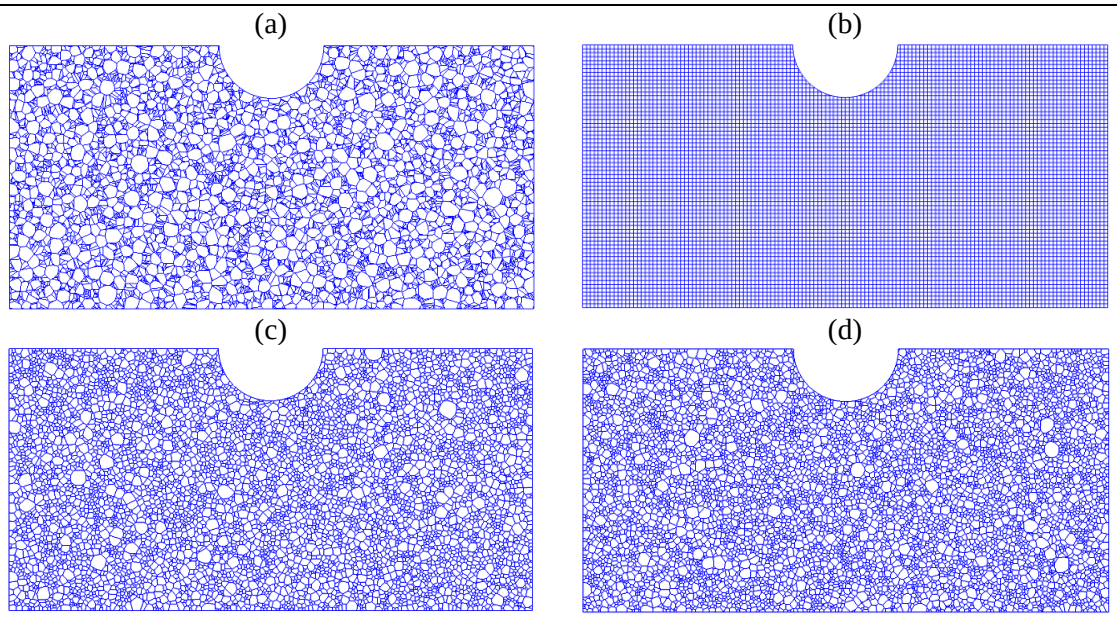

Figure IV-15: Illustrations of different grain morphology configurations: (a) Gaussian distributed Voronoi polygon (b) uniform distributed quadrangle (c) log-normal distributed Voronoi 1 (d) log-normal distributed Voronoi 2

The predictions from the fatigue criteria of two non-local methods are shown in Figure IV-16. Regarding the sensitivity of the grain morphology for small defects where the defect size is within the range of two grains, the uniform distributed tessellation gives the highest prediction. The Gaussian distributed tessellation has the intermediate result. For the log-normal distributed tessellation, the more deviated is the distribution, the lower is the prediction. Hence, for small defect, both the neighbor layer method and the critical radius method lessen the predictions if more and more small grains are involved in the effective zone. Comparing the numerical values of prediction, the difference of averages generated by different tessellation is about 1% in the neighbor layer method's prediction and does not exceed 5% in the critical radius method's prediction. Both predictions can be considered stable.

When the defect size increases to several grains' size, different trends are observed for the two methods. The critical radius method gives similar predictions for all the four tessellations which means only the defect size has an influence on the fatigue performance compared to the grain morphology. The neighbor layer method shows the competition between defect and grain morphology. For instance, the difference between the prediction of the second log-normal distributed model and the square tessellated model for a 120 μm defect is more than 20%. Figure IV-17 shows the effective areas considered in the two methods from different tessellated models. Effective area in neighbor layer method is very dependent upon the microstructure (size and shape of grains) while the area in critical radius method is independent of the grain size and morphology.

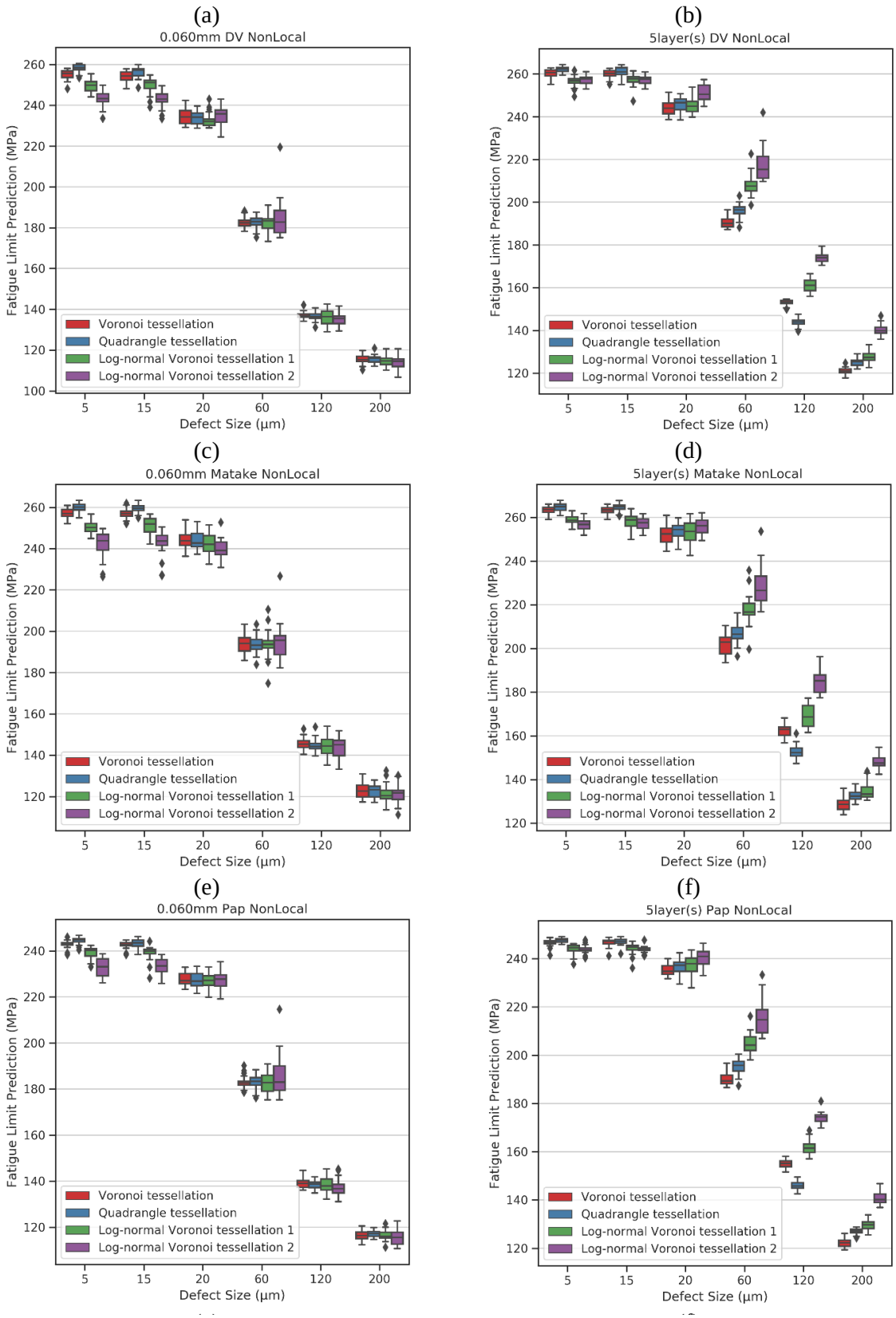

Figure IV-16: Fatigue limit intervals of 24 models containing same defects but different grain morphology from (a) critical radius Dang Van criterion;(b) neighbor layer Dang Van criterion;(c) critical radius Matake criterion; (d) neighbor layer Matake criterion; (e)critical radius Papadopoulos criterion; (f) neighbor layer Papadopoulos criterion

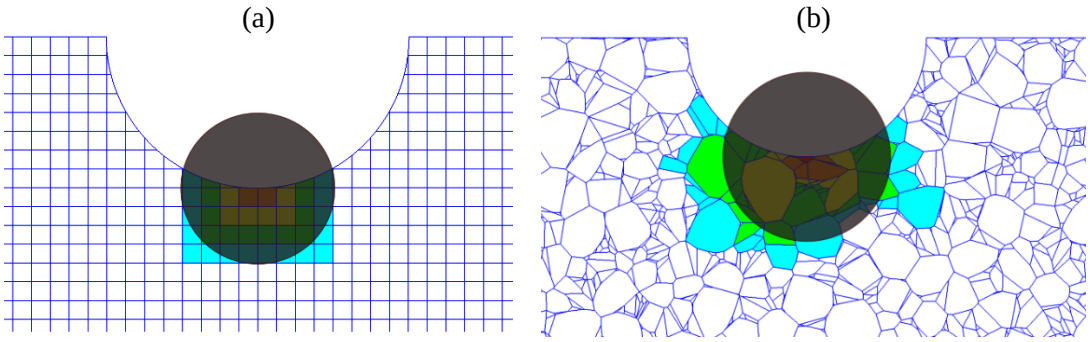

Figure IV-17: Effective areas of critical radius method and neighbor layer method in different studied microstructures: (a) uniform distributed grains and (b) log-normal distributed grains

The analysis reveals that when using the neighbor layer method, the microstructure should be considered while a simple tessellation can be used with the critical radius method without changing predictions.

Unlike conventional fabricated materials where equiaxed grains are frequently encountered, in additive manufacturing, as-built parts often have elongated grain morphology along with the presence of very fine grains near the surface. The neighbor layer method could be a better choice in this situation because it can reflect more microstructural characteristics.

IV.3.2.2. *Effect of grain size*

Regarding the explicit microstructure modeling, the role of grain size should be explored. Based on the simulations presented in the previous section, two more batches of numerical models representing coarse grains having the size of 30 µm and 100 µm, respectively, were built up and tested. Figure IV-18 shows the schematic of numerical models with different grain sizes.

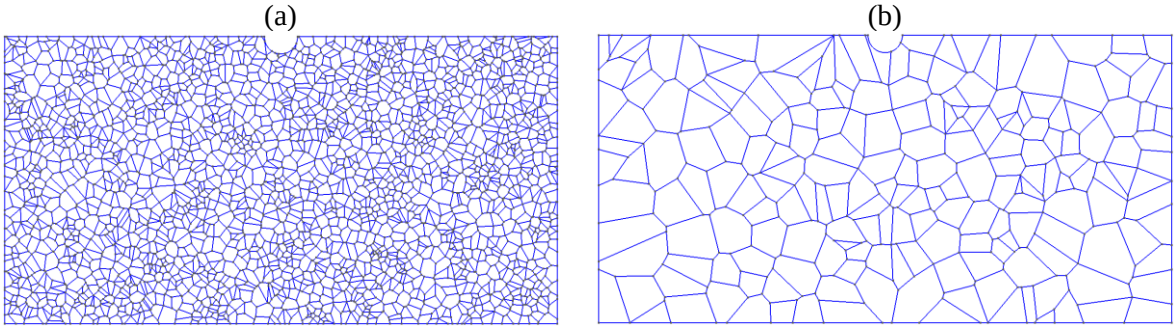

Figure IV-18: Illustrations of different grain size configurations: (a) 30 µm; (b)100 µm

It is generally accepted that the fatigue or endurance strength of planar slip materials, such as steel and brass, is increased by refining the grain size, whereas, in wavy slip materials, such as pure copper and pure aluminum, the fatigue strength is unaffected. For example, experiments of alpha brass indicated the decreasing grain size acts to increase fatigue life while the copper and aluminum show the opposite tendency that grain size has a negligible effect on fatigue behavior (Thompson and Backofen, 1971).

For the defective materials, it is reported that the critical defect size varies linearly with grain size for steel (Masounave and Baflon, 1976). The plot of effective defect size against the average grain size is presented in Figure IV-19. Nevertheless, the exact relation between fatigue phenomenon and defective materials' microstructure remains an open question because of limited literature.

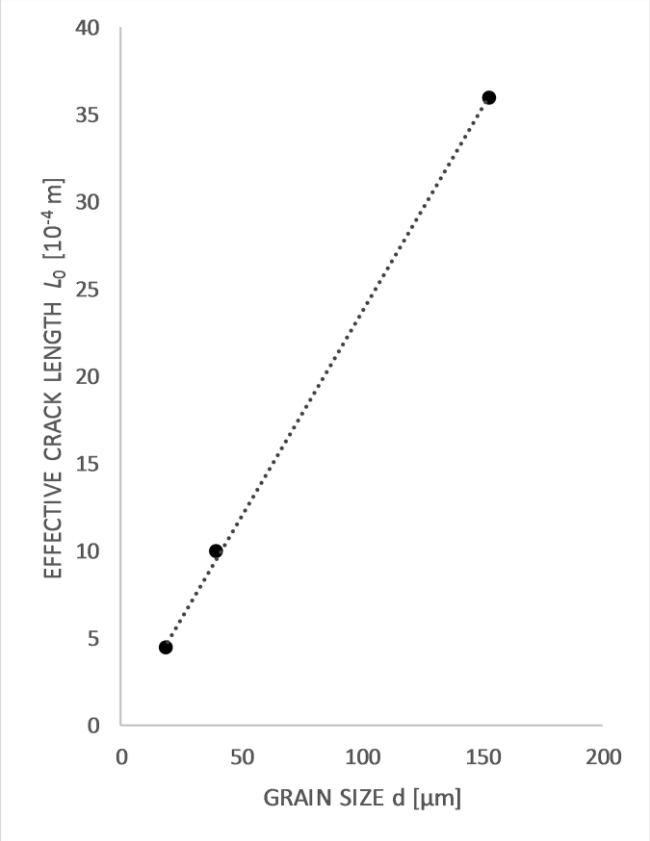

Figure IV-19: Relationship between grain size and effective crack length (replot from (El Haddad, Smith and Topper, 1979))

The choice of non-local method parameters for this batch of models cannot be quantitatively verified due to the lack of experimental results. So, R^* and N^* are set to 60µm and 5 respectively from the previous calibrations from benchmark models. The hypothesis behind the choice of R^* is that a circular area with a radius of 60 µm is effective when fatigue crack initiates. And the choice of N^* implies 5 layers of adjacent grains contribute together to result in fatigue initiation. The effective defect size is defined as the critical size where the predicted fatigue limit drops 10% compared to the prediction of the smooth model. Due to the geometrical size of our finite element model, effective crack length defined by Haddad (El Haddad, Smith and Topper, 1979), which corresponds to a defect causing fatigue strength drop to 70%, is not achievable. The value is linearly interpolated from the Kitagawa-Takahashi diagram based on the threshold stress intensity theory. As can be seen in Figure IV-20, the critical radius method shows a strong sensitivity to the grain size. It corresponds to the experimental trends for the steels. Unlike the critical radius method, the neighbor layer method yields similar results when the grain size changes when the value of N^* is fixed at 5. These tests regarding grain size reveal that for a non-local

parameter whose value is pre-fixed, the effective area considered for critical radius method or for neighbor layer method may vary if the microstructure is changed. The critical radius method emphasizes the influence of defect size while the neighbor layer method pays more attention to microstructural factors. Considering the realities in experiments, both methods have their application scenario, but care must be taken when choosing the parameter value. Under certain circumstances where exact calibrations of non-local parameters are not attainable, for materials like the steel of which a linear relationship between critical defect size and grain size was reported, an approximate value of R^* can be applied as it displays sensitivity to the change of grain size. For other materials like cast aluminum alloy where the microstructure is often characterized not by grain size but by dendrite arm spacing, similar N^* may be used because of its independence of the specific size of grain.

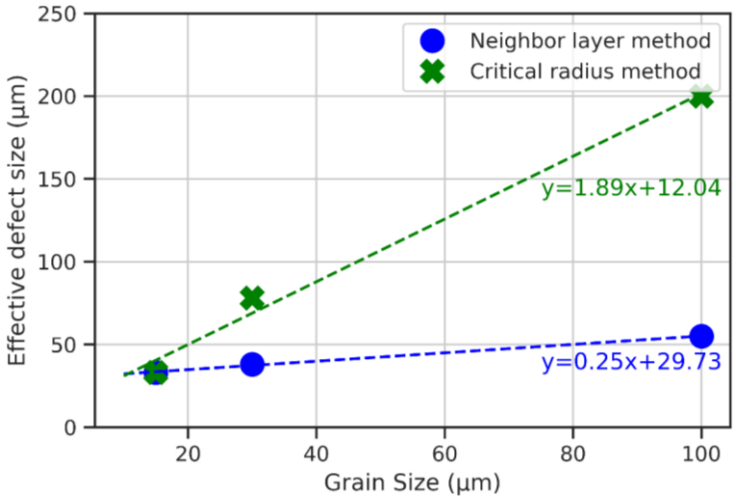

Figure IV-20: Effective defect sizes for different average grain size configurations of proposed realizations of non-local method and pre-fixed parameter values

IV.4. Conclusions

The effect of defects and microstructure, as well as their competition on the fatigue behavior of polycrystal aggregate, are investigated by the non-local method along with the finite element method.

By creating an explicit virtual microstructure finite element model, the local mechanical response from elements and mesoscopic grain-average characteristic stress distribution are obtained. It is revealed by the mechanical analysis that the microstructure introduces a strong heterogeneity as the defect brings a strong stress concentration. To better assess the effect of defects on fatigue behavior, the microstructure is an essential factor.

However, a local approach cannot reflect the Kitagawa-Takahashi effect properly during numerical simulation since the LEFM theory does not work well in the fatigue crack initiation stage. Overemphasized results are obtained from the local approach in this study.

By introducing the non-local method, the fatigue prediction based on both defects and microstructure can be achieved. In terms of the influence of changing defect size on fatigue performance, the simulations and experiments are in good agreement in the qualitative aspect. The tolerance of small defect and the perceptible influence of larger defects can be clearly shown with the application of the non-local method. The dispersion of results due to microstructure attributes are shown and discussed. Especially, for the medium-sized defect, the wide dispersion demonstrates the competition between defect and local microstructure.

Three multi-axial stress-based fatigue criteria are used and evaluated. All three criteria can present the Kitagawa-Takahashi effect that a very small defect has a negligible influence on high cycle fatigue strength. Matake criterion always provides the most elevated fatigue limit. Because the secondary parameter initiator is normal stress in Matake criterion and is hydrostatic stress in the other two criteria. Further comparison between Dang Van and Papadopoulos criteria shows the influence of stochasticity in microstructure, the maximum resolved shear stress in slip directions in Dang Van criterion is not always higher than its integrated counterpart in Papadopoulos criterion.

Regarding the realizations of the non-local method, the neighbor layer method is more sensitive to the microstructure. Stronger scatters can be seen in the results of different configurated models from the neighbor layer method compared to those from the critical radius method.

Further investigations on grain morphology and grain size distinguish the difference between the proposed critical radius method and neighbor layer method. The sensitivity to the grain size is also dependent upon the non-local model employed. Each method has its advantages in different application scenarios. With an appropriate choice of non-local parameter as well as understandings of materials' sensitivity to microstructure, it is expected the non-local method can be applied to different metallic materials.

Synthesis

- An explicit virtual microstructure finite element model is created to conduct fatigue simulations.

- Different stress-based criteria frequently applied in fatigue assessment are tested with combination of non-local method. Two realizations of non-local method are used and compared.

- Simulation results are compared to experimental results of 316L. From the parametric simulations, better qualitative understandings on the choice of non-local method as well as its parameters are obtained.

- The effect of Kitagawa-Takahashi can be reproduced and explained by this proposed framework of microstructure modeling simulation

Chapter V.

Numerical study of the effect of roughness and porosity on the HCF performance of AM 316L

V.1. Preparatory investigations on the modeling of SLM steel 316L 129

V.1.1. Crystallographic orientation & grain morphology 130

V.1.1.1. Grain morphology and grain size 130

V.1.1.2. Grain orientation 133

V.1.2. Surface roughness & Pores 136

V.2. Modeling configurations 141

V.2.1. Design of geometrical models 141

V.2.1.1. Smooth models 141

V.2.1.2. Models with defects 142

V.2.2. Constitutive models 144

V.2.2.1. Calibration of parameters in the elastic constitutive model 144

V.2.2.2. Identification of parameters in polycrystal plastic model 144

V.2.3. Loading condition 148

V.2.4. Fatigue criteria 148

V.3. Fatigue simulations of smooth models 148

V.3.1. Discussion on the experimental reference for simulation 148

V.3.2. Statistical method for microstructural heterogeneity 149

V.3.3. Investigations on R* 155

V.4. Fatigue simulations using models with roughness and defects 159

V.4.1. Models with artificial semi-ellipsoidal defects 159

V.4.2. Models with roughness 162

V.4.3. Models containing artificial defect and roughness 169

V.5. Role of plasticity in fatigue simulation 172

V.5.1. Comparisons between elastic and plastic constitutive models in smooth models 172

V.5.2. Comparisons between elastic and plastic predictions in defective models 174

V.5.3. Summary 176

V.6. Conclusions 177

Syntheses 179

The framework of the microstructure sensitive modeling method for polycrystal aggregate was used successfully in the previous chapter to reproduce the K-T effect numerically in a wrought SS 316L. In this chapter, based on the modeling framework for conventional 316L, the numerical study about HCF behavior of SLM SS 316L is presented. This chapter is organized as follows.

First, from the EBSD observations, geometrical models with explicit microstructure are built. From the profilometry and tomography analyses, an understanding of the inherent roughness and defects of SLM parts has been obtained. The fractography observations provide the characteristics of the fatigue-driven defects that are added to the numerical model. The outputs of finite element results are post-treated by the non-local methods and a statistical method in the context of fatigue prediction.

Second, details about the employed numerical models are presented. Besides the geometrical model, constitutive material equations need to be reconsidered for this material. Since both the elastic and plastic constitutive models are to be used, the process of identification and calibration of parameters' values are detailed.

Finally, from simulations carried out on smooth models and models with roughness and/or defects, the effects of roughness, LoF defects and microstructure are discussed based on an important number of simulation results.

The application of the crystal plasticity constitutive equation is presented at the end of the chapter to check if plasticity affects the fatigue simulation of the studied material.

V.1. Preparatory investigations on the modeling of SLM steel 316L

The numerical model in the previous chapter is a commonly used polycrystalline aggregate model. Normal distributed Voronoi tessellation is a representative description of the conventional fabricated material's microstructure. Isotropic grain orientations set implies that grain has no preferential orientation. But many differences can be enumerated between the microstructure of conventional material and that of AM material. In this study, we deal with two major microscopic attributes: grain orientation and grain morphology. AM products, especially those not heat-treated, often have a strongly textured and non-equiaxed microstructure. Because of the temperature gradient from laser projection, the majority of grains in AM material possess crystallographic orientation parallel to the laser scanning direction which coincides approximatively with the building direction. The heterogeneous temperature field leads to the presence of large elongated grains along with many small grains. To better present these microstructural attributes of AM parts, a quasi-realistic virtual explicit microstructure finite element model is proposed in this study. The word "quasi-realistic" means that the data are based on experimental measurements. "Virtual" means that we parametrize the microstructure attributes and artificially generate more statistically equivalent models to present the stochasticity of microstructure.

V.1.1. Crystallographic orientation & grain morphology

EBSD analyses were presented in Chapter II to illustrate the microstructure of the studied material. To build up a quasi-realistic microstructure for the polycrystalline aggregate model, these data are post-treated quantitatively to generate characteristic information.

V.1.1.1. *Grain morphology and grain size*

The first challenge in explicit microstructure modeling of polycrystalline aggregate is to adequately represent the grains. The grains can be intuitively described by their shape and size.

It is possible, based on the results of the EBSD analyzes, to determine the average grain size. Several definitions of average grain size are proposed in the literature. We will rely on that recommended by the NF EN ISO 643/2624 standard (Barralis and Maeder, 2005). According to this standard, the average grain size D_m is simply defined, based on the average grain area A_m, by the following equation:

$$D_m = \sqrt{A_m} \qquad A_m = \frac{A_t}{N_g} \qquad (V.1)$$

With A_t and N_g respectively corresponding to the total area and the number of grains.

It may be interesting to specify how the grain size is distributed in a polycrystal. The size of a grain is commonly defined by the diameter of the "equivalent circle" D_{eq}, that is to say the circle with the same area as the grain denoted A_g. Thus, the grain size D_{eq} is calculated by using the following relationship:

$$D_{eq} = \sqrt{\frac{4A_g}{\pi}} \qquad (V.2)$$

Band contrast (BC) is used to present the grain boundaries. Because electron beam scattering patterns (EBSPs) along grain boundaries tend to show poor BC, they appear dark in a map. Conversely, EBSPs in undeformed regions of grain appear light. BC maps of the measured area in the X/Y plane of specimens are shown in Figure V-1.

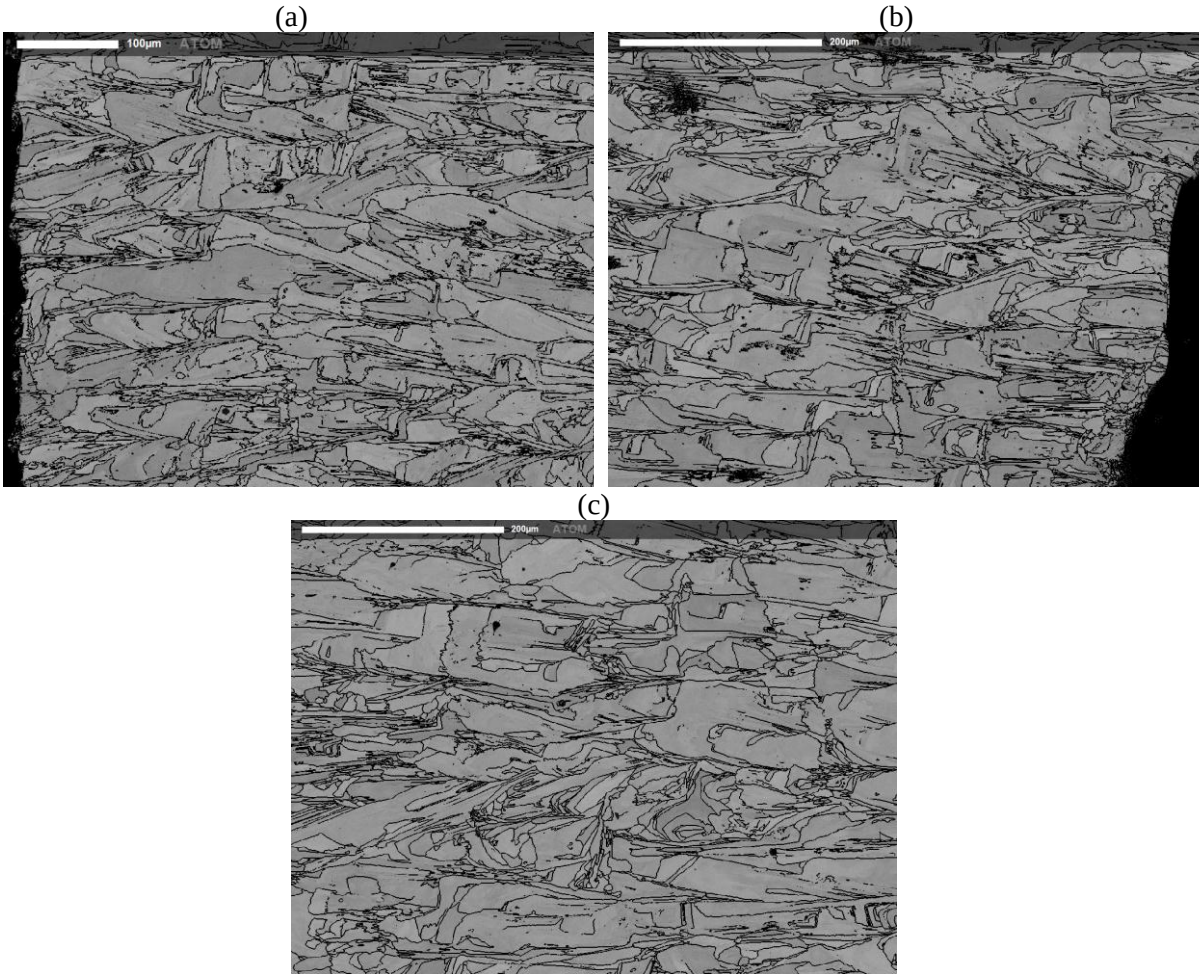

Figure V-1: BC maps of SLM 316L: (a) bottom (b) top (c) middle part of the sample

After eliminating the very small grains (D_{eq}<2µm), the numbers of detected grains are 545, 563 and 550 with respect to the three sample areas. These three similar values indicate that the microstructural patterns are consistent in different locations of the fabricated sample. Considering the sample area has a size of 600*450 µm², an approximate estimation of grain size using the Eq. (*V.1*) and Eq. (*V.2*) can be obtained and is about 25 µm.

One certain conclusion from EBSD scans is that the polycrystalline aggregates are mainly tessellated by large elongated grains with a quadrangle shape, visible in Figure V-1. The first proposed virtual finite element model is designed to emphasize the predominant role of elongated grains. Hence, quadrangles are used to tessellate the studied area of the material. The elongated grains often have a large aspect ratio. We process the raw EBSD data by filtering small grains to consider only the pronounced large elongated grains. The threshold chosen is such as the D_{eq} is lower than 5 µm. The treatments are conducted for the top, middle and bottom areas separately and all three studied areas have similar outputs, which again confirm the microstructures have similar patterns in the whole sample. The grains exceeding this threshold occupy 98% of the whole area. The original scanned area has an area of 269859 µm² while the detected grains have a total area of 264606 µm². The average grain size calculated is such

that D_{eq} equals 54 µm. This value is later used as a reference value for the quadrangle tessellated geometrical finite element model. For the quadrangles in the numerical model, the average aspect ratio of the imitating elongated grains is set to 3. This value was chosen from an ellipse approximation process applied to the large grains (see Figure V-2).

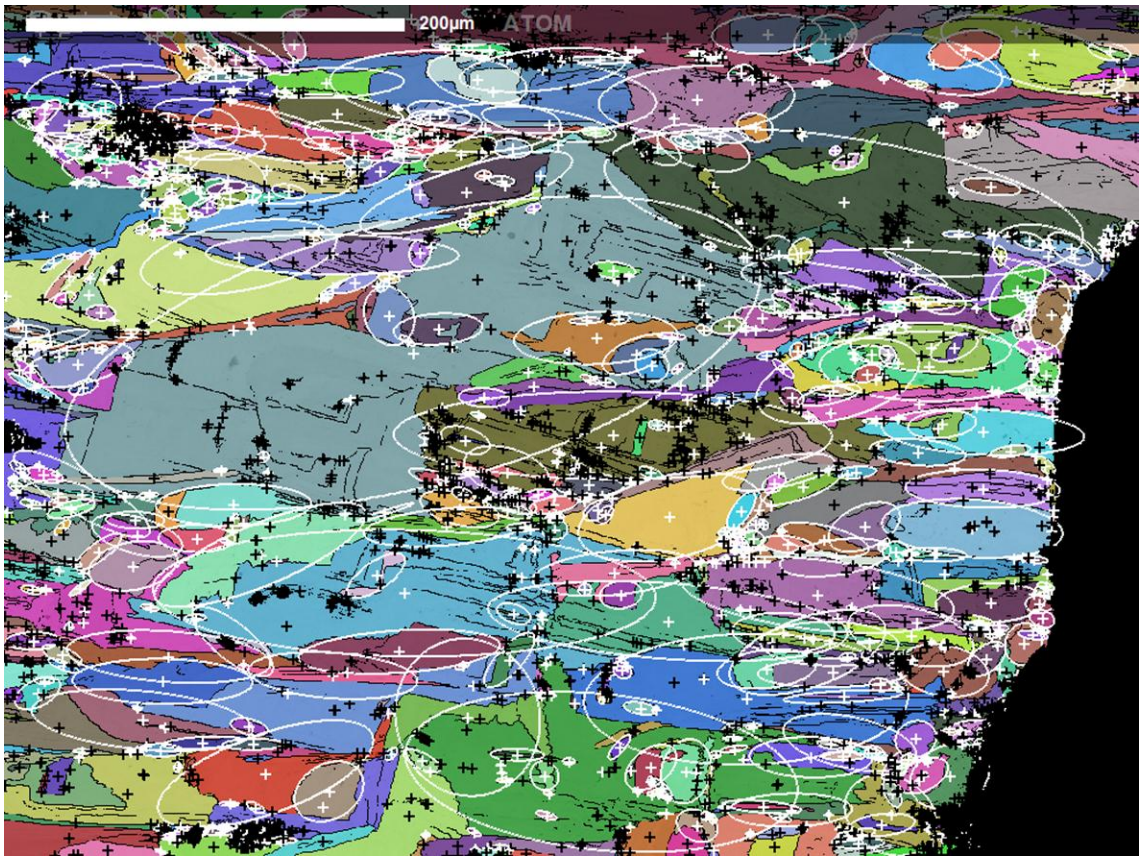

Figure V-2: Ellipticity measurement of EBSD map (top area of the sample)

Voronoi tessellation is also used to build other models because, in the quadrangle-tessellated model, grain size is almost homogeneous and the presence of small grains which might have an influence are omitted. We adopt another realization of virtual microstructure by using log-normal distributed Voronoi polygon. In the case of the present grain size distribution, the parameters of the log-normal probability distribution are $\mu = 15$ (µm) and $\sigma = 0.6$. The distribution function of the log-normal probability distribution is plotted for this set of parameters in Figure V-3 and is compared to the empirical distribution function. A good agreement is observed. For the Voronoi-polygon-tessellated model, the positions of grains are decided by the random seeds of the polygon. We use two random seed sets to qualitatively investigate different grain position configurations. In terms of distributions of D_{eq}, the simulations are similar to the realistic condition (see Figure V-4).

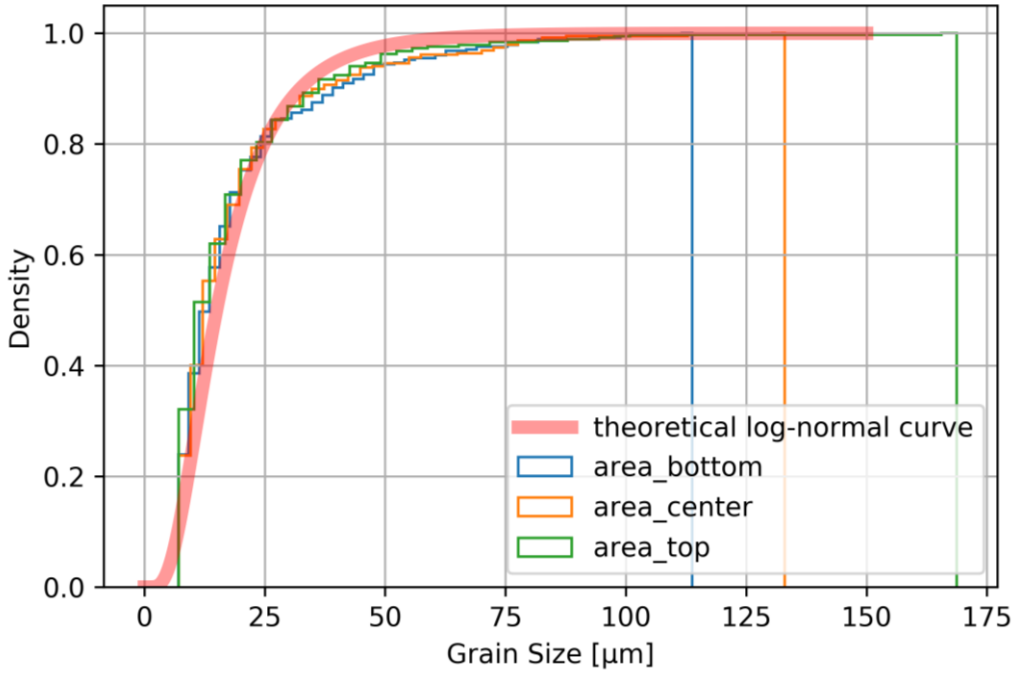

Figure V-3: Theoretical log-normal distribution and empirical distributions of grain size

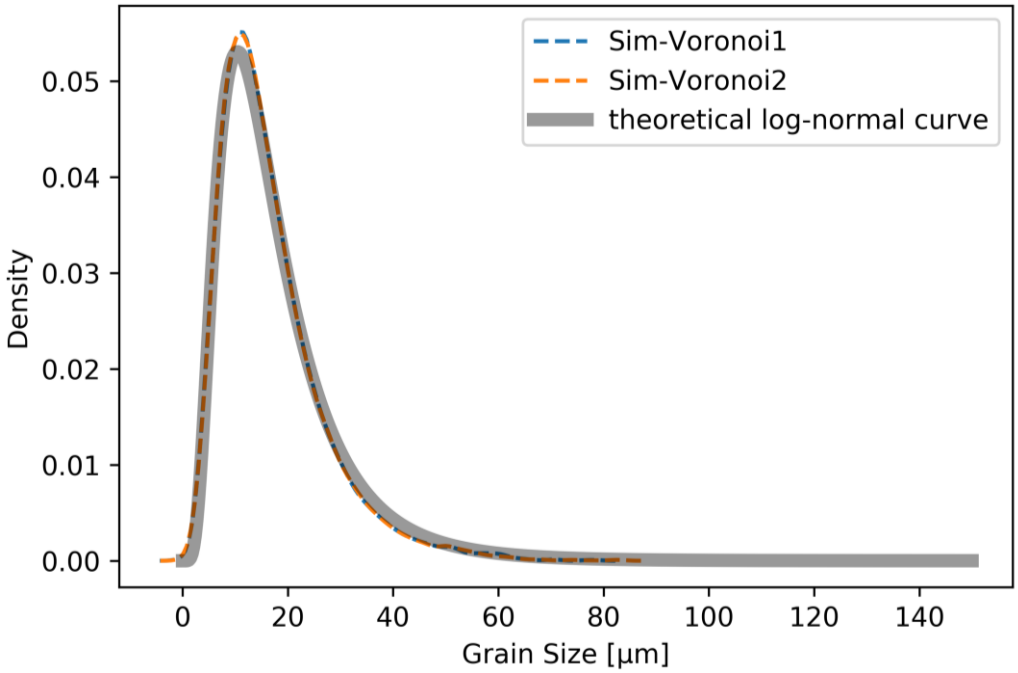

Figure V-4: Comparison of theoretical log-normal distribution curve and probability density of grain size of generated models

V.1.1.2. *Grain orientation*

In the modeling of polycrystal aggregate, a set of crystallographic orientations is assigned to the grains. In the previous experimental investigation, we found that the studied material is in a strongly

textured state. The monotonic tensile test reveals that the Young's modulus is lower than the nominal value of steel. A series of preliminary investigations are done to choose characteristic crystallographic orientation sets to reproduce this experimental observation.

In the EBSD analysis, we can collect the actual size and orientation of each detected grain. A self-consistent scheme (Robert and Mareau, 2015) is used to simulate the tensile test. The estimation of the macroscopic Young's modulus is simply deduced by using the macroscopic stress divided by the macroscopic strain in the loading direction. The objective is to choose appropriate grain orientations to reflect the textured microstructure of our sample. We hence use the EBSD data from the plane X/Y to make sure of the consistence between experiments and simulations. The cubic elastic constitutive model is adopted. The values of C_{1111}, C_{1122}, and C_{1212} are the ones of γ-Fe (Huntington, 1958). Raw data from the upper, middle, and bottom areas in the tested specimen are processed separately to check the results' consistency from different positions and are concatenated together to have an overall estimation of the Young's modulus. The calculated Young's moduli are listed in Table V-1. From the table, we can see that the estimations reached from different simulations are similar. The upper part has the lowest value and the bottom part has the highest value. The value from the middle part is approximately the same as the value from the concatenated model. However, the simulated moduli have a trivial difference of about 10% with the experimental measurement. A possible explanation is that we have no available exact cubic elasticity model parameters. The parameters from γ-Fe seem to provide good approximations even though a certain deviation exists.

Table V-1: Calculated Young's moduli and Poisson ratios for different sampling areas of EBSD specimen

	Middle	Upper	Bottom	Overall	Experimental	Isotropically distributed	316L Nominal
Number of orientations	2143	4500	3096	9739	-	9000	-
Young's modulus [GPa]	145.1	140.9	146.6	144.6	150-157	194	190-205
Poisson ratio	0.325	0.312	0.304	0.312	N/A	0.284	0.265-0.275

To generate a representative realistic grain orientation set, the crystallographic orientations extracted from the EBSD need further processing. EBSD returns the Euler angles for every grain detected in the sample. Nevertheless, our numerical model shows a virtual microstructure. We create the microstructure with randomness to simulate more different configurations. The distributions of grain size and morphology are only equivalent to realistic conditions from a statistical perspective. If we assign orientations to the grains in numerical models by using the thousands of crystallographic orientations from EBSD directly, there will be a risk that we overemphasize the influence of small grains while lowering the dominant role of large elongated grains. An alternative is proposed hereby to avoid the

misassignment. We duplicate the measured orientations from the middle part of the specimen according to the sizes of the grains where they belong to. Then, a randomly sampling is carried out from the generated orientation set. To verify the choice of orientation set, we assign the orientations to a numerical model with a synthetic Voronoi-polygon-tessellated microstructure and calculate the estimated Young's modulus. The results from the 24 chosen orientation sets are shown in Figure V-5. The benchmark value is 145 GPa from the previous simulation using actual grain sizes and grain orientations from the middle part of the EBSD specimen. Two dashed lines represent differences within 1%. We can see that the proposed method can generate the characteristic textured grain orientations set.

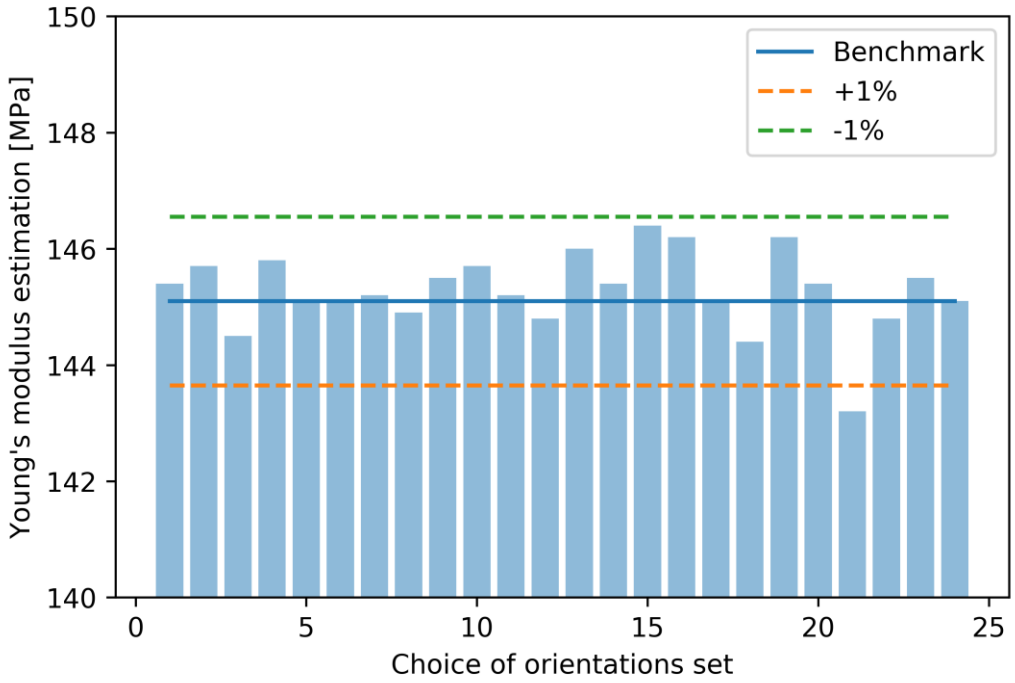

Figure V-5: Calculated Young's moduli for 24 realistic textured grain orientations sets generated randomly

Besides the realistic grain orientations set, isotropically distributed grain orientation is used in the simulations as a reference to show the effect of the textured microstructure of AM material. For the isotropically distributed grain orientation set, the crystallographic orientation has no preferential direction. Hence the orientations are homogeneously distributed in the 3D space. The isotopically distributed grain orientations sets used in this study are generated using the software Neper (Quey, Dawson and Barbe, 2011). To present the distribution of orientations in isotropic and realistic configurations, pole figures are shown in Figure V-6.

Isotropically distributed crystallographic orientations

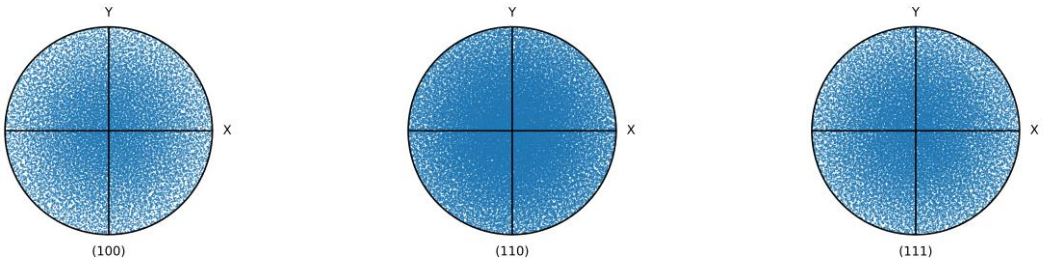

Realistic distributed crystallographic orientations in SLM SS 316L

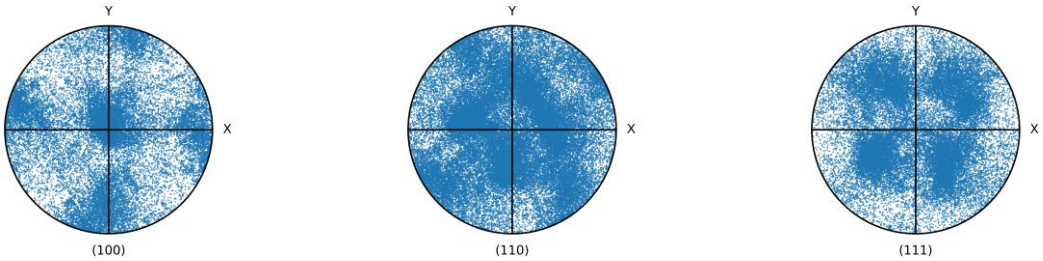

Figure V-6: Pole figures in direction 100, 110 and 111 of employed orientation sets

Young's modulus and Poisson ratio are calculated for the isotropically distributed orientations set in the same way as the realistic configuration. The values are also listed in Table V-1.

V.1.2. Surface roughness & Pores

Besides the microstructural attributes, an ideal quasi-realistic numerical model for the additive manufactured material should be able to consider the most crucial parameter of fatigue performance, the poor surface state. Generally, the surface state is defined by its roughness and the presence or not of pores.

Roughness recording using profilometry technique is presented in Chapter II. The scanned surface returns 3D data, which means the raw data from profilometry can be discretized into thousands of 2D profiles. To choose representative roughness profiles, some post-treatments are conducted.

The scanned surface has a size of 6*10 mm². The resolution of the scanner is 2 µm. After filtering the data near the border of the sample that often show greater measuring errors, we have 2731 2D roughness profiles which are discretized according to the Y coordinate. The 2D numerical model built has a length of 5 mm. Hence, we cut the profiles at the two ends and only keep the middle parts. The standard for choosing the profile which can represent the surface features is hard to decide as the typical representative parameter to characterize the influence of surface roughness on fatigue performance is still in dispute. The most commonly used parameter is the arithmetical mean deviation (R_a). Also, there are more proposed parameters, i.e. root mean squared (*Rq*), maximum valley depth (*Rv*), maximum peak height (*Rp*), maximum height (*Rt*), skewness (*Rsk*), kurtosis (*Rku*) and mean depth from Japanese industrial standard (*RzJIS*). An illustration of surface roughness parameters is provided in Figure V-7.

In this study, we use the *Ra* as the predominant parameter and take into account other parameters as well. The ideal profiles should have very similar *Ra* as the whole scanned surface while the other parameters are in reasonable ranges. Profiles are chosen from different positions to prevent the similarity of geometry. The selected roughness profiles are shown in Figure V-8. P1 is the profile measured in the very middle of the specimens. Besides, P1 is relatively smooth considering its characteristic parameters. All the parameters from P2 are within one standard deviation of mean results from the whole scanned surface which makes this profile the supposed "most" representative. P3, on the contrary, is the one with parameters deviating from the references. P4 and P5 are chosen so that they have the same *Ra* values as the experimental ones. P4 has a large *Rv* while P5 has a large *Rp*. The comparison between P4 and P5 can indicate the difference between intrusion and extrusion cases. The calculated parameters of each profile are listed in Table V-2. It is important to point out that 24 additional profiles chosen by the shuffle algorithm from the scanned surface are used to keep the stochasticity of the roughness. We will compare the results from selected profiles and that from randomly chosen ones to verify whether the characteristic roughness parameters can be of value in terms of fatigue predictions.

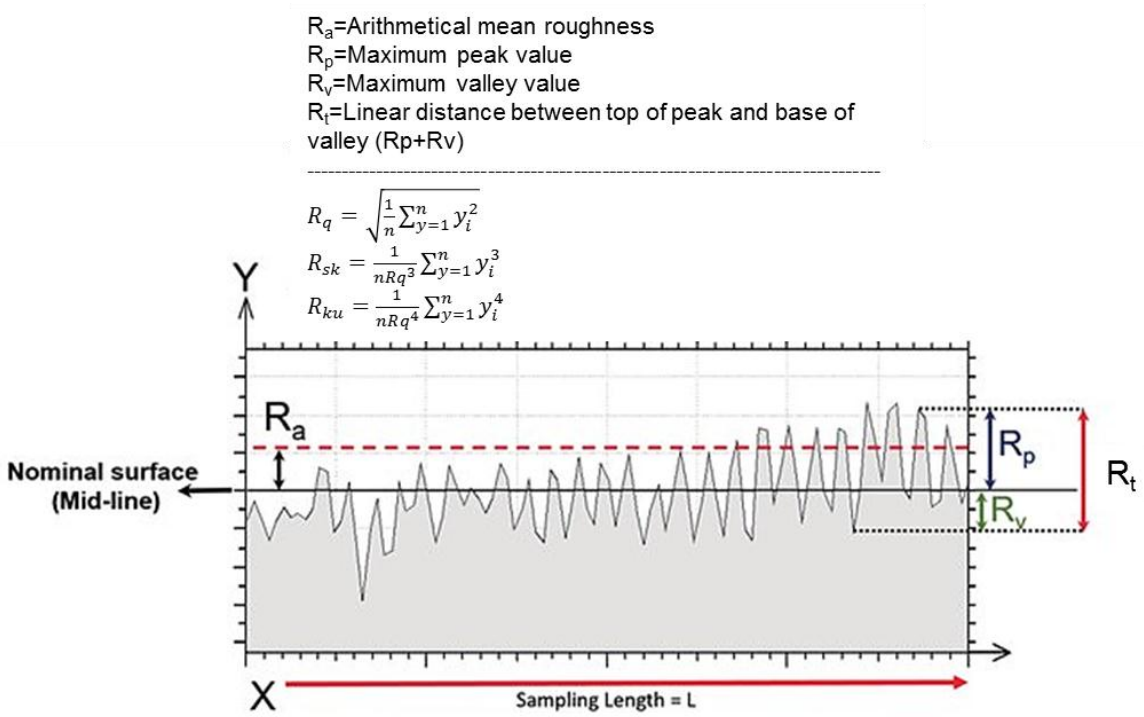

Figure V-7: Schematic illustration of several surface roughness parameters (adapted from (Tekçe *et al.*, 2018))

Table V-2: Characteristic roughness parameters of the 5 selected profiles

	Scanned surface	P1	P2	P3	P4	P5
Ra [µm]	7.23±1.13	6.93	7.24	19.71	7.23	7.23
Rq [µm]	9.35±1.51	8.65	9.59	22.01	10.83	11.16
Rv [µm]	23.0±5.51	15.80	22.05	50.01	43.14	24.16
Rp [µm]	30.8±7.02	26.61	37.06	20.72	42.72	63.54
Rt [µm]	69.1±15.2	42.41	59.11	70.73	85.86	87.70
Rsk	0.447±0.373	1.20	0.76	-1.24	0.79	2.70
Rku	3.92±1.09	2.85	4.34	1.70	6.19	12.95
Rz(JIS) [µm]	53.9±10.2	41.52	58.78	69.67	84.12	87.24

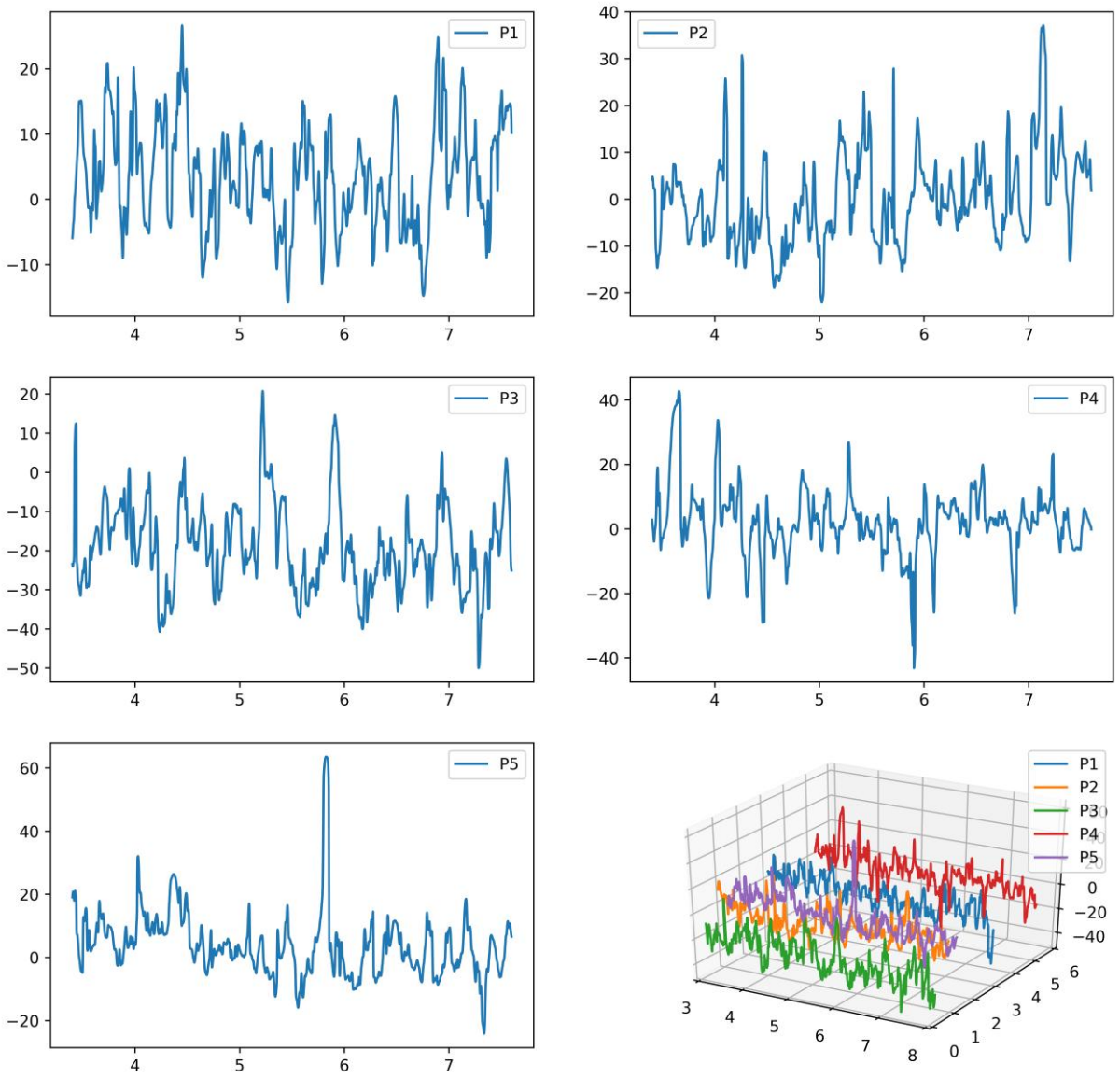

Figure V-8: Selected roughness profiles

In the experimental investigations described in Chapter II, µCT (computed tomography) allowed checking the inherent porosity of our material. Most of the manufacturing process parameters used to build our samples are optimized ones and are supposed to ensure a low fraction porosity.

From the data collected (illustrated in Figure V-9), we analyze the pores inside the sample which are often gas pores. A statistical investigation is conducted for the detected 898 internal pores. The results are listed in Table V-3. The detailed distribution of pore size is shown in Figure V-10. Most of the pores are very small. The largest detected pore has an equivalent diameter of 46 µm. Given the Kitagawa-Takahashi effect, these internal gas pores are likely not to show any effect. Hence, the internal pores will be omitted in the numerical investigation.

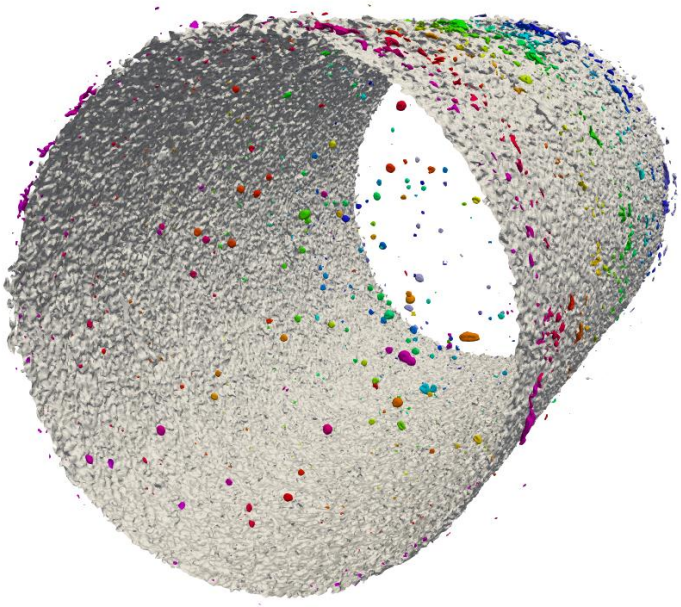

Figure V-9: Reconstructed pores detected by µCT

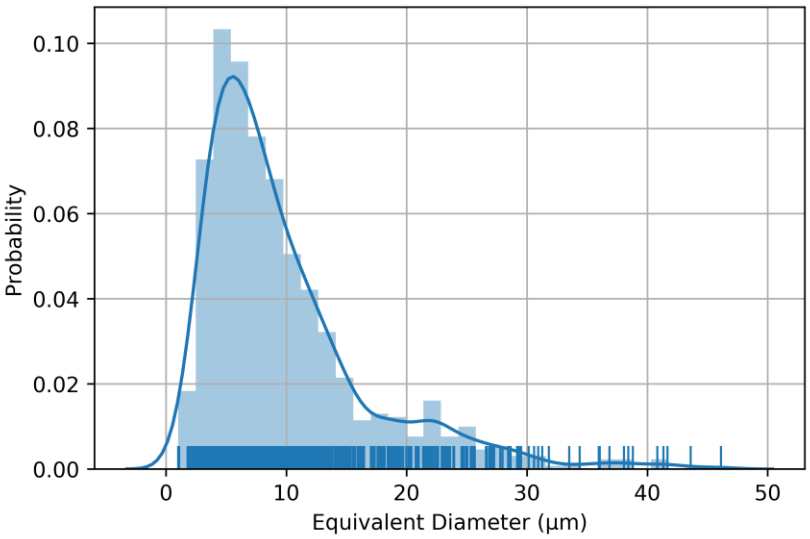

Figure V-10: Histogram and kernel density estimation curve of pores' sizes

Table V-3: Statistical information of detected pores

Pore number	average [µm]	median [µm]	min [µm]	max [µm]	
898	7.0+/-1.0	9.86	1	46.1	
D_{eq} range [µm]	(0,10]	(10,20]	(20,30]	(30,40]	(40,50]
number	581	229	70	13	5

On the fracture surfaces of the fatigue failed specimens, lack-of-fusion defects are always seen and are considered as the most harmful factor of crack initiation. But this kind of defect is often not detectable by µCT. To take into account that defect type, the estimation of an effective size from the fracture surface analyses in Chapter III is required. More exactly, we need to represent the 3D defects observed at the crack initiation sites by an equivalent 2D defect to be introduced in the numerical model. A similar solution using the Murakami equation as introduced in Chapter IV is applied. The average Murakami parameter of LoF defects in as-built specimens is about 300 µm (see Figure III-28). It is decided to use a semi-elliptical defect with a depth of 100 µm to imitate the realistic LoF defect. The observations are conducted in the transversal section while the modeling is along the longitudinal direction. The semi-minor axis representing the thickness of the LoF defect is set to 30 µm which is the layer thickness. Figure V-11 illustrates the way to design LoF defect in the 2.5D numerical model.

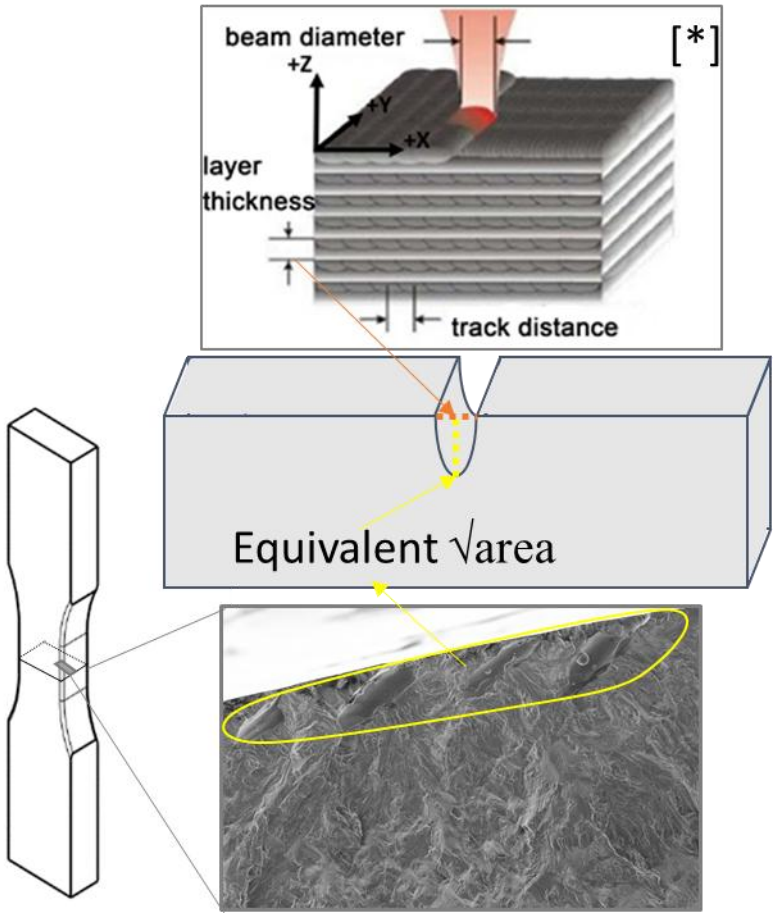

Figure V-11: Schematic illustration of designing imitating LoF defect in the numerical model(*: adapted from (Mergulhão and Das Neves, 2018))

V.2. Modeling configurations

V.2.1. Design of geometrical models

V.2.1.1. *Smooth models*

Smooth models containing explicit microstructure attributes are built up to demonstrate the effect of grain morphology and grain orientations. Five tessellations are used to compare different grain morphologies. Two types of grain orientation are used. The details of each model configuration are listed in Table V-4. The selection of morphology parameters for the latter three tessellations has been explained previously in Chapter V.1. Quadrangle tessellation 1 and Voronoi tessellation are purely based on the approximate estimation of grain size. The parameters of the other three tessellations are decided by certain microstructural patterns respectively. Tens of sets of grain orientations are employed. Half are isotropically distributed and half are realistic. Simulations of these models are conducted using the LAMPA's cluster. Only tension loading is applied to these models.

Two extra log-normal Voronoi tessellations are used to imitate the realistic microstructure. The quadrangle tessellation 2 is added to emphasize the influence of elongated grains. Simulations for these two last cases are conducted using the ISAE-Supaero cluster "Pando". Similarly, isotropically and realistically distributed orientations are used but in fewer numbers. Both tension and bending loading conditions are applied. Figure V-12 shows examples of the five tessellations used.

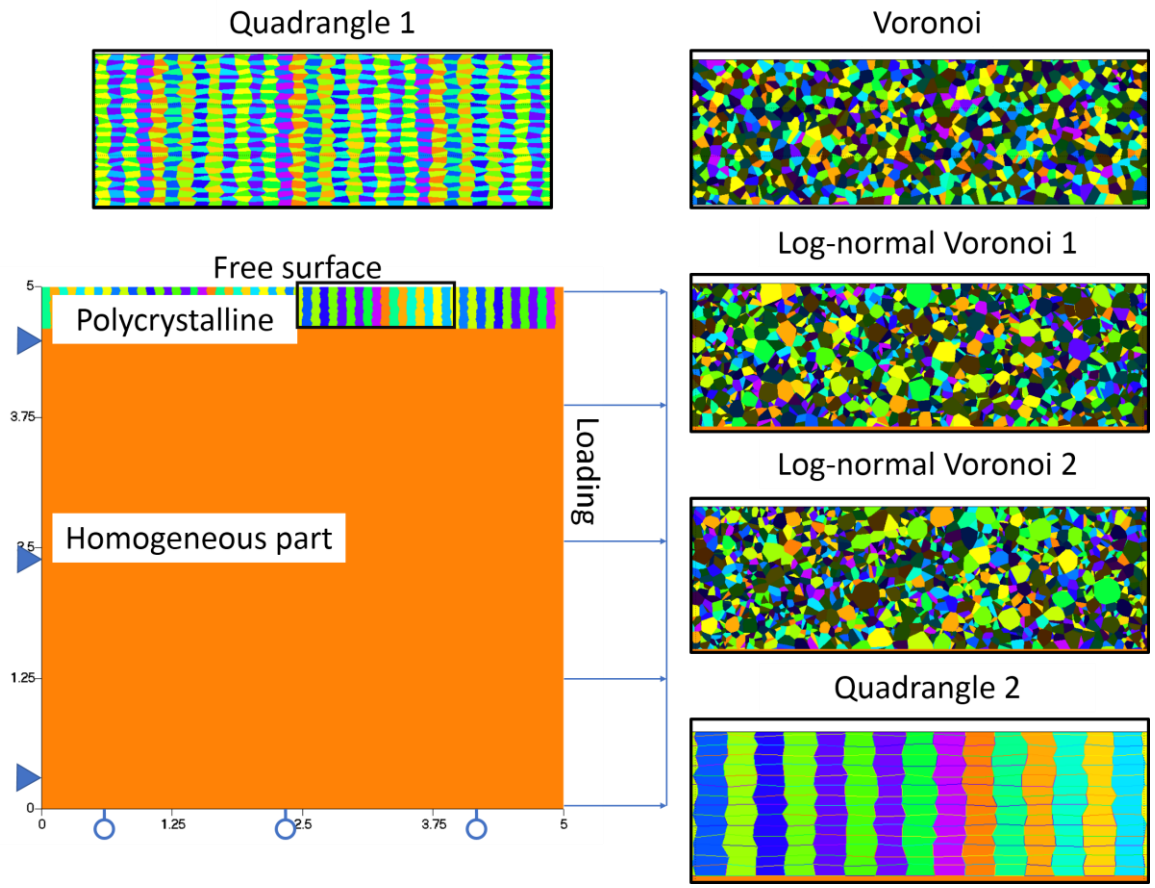

Figure V-12: Illustrations of 5 tessellations involved in the numerical model

Table V-4: Configurations of the models employed in the simulations

Tessellation			Orientation		Loading	
Name	Grain number	Average grain size [µm]	Isotropic set number	Realistic set number	Tension	Bending
*Quadrangle 1	5070	25	50	50	✓	×
*Voronoi	5070	25	50	50	✓	×
#Log-normal Voronoi 1	8400	19	24	24	✓	✓
#Log-normal Voronoi 2	8400	19	24	24	✓	✓
#Quadrangle 2	1080	54	24	24	✓	✓

*: only used in smooth models; #: used in all models

V.2.1.2. *Models with defects*

The models with semi-ellipsoidal defects are designed to simulate the effect of LoF defects. Let us recall that, for the simple-polished specimens, roughness is eliminated by the polishing operations. But LoF defects remain on or near the polished surface. As previously mentioned, equivalent 2D defects are

introduced in the models to reflect the role of LoF defects. Same microstructures as the ones of the smooth models stored in the cluster "pando" are used, as listed in Table V-4 with a mark "#".

The selected five roughness profiles discussed previously are added to the smooth models by geometrical Boolean operations. The models are approximations of as-built specimen lateral projections. Likewise, the detailed configurations are listed in Table V-4 with a mark "#".

The as-built specimens show not only significant roughness but also LoF defects. The models with roughness and geometrical defects aim at taking both detrimental factors into considerations. All other microstructural configurations are kept the same.

Schematic pictures of defective models mentioned above are presented in Figure V-13.

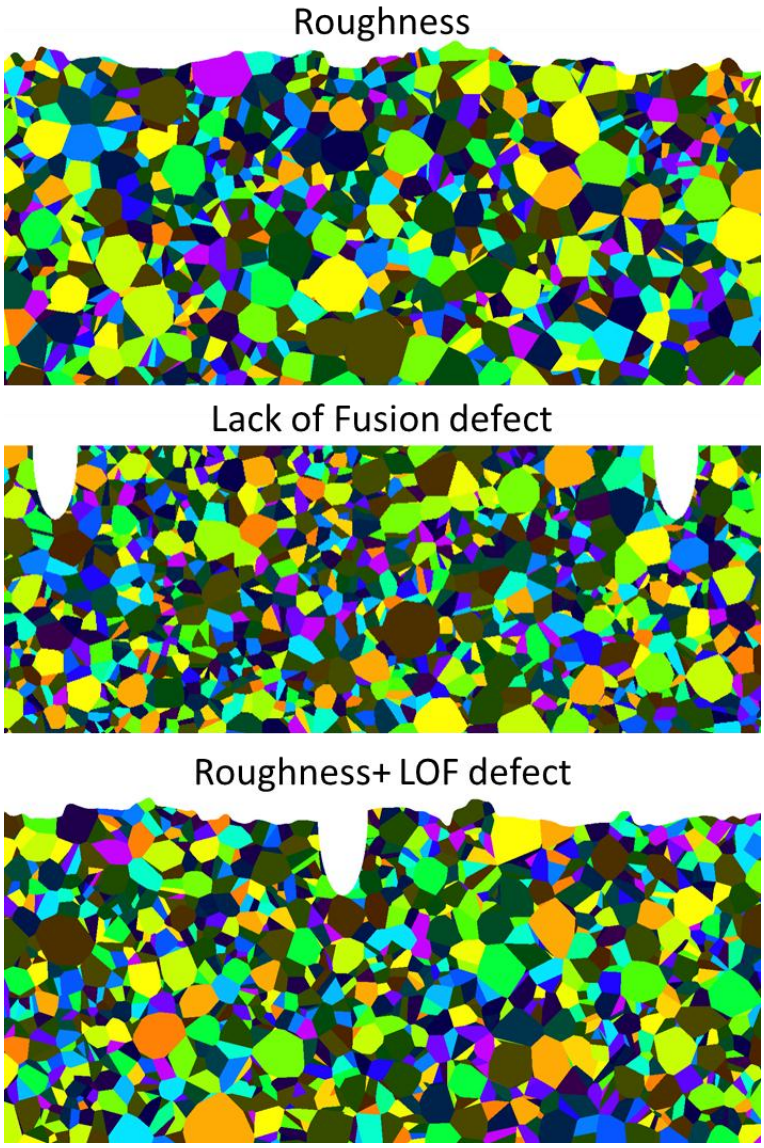

Figure V-13: Different types of defective models (zoom view of the local top surface)

Meshes are generated by the software Gmsh. For the polycrystal part, a characteristic length of 2 µm is used in the top half creating a very fine mesh. In the lower half, mesh size is set to 20 µm. A coarse mesh with a size of 100 µm is used for the homogenous part.

V.2.2. Constitutive models

V.2.2.1. *Calibration of parameters in the elastic constitutive model*

The material constitutive equations used in the current simulations are of three types: isotropic elasticity, cubic elasticity and crystal plasticity. Regarding cubic elasticity, the same values as the ones detailed in Chapter IV are used. For the case of isotropic elasticity, a detailed discussion is presented as follows.

As the finite element model is composed of one homogeneous part and one polycrystal part, isotropic elasticity is attributed to the homogeneous part.

The aim of calibrating the isotropic elastic model is to make the homogeneous part consistent with the polycrystal part. Since the cubic elastic parameters C_{1111}, C_{1122} and C_{1212} are already determined, Young's modulus and Poisson ratio are calibrated considering the macroscopic responses of a polycrystalline aggregate containing numerous grains. It should be noted that two sets of parameters' values in isotropic elasticity are used. The parameters are calibrated by a model with isotropically distributed grain orientations and a model with textured microstructure.

Table V-5: Isotropic elastic constitutive model parameters for studied 316L steel with regards to the different texture configuration

	E [MPa]	ν
Isotropic (Non-textured)	194000	0.284
Realistic (Textured)	145100	0.330

V.2.2.2. *Identification of parameters in polycrystal plastic model*

Meric et al. (Méric, Cailletaud and Gaspérini, 1994) proposed a phenomenological crystal visco-plasticity model that contains non-linear isotropic and kinematic hardening. The plastic slip velocity of every system follows a Norton type visco-plastic flow law

$$\dot{\gamma}_s = \langle \frac{|\tau_s - x_s| - r_s}{K} \rangle_+^n \; sign(\tau_s - x_s) \qquad (V.3)$$

where

$$sign(y) = \begin{cases} -1 & if\ y < 0 \\ 0 & if\ y = 0 \\ 1 & if\ y > 0 \end{cases}$$

$$\langle y \rangle_+ = \max(y, 0) \qquad (V.4)$$

and K and n are viscosity parameters. x_s and r_s are the kinematic hardening variable and the isotropic hardening variable on the slip system denoted by s, respectively.

$$x_s = c\alpha_s \; and \; \dot{\alpha}_s = \dot{\gamma}_s - d\dot{v}_s\alpha_s \qquad (V.5)$$

where c and d are material parameters.

$$r_s = r_0 + Q\sum_{r=1}^{12} h_{sr}[1 - \exp(-bv_r)] \; and \; \dot{v}_r = |\dot{\gamma}_r| \qquad (V.6)$$

where r_0 is the initial critical shear stress and b is a coefficient of material sensitivity to saturation. This equation contains an interaction matrix h_{sr} which has 6 parameters.

The identification of the crystal plasticity behavior law can be a long process on the one hand due to the large numbers of parameters of the model (7 for the model of Méric and Cailletaud), and on the other hand because of the time of high computation for the nonlinear simulation of a polycrystalline aggregate.

Regarding the identification methodology, the choice was made to use a self-consistent model because it allows achieving a good estimate of the macroscopic fields while having a relatively short calculation time (in our case, the local fields are not necessary) compared to computation in full fields (finite element method or spectral method)(Robert and Mareau, 2015).

Table V-6: Interaction matrix of FCC structure and the associated slip systems

h_0	h_1	h_1	h_3	h_4	h_4	h_2	h_4	h_5	h_2	h_5	h_4	A2
h_1	h_0	h_1	h_4	h_2	h_5	h_4	h_3	h_4	h_5	h_2	h_4	A3
h_1	h_1	h_0	h_4	h_5	h_2	h_5	h_4	h_2	h_4	h_4	h_3	A6
h_3	h_4	h_4	h_0	h_1	h_1	h_2	h_5	h_4	h_2	h_4	h_5	B2
h_4	h_2	h_5	h_1	h_0	h_1	h_5	h_2	h_4	h_4	h_3	h_4	B4
h_4	h_5	h_2	h_1	h_1	h_0	h_4	h_4	h_3	h_5	h_4	h_2	B5
h_2	h_4	h_5	h_2	h_5	h_4	h_0	h_1	h_1	h_3	h_4	h_4	C1
h_4	h_3	h_4	h_5	h_2	h_4	h_1	h_0	h_1	h_4	h_2	h_5	C3
h_5	h_4	h_2	h_4	h_4	h_3	h_1	h_1	h_0	h_4	h_5	h_2	C5
h_2	h_5	h_4	h_2	h_4	h_5	h_3	h_4	h_4	h_0	h_1	h_1	D1
h_5	h_2	h_4	h_4	h_3	h_4	h_4	h_2	h_5	h_1	h_0	h_1	D4
h_4	h_4	h_3	h_5	h_4	h_2	h_4	h_5	h_2	h_1	h_1	h_0	D6
A2	A3	A6	B2	B4	B5	C1	C3	C5	D1	D4	D6	

Slip system	A2	A3	A6	B2	B4	B5	C1	C3	C5	D1	D4	D6
Slip plane	$\{\bar{1}11\}$				$\{111\}$			$\{11\bar{1}\}$			$\{1\bar{1}1\}$	
Slip direction	$<0\bar{1}1>$	$<101>$	$<110>$	$<0\bar{1}1>$	$<\bar{1}01>$	$<\bar{1}10>$	$<011>$	$<101>$	$<\bar{1}10>$	$<011>$	$<\bar{1}01>$	$<110>$

For the optimization algorithm, the choice of a genetic algorithm was made because, unlike gradient algorithms, it does not depend on the choice of initial parameters, and therefore makes it easier to detect the global minimum. In addition, parallelization is easier. The NSGA II algorithm (Deb *et al.*, 2002) is employed here.

Only the experimental cyclic curves with imposed strains of 0.30% and 0.45% were used for the identification process. This choice is made because the stress and strain levels encountered around the fatigue limit is low

The objective function used is as follows:

$$F = 0.5F_{0.3\%} + 0.5F_{0.45\%} \qquad (V.7)$$

with

$$F(x) = \frac{1}{N}\sum_{1}^{N}\frac{\sigma_{exp}^{N} - \sigma_{num}^{N}}{\sigma_{num}^{N}} \qquad (V.8)$$

The population of the genetic algorithm consists of 768 individuals (1 per CPU) and 50 generations are performed. The self-consistent model consists of 400 grains whose crystalline orientations are the ones of the largest grains measured by EBSD. The loading is discretized with 1200 and 1800 timesteps per cycle for the imposed deformations of 0.30% and 0.45% respectively. 5 cycles are simulated. The objective functions are calculated over the last cycle.

The parameters K and n of the Meric and Cailletaud model are chosen constant with the same value of 10, and the interaction matrix h is the one identified by Guerchais (Guerchais, 2014).

The other parameters of the model are shown as follows (Table V-7):

Table V-7: Searched intervals of objective parameters

	min	max
r_0 [MPa]	50	150
Q [MPa]	5	100
B	1	10
a [MPa]	1E3	5E5
d	1E2	5E3

The identified parameters from optimizations as well as the values in matrix h cited from Guerchais thesis are listed in Table V-8.

Table V-8: Identified parameters of the Méric&Cailletaud crystal plasticity constitutive model

C_{1111} [GPa]	C_{1122} [GPa]	C_{1212} [GPa]	K [MPa.s$^{1/n}$]	m	
197	125	122	10	10	
r_0 [MPa]	Q [MPa]	B	a [MPa]	d	
83.8	5.30	1.44	2.18E5	2.61E3	
h0	h1	h2	h3	h4	h5
1	1	0.438	77.2	4.31	2.41

Comparisons between simulations and experiments are plotted in Figure V-14. The identified parameters yield stress-strain curves in good agreement with the experimental ones.

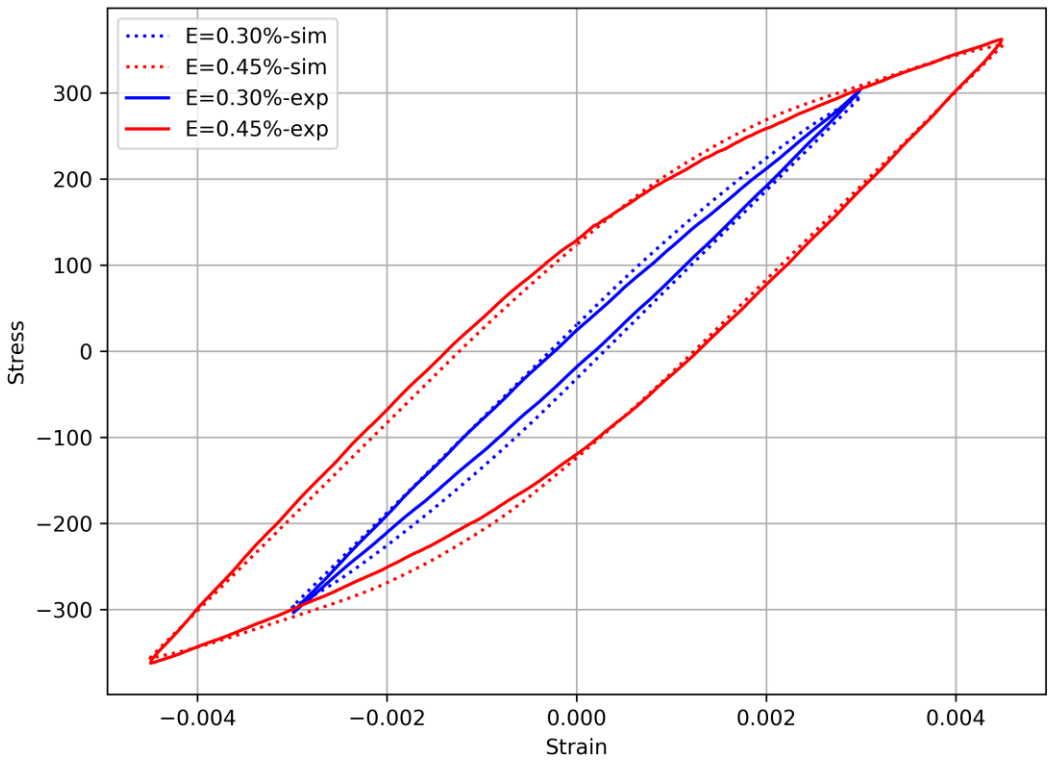

Figure V-14: Comparison between the experimental responses of 316L steel under different imposed amplitudes and the predictions of the crystal plasticity model

V.2.3. Loading condition

The present simulations involve two loading modes: cyclic bending and cyclic tension. The loading ratio is always -1. Regarding the elastic models, the stress amplitude is arbitrarily set to 100 MPa since all generated responses are linear. Results are linearly transformed in post-treatment.

V.2.4. Fatigue criteria

The fatigue criteria used are the same as the ones in Chapter IV.

V.3. Fatigue simulations of smooth models

V.3.1. Discussion on the experimental reference for simulation

Since the geometrical model has been thoroughly described before, one of the remaining questions is how to decide the reference fatigue limit for future comparison. Several potential choices can be

enumerated: fatigue tests in literature which are discussed in Chapter I; experimental data collected during the current investigation which are presented in Chapter II and III; previously used reference values in Chapter IV (conventionally fabricated 316L). The eventual reference is decided to be the same with that from the previous chapter and the reasons are explained as follows.

In the literature, the reported fatigue limits of SLM SS 316L are not always consistent. One consensus is that fatigue performance is strongly dependent on the fabrication and post-processing processes. The characteristics of the microstructure are not always available in the reported investigations of the literature. Moreover, torsional fatigue tests are rarely mentioned. The torsional fatigue limit is essential to calibrate the parameters in fatigue criteria. Material constants α and β in the stress criteria are usually deduced from both the tension fatigue tests and the torsion fatigue tests. Therefore, finding the referential fatigue limits of SLM SS 316L from the literature seems to be unachievable at the moment.

With regard to the experimental results from our own fatigue tests, we believe that the experimental investigations conducted provide very exclusive findings in terms of SLM SS 316L's fatigue performance and data from both tension fatigue tests and torsion fatigue tests are available. However, the fractography analysis revealed the LoF defects cannot be eliminated completely by mechanical surface treatment. From the Kitagawa-Takahashi diagram in Chapter III, in the left end of Figure III-28, the fatigue limit still tends to increase as the defect size decreases. Hence, we do not have a definite fatigue limit for smooth models without defects from the previously presented fatigue tests.

In Chapter IV, the fatigue limits used to calibrate the simulations for the SLM SS 316L are 230 MPa in tension-compression loading with a ratio of -1 and 147 MPa in fully reversed torsion, respectively. These values are from the previous research of Guerchais on wrought SS 316L. Consistent values are decided to be used in this chapter in particular to calibrate the material parameter α. It is also important to stress that, in the study of Riemer et al., the fatigue limit of SLM SS 316L is in the range of 250 to 280 MPa under bending loading (see Figure I-11). Using 230 MPa as the fatigue limit t_{-1} from the investigation of Guerchais seems to be a reasonable choice. Furthermore, the current numerical investigations are performed mostly under the cubic elastic constitutive model in which the responses can be changed proportionally. In other words, the tendencies observed from our simulations should remain valid even though the reference limit is different.

Consequently, for the following simulations, the results will be compared to 230 MPa which is assumed to be the reference fatigue limit for smooth models with no texture under bending loading. The parameter α is supposed to be the same as in the work of Guerchais.

V.3.2. Statistical method for microstructural heterogeneity

The poly-crystalline model can capture the multi-axial nature of the stress field thanks to its microscopic vision. Distributions of equivalent stress in models with one defect have been presented in

the previous chapter. Even without any defect, heterogeneity is visible throughout the model. The different grain orientations result in a strong scatter of stress distribution, as shown in Figure V-15. The remote loading level applied is 100 MPa. The extreme value that appears at certain grain boundaries can reach twice this stress while the lowest equivalent stress can be as low as half of the remote loading level.

From the fatigue results on AM SS 316L presented in the previous chapters, the fatigue performance seems dependent on several factors such as surface state, crystallographic orientations, grain morphology, etc. What is difficult here is to know the actual role played by each of these parameters. Our limited number of experiments and observations do not allow us to quantitatively evaluate the effect of each factor. We hence turn to the simulation outcomes to get a better insight into this issue. Using the numerical tools permits us to generate numerous instantiations of fatigue test. To deal with the stochasticity in the configurations of the microstructural attributes as well as the surface state, the statistical method is required.

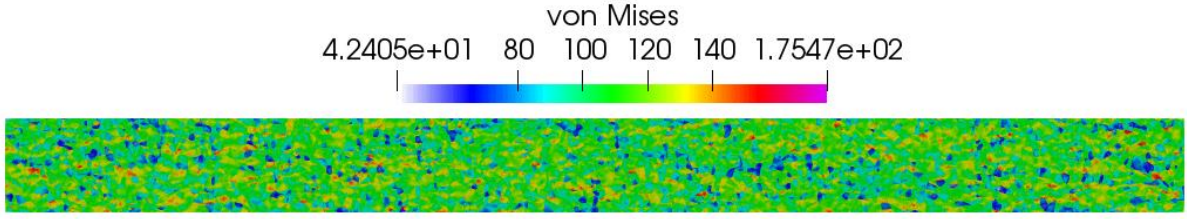

Figure V-15: Von Mises stress distribution in a smooth polycrystalline model subjected to a tension loading of 100 MPa

A comprehensive study dealing with the statistical assessment of the fatigue strength dispersion of pure copper is reported in the literature (Hor *et al.*, 2014). The main contribution of this work is that generalized extreme value (GEV) distribution is applied on a mesoscopic scale to describe the extreme essence of fatigue phenomenon. Details on the GEV theory can be found in (Fisher and Tippett, 1928; Freudenthal and Gumbel, 1954). A generalized single parametric expression is proposed by Jenkinson (Jenkinson, 1955). The formula is shown in Eq. (*V*.3).

$$G_{s,\xi} = \begin{cases} \exp\left(-(1+\xi s)^{-\frac{1}{\xi}}\right) & if\ \xi \neq 0 \\ \exp(-exp(-s)) & if\ \xi = 0 \end{cases} \qquad (V.3)$$
$$s = (x-\mu)/\sigma$$

Where μ and σ are the location parameter and scale parameter, respectively. The shape factor is denoted as ξ. The variable *s* is considered as the normalized extreme value. In the case where ξ=0, the function is a Gumbel distribution. If ξ>0, the function is equivalent to Weibull distribution when *s*> -1/ξ. If ξ<0, the function equals to Fréchet distribution when *s*< -1/ξ.

A series of simulations on the fatigue tests of smooth polycrystalline aggregate with different microstructures following the statistical-analysis protocol proposed by Hor is carried out. Details are presented here.

For one polycrystal FE model, a scatter map of hydrostatic stress and maximum resolved shear stress from every element and every grain is plotted in Figure V-16a and Figure V-16b respectively. The hydrostatic stress and the maximum resolved shear stress in all the slip directions are the two components of Dang Van stress. The grey dashed line illustrates the macroscopic threshold of the Dang Van criterion as the Dang Van stress is calculated by a linear combination of the two components. Strong variability is seen in the responses from each element and most of the elements exceed the macroscopic threshold. Apparently, taking values locally in the elements overemphasizes the effect of microstructure. It corroborates the necessity of taking values at the mesoscopic scale. A specific approach is applied in Hor's work to deal with the divergence of the local element response with regard to the macroscopic threshold. Firstly, the fatigue indicating parameter (FIP), i.e. Dang Van stress in this case, is defined at the mesoscopic scale. That is to say, the FIP is averaged in each grain of the aggregate. Secondly, the right part of the criterion is replaced by a new material parameter β^* which is the fatigue threshold at the mesoscopic scale. In this case, β^* should be defined as 183 MPa if the actual macroscopic loading amplitude is the exact fatigue limit (232 MPa).

(a)

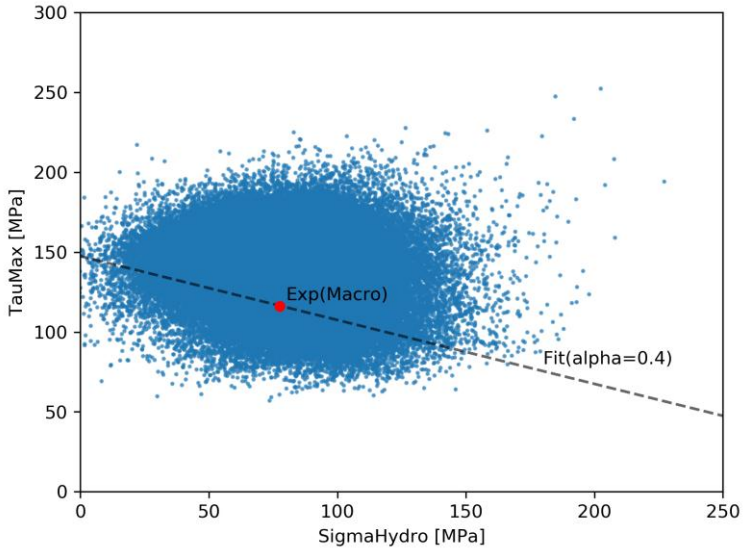

(b)

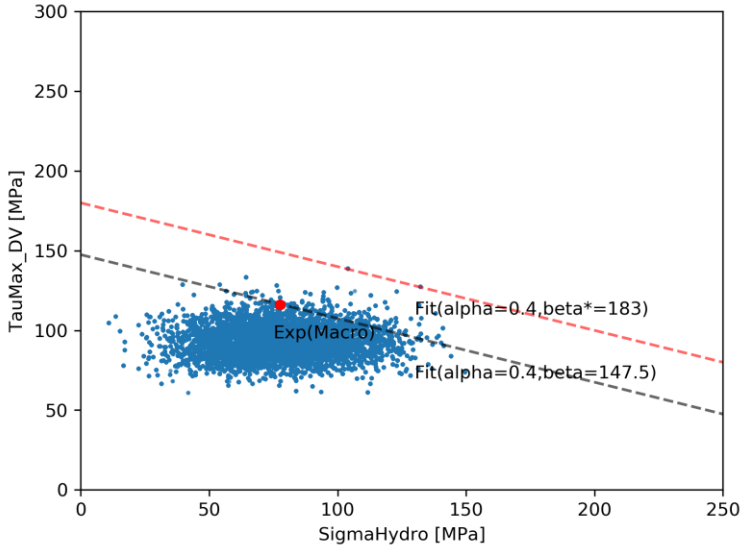

Figure V-16: Scatter maps of hydrostatic stress and maximum shear stress (a) from every element or (b) from every grain in a polycrystal FE model

100 instantiations with isotropic textures of statistical volume element (SVE) are used to generate the evolution of extreme values. Half of the instantiations are tessellated by quadrangles and the other half are tessellated by Voronoi polygons. Elastic constitutive models are used in the simulations which allows predicting the fatigue limits by a linear transformation. The applied loading is cyclic reversed tension with an amplitude of 230 MPa. Without knowing the exact value of β*, we adopt the original β from the torsion fatigue experiments according to the conclusion in Hor's work that the β* for Dang Van criterion is close to β. In Figure V-17, it is shown that the estimated values of β* in Dang Van criterion are approximate 1.1 times of the macroscopic threshold under different loading conditions. By using the GEV fitting method to correlate the scattered predictions (Figure V-18), we can note that Weibull distribution can characterize the actual fatigue limits distribution. But quantitative analysis (see

Table V-9) shows that the estimated fatigue limit is significantly lower compared to the experimental tension fatigue limit (230 MPa). This discrepancy can be due to many factors. First, assuming β and β* equal is maybe questionable. Second, the premise of defining β* is based on the validity of grain-averaged FIP. The grain-averaged responses should be further analyzed to check if the effective area for fatigue mechanisms is at a one-grain-scale.

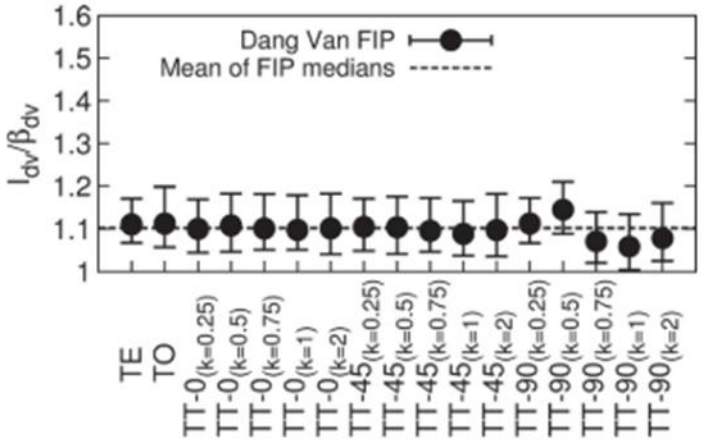

Figure V-17: Evolution of the median of the extreme value distributions of Dang Van FIP as a function of loading conditions. The black dots correspond to the median (probability of 0.5), the two limits of the interval correspond to a probability of 0:1 and 0:9 (i.e. 80% of the results are within this interval).(Hor *et al.*, 2014)

The hydrostatic stress versus the resolved shear stress of the Dang Van criterion from the critical grains of each instantiation is plotted in Figure V-18. The stochasticity of microstructure in the quadrangle models is distinguished only by the crystallographic orientations while the Voronoi models show more variability in grain shape and size. Hence, the yielded responses for the quadrangle tessellated models are less scattered compared to its counterpart for Voronoi polygon tessellated models. Regarding the estimation of β*, most of the extreme values lie in the range of 167.5 to 217.5 MPa. Nevertheless, in certain instances, extreme values are strongly deviated from this range leading to higher Dang Van stress estimations and lower fatigue limits.

In what follows, a non-local method is introduced and investigated under the current microstructure-sensitive modeling framework, FIPs are calculated over "effective areas". Instead of restraining the investigation on a one-grain-scale, more grains are involved in the estimation of fatigue initiation. We will keep a constant β* value, equal to the macroscopic threshold β but we will change the non-local parameters to perform a parametric investigation.

a) Dang Van + Quadrangle tessellation

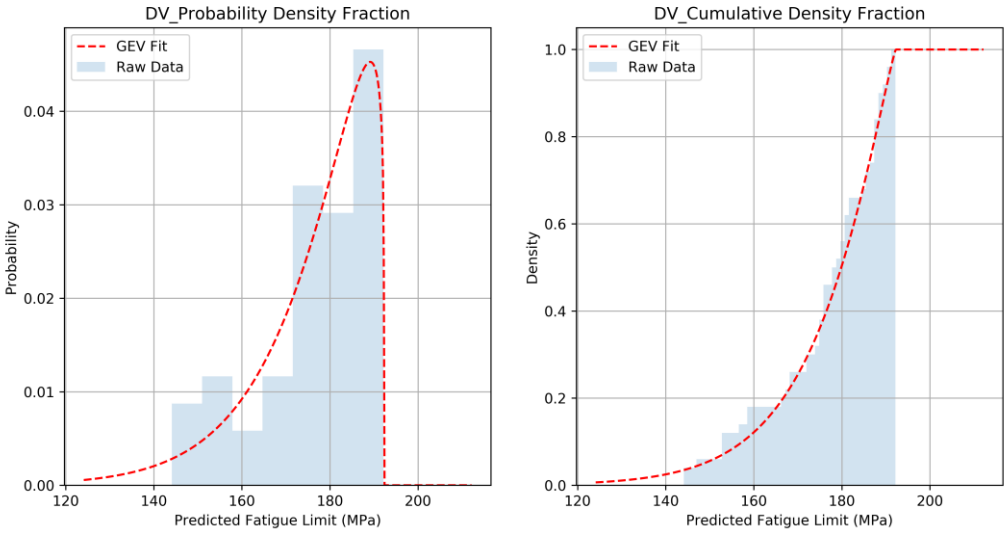

b) Dang Van + Voronoi tessellation

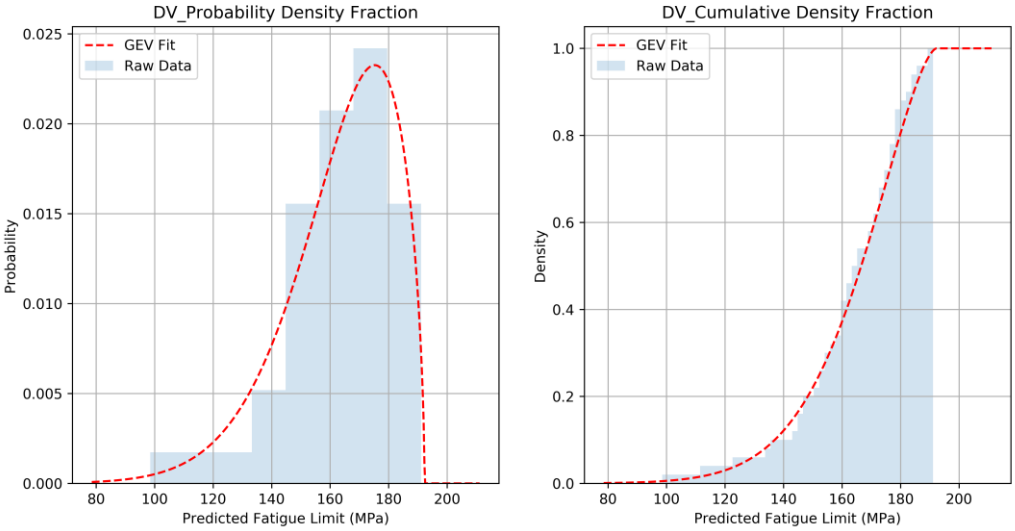

Figure V-18: GEV fitting for predicted fatigue limits using Dang Van criterion from different tessellated polycrystal models: (a) Quadrangle (b) Voronoi

Table V-9: Quantitative estimations of fatigue limit for different tessellated models

	Median [MPa]	10%-90% quintiles [MPa]
Quadrangle	180	157-190
Voronoi polygon	167	137-184

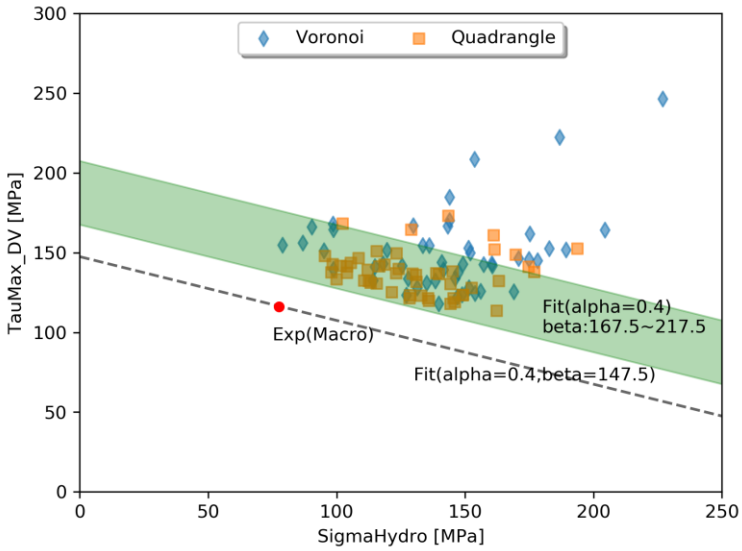

Figure V-19: Scatter map of the two components in Dang Van criterion from the critical grains in 100 instantiations

V.3.3. Investigations on R*

The non-local approach using integration over a sphere of critical radius R* was presented in Chapter IV. From previous findings, this method is not very sensitive to the grain morphology and grain size. For the sake of comparison, we choose the Voronoi polygon tessellated model with isotropically distributed grain orientations as reference. The simulated responses are calibrated by the experimental results of wrought conventional fabricated 316L which has been investigated thoroughly.

As shown in Figure V-20, we test 3 different values of R*: 15 µm, 60 µm and 100 µm. Loading mode is tension. The distributions of FIPs (Dang Van stress in this case) averaged are presented. The parameter β_{DV} equals 147 MPa which is the torsional fatigue limit for wrought 316L. The effective zone with a radius of 15 µm yields a maximum Dang Van stress of about 180 MPa which implies a fatigue limit of about 190 MPa. This value is considered to overemphasize the effect of stress heterogeneity. The prediction of fatigue limit (240 MPa) from R* equating 60 µm is higher than the experimental result (230 MPa). As the previous prediction is from one single model, we conduct simulations with 50 different isotropically distributed orientations sets then fit the response with Weibull distribution (Figure V-21). Based on the assumption that the critical fatigue limit is the value at which 50% of the cracks initiate, we use the median value of the GEV fitted data to represent the predicted fatigue limit. The predicted fatigue limit from the benchmark models is 232 MPa. The interval of 95% confidence is from 227 to 242 MPa. The simulations have hence a good agreement with the experimental results when R*=60 µm is applied.

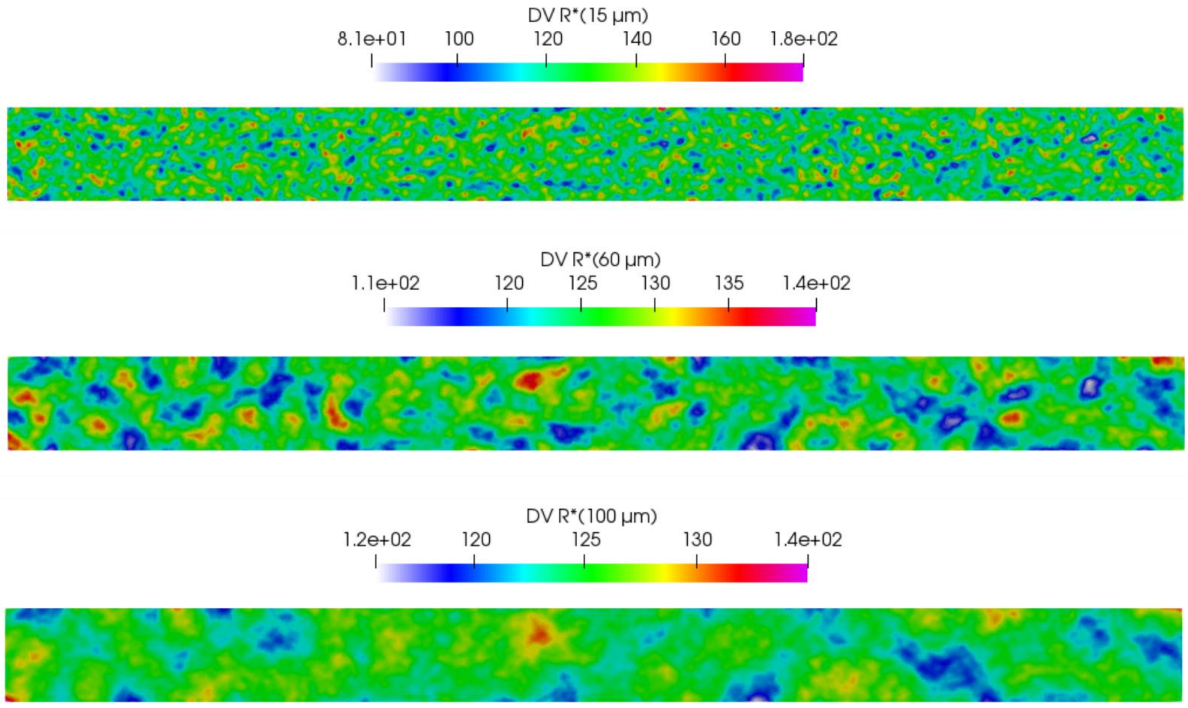

Figure V-20: Dang Van stress distributions with respect to different non-local parameters in a smooth polycrystalline model subjected to a tension loading of 100 MPa

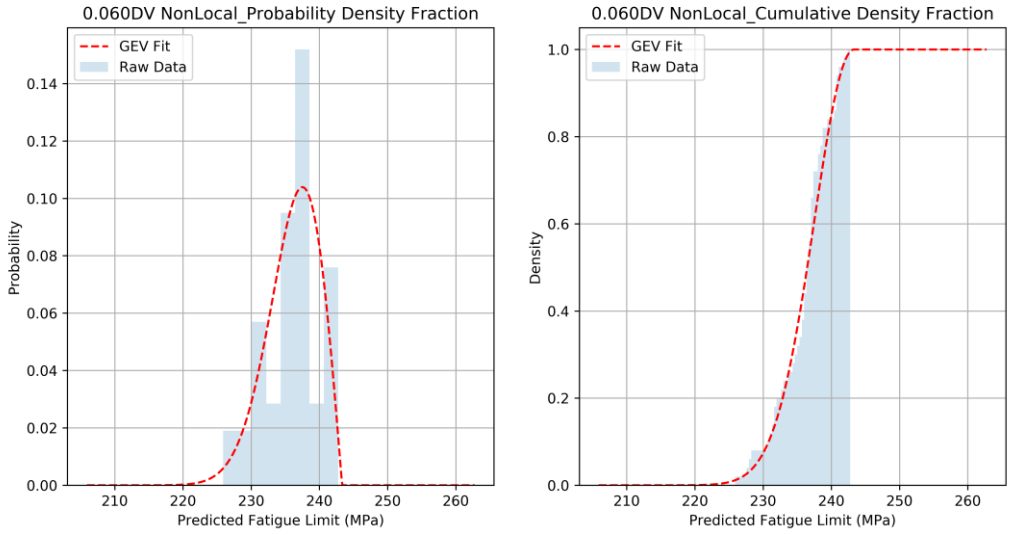

Figure V-21: PDF and CDF curves fitting the stochastic responses of FIP in polycrystalline models with different microstructural configurations using R*= 60 µm

For the different investigated models, one can wonder whether a single value of R* can be used as different tessellations with different grain sizes are adopted in the numerical models. For instance, the Voronoi tessellation used in the batch of simulations has an average grain size of 25 µm while the log-normal Voronoi tessellation has a value of 15 µm.

It should be recalled that the main objective is to compare the effect of microstructural attributes from a qualitative perspective. The previous study in Chapter IV shows that, for the smooth model, the same R* can result in different FIP values for different tessellated models, but the sensitivity to the grain morphology and grain size of the R* method is not significant. In the results of chapter IV, we have seen that log-normal Voronoi tessellations tend to give lower predictions compared to standard Voronoi tessellation. But the differences can be tolerated under a qualitative view since the difference between predicted fatigue limits in these cases are of 20 MPa at most. In the current study, we will keep 60µm as the choice of R* for all the simulations.

The fatigue limit predictions from Dang Van, Matake and Papadopoulos criteria for the smooth models are plotted for different loading modes, orientations and tessellations (see Figure V-22). The difference between the two orientation types is noticeable while the effect of loading mode is negligible. The models with isotropically distributed orientations yield predictions in the range from 220 to 250 MPa which is consistent with the conventional fatigue limit. The models containing orientations collected from AM specimens have obvious weaker performances.

(a) Matake

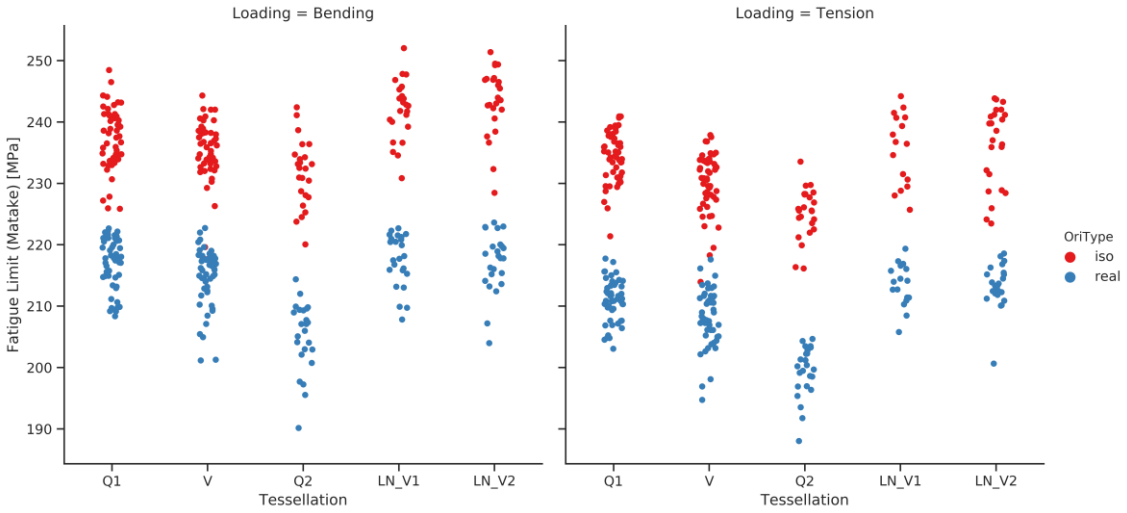

(b) Dang van

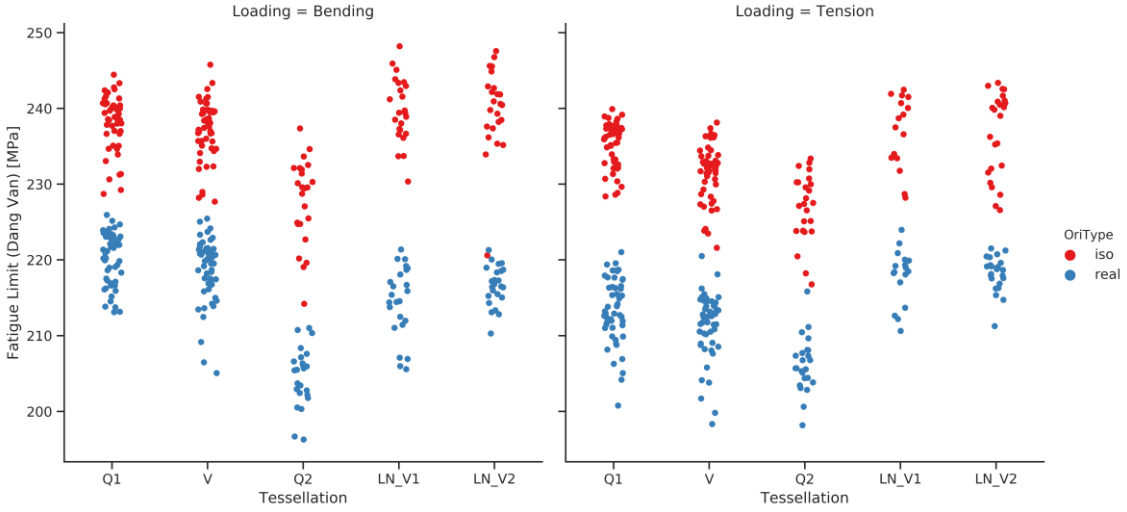

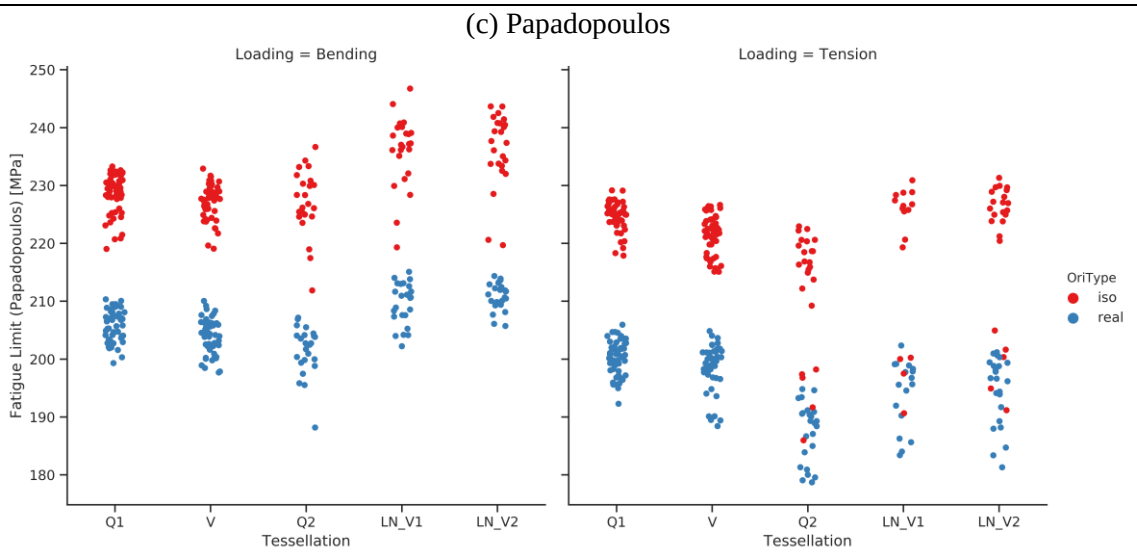

Figure V-22: Scattered predicted fatigue limits from three fatigue criteria((a) Matake; (b) Dang Van; (c) Papadopoulos) regarding texture types and categorized by the tessellation type

All three criteria produce similar results. Hence, we use only the predictions from the Dang Van criterion to conduct further quantitative analysis. The median values of predicted fatigue limits from models with the same type of loading, tessellation and orientation are calculated. The data are listed in Table V-10. It can be concluded that the realistic texture can lead to a drop in the predicted fatigue limit of around 10%. It is noteworthy that the average grain size of each batch is not equivalent. But the yielded results are close to each other.

Table V-10: Median values of predicted fatigue limits from models with the same type of loading, tessellation and orientation using non-local criteria (R*=60 µm)

		Bending			Tension		
	Tessellation	Isotropic	Realistic	Difference [%]	Isotropic	Realistic	Difference [%]
Matake	Q1	238	218	8.6	235	211	10.0
	V	236	216	8.5	231	208	10.0
	Q2	232	207	11.2	226	200	11.4
	LN_V1	243	218	10.2	237	214	9.6
	LN_V2	244	218	10.6	238	213	10.3
Dang Van	Q1	239	221	7.6	236	213	9.8
	V	238	220	7.6	232	212	8.5
	Q2	230	205	10.5	227	206	9.6
	LN_V1	239	215	10.2	238	218	8.2
	LN_V2	241	217	9.9	239	219	8.6
Papadopoulos	Q1	229	205	10.3	225	201	10.9
	V	228	204	10.2	222	200	10.1
	Q2	226	203	10.5	217	189	12.7
	LN_V1	237	211	11.2	226	196	13.4
	LN_V2	238	211	11.0	226	196	12.9

Even though R* is always set to 60 µm in the previous analyses, we cannot state it is the correct value to be used. More differently configured experiments and simulations will be needed to validate or refute the current choice. So far, this value of R* yields possible comparisons with experimental data and provides some qualitative findings with respect to the effect of microstructure.

Apparently, different values of R* will generate different predictions. The results reached with other values of R* using the Dang Van criterion are listed in Table V-11. As the value of R* increases, the predicted fatigue limit increases. In terms of the difference between the two different textures and as expected, the effect of grain orientation is higher when using small R*.

Table V-11: Median values of predicted fatigue limits from models with the same type of loading, tessellation and orientation using Dang Van criterion with different values of R*

R*		Bending			Tension		
[µm]	Tessellation	Isotropic	Realistic	Difference [%]	Isotropic	Realistic	Difference [%]
15	Q2	192	169	12.4	187	165	12.0
	LN_V1	203	180	11.2	204	180	11.7
	LN_V2	202	182	9.9	200	180	10.0
30	Q2	210	186	11.5	208	183	11.7
	LN_V1	219	197	10.3	223	201	10.1
	LN_V2	221	201	9.4	221	201	9.2
45	Q2	219	196	10.8	220	197	10.5
	LN_V1	230	207	10.0	232	211	8.9
	LN_V2	235	211	10.3	232	212	8.7
60	Q2	230	205	10.5	227	206	9.6
	LN_V1	239	215	10.2	238	218	8.2
	LN_V2	241	217	9.9	239	219	8.6

The above analysis is carried out using the critical radius method. For the neighbor layer method, since the realistic microstructure has specific characteristics, e.g. non-constant grain size and non-equiaxed grain shape, the identification of N* as well as the validation of the framework would require more experimental data which are insufficient at the moment. However, the endeavors of the application of the neighbor layer method are described in Appendix C.

V.4. Fatigue simulations using models with roughness and defects

V.4.1. Models with artificial semi-ellipsoidal defects

The models with artificial semi-ellipsoidal defects are imitations of as-built specimens with regard to the equivalent Murakami parameter. The numerical models do not keep the exact geometries of the as-built specimen. The 3D realistic defects are transferred to 2D and their shape complexity is greatly simplified.

In Chapter IV, preliminary investigations have been conducted to evaluate the HCF sensitivity to defect and microstructure. But the microstructure involved was the one of a wrought steel. In this section, the microstructure is built up based on the SLM steel. Non-equiaxed grains are used as well as the textured crystallographic orientations. Different numerical models are tested. The configurations are categorized by the tessellation, the loading type and the crystallographic orientations type. Both tension and bending loading modes are used to check the effect of stress gradient. Moreover, realistic crystallographic orientations are added. For each configuration, 24 simulations with different realizations of crystallographic orientations are conducted.

All the defects show the same size and shape. They are located separately on the surface and are far from each other. Therefore, we assume that no interaction exists between defects. Figure V-23 shows the distributions of the non-local fatigue indicating parameter using the non-local model (R*) together with the Dang Van criterion. One model is attributed to isotropic crystallographic orientations while the other one has a textured microstructure as in the SLM steel. Considering the critical radius method, R* is set to 60 µm which is consistent with the value used for smooth models in previous simulations. On one hand, the responses from the textured model are higher compared to that of the isotropic model which demonstrates the effect of grain orientation. On the other hand, although the hot spots are always in the defect root, their forms are dissimilar, especially for the textured model. The crystallographic texture changes the distribution of Dang Van stress. This phenomenon is emphasized in the textured case.

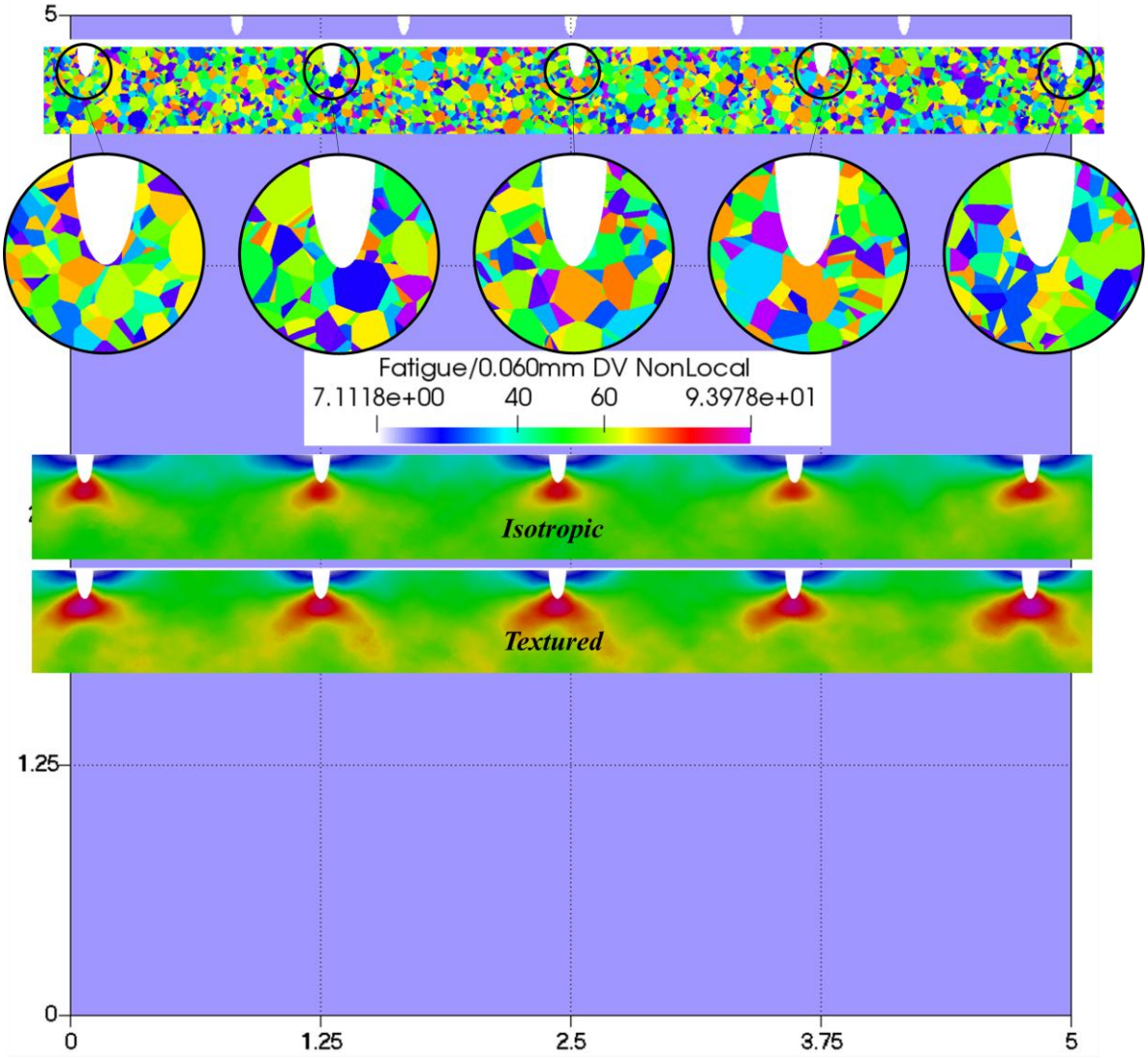

Figure V-23: Distributions of the non-local fatigue indicating parameters (Dang Van (R*=60µm)) in non-textured and textured numerical models under tension loading of 100 MPa

In Chapter III, we compared different methods for Murakami parameter measurement. The fatigue crack initiation is always caused by a cluster of adjacent LoF defects. This observation is not commonly encountered and few reported in the literature. Our proposal for multiple adjacent defects measurement is made to encompass all the defects presented at the crack initiation site. This method is qualitatively verified by the linearity shown in the plotted K-T diagram (Figure III-28). The simulations are expected to verify the experimental defect measurement process quantitatively. In the experiments, the polished specimens under bending loading have an approximate fatigue limit of 138 MPa and the as-built specimens have a fatigue limit of about 90 MPa. The inherent defects lead to a decrease in fatigue strength of about 35%.

By comparing the simulation results from smooth models and models with pores, the influence of introducing pores can be revealed.

To keep results consistent, R* is set to 60 µm for both the smooth models and the models with pores. The average values of the predictions are listed in Table V-12. From the table, the added artificial defects result in a decrease of about 25% for all the configurations. Considering the limited numbers of experiments leading to uncertainty regarding the actual fatigue limit of AM 316L, the difference between experiments and simulations is acceptable. The effect of crystallographic texture can be highlighted by comparing the two grain orientation sets. The differences are around 10 MPa. The bending loading and the tension loading lead to negligible differences.

Table V-12: Mean values of predicted fatigue limits from models containing geometrical defects with the same type of loading, tessellation and orientation using non-local Dang Van criterion (R*=60 µm)

Configuration ("Tessellation", "Orientation", "Loading")	Smooth Model [MPa]	Pores model [MPa]	Drop of fatigue limit [%]
('LN_V1', 'Realistic', 'Bending')	215	161	25%
('LN_V2', 'Realistic', 'Bending')	217	160	26%
('Q2', 'Realistic', 'Bending')	205	159	22%
('LN_V1', 'Isotropic', 'Bending')	239	174	27%
('LN_V2', 'Isotropic', 'Bending')	241	175	27%
('Q2', 'Isotropic', 'Bending')	230	172	25%
('LN_V1', 'Realistic', 'Tension')	218	156	28%
('LN_V2', 'Realistic', 'Tension')	219	156	29%
('Q2', 'Realistic', 'Tension')	206	156	24%
Experiments ('Realistic', 'Bending')	138	90	35%

V.4.2. Models with roughness

The most detrimental factor controlling fatigue performance according to our experimental investigations is lack-of-fusion defect. Even when the roughness is completely removed by polishing, LoF defects are always found at the crack initiation sites. The sole effect of roughness is hence tough to quantify. Nevertheless, with the proposed simulation framework, we can qualitatively examine the evolution of fatigue indicating parameters from stress concentration due to roughness. The roughness profiles measured from an as-built specimen are the basis for building new models. 29 different roughness profiles are applied to create rough surfaces. For each model with roughness profile, 24 sets of realistic grain orientations are built. Finite element analysis and fatigue post-treatment are then performed. The applied loading mode is tension.

Figure V-24 shows the non-local Dang Van stresses using different R*, namely 15, 30, 45 and 60 µm, for a log-normal Voronoi-polygon-tessellated model with roughness. If a small effective zone is considered, i.e. R* equals 15 µm, the effect of stress concentration is emphasized. The hotspot always emerges in a groove of the roughness. As the R* increases, the critical position is found to move from the root of the surface defect to the grain boundaries. The hot spot shift is due to the competition between roughness and microstructure. In the defect root, stress concentration is strong, but the affected area is

dependent on the defect size. Considering the roughness of SLM material, the *Ra* is often of about 10~20 µm. Therefore, the highly stressed zone is small in size. The grain boundaries, however, experience heterogeneous load levels from the local texture. Though the stress increase due to the neighboring grain effect is not as strong as the stress concentration in defect root in terms of amplitude, the related distributions are quite different. The results from4 different R* values show that the effect of roughness is more pronounced by using a smaller R* value while the effect of microstructure (texture in this case) overwhelms the effect of roughness with a larger R* value. In Table V-11, we have shown that the textured crystallographic orientations lead to an approximate 10% drop of fatigue limit compared to the isotropically distributed orientations regardless of the R* value applied. In this section, we will use a small R* to emphasize the effect of roughness.

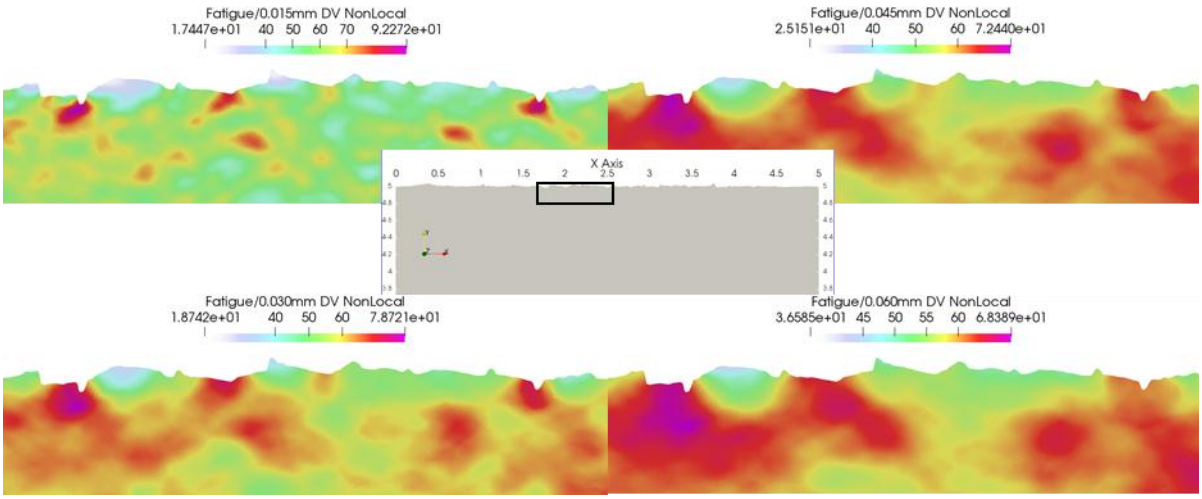

Figure V-24: Non-local Dang Van stresses using different R* (15, 30, 45 and 60 µm) for a log-normal Voronoi-polygon-tessellated model with roughness

Figure V-25 shows the results from the three criteria using critical radius R*=15 µm. In terms of maximum value, Dang Van stress is lower compared to Matake stress while Papadopoulos stress is the largest. In the meantime, from the contour plot, more hot spots are predicted by Papadopoulos criterion. The Dang Van criterion gives the most conservative predictions. Even though the remote loading is uniaxial tension, the local stress state is multiaxial.

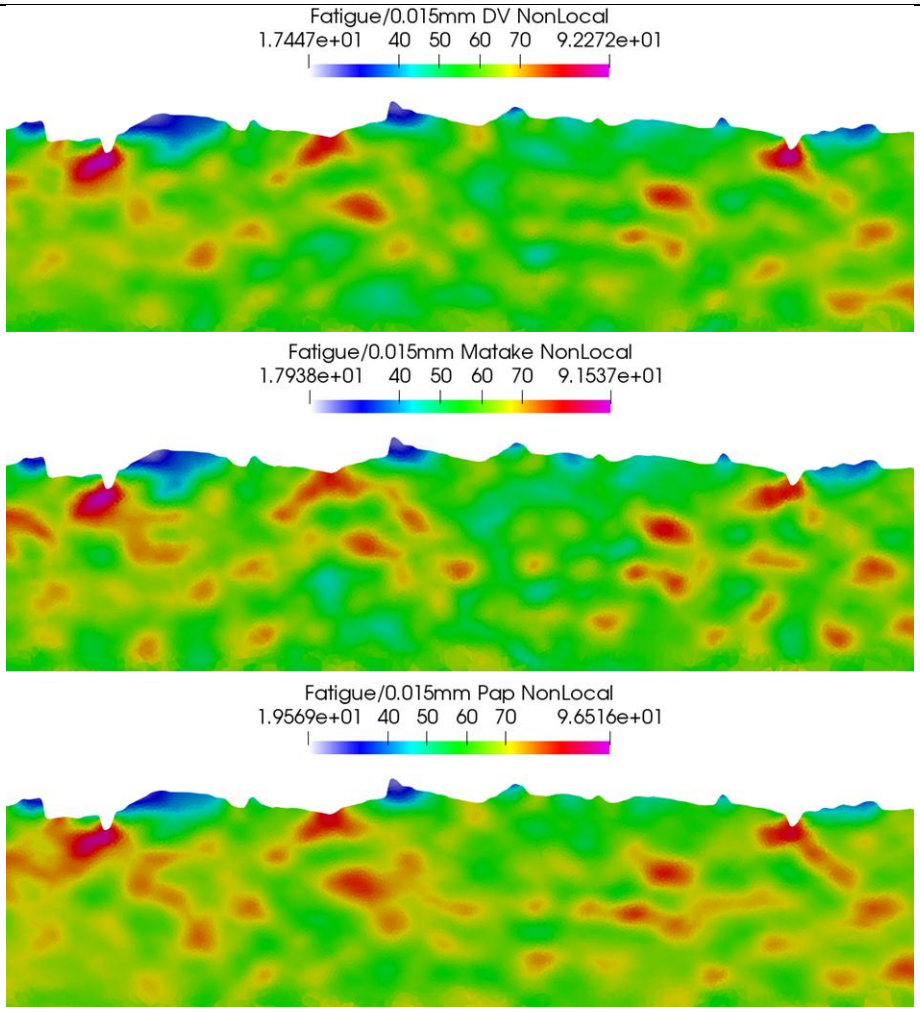

Figure V-25: Distributions of three non-local FIPs (Dang Van, Matake, Papadopoulos) with R*=60 µm in models with roughness under cyclic tension loading

The above analysis shows the details of just one model from the perspectives of non-local methods and fatigue criteria. For the selected profiles, a series of statistical analyses are conducted.

Roughness profile P2 is considered as the most representative one for the reasons explained in section V.1.2. Simulated results from models using this profile are firstly analyzed. The predictions using Dang Van criterion are fitted by the GEV distribution and are plotted in Figure V-26. The solid lines represent predictions of critical radius method while the dashed lines illustrate the yielded values of the neighbor layer method. Histograms of raw data are provided by the semi-transparent contours of the side-by-side bars. Scatters can be seen in every group because of the stochastic microstructure. It is observed that the larger the non-local parameters, the lower the scatter. Considering the predictions, it is difficult to decide which non-local parameters are the most appropriate since no experimental results can be used as reference. We may only offer some conjectures knowing the roughness has a negative influence on fatigue performance. And for the case in which R*=60 µm, the predictions may underestimate the danger of roughness.

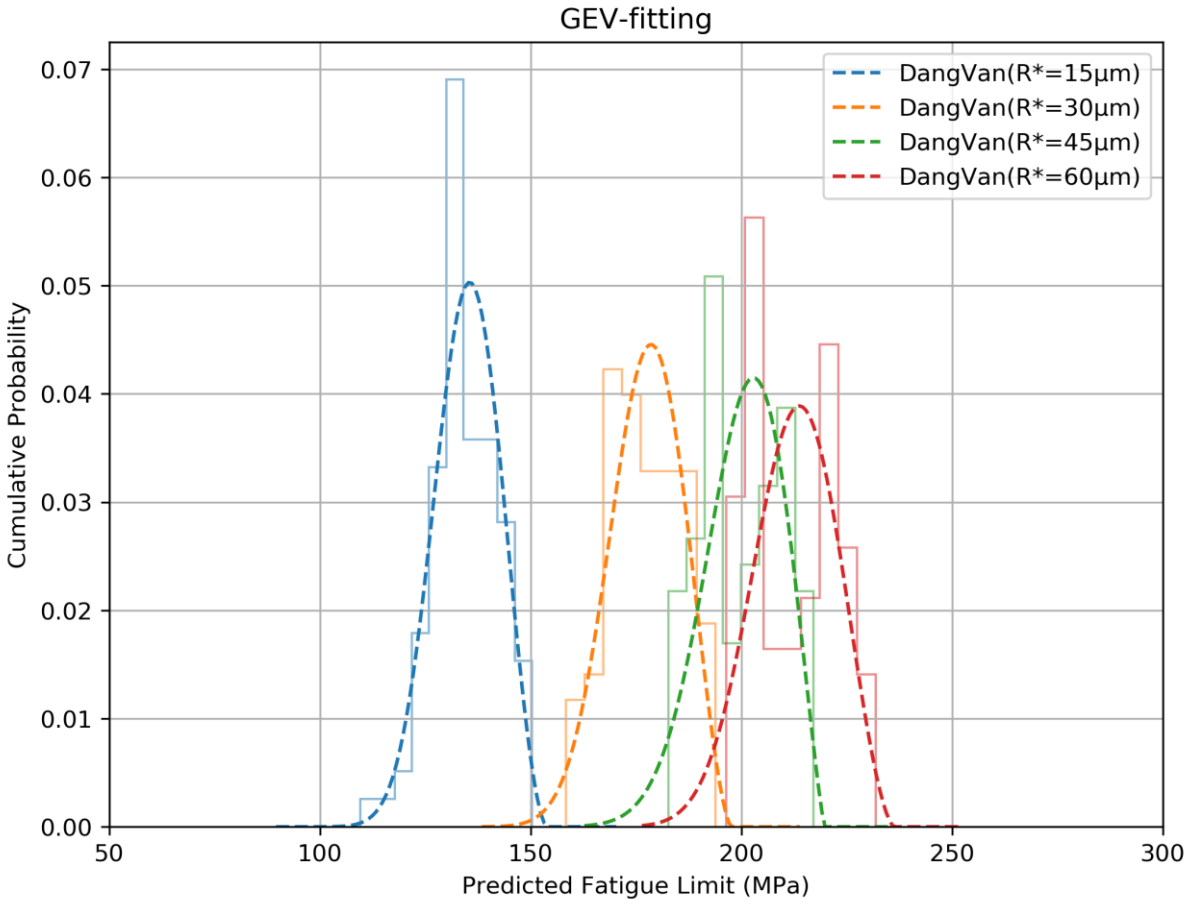

Figure V-26: Histograms and fitted Weibull distribution curves of predicted fatigue limits using different non-local parameter values for stochastic configured polycrystalline models

The predictions from the 5 selected profiles are plotted in a bar chart (see Figure V-27). By comparing the selected profiles, several findings can be obtained. First of all, most of the results from these profiles are quantitatively approximate. Considering the profile P1 which is selected because of its unique position (in the middle) as well as its smoothness, the predictions are always the highest. About the profile P2 who fits the metrics best, the predictions are always intermediate. Profiles P4 and P5 are chosen because their *Ra* are identical. P4 shows a high *Rv* meaning a large maximum valley depth, whilst P5 has a high *Rp* meaning a large maximum peak value. It seems that the concave defect is more harmful than the convex defect since the results from P4 are always lower than the ones from P5. P3 is a profile noticeably rougher than the others. However, the lowest fatigue strengths are not always fromP3. Except for the cases where R*=60 µm, the most conservative predictions are attributed to P4. But comparing the *Rv* of 50 µm from P3 and of 43 µm from P4, it is found that P3 has a higher maximum valley depth.

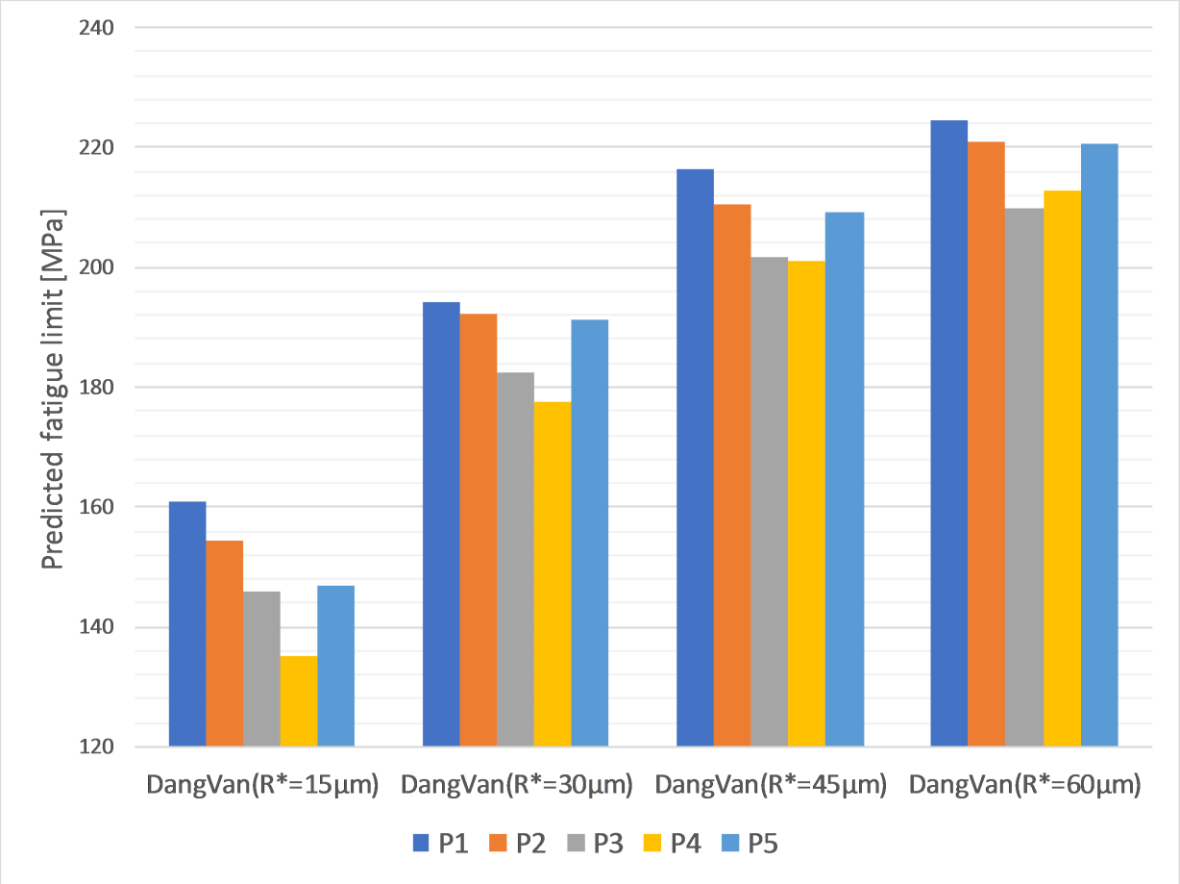

Figure V-27: Medium values of predicted fatigue limits using different non-local FIPs with respect to different roughness profiles

Further comparison between P3 and P4 is conducted. We choose two models with identical microstructure (grain distribution and crystallographic texture) but with different roughness profiles P3 and P4. Since the major differences are observed in the case where R*=15 µm, distributions of the Dang Van stress are illustrated in this case (Figure V-28). The critical element is found to be in the deepest valley for the P3 but not in the deepest valley for the P4. The common feature of these hot spots is that they appear in the concave part of profiles, in particular somewhere in or near a deep groove.

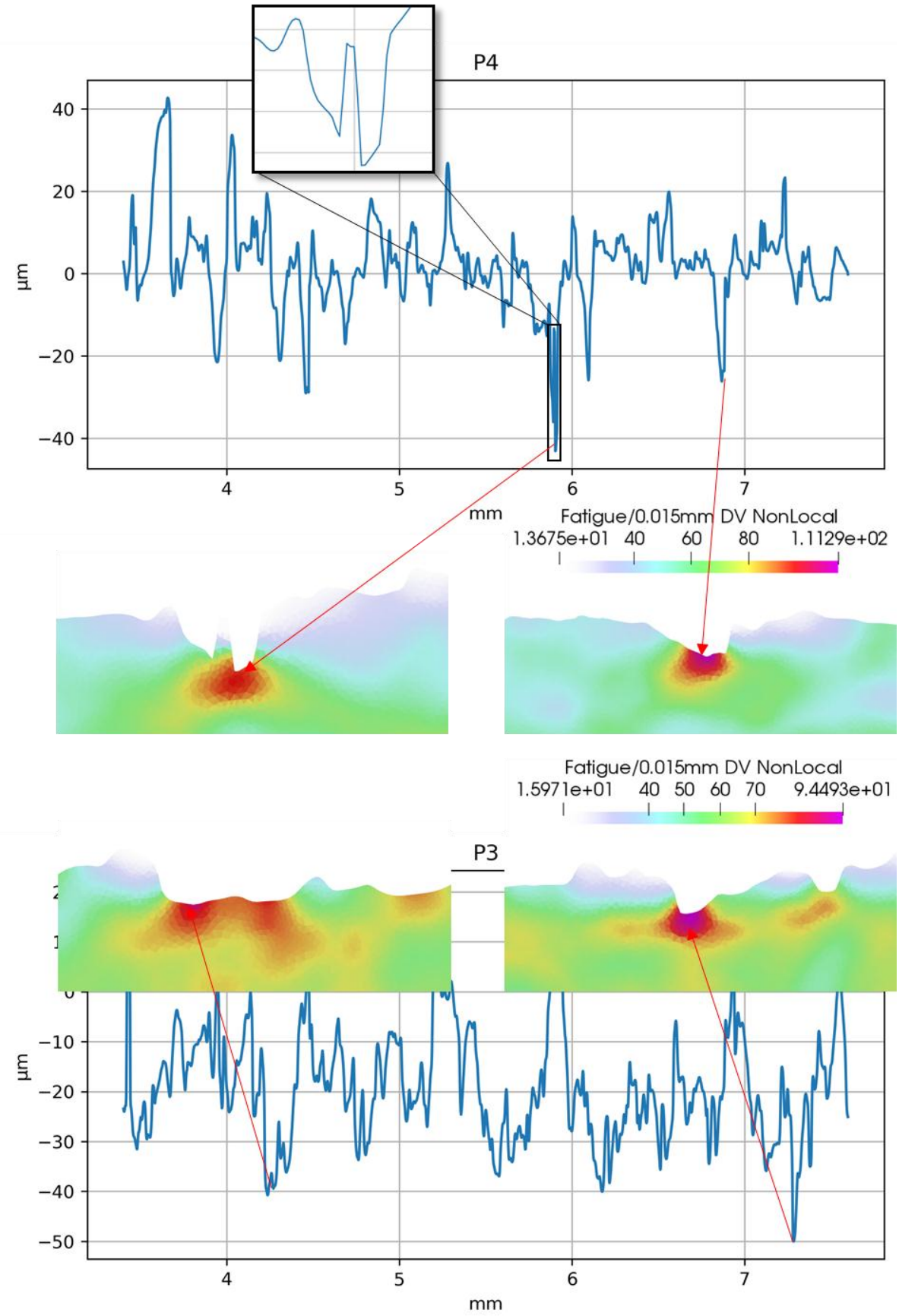

Figure V-28: Distributions of non-local Dang Van stress and roughness profiles for model P3 and model P4

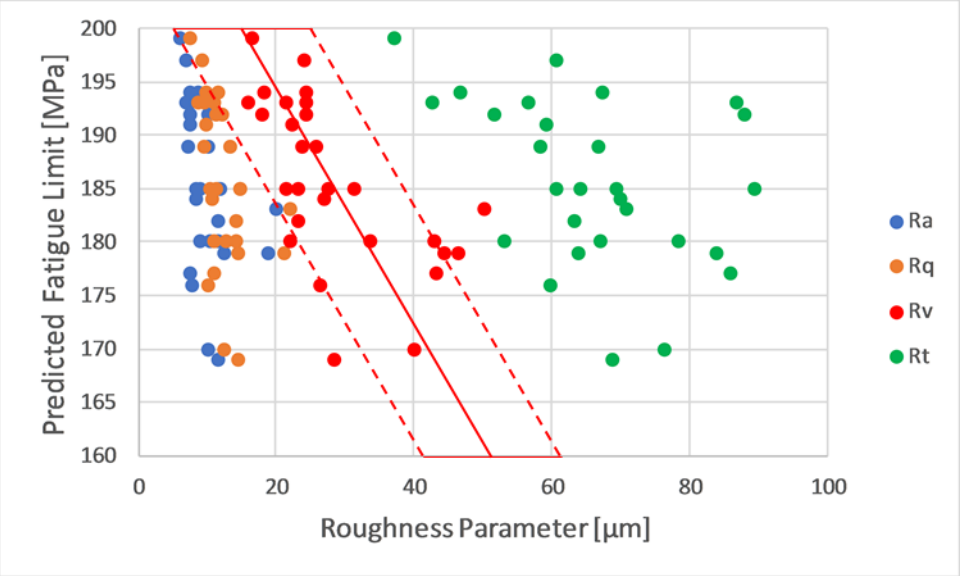

Figure V-29: Predicted fatigue limit of models containing surface roughness versus roughness characteristic parameters

It seems that the predicted fatigue performance cannot be directly linked to the metrics of roughness. To better explore the relationship between the fatigue performance and the surface roughness, results from the 24 randomly chosen profiles are also taken into consideration. In Figure V-29, the predicted fatigue limits versus their corresponding roughness metrics are plotted. Each point refers to the average value of 96 instantiations constituted by 48 crystallographic orientations in 2 differently tessellated polycrystal models using the same roughness profile. The investigated roughness metrics are *Ra*, *Rq*, *Rv* and *Rt*. *Ra* and *Rq* which describe the surface status globally do not present an evident correlation with the fatigue limit predictions. *Rv* which indicates the local extreme situation, as expected, seems to have an evident negative correlation with the predicted fatigue limits. But the limitation of *Rv* has already been pointed out in Figure V-28. Indeed, the critical position has a connection with the grooves in the profile but does not necessarily locate at the lowest point that is represented by *Rv*. Likewise, *Rt* shows a similar tendency with *Rv* while the scatter of results is stronger. Considering that Rt is the sum of *Rv* and *Rp*, it can be implied that *Rt* and *Rv* are closely related. Another conclusion from this figure is that the *Rp* is always higher than *Rv* which is in line with the observation of protruding spherical substances due to the balling effect.

In conclusion, the current investigation reveals that the characteristic parameters of roughness have certain relevance with fatigue performance. But a direct connection between fatigue strength and one or several roughness parameters cannot be found. Proposing a new fatigue-describing roughness characteristic parameter requires more further in-depth study and is out of the scope of the current project. The simulation approach built in this study can nonetheless be a useful tool to carry out such an investigation.

V.4.3. Models containing artificial defect and roughness

According to the experimental findings, the effect of the LoF defect is assumed to be much more detrimental than the effect of roughness since a simple polishing does not improve significantly the fatigue strength. A batch of models containing both artificial defects imitating LoF defect and roughness are built up. Finite element analyses and fatigue post-treatments are performed. Via comparison to the previous findings from models with defects only and models with roughness only, the results are expected to provide some qualitative understandings about the differences introduced by the defect and the roughness.

Figure V-30 shows the distributions of FIP (Dang Van stress) of models with the same microstructure configurations (morphology and orientation of grain). To better present the effect of roughness, R* is set to 30 µm. As explained in the previous section, an intermediate R* value seems to be logical for the current scale of roughness. For the model with roughness only, the groove in the roughness profile yields an extreme response for the prediction. However, in Figure V-30(c), the defect roots generate much higher FIP values. Moreover, the maximum value of FIP in Figure V-30(c) turns out to be even a bit lower than that in Figure V-30(b) which leads to a counterintuitive conclusion that the roughness may result in a positive effect on fatigue strength. Anyway, it is a rare example because of the arrangement of those irregularities in the roughness profile. Generally, the high stressed areas are dominated by the introduced large LoF defects. The irregularities from roughness generate stress concentrations as well as stress relief in certain zones. To better evaluate the effect brought by roughness on the effect of large defects, more simulations are needed.

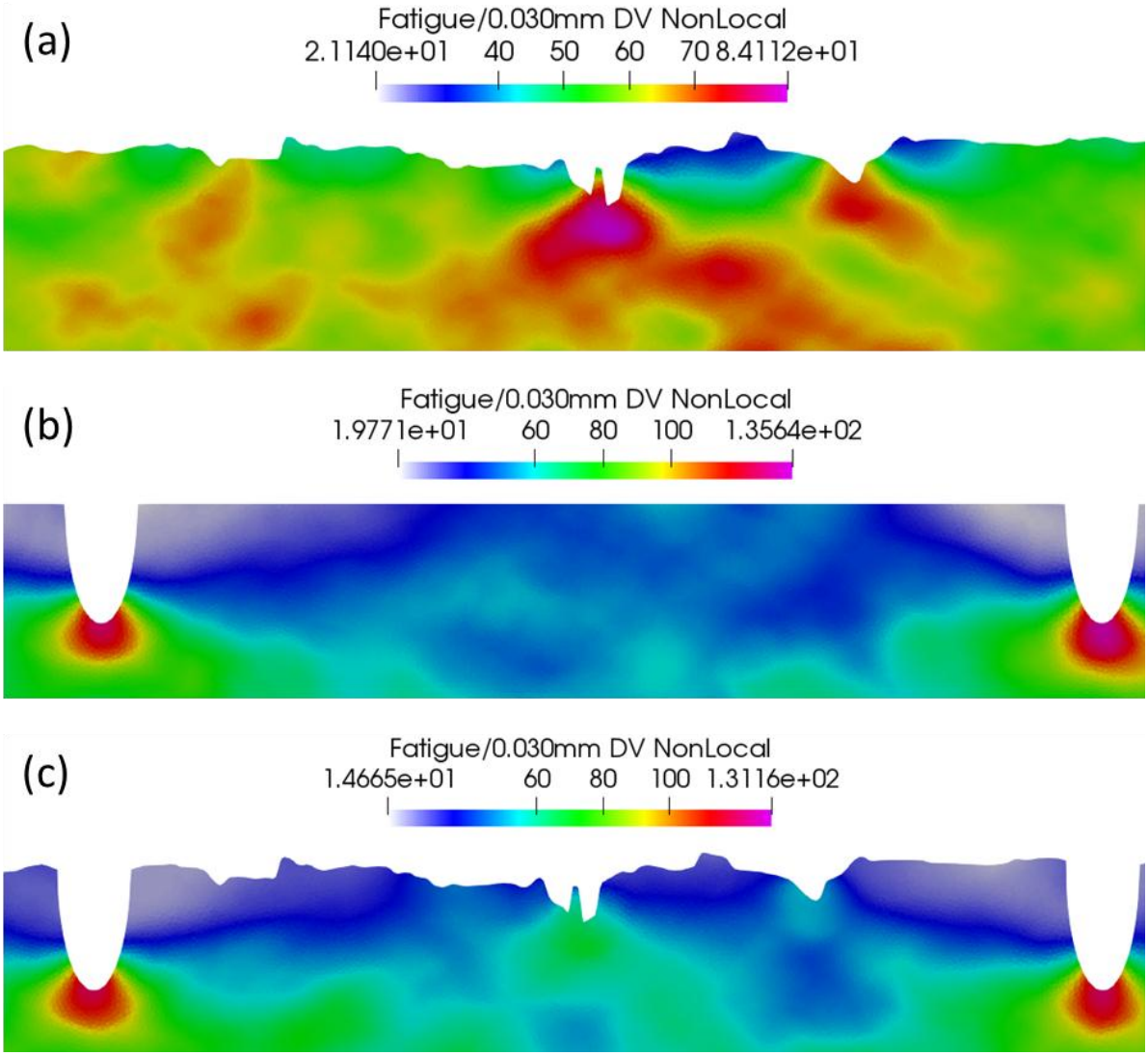

Figure V-30: Distributions of FIP (non-local Dang Van stress with R* = 30 µm) of models with the same microstructure configurations (morphology and orientation of grain) but different defect(s): (a) surface roughness, (b) LoF defects, (c) surface roughness + LoF defects

Simulations with models containing geometrical defects with or without roughness are conducted. The employed loading mode is bending. The textures of the microstructure are of a realistic type. 24 instantiations of crystallographic orientations are used. Dang Van stresses assessed from the critical radius method are categorized by the tessellation type and are shown in Figure V-31. First, none of the tessellations shows an evident difference with the other two. LN_V1 and LN_V2 are two different tessellations in terms of grain positioning. But the results from both models are similar. Even though there are fewer grains used in the Q2 tessellation, it still generates consistent results compared to the Voronoi-polygon tessellated models. Second, the comparisons between models with or without roughness demonstrate that in the tested configurations where the geometrical defect is large and the

roughness is relatively small in scale, the roughness seems to be negligible. Although it cannot yet be proved by the experiments, the tendency is shown by simulations.

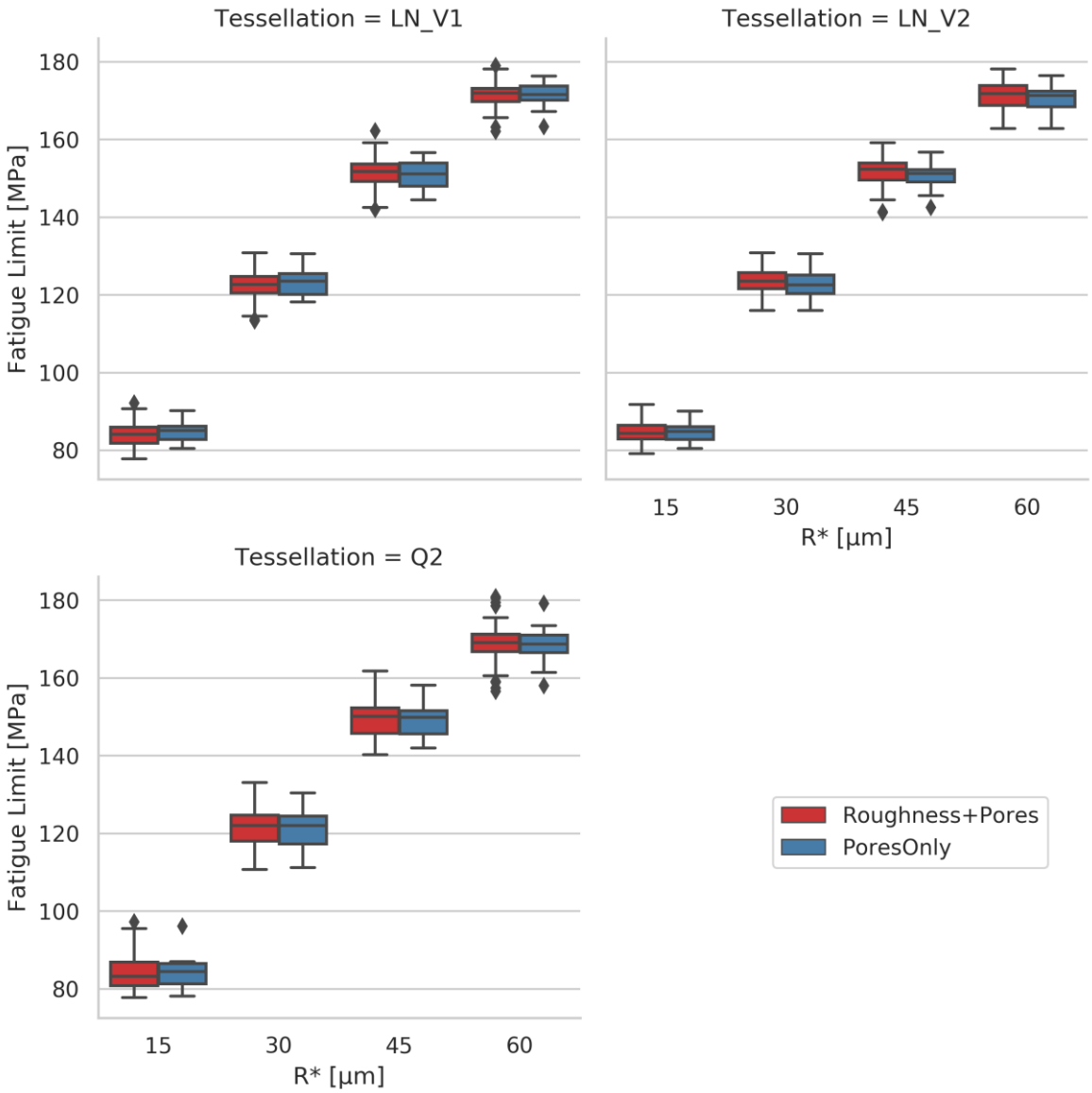

Figure V-31: Predictions of fatigue limit from Dang Van criterion using different values of R* categorized by the tessellation type (2 log-normal distributed Voronoi tessellations:LN_V1, LN_V2 and 1 quadrangle tessellation: Q2)

It may be controversial that the current simulations cannot represent the realistic condition of SLM material because it involves several conjectures about the transition from 3D to 2D, defects' shape and arrangement… Nevertheless, it reveals that the effect on fatigue strength of the combination of several large defects and a series of small defects is mainly controlled by the large defects.

V.5. Role of plasticity in fatigue simulation

V.5.1. Comparisons between elastic and plastic constitutive models in smooth models

For the plasticity-involved models, one major challenge is to decide the loading level as the non-linearity in mechanical response raises issues in predicting the fatigue limit. To solve this problem, the only solution is to conduct iterative simulations. However, for qualitative research in this section that aims at revealing the role of plasticity in fatigue simulation, we will choose certain representative loading levels.

Without loss of generality, the smooth model with isotropic texture is considered as a conventional wrought 316L whose fatigue limit has been determined in Guerchais's research. The tension loading level is thus set to 232 MPa. As a comparison, the smooth model with realistic texture is subjected to the same loading to show the effect of grain orientation.

The first test is realized by using the smooth model with isotropic texture and realistic texture under cyclic tension loading. The geometry of the smooth model is the same as the one used in the previous section. The stabilized cycle is considered achieved in the 5th cycle.

In Figure V-32, the distribution of accumulated plastic strain after the reverse cyclic tension loading with an amplitude of 232 MPa is illustrated. In the elastic model, the plastic strain does not exist. Due to the heterogeneity of microstructure, the accumulated plastic strain is not uniformly distributed in the smooth model but strongly concentrated at the grain boundaries. Compared to a polycrystal aggregate with only elastic constitutive model, the plasticity-involved model does not exhibit a remarkable difference in the distribution of von Mises equivalent stress. As can be seen in Figure V-33, for the majority of elements in the numerical model, the plasticity reduces the equivalent stress by less than 20 MPa. Nevertheless, in certain grain boundaries, the differences can reach 70 MPa.

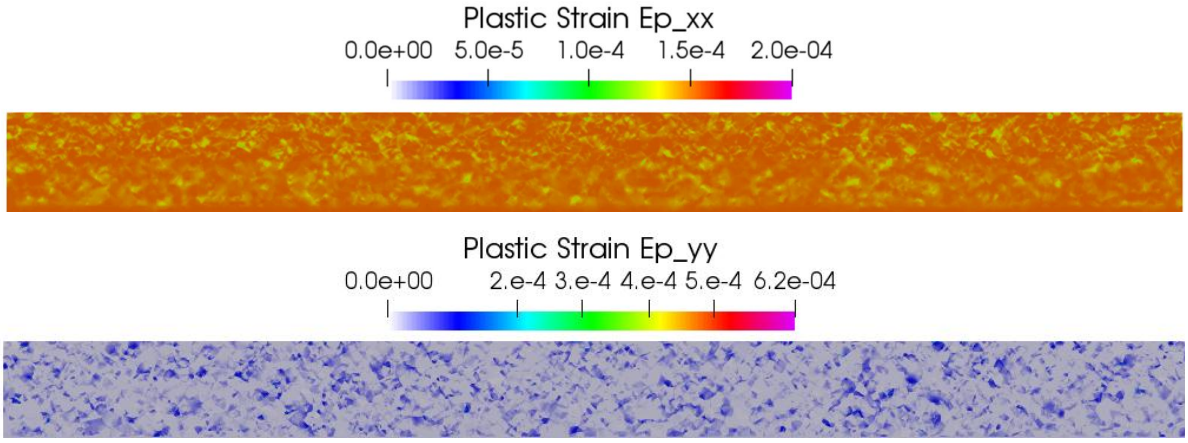

Figure V-32: Distribution of plastic strain in a smooth polycrystal aggregate with isotropic texture after a cyclic tension loading at 232 MPa

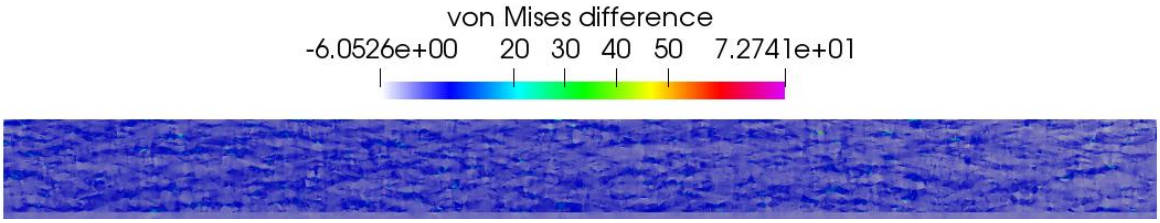

Figure V-33: Distribution of the difference of von Mises stress between elastic constitutive model and plastic constitutive model in a smooth polycrystal aggregate with isotropic texture in the most stressed timestep in the last cycle of a cyclic tension loading at 232 MPa

The distributions of FIPs with the non-local method applied are shown in Figure V-34. The chosen FIP is Dang Van stress with an R* equal to 60 µm which is the same as that used in the previous section. The two constitutive models generate very similar results. Comparing the responses in the same hotspot, the yielded response is 136 MPa in the plastic model while it is 140 MPa in the elastic model. The elastic model does overestimate the stress response, but the difference can be neglected when predicting fatigue failure.

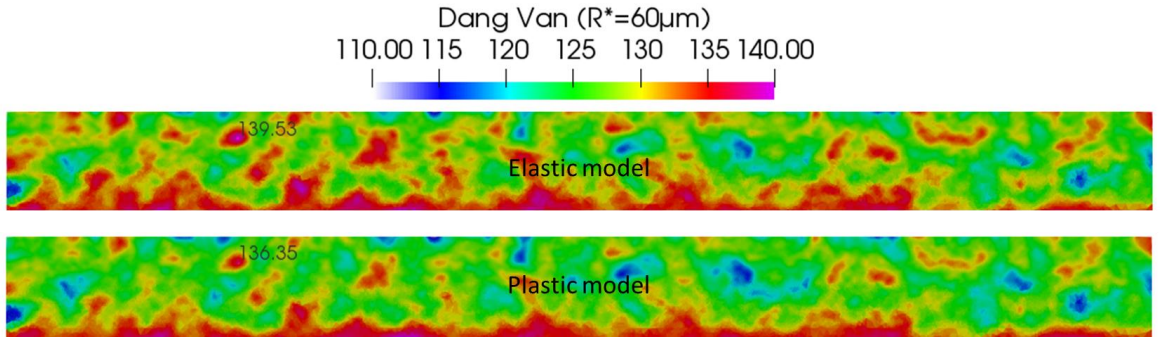

Figure V-34: Distribution of the Dang Van stress (R*=60 µm) in smooth polycrystal aggregates using plastic and elastic constitutive models respectively with isotropic texture after a cyclic tension loading at 232 MPa

Similar analyses are carried out for the realistically textured smooth model which is considered as an imitation of the SLM 316L. Theoretically, the strongly textured microstructure in SLM 316L should result in a more stressed state. As can be seen from Figure V-35, with the added plasticity, the responses from the plastic model are lower than that from the elastic model. Due to the preferential grain orientation, the plastic deformation is more pronounced compared to that in the same model but with isotropic texture. A decrease of 4.3% in the extreme value of non-local Dang Van stress is seen, 157 MPa in the elastic model whilst it is 150 MPa in the plastic model. It should be noted that the applied loading is 232 MPa which is the fatigue limit for conventional 316L with isotropic texture. And the extreme values in both configurations exceed the threshold which indicates that the current loading is over the critical fatigue limit. It can be assumed that the real fatigue limit should be lower than 232 MPa.

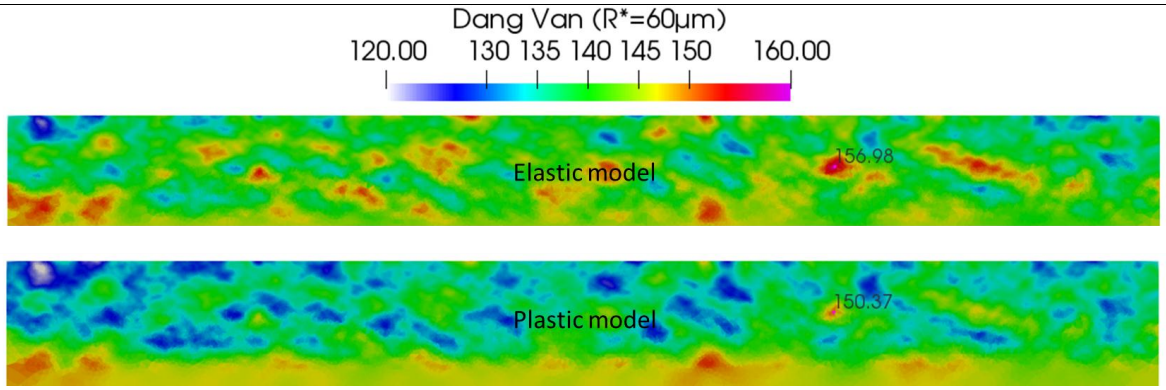

Figure V-35: Distribution of the Dang Van stress (R*=60 μm) in smooth polycrystal aggregates using plastic and elastic constitutive models respectively with realistic texture after a cyclic tension loading at 232 MPa

The absence of plasticity in the previous batches of simulations of smooth models does not evidently change the fidelity of results. However, with the presence of defects, the stress concentration occurs in the defective models. The role of plasticity is thus evaluated for defective models in the following section.

V.5.2. Comparisons between elastic and plastic predictions in defective models

In the previous simulations, three types of models were used: model with roughness, model with artificial defect and model with combined roughness and artificial defect. The geometries are kept as well as the grain orientation sets. That is to say, the only change made in this batch of simulation is to change the constitutive model which allows us to check the differences brought by plasticity. Three loading levels representing the fatigue limits of as-built, simple-polished and total-polished bending samples are tested: 90, 120 and 150 MPa.

For the most critical configuration in which both roughness and defects appear, the distribution of non-local Dang Van stress is plotted in Figure V-36. With a R* value set to 60 μm, no evident difference can be found between the plastic and elastic model. The heterogeneity in microstructure does not lead to perceptible plastic deformation. In terms of the contour plot, compared to Figure V-35, the two models yield even more similar distributions.

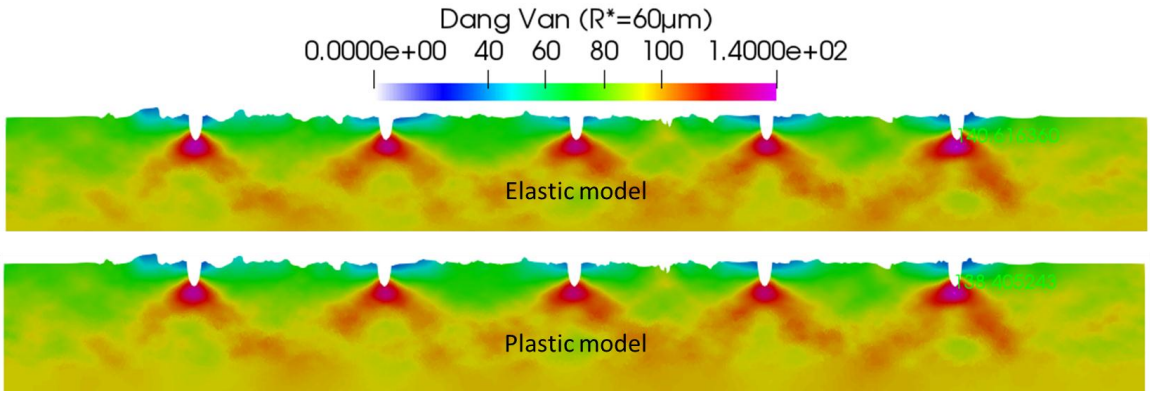

Figure V-36: Distribution of the Dang Van stress (R*=60 µm) in defective polycrystal aggregates using plastic and elastic constitutive models respectively with realistic texture after a cyclic tension loading at 150 MPa

A comprehensive comparison is performed for all the defective models. In the three configurations, the relative responses of fatigue prediction in the plastic model compared to the one in the elastic model under a cyclic tension loading at 150 MPa are listed in Table V-13. It should be noted that certain data are not available since the convergence is not reached in those configurations.

Roughness which can be considered as a series of small defects has the smallest difference after adding plasticity in simulation. Nevertheless, even if the large geometrical defects are combined with the surface roughness, the generated results do not significantly change. Different R* are compared. Generally, as the R* increases, the difference between the plastic model and elastic model decreases. Overall, the effect of plasticity is negligible if the considered effective area is relatively large.

Table V-13: Predictions from a crystal plasticity model and a purely elastic model under a cyclic tension loading at 150 MPa

		R* (µm)			
		15	30	45	60
Roughness	Dang Van	-	98.8%	99.5%	99.5%
	Matake	83.7%	98.0%	99.3%	99.3%
	Papadopoulos	87.0%	98.9%	99.5%	99.6%
Defect	Dang Van	-	95.3%	97.8%	98.5%
	Matake	-	95.1%	97.1%	98.3%
	Papadopoulos	-	95.6%	97.8%	98.4%
Roughness + Defect	Dang Van	-	94.7%	97.0%	98.4%
	Matake	88.7%	94.5%	96.8%	98.3%
	Papadopoulos	90.6%	95.1%	97.7%	98.9%

For the lower loading levels, similar comparisons are also carried out. The results are listed in Table V-14 and Table V-15. As could be expected, with a lower loading level, the difference introduced by the plasticity is reduced.

Table V-14: Predictions from a crystal plasticity model and a purely elastic model under a cyclic tension loading at 90 MPa

		R* (μm)			
		15	30	45	60
Roughness	Dang Van	95.5%	99.4%	99.8%	100.1%
	Matake	94.8%	99.4%	99.7%	99.9%
	Papadopoulos	96.0%	99.4%	99.8%	99.9%
Defect	Dang Van	-	99.9%	100.0%	99.9%
	Matake	99.5%	99.8%	100.0%	99.9%
	Papadopoulos	99.8%	100.0%	100.0%	100.0%
Roughness + Defect	Dang Van	97.4%	99.1%	99.6%	99.6%
	Matake	97.5%	99.1%	99.5%	99.8%
	Papadopoulos	97.8%	99.2%	99.7%	99.9%

Table V-15: Predictions from a crystal plasticity model and a purely elastic model under a cyclic tension loading at 120 MPa

		R* (μm)			
		15	30	45	60
Roughness	Dang Van	92.4%	97.6%	99.1%	99.4%
	Matake	89.7%	97.7%	98.8%	99.4%
	Papadopoulos	91.9%	98.1%	99.2%	99.5%
Defect	Dang Van	98.1%	99.5%	99.9%	99.9%
	Matake	98.3%	99.3%	99.7%	99.8%
	Papadopoulos	98.8%	99.7%	99.9%	99.9%
Roughness + Defect	Dang Van	-	97.4%	98.6%	99.5%
	Matake	93.7%	97.4%	98.6%	99.4%
	Papadopoulos	94.6%	97.6%	99.1%	99.7%

V.5.3. Summary

The introduction of plasticity to the current simulation framework does not bring significant differences in the yielded fatigue predictions. All comparisons are performed between models with the same configuration except the constitutive models. In the smooth models, the plastic zone originates at the grain boundaries because of the heterogeneous microstructural texture. The isotropically textured smooth model exhibits local plastic deformations in certain places at its macroscopic fatigue limit. And it is more noticeable in the model with realistic texture. But in terms of fatigue prediction, the difference between models with or without plasticity is insignificant. In the defective models, the defect brings strong stress concentration at its root which causes plastic deformation. Due to lower macroscopic loading levels compared to the one for smooth models, the plastic deformation from microstructure heterogeneity is not noticeable. The accumulated plastic deformation at the grain boundaries is thus less in these configurations. Overall, the role of plasticity in the defective model is also negligible.

Without using the plastic constitutive model, the prediction of fatigue failure can still be achieved by using the cubic elastic constitutive model. On one hand, the scatter of local mechanical responses in polycrystal aggregate is mainly due to the anisotropy of microstructure which in this study is brought by the explicit grain and texture. The adoption of plasticity provides a more accurate description of the stress state in certain highly stressed places. But in the context of high cycle fatigue, the macroscopic loading is in the elastic domain. So, the existence of plastic deformation is limited. On the other hand, with a relatively large R* applied, the stress distribution in the effective area is not notably changed as the plastic deformation only occurs in local area near the grain boundary.

V.6. Conclusions

With the previous investigations about microstructure and defects, we have been able to propose an explicit microstructure sensitive finite element modeling approach. Crystallographic orientations measured from EBSD scans are processed to create a realistic texture. As for the grain morphology, the non-constant grain size as well as the non-equiaxed shape put forward certain challenges for the parametric modeling. Thus, different tessellation methods are used. Roughness profiles extracted from the surface scan are added to the numerical models. Commonly used industrial roughness metrics are calculated for the selected profiles for further correlation with fatigue performance. Numerical 3D reconstruction of the as-built sample using the μ-CT data demonstrates that the internal porosity can be neglected, whereas the LoF defects on the surface are undetectable via tomography. An alternative for the representation of the LoF defect is then proposed.

As presented in the experimental part, the free surface effect is investigated by polishing the surface at different levels. However, this surface modification cannot decouple the effects of roughness and porosity. Four batches of models are designed to represent the specimens in different references. For the models with geometrical defects, the results are compared to experimental data. The geometrical defects are a simplification of realistic LoF defects. Models with roughness are fictitious since the experiments revealed that LoF defects dominate the fatigue crack initiations and exist with roughness simultaneously. However, this batch of models can deliver the sole effect of roughness. By combining the surface roughness and geometrical defects, a batch of models is created. The effect of crystallographic texture on the fatigue behavior of SLM SS 316L is assumed to reduce the endurance limit by 10% regardless of the non-local model parameter values. Results concerning the effect of grain morphology are dependent on the configuration of non-local methods. However, this effect is found to be minor compared to other effects as texture or defects.

Several preliminary tests have been performed to check the effect of plasticity in the current simulation framework. Results show that the effect of plasticity is negligible in the conditions where a

certain large effective zone is considered. Hence, for the studied material, disregarding plasticity reduces the computational expense without losing the fidelity of outputs.

Syntheses

- Textured crystallographic orientations and non-constant grain sizes are used in the modeling process to characterize the microstructure of AM material.

- The effect of preferential grain orientation on the fatigue behavior of SLM SS 316L is found to reduce the endurance limit by 10% regardless of the value of non-local parameters.

- LoF defects that often cluster beneath the free surface and have elongated shape are considered to be the most detrimental factor in HCF failure. LoF defects are dominant over texture, roughness and grain size and morphology.

- Different roughness parameters are compared to correlate the fatigue performance and the roughness metrics. *Rv* which reflects the deepest valley in the roughness profile shows certain relevance with the predicted fatigue limit.

- The roughness of SLM material is small in dimension compared to the LoF defect. So is its effect on fatigue strength.

- In the current simulation framework for fatigue prediction of 316L, the plasticity is found to have a negligible effect.

Conclusions and prospects

- Conclusions

Main points of this work are listed as follows:

1. The review of the existed literature confirms that the surface finish has a strong influence on high cycle fatigue behavior of SLM SS 316L because of the frequent presence of surface and subsurface defects inherited from the fabrication process which dominates the crack initiation stage. The microstructure attributes have certain influences that change fatigue behavior either. As can be seen that the noticeable variance in the results of the reported fatigue tests, the specimens have different microstructural characteristics because the researchers use different types of machines and different fabrication parameters.
2. Unlike most literature, industry-used recycled powder rather than new powder is used to fabricate the utilized specimens. The recycled powder has more small particles and a certain portion of satellite-shaped particles. Plus, contouring is intentionally omitted to produce rougher surfaces. But the monotonic test confirms the fabricated specimen has comparable mechanical properties with conventionally fabricated specimens. The measured surface roughness and porosity rate are consistent with the reference in the literature. Microscope observations demonstrate the preferential grain orientation of the building direction and elongated quadrangle-shaped grain morphology as well as the existence of many fine grains in the boundary.
3. Fatigue tests with regard to the surface state, the loading type and the building direction are conducted. By removing the surface roughness, fatigue strength has been improved. An additional polishing process further increases the endurance limit. The bending loading and the tension loading yield similar high cycle fatigue behavior while the torsion fatigue limit is found to be higher than the tension fatigue limit and the bending fatigue limit.
4. Fractographic analyses reveal that the LoF defects provoke fatigue failure in most of the cases. Hence, the LoF defects are considered as the most detrimental factor in the durability of fabricated parts. The explanation of the benefit of the additional polishing process is that the exclusion of contouring brings out many LoF defects beneath the surface. For the torsion fatigue tests, observations on the fracture surfaces disclose the mechanism of crack initiation and propagation under fatigue torsion loading. The shear stress activates the crack initiation and the principle stress governs the crack propagation.
5. Critical defects are measured for all the bending specimens. Using Murakami's theory about the fatigue behavior defective material and Kitagawa-Takahashi diagram, it is found that the clustering defects should be treated as one large defect. Using the proposed measurement of

defects, the correlation between the defect size and the fatigue limit is in line with the trend of a typical K-T diagram.

6. The microstructure sensitive modeling framework is adopted in the numerical part of the current study. A parametric explicit virtual microstructure finite element model for 316L is built up based on the experimental data in the literature. Two non-local method realizations, namely the critical radius method and the neighbor layer method, are introduced to the simulations and are investigated. Different stress-based fatigue criteria are implemented. The proposed simulation framework can reflect the microstructural features, for instance, the grain morphology, the crystallographic orientation, the slip systems in the crystal, etc. The K-T effect has been successfully reproduced using the proposed simulation framework.
7. By processing the data from the material characterization experiments, the microstructural attributes and surface state of SLM SS 316L are quantitatively evaluated. The statistical method, particularly the general extreme value distribution theory, is introduced to deal with the complex predictability of fatigue strength as many stochastic factors are involved in the model.
8. Numerical study reveals that the roughness and surface defects strongly affect the estimated fatigue limit. However, with the presence of large surface defects, the sole effect of roughness is much less pronounced as the large defects dominate the fatigue behavior. The effect of textured microstructure has a perceptible influence on fatigue strength. The vertically built parts are more vulnerate in its building direction under fatigue loading compared to non-textured parts. Competition between defect(roughness) and microstructure is observed. The microstructure can change the position of the hot spot when the defect is small in dimension, which is the case of a model containing roughness. Even if large defects are presented, the different grain morphology and orientation will slightly change the estimated fatigue limit, which is the reason for scattered fatigue test results observed in experiments.

- Prospects

In the future, there are also several studies that can be proposed to continue along with the current one:

1. The specimens used in the fatigue tests are all vertically fabricated. More tests using horizontally built or diagonally built specimens could offer more insights into the mechanism of fatigue behavior.
2. We used only recycled powder during fabrication. The effect of recycled powder was presumed to be insignificant. Regrettably, with the results from the current study, we cannot offer a direct answer to this issue. But, the negligible effect on several characteristic mechanical properties, for instance, hardness, yield strength, etc., is confirmed in this study. A comparative study with virgin powder should be conducted to reveal the effect of recycling on fatigue behavior which helps the sustainability of the industrial application of SLM.
3. The current simulations only compare two loading modes: reversed tension loading and bending loading. Torsion loading has not been tested in this simulation framework. As the shear stress is considered as the main driven force for crack initiation, the macroscopic pure shear state from torsion loading is the best candidate to explore the role of shear stress. Upgrade of the locally developed software dodoFEM is in progress to support more configurations of polycrystal simulation.
4. More configuration of microstructures and defects can be tested to better demonstrate the interaction and competition. The defects observed in the tomography analysis have distinguished geometries. Using numerical method to reconstruct the realistic defects can provide further understanding of crack initiating from inherent defects. Besides, the spatial distribution of defects can be manipulated in the simulation.
5. The proposed simulation method is supposed to be compatible with other AM materials. But further efforts will be needed to complement the framework. On one hand, more experiments should be conducted to identify and calibrate the parameters of the numerical model of other materials. On the other hand, in terms of materials having different qualities, for instance, Ti-alloy, it is expected that the fatigue sensitivity to defect is different from the current studied 316L as well as its multi-phased microstructure.
6. The current simulations are realized by 2D models due to the limitation of computational resources. If 3D numerical models can be used, the results will be much more quantitatively convincing. Specifically, the observed inherent defects of AM materials have complex geometries. If the defects can be faithfully rebuilt in the 3D models, more insights about the effect of defects on fatigue behavior can be obtained.

References

Abroug, F. *et al.* (2018) 'HCF of AA7050 alloy containing surface defects: Study of the statistical size effect', *International Journal of Fatigue*. Elsevier, 110, pp. 81–94. doi: 10.1016/j.ijfatigue.2018.01.012.

Afkhami, S. *et al.* (2019) 'Fatigue characteristics of steels manufactured by selective laser melting', *International Journal of Fatigue*. Elsevier, 122, pp. 72–83. doi: 10.1016/j.ijfatigue.2018.12.029.

Agarwala, M. *et al.* (1995) 'Direct selective laser sintering of metals', *Rapid Prototyping Journal*. Emerald Group Publishing Ltd., 1(1), pp. 26–36. doi: 10.1108/13552549510078113.

Ahmadi, A. *et al.* (2016) 'Effect of manufacturing parameters on mechanical properties of 316L stainless steel parts fabricated by selective laser melting: A computational framework', *Materials & Design*, 112, pp. 328–338. doi: 10.1016/j.matdes.2016.09.043.

Almufleh, B. *et al.* (2018) 'Patient satisfaction with laser-sintered removable partial dentures: A crossover pilot clinical trial', *Journal of Prosthetic Dentistry*. Editorial Council for the Journal of Prosthetic Dentistry, 119(4), pp. 560-567.e1. doi: 10.1016/j.prosdent.2017.04.021.

Andreau, O., Pessard, E., *et al.* (2019) 'A competition between the contour and hatching zones on the high cycle fatigue behaviour of a 316L stainless steel: Analyzed using X-ray computed tomography', *Materials Science and Engineering A*. Elsevier, 757, pp. 146–159. doi: 10.1016/j.msea.2019.04.101.

Andreau, O., Koutiri, I., *et al.* (2019) 'Texture control of 316L parts by modulation of the melt pool morphology in selective laser melting', *Journal of Materials Processing Technology*. Elsevier, 264(October), pp. 21–31. doi: 10.1016/j.jmatprotec.2018.08.049.

Asgari, H. *et al.* (2017) 'On microstructure and mechanical properties of additively manufactured AlSi10Mg_200C using recycled powder', *Materials Science and Engineering: A*. Elsevier, 707, pp. 148–158. doi: 10.1016/J.MSEA.2017.09.041.

ASTM International (2018) *ASTM A240 / A240M - 18 Standard Specification for Chromium and Chromium-Nickel Stainless Steel Plate, Sheet, and Strip for Pressure Vessels and for General Applications, West Conshohocken, PA*. doi: 10.1520/A0240_A0240M-18.

Bahl, S. *et al.* (2019) 'Non-equilibrium microstructure, crystallographic texture and morphological texture synergistically result in unusual mechanical properties of 3D printed 316L stainless steel', *Additive Manufacturing*. Elsevier B.V., 28, pp. 65–77. doi: 10.1016/j.addma.2019.04.016.

Barralis, J. and Maeder, G. (2005) *Précis de métallurgie Élaboration, structures-propriétés, normalisation*. AFNOR-NATHAN.

Baudoin, P. *et al.* (2016) 'Numerical investigation of fatigue strength of grain size gradient materials under heterogeneous stress states in a notched specimen', *International Journal of Fatigue*. Elsevier, 87, pp. 132–142. doi: 10.1016/j.ijfatigue.2016.01.022.

Bellett, D. *et al.* (2005) 'The fatigue behaviour of three-dimensional stress concentrations', *International Journal of Fatigue*. Elsevier, 27(3), pp. 207–221. doi: 10.1016/j.ijfatigue.2004.07.006.

Billaudeau, T., Nadot, Y. and Bezine, G. (2004) 'Multiaxial fatigue limit for defective materials: Mechanisms and experiments', *Acta Materialia*. Pergamon, 52(13), pp. 3911–3920. doi: 10.1016/j.actamat.2004.05.006.

Blinn, B. *et al.* (2019) 'Investigation of the anisotropic fatigue behavior of additively manufactured structures made of AISI 316L with short-time procedures PhyBaL LIT and PhyBaL CHT', *International Journal of Fatigue*. Elsevier, 124, pp. 389–399. doi: 10.1016/j.ijfatigue.2019.03.022.

Bracquart, B. *et al.* (2018) 'Experimental study of the impact of geometrical defects on the high cycle fatigue behavior of polycrystalline aluminium with different grain sizes', *International Journal of Fatigue*. Elsevier, 109, pp. 17–25. doi: 10.1016/j.ijfatigue.2017.12.009.

Briffod, F., Shiraiwa, T. and Enoki, M. (2017) 'Microstructure modeling and crystal plasticity simulations for the evaluation of fatigue crack initiation in α-iron specimen including an elliptic defect', *Materials Science and Engineering A*. Elsevier, 695, pp. 165–177. doi: 10.1016/j.msea.2017.04.030.

Bryson, W. E. (2005) 'Heat Treatment, Selection, and Application of Tool Steels', in *Heat Treatment, Selection, and Application of Tool Steels*. München: Carl Hanser Verlag GmbH & Co. KG, pp. I–XV. doi: 10.3139/9783446436701.fm.

Chen, Z. *et al.* (2018) 'Surface roughness of Selective Laser Melted Ti-6Al-4V alloy components', *Additive Manufacturing*. Elsevier, 21, pp. 91–103. doi: 10.1016/J.ADDMA.2018.02.009.

Cherry, J. A. *et al.* (2014) 'Investigation into the effect of process parameters on microstructural and physical properties of 316L stainless steel parts by selective laser melting', *International Journal of Advanced Manufacturing Technology*, 76(5–8), pp. 869–879. doi: 10.1007/s00170-014-6297-2.

Choo, H. *et al.* (2019) 'Effect of laser power on defect, texture, and microstructure of a laser powder bed fusion processed 316L stainless steel', *Materials and Design*. Elsevier Ltd, 164, p. 107534. doi: 10.1016/j.matdes.2018.12.006.

Davies, C. M. (2017) 'Fatigue crack initiation and growth behavior of 316L stainless steel manufactured through selective laser melting', in *Proceedings of the ASME 2017 Pressure Vessels and Piping Conference*. Hawaii,USA, pp. 1–7.

Deb, K. *et al.* (2002) 'A fast and elitist multiobjective genetic algorithm: NSGA-II', *IEEE Transactions on Evolutionary Computation*, 6(2), pp. 182–197. doi: 10.1109/4235.996017.

DebRoy, T. *et al.* (2018) 'Additive manufacturing of metallic components – Process, structure and properties', *Progress in Materials Science*. Elsevier Ltd, pp. 112–224. doi: 10.1016/j.pmatsci.2017.10.001.

Dewidar, M. M., Khalil, K. A. and Lim, J. K. (2007) 'Processing and mechanical properties of porous 316L stainless steel for biomedical applications', *Transactions of Nonferrous Metals Society of China (English Edition)*. Elsevier, 17(3), pp. 468–473. doi: 10.1016/S1003-6326(07)60117-4.

Dixon, W. J. and Mood, A. M. (1948) 'A Method for Obtaining and Analyzing Sensitivity Data', *Journal of the American Statistical Association*, 43(241), pp. 109–126. doi: 10.1080/01621459.1948.10483254.

Elangeswaran, C. *et al.* (2019) 'Effect of post-treatments on the fatigue behaviour of 316L stainless steel manufactured by laser powder bed fusion', *International Journal of Fatigue*. Elsevier, 123, pp. 31–39. doi: 10.1016/j.ijfatigue.2019.01.013.

Fisher, R. A. and Tippett, L. H. C. (1928) 'Limiting forms of the frequency distribution of the largest or smallest member of a sample', *Mathematical Proceedings of the Cambridge Philosophical Society*. Cambridge University Press, 24(2), pp. 180–190. doi: 10.1017/S0305004100015681.

Freudenthal, A. M. and Gumbel, E. J. (1954) 'Minimum Life in Fatigue', *Journal of the American Statistical Association*, 49(267), pp. 575–597. doi: 10.1080/01621459.1954.10483522.

Gao, Y. *et al.* (2007) 'High-cycle fatigue of nickel-base superalloy René 104 (ME3): Interaction of microstructurally small cracks with grain boundaries of known character', *Acta Materialia*. Pergamon, 55(9), pp. 3155–3167. doi: 10.1016/j.actamat.2007.01.033.

Gerber, H. (1874) *Bestimmung der zulässigen spannungen in eisen-constructionen*. Wolf.

Geuzaine, C. and Remacle, J. F. (2009) 'Gmsh: A 3-D finite element mesh generator with built-in pre- and post-processing facilities', *International Journal for Numerical Methods in Engineering*, 79(11), pp. 1309–1331. doi: 10.1002/nme.2579.

Goodman, J. (1899) *Mechanics applied to engineering*. London: Longmans Green.

Gorji, N. E. *et al.* (2019) 'Recyclability of stainless steel (316 L) powder within the additive manufacturing process', *Materialia*. Elsevier, 8, p. 100489. doi: 10.1016/J.MTLA.2019.100489.

Guerchais, R. (2014) *Influence d'accidents geometriques et du mode de chargement sur le comportement en fatigue a grand nombre de cycles d'un acier inoxydable austenitique 316L*. Ecole nationale supérieure d'arts et métiers - ENSAM.

Guerchais, R. *et al.* (2014) 'Micromechanical investigation of the influence of defects in high cycle fatigue', *International Journal of Fatigue*. (Multiaxial Fatigue 2013), 67, pp. 159–172. doi: 10.1016/j.ijfatigue.2014.01.005.

Guerchais, R. *et al.* (2015) 'Influence of the microstructure and voids on the high-cycle fatigue strength of 316L stainless steel under multiaxial loading', *Fatigue and Fracture of Engineering Materials and Structures*, 38(9), pp. 1087–1104. doi: 10.1111/ffe.12304.

Guerchais, R., Morel, F. and Saintier, N. (2017) 'Effect of defect size and shape on the high-cycle fatigue behavior', *International Journal of Fatigue*. (Multiaxial Fatigue 2016: Experiments and Modeling), 100(Part 2), pp. 530–539. doi: 10.1016/j.ijfatigue.2016.12.010.

Guilhem, Y. *et al.* (2010) 'Investigation of the effect of grain clusters on fatigue crack initiation in polycrystals', *International Journal of Fatigue*, 32(11), pp. 1748–1763. doi: 10.1016/j.ijfatigue.2010.04.003.

Guilhem, Y. (2011) *Etude numérique des champs mécaniques locaux dans les agrégats polycristallins d'acier 316L sous chargement de fatigue*. Ecole Nationale Superieure des Mines de Paris-Paris.

El Haddad, M. H., Smith, K. N. and Topper, T. H. (1979) 'Fatigue Crack Propagation of Short Cracks', *Journal of Engineering Materials and Technology*, 101(1), p. 42. doi: 10.1115/1.3443647.

Herzog, D. *et al.* (2016) 'Additive manufacturing of metals', *Acta Materialia*. Pergamon, 117, pp. 371–392. doi: 10.1016/J.ACTAMAT.2016.07.019.

Hor, A. *et al.* (2014) 'Statistical assessment of multiaxial HCF criteria at the grain scale', *International Journal of Fatigue*. (Multiaxial Fatigue 2013), 67, pp. 151–158. doi: 10.1016/j.ijfatigue.2014.01.024.

HOURIA, I. (2015) *Etude expérimentale et modélisation de la durée de vie en fatigue d ' un alliage d ' aluminium de fonderie A356-T6 sous chargement multiaxial*. ISAE-ENSMA Ecole Nationale Supérieure de Mécanique et d'Aérotechique - Poitiers.

Huntington, H. B. (1958) 'The Elastic Constants of Crystals', *Solid State Physics - Advances in Research and Applications*. Academic Press, 7(C), pp. 213–351. doi: 10.1016/S0081-1947(08)60553-6.

Jenkinson, A. F. (1955) 'The frequency distribution of the annual maximum (or minimum) values of meteorological elements', *Quarterly Journal of the Royal Meteorological Society*. John Wiley & Sons, Ltd, 81(348), pp. 158–171. doi: 10.1002/qj.49708134804.

Jiang, R. *et al.* (2018) 'Strain accumulation and fatigue crack initiation at pores and carbides in a SX superalloy at room temperature', *International Journal of Fatigue*. Elsevier, 114, pp. 22–33. doi: 10.1016/j.ijfatigue.2018.05.003.

El Khoukhi, D. *et al.* (2019) 'Experimental investigation of the size effect in High Cycle Fatigue: role of the defect population in cast aluminium alloys', *International Journal of Fatigue*. Elsevier, 129,

p. 105222. doi: 10.1016/J.IJFATIGUE.2019.105222.

Kitagawa, H. and Takahashi, S. (1976) 'Applicability of Fracture Mechanics to Very Small Cracks or the Cracks in the Early Stage', *Proc. 2nd Int. Conf. Mech. Behav. Mater.*, pp. 627–639.

Konečná, R. *et al.* (2016) 'Long fatigue crack growth in Inconel 718 produced by selective laser melting', *International Journal of Fatigue*. Elsevier, 92, pp. 499–506. doi: 10.1016/j.ijfatigue.2016.03.012.

Kruth, J. *et al.* (2005) 'Binding mechanisms in selective laser sintering and selective laser melting', *Rapid Prototyping Journal*. Emerald Group Publishing Limited, 11(1), pp. 26–36. doi: 10.1108/13552540510573365.

Kruth, J. P. *et al.* (2005) 'Benchmarking of different SLS/SLM processes as Rapid Manufacturing techniques', in *International Conference Polymers & Moulds Innovations (PMI)*, p. 525.

Kruth, J. P. *et al.* (2010) 'Part and material properties in selective laser melting of metals', *16th International Symposium on Electromachining, ISEM 2010*, pp. 3–14.

Krzyżak, D., Robak, G. and Łagoda, T. (2017) 'Non-local line method for notched elements with use of effective length calculated in an elasto-plastic condition', *Fatigue and Fracture of Engineering Materials and Structures*. Wiley/Blackwell (10.1111), 40(1), pp. 89–102. doi: 10.1111/ffe.12478.

Kuznetsov, P. A. *et al.* (2016) 'Structure and mechanical properties of austenitic 316L steel produced by selective laser melting', *Russian Metallurgy (Metally)*. Maik Nauka-Interperiodica Publishing, 2016(10), pp. 930–934. doi: 10.1134/S0036029516100104.

Lackey, A. D. (2016) *Comparative Study of Mechanical Properties of 316L Stainless Steel Between Traditional Production Methods and Selective Laser Melting*. Western Carolina University.

Le, V. D. *et al.* (2018) 'Investigation of the effect of porosity on the high cycle fatigue behaviour of cast Al-Si alloy by X-ray micro-tomography', *International Journal of Fatigue*. Elsevier, 106, pp. 24–37. doi: 10.1016/j.ijfatigue.2017.09.012.

Le, V. D. *et al.* (2019) 'Interpretation of the fatigue anisotropy of additively manufactured TA6V alloys via a fracture mechanics approach', *Engineering Fracture Mechanics*. Elsevier, 214(March), pp. 410–426. doi: 10.1016/j.engfracmech.2019.03.048.

Leuders, S. *et al.* (2014) 'On the fatigue properties of metals manufactured by selective laser melting – The role of ductility', *Journal of Materials Research*, 29(17), pp. 1911–1919. doi: 10.1557/jmr.2014.157.

Li, Z. *et al.* (2019) 'Tensile properties, strain rate sensitivity, and activation volume of additively manufactured 316L stainless steels', *International Journal of Plasticity*. Elsevier Ltd, 120, pp. 395–410. doi: 10.1016/j.ijplas.2019.05.009.

Liu, X., Chu, P. K. and Ding, C. (2004) 'Surface modification of titanium, titanium alloys, and related materials for biomedical applications', *Materials Science and Engineering: R: Reports*. Elsevier, 47(3–4), pp. 49–121. doi: 10.1016/J.MSER.2004.11.001.

Liverani, E. *et al.* (2017) 'Effect of selective laser melting (SLM) process parameters on microstructure and mechanical properties of 316L austenitic stainless steel', *Journal of Materials Processing Technology*. Elsevier, 249, pp. 255–263. doi: 10.1016/j.jmatprotec.2017.05.042.

Lou, X. *et al.* (2017) 'On the stress corrosion crack growth behaviour in high temperature water of 316L stainless steel made by laser powder bed fusion additive manufacturing', *Corrosion Science*. Pergamon, 128, pp. 140–153. doi: 10.1016/j.corsci.2017.09.017.

Lukáš, P. and Kunz, L. (1994) 'Comparison of fatigue behaviour of single crystals and polycrystals', *Materials Science and Engineering A*, 189(1–2), pp. 1–7. doi: 10.1016/0921-5093(94)90395-6.

Masounave, J. and Baflon, J. P. (1976) 'Effect of grain size on the threshold stress intensity factor in fatigue of a ferritic steel', *Scripta Metallurgica*, 10(2), pp. 165–170. doi: 10.1016/0036-9748(76)90142-3.

El May, M. *et al.* (2015) 'Non-local high cycle fatigue strength criterion for metallic materials with corrosion defects', *Fatigue and Fracture of Engineering Materials and Structures*. John Wiley & Sons, Ltd (10.1111), 38(9), pp. 1017–1025. doi: 10.1111/ffe.12329.

McDowell, D. L. (2007) 'Simulation-based strategies for microstructure-sensitive fatigue modeling', *Materials Science and Engineering A*. (The McEvily Symposium: Fatigue and Fracture of Traditional and Advanced Materials, TMS 2006), 468–470(SPEC. ISS.), pp. 4–14. doi: 10.1016/j.msea.2006.08.129.

McDowell, D. L. and Dunne, F. P. E. (2010) 'Microstructure-sensitive computational modeling of fatigue crack formation', *International Journal of Fatigue*. (Emerging Frontiers in Fatigue), 32(9), pp. 1521–1542. doi: 10.1016/j.ijfatigue.2010.01.003.

Meiners, W., Wissenbach, K. and Gasser, A. (1996) 'Shaped Body Especially Prototype or Replacement Part Production'.

Mergulhão, M. V. and Das Neves, M. D. M. (2018) 'Characteristics of Biometallic Alloy to Additive Manufacturing Using Selective Laser Melting Technology', *Journal of Biomaterials and Nanobiotechnology*. Scientific Research Publishing, Inc, 09(01), pp. 89–99. doi: 10.4236/jbnb.2018.91008.

Méric, L., Cailletaud, G. and Gaspérini, M. (1994) 'F.E. calculations of copper bicrystal specimens submitted to tension-compression tests', *Acta Metallurgica Et Materialia*, 42(3), pp. 921–935. doi: 10.1016/0956-7151(94)90287-9.

Mower, T. M. and Long, M. J. (2016) 'Mechanical behavior of additive manufactured, powder-bed laser-fused materials', *Materials Science and Engineering: A*, 651, pp. 198–213. doi: 10.1016/j.msea.2015.10.068.

Mu, P. *et al.* (2013) 'Influence of the crystalline orientations on microcrack initiation in low-cycle fatigue', *Materials Science and Engineering A*. Elsevier, 573, pp. 45–53. doi: 10.1016/j.msea.2013.02.046.

Müller, C. *et al.* (2017) 'Accuracy of fatigue limits estimated by the staircase method using different evaluation techniques', *International Journal of Fatigue*. Elsevier, 100, pp. 296–307. doi: 10.1016/j.ijfatigue.2017.03.030.

Murakami, Y. (2002) *Metal Fatigue:Effects of Small Defects and Nonmetallic Inclusions*. Oxford: Elsevier Science Ltd.

Nadot, Y. *et al.* (1999) 'Fatigue life assessment of nodular cast iron containing casting defects', *Fatigue and Fracture of Engineering Materials and Structures*. John Wiley & Sons, Ltd (10.1111), 22(4), pp. 289–300. doi: 10.1046/j.1460-2695.1999.00162.x.

O'Leary, R. *et al.* (2015) 'An Investigation into the Recycling of Ti-6Al-4V Powder Used Within SLM to Improve Sustainability', *SDM'2015: 2nd International Conference on Sustainable Design and Manufacturing , (2015)*, pp. 14–17.

Patterson, A. E., Messimer, S. L. and Farrington, P. A. (2017) 'Overhanging Features and the SLM/DMLS Residual Stresses Problem: Review and Future Research Need', *Technologies*. Multidisciplinary Digital Publishing Institute, 5(2), p. 15. doi: 10.3390/technologies5020015.

PILLOT, S. (2016) *Fusion laser sélective de lit de poudres métalliques, Ref : BM7900 v1*. Editions T.I. | Techniques de l'Ingénieur.

Puchi-Cabrera, E. S. *et al.* (2004) 'On the fatigue behavior of an AISI 316L stainless steel coated with a PVD TiN deposit', *Surface and Coatings Technology*. Elsevier, 182(2–3), pp. 276–286. doi: 10.1016/j.surfcoat.2003.07.003.

Pyttel, B., Schwerdt, D. and Berger, C. (2011) 'Very high cycle fatigue - Is there a fatigue limit?', *International Journal of Fatigue*. Elsevier, 33(1), pp. 49–58. doi: 10.1016/j.ijfatigue.2010.05.009.

Quey, R., Dawson, P. R. and Barbe, F. (2011) 'Large-scale 3D random polycrystals for the finite element method: Generation, meshing and remeshing', *Computer Methods in Applied Mechanics and Engineering*. North-Holland, 200(17–20), pp. 1729–1745. doi: 10.1016/j.cma.2011.01.002.

Qylafku, G. *et al.* (1999) 'Application of a new model proposal for fatigue life prediction on notches and key-seats', *International Journal of Fatigue*. Elsevier, 21(8), pp. 753–760. doi: 10.1016/S0142-1123(99)00046-8.

Riemer, A. *et al.* (2014) 'On the fatigue crack growth behavior in 316L stainless steel manufactured by selective laser melting', *Engineering Fracture Mechanics*. Pergamon, 120, pp. 15–25. doi: 10.1016/j.engfracmech.2014.03.008.

Robert, C. *et al.* (2012) 'Micro-mechanical modelling of high cycle fatigue behaviour of metals under multiaxial loads', *Mechanics of Materials*. Elsevier Ltd, 55, pp. 112–129. doi: 10.1016/j.mechmat.2012.08.006.

Robert, C. and Mareau, C. (2015) 'A comparison between different numerical methods for the modeling of polycrystalline materials with an elastic-viscoplastic behavior', *Computational Materials Science*. Elsevier, 103, pp. 134–144. doi: 10.1016/j.commatsci.2015.03.028.

Roland, T. *et al.* (2006) 'Fatigue life improvement through surface nanostructuring of stainless steel by means of surface mechanical attrition treatment', *Scripta Materialia*. Pergamon, 54(11), pp. 1949–1954. doi: 10.1016/J.SCRIPTAMAT.2006.01.049.

Romano, S., Miccoli, S. and Beretta, S. (2019) 'A new FE post-processor for probabilistic fatigue assessment in the presence of defects and its application to AM parts', *International Journal of Fatigue*. Elsevier, 125, pp. 324–341. doi: 10.1016/j.ijfatigue.2019.04.008.

Salman, O. O. *et al.* (2019) 'Effect of heat treatment on microstructure and mechanical properties of 316L steel synthesized by selective laser melting', *Materials Science and Engineering A*. Elsevier Ltd, 748, pp. 205–212. doi: 10.1016/j.msea.2019.01.110.

Sauzay, M. (2007) 'Cubic elasticity and stress distribution at the free surface of polycrystals', *Acta Materialia*. Pergamon, 55(4), pp. 1193–1202. doi: 10.1016/J.ACTAMAT.2006.09.035.

Schütz, W. (1996) 'A history of fatigue', *Engineering Fracture Mechanics*. Pergamon, 54(2), pp. 263–300. doi: 10.1016/0013-7944(95)00178-6.

Schwartz, J., Fandeur, O. and Rey, C. (2013) 'Numerical approach of cyclic behaviour of 316LN stainless steel based on a polycrystal modelling including strain gradients', *International Journal of Fatigue*, 55, pp. 202–212. doi: 10.1016/j.ijfatigue.2013.07.003.

Shellabear, M. and Nyrhilä, O. (2004) 'DMLS – Development History and State of the Art', in *Lane 2004*. Bamberg, Germany: Meisenbach (LASER ASSISTED NET SHAPE ENGINEERING -CD-ROM EDITION-), pp. 1–12.

Shrestha, R., Simsiriwong, J. and Shamsaei, N. (2019) 'Fatigue behavior of additive manufactured 316L stainless steel parts: Effects of layer orientation and surface roughness', *Additive Manufacturing*. Elsevier, 28, pp. 23–38. doi: 10.1016/j.addma.2019.04.011.

Solberg, K. *et al.* (2019) 'Fatigue of additively manufactured 316L stainless steel: The influence of porosity and surface roughness', *Fatigue & Fracture of Engineering Materials & Structures*, 42(9), pp.

2043–2052. doi: 10.1111/ffe.13077.

Spierings, A. B., Herres, N. and Levy, G. (2011) 'Influence of the particle size distribution on surface quality and mechanical properties in AM steel parts', *Rapid Prototyping Journal*, 17(3), pp. 195–202. doi: 10.1108/13552541111124770.

Spierings, A. B., Starr, T. L. and Wegener, K. (2013) 'Fatigue performance of additive manufactured metallic parts', *Rapid Prototyping Journal*, 19(2), pp. 88–94. doi: 10.1108/13552541311302932.

Strondl, A. *et al.* (2015) 'Characterization and Control of Powder Properties for Additive Manufacturing', *JOM*. Minerals, Metals and Materials Society, 67(3), pp. 549–554. doi: 10.1007/s11837-015-1304-0.

Sun, S. H. *et al.* (2019) 'Excellent mechanical and corrosion properties of austenitic stainless steel with a unique crystallographic lamellar microstructure via selective laser melting', *Scripta Materialia*. Acta Materialia Inc, 159, pp. 89–93. doi: 10.1016/j.scriptamat.2018.09.017.

Suryawanshi, J., Prashanth, K. G. and Ramamurty, U. (2017) 'Mechanical behavior of selective laser melted 316L stainless steel', *Materials Science and Engineering A*. Elsevier, 696, pp. 113–121. doi: 10.1016/j.msea.2017.04.058.

Taylor, D. (1999) 'Geometrical effects in fatigue: a unifying theoretical model', *International Journal of Fatigue*. Elsevier, 21(5), pp. 413–420. doi: 10.1016/S0142-1123(99)00007-9.

Tekçe, N. *et al.* (2018) 'The effect of glazing and aging on the surface properties of CAD/CAM resin blocks', *Journal of Advanced Prosthodontics*. Korean Academy of Prosthodontic, 10(1), pp. 50–57. doi: 10.4047/jap.2018.10.1.50.

Teklu, A. *et al.* (2004) 'Single-crystal elastic constants of Fe-15Ni-15Cr alloy', *Metallurgical and Materials Transactions A: Physical Metallurgy and Materials Science*. Springer-Verlag, 35 A(10), pp. 3149–3154. doi: 10.1007/s11661-004-0059-y.

Thompson, A. W. and Backofen, W. A. (1971) 'The effect of grain size on fatigue', *Acta Metallurgica*. Pergamon, 19(7), pp. 597–606. doi: 10.1016/0001-6160(71)90012-5.

Tolosa, I. *et al.* (2010) 'Study of mechanical properties of AISI 316 stainless steel processed by "selective laser melting", following different manufacturing strategies', *International Journal of Advanced Manufacturing Technology*, 51(5–8), pp. 639–647. doi: 10.1007/s00170-010-2631-5.

Toth, L. S. *et al.* (2013) 'Notes on representing grain size distributions obtained by electron backscatter diffraction', *Materials Characterization*. Elsevier Inc., 84, pp. 67–71. doi: 10.1016/j.matchar.2013.07.013.

Tucho, W. M. *et al.* (2018) 'Investigation of effects of process parameters on microstructure and hardness of SLM manufactured SS316L', *Journal of Alloys and Compounds*. Elsevier Ltd, 740, pp. 910–

925. doi: 10.1016/j.jallcom.2018.01.098.

Uhlmann, E. *et al.* (2017) 'Dynamical Fatigue Behavior of Additive Manufactured Products for a Fundamental Life cycle Approach', *Procedia CIRP*. The Author(s), 61, pp. 588–593. doi: 10.1016/j.procir.2016.11.138.

Vayssette, B. *et al.* (2019) 'Numerical modelling of surface roughness effect on the fatigue behavior of Ti-6Al-4V obtained by additive manufacturing', *International Journal of Fatigue*. Elsevier, 123, pp. 180–195. doi: 10.1016/j.ijfatigue.2019.02.014.

Vincent, M. *et al.* (2016) 'Interaction between a surface defect and grain size under high cycle fatigue loading: Experimental approach for Armco iron', *International Journal of Fatigue*. Elsevier, 87, pp. 81–90. doi: 10.1016/j.ijfatigue.2016.01.013.

Walker, K. (1970) 'The Effect of Stress Ratio During Crack Propagation and Fatigue for 2024-T3 and 7075-T6 Aluminum', in *Effects of Environment and Complex Load History on Fatigue Life*, pp. 1-1–14. doi: 10.1520/stp32032s.

Wentzel, H. and Huang, X. (2015) 'Experimental characterization of the bending fatigue strength of threaded fasteners', *International Journal of Fatigue*. Elsevier, 72, pp. 102–108. doi: 10.1016/j.ijfatigue.2014.11.005.

Yadollahi, A. and Shamsaei, N. (2017) 'Additive manufacturing of fatigue resistant materials: Challenges and opportunities', *International Journal of Fatigue*. Elsevier, 98, pp. 14–31. doi: 10.1016/j.ijfatigue.2017.01.001.

Yang, T. *et al.* (2019) 'The influence of process parameters on vertical surface roughness of the AlSi10Mg parts fabricated by selective laser melting', *Journal of Materials Processing Technology*. Elsevier, 266, pp. 26–36. doi: 10.1016/J.JMATPROTEC.2018.10.015.

Yao, W., Xia, K. and Gu, Y. (1995) 'On the fatigue notch factor, Kf', *International Journal of Fatigue*, 17(4), pp. 245–251. doi: 10.1016/0142-1123(95)93538-D.

Yap, C. Y. *et al.* (2015) 'Review of selective laser melting: Materials and applications', *Applied Physics Reviews*, 2(4). doi: 10.1063/1.4935926.

Zhang, M. *et al.* (2017) 'Fatigue and fracture behaviour of laser powder bed fusion stainless steel 316L: Influence of processing parameters', *Materials Science and Engineering A*. Elsevier, 703, pp. 251–261. doi: 10.1016/j.msea.2017.07.071.

Zhang, M. *et al.* (2019) 'High cycle fatigue and ratcheting interaction of laser powder bed fusion stainless steel 316L: Fracture behaviour and stress-based modelling', *International Journal of Fatigue*. Elsevier, 121, pp. 252–264. doi: 10.1016/j.ijfatigue.2018.12.016.

Zhong, Y. *et al.* (2016) 'Intragranular cellular segregation network structure strengthening 316L

stainless steel prepared by selective laser melting', *Journal of Nuclear Materials*. Elsevier, 470, pp. 170–178. doi: 10.1016/j.jnucmat.2015.12.034.

Appendix A. Experimental data of vertically fabricated SLM 316L high cycle fatigue tests

A.1. Staircase method

Fatigue limit identification is laborious since the results are often highly dispersed. To have a statistical valid value as the fatigue limit, the tests are carried out using the staircase method (Dixon and Mood, 1948). This method is relatively simple in the choice of load levels and achievable with a small number of tests; however, the accuracy remains dependent on the sample number. Following this method, first the maximum number of N cycles should be chosen. Then, an increment of the stress level which should be close to the value of the assumed standard deviation is determined. The tests of the specimens are carried out as follows.

The loading level for the first test is chosen close to the assumed fatigue limit. If the test piece breaks, the second test piece will be tested at the next lower level; otherwise - the level of charge must be increased compared to the initial one. Thus, each level of charge is chosen according to the rule:

$$\sigma_{i+1} = \sigma_i \pm d \qquad (A.1)$$

This process is then continued until all available test pieces are exhausted.

The type of event that occurs least frequently - break or no break - is determined first. This eliminates a sequence of results, all of the same type, due to a choice of the first level of tests too far from the desired value. Let Ni - the number of least frequent events chosen for each level of tests. where i denotes the test level number, the value i = 0 is assigned to the lowest of those at which the event was observed at least once.

The median estimate σ_D is given by:

$$\begin{gathered} \sigma_D = S_0 + d\left(\frac{A}{N} \pm \frac{1}{2}\right) \\ N = \sum n_i \\ A = \sum i * n_i \end{gathered} \qquad (A.2)$$

+ if the calculation is based on the test requirements of unbroken test pieces;

- if the calculation is based on the test constraints of the broken test pieces.

The staircase method also provides an estimate of the standard deviation s of the stress response curve:

$$s = 1.62d\left(\frac{NB - A^2}{N^2} + 0.029\right) \qquad (A.3)$$
$$B = \sum i^2 * n_i$$

where S_0 is the lowest level used with the least frequent event, d denotes the stress level increment.

Figure 2 explains how to calculate these values from the test data in a case where the retained results relate to breaks. According to the authors (Dixon and Mood, 1948), the latter formula can only be used if:

$$\frac{NB - A^2}{N^2} > 0.3 \qquad (A.5)$$

Further discussion on the staircase method can be referred by the study of Muller et al.(Müller *et al.*, 2017).

A.2. Tensile fatigue tests

The staircase method for the as-built and the simple-polished specimens (the ones from the tray 1 are in blue and italic, the ones from the tray 2 are in red with an underline) is shown in Table A-1.

Table A-1: Staircase method for as-built and simple-polished tensile specimens

Surface state	Stress amplitude [MPa]	Test number									
		1	2	3	4	5	6	7	8	9	10
As-built	100	~~*X50*~~		*X33*		*X20*				*X46*	
	90		*O41*		*O24*		*X22*		*O37*		
	80							*O9*			
Simple-polished	130	~~*X12*~~									
	120		~~*X25*~~		*X39*		*X35*		*X19*		*X15*
	110			*O48*		*O36*		*O3*		*O27*	

In the table, Oxx stands for run-out, while Xxx stands for failure. xx represents the specimen labeling number. When using staircase method to estimate the fatigue strength, the first valid datum should come from run-out test. The first test of as-built samples and the first two tests of simple-polished samples failed before reaching $2*10^6$ cycles. Hence, they are not considered during the calculation. Strikethrough line is used to denote that case. In both of the cases, the run-outs are the least frequent events; the calculations for the parameters are shown in Table A-2.

Table A-2: Parameters identification of staircase method for as-built and simple-polished tensile specimens

Surface state	i	fi	i*fi	i²*fi
As-built	1	3	3	3
	0	1	0	0
	Σ	N=4	A=3	B=3
Simple-polished	0	4	0	0
	Σ	N=4	A=0	B=0

Finally, the endurance limit for the as-built samples is:

$$\sigma_D = \sigma_0 + d * \left(\frac{A}{N} + \frac{1}{2}\right) = 92.5\ MPa \qquad (A.6)$$

In this case, the formula for the standard deviation is not valid, since the condition explained in (Eq. A.5) is not satisfied.

$$\frac{B * N - A^2}{N^2} = 0.1875 < 0.3 \qquad (A.7)$$

Following the same process, the endurance limit for the polished samples is 115 MPa. Also, in this case, the formula for the standard deviation is not valid, since the condition explained in (Eq. A.5) is not satisfied.

As expected, the fatigue limit for the polished specimens was greater than the one for the as-built specimens, in particular with a 24% raise. As already explained, the intact specimens were tested at higher stress values, as can be seen in Table A-3.

Table A-3: Summary of all the tensile fatigue tests conducted

Surface state	Sample number	Stress amplitude [MPa]	Rupture cycles
As-built	*26*	120	711318
	50	100	1090413
	41	90	-
	33	100	1399298
	24	90	-
	20	100	1222525
	22	90	1588420
	9	80	-
	9	150	389131
	37	90	-
	37	130	563075
	46	100	1420531
	17	110	969382
	29	160	281144
Simple-polished	*12*	130	866574
	25	120	1353541
	48	110	-
	48	150	725523
	39	120	950773
	36	110	-
	36	140	1062775
	35	120	1162360
	3	110	-
	19	120	1434796
	27	110	-
	15	120	1278695
	8	170	447987
	10	180	329954
	31	200	250285

A.3. Torsional fatigue tests

The staircase method for the for as-built, simple-polished, and total polished torsional specimens (the ones from the tray 1 are in blue and italic, the ones from the tray 2 are in red with an underline) is shown in Table A-4.

Table A-4: Staircase method for as-built, simple-polished, and total polished torsional specimens

Surface state	Stress amplitude [MPa]	Test Number												
		1	2	3	4	5	6	7	8	9	10	11	12	13
As-built	140										X13		X7	
	130	~~X11~~		X24				X15		O25		O6		X23
	120		O20		X4		O27		O8					
	110					O5								
Simple polished	150	~~X16~~				X5		X6		X25				
	140		~~X22~~		O18		O27		O10		O2			
	130			O30										
Total polished	180			X29				X10		X28				
	170		O14		X1		O2		O18		O30			
	160	O3				O21								

For the as-built specimens, the run-outs are the least frequent events; for the simple-polished ones, the run-outs and the failures are equally frequent; for the total polished ones, the failures are the less frequent events; the calculations for the parameters are shown in Table A-5.

Table A-5: Parameters identification of staircase method for as-built, simple-polished, and total polished torsional specimens

Surface state	i	f_i	$i*f_i$	i^2*f_i
As-built	2	2	4	8
	1	3	3	3
	0	1	0	0
	Σ	N=6	A=7	B=11
Simple-polished	1	4	4	4
	0	1	0	0
	Σ	N=5	A=4	B=4
Total polished	1	3	3	3
	0	1	0	0
	Σ	N=4	A=3	B=3

The endurance limit for the as-built specimens is calculated. The fatigue limit under torsional loading is 127 MPa with a standard deviation of 8 MPa. Likewise, the endurance limits for the simple-polished specimens and the total-polished specimens are 143 MPa and 172MPa, respectively. However, standard deviations cannot be estimated due to the limited tests.

All torsional fatigue tests including further LCF tests of the intact specimens from HCF tests are presented in Table A-6.

Table A-6: Summary of all the torsional fatigue tests conducted

Surface state	Sample number (*Tray 1*; Tray 2)	Stress amplitude [MPa]	Rupture cycles
As-built	*7*	150	634502
	11	130	1686003
	20	120	-
	20	180	263201
	24	130	1405000
	4	120	1661001
	5	110	-
	5	150	858506
	27	120	-
	15	130	1993002
	8	120	-
	8	170	793004
	25	130	-
	25	160	851003
	13	140	849507
	6	130	-
	6	200	283004
	7	140	992000
	23	130	1112505
Simple-polished	*3*	180	568007
	1	170	668503
	16	150	1328000
	22	140	1246500
	30	130	-
	30	160	776003
	18	140	-
	18	200	290203
	5	150	843505
	27	140	-
	27	210	262257
	6	150	1298005
	10	140	-
	10	190	461006
	25	150	1285002
	2	140	-
	18	200	290203
Total polished	3	160	-
	3	220	649754
	14	170	-
	14	190	773005

29	180	1669000
1	170	873004
21	160	-
2	170	-
2	240	360444
10	180	1563000
18	170	-
18	200	1216004
28	180	705173
30	170	-
30	250	157506

A.4. Bending fatigue tests

Before a detailed analysis of the fatigue performance of SLM 316L, it can be noticed that the calculated endurance limit is lower compared to that of conventional 316L from literature. For the bending case, we add a group of wrought machined specimens besides the three groups of SLM specimens which are as-built, simple-polished and total polished. The staircase method for all the four differently configurated bending specimens (the ones from the tray 1 in blue, the ones from the tray 2 in red) is shown in Table A-7.

Table A-7: Staircase method for all bending specimens

Surface state	Stress amplitude [MPa]	Test Number													
		1	2	3	4	5	6	7	8	9	10	11	12	13	14
As-built	100	*X1*				*X12*		*X7*						*X8*	
	90		*X28*		*O25*		*O4*		*X29*		*X17*		*O18*		*X30*
	80			*O22*						*O2*		*O19*			
Simple polished	130		*X23*		*X16*										
	120	*O5*		*O21*		*X11*				*X9*		*X24*		*X20*	
	110						*X27*		*O6*		*O3*		*O13*		*O15*
	100							*O26*							
Total polished	150							X3							
	140		X4		X26		O2		X6						
	130	O22		O13		O10				O28					
Wrought machined	300					X6				X10					
	290				O5		X7		O9		O11				
	280	X2		O4				O8							
	270		O3												

For the four cases, the failures were the least frequent events; the calculations for the parameters are shown in Table A-8.

Table A-8: Staircase method calculations for all bending specimens

Surface state	i	f_i	$i*f_i$	i^2*f_i
As-built	1	3	3	3
	0	3	0	0
	Σ	N=6	A=3	B=3
Simple-polished	2	2	4	8
	1	4	4	4
	0	1	0	0
	Σ	N=7	A=8	B=12
Total polished	1	1	1	1
	0	3	0	0
	Σ	N=4	A=1	B=1
Wrought machined	2	2	4	8
	1	1	1	1
	0	1	0	0
	Σ	N=4	A=5	B=9

Using the staircase method, we get the estimated endurance limits under bending loading for as-built, simple-polished, total polished and wrought machined specimens which are 90MPa, 116MPa, 138MPa and 288MPa, respectively.

All bending fatigue tests including further LCF tests of the intact specimens from HCF tests are presented in Table A-9.

Table A-9: Summary of all the bending fatigue tests conducted

Surface state	Sample number (*Tray 1*; Tray 2; Wrought)	Stress amplitude [MPa]	Rupture cycles
As-built	*22*	80	-
	2	80	-
	19	80	-
	29	90	2575000
	30	90	1737000
	28	90	1849000
	17	90	2055000
	25	90	-
	4	90	-
	18	90	-
	1	100	1047000
	12	100	1511000
	7	100	2055000
	8	100	2204000
	25	110	730000
	19	120	375000
	18	140	189000
	2	160	110000
	4	170	100000
Simple-polished	*26*	100	-
	27	110	1525000
	6	110	-
	3	110	-
	13	110	-
	15	110	-
	5	120	-
	21	120	-
	11	120	1600000
	9	120	1357000
	24	120	1587000
	20	120	1139000
	23	130	888000
	16	130	911000
	21	140	580000
	15	150	548000
	13	170	319000
	3	190	204000
	6	210	140000
	26	230	100000
Total polished	22	130	-

	22	160	567501
	4	140	1205008
	13	130	-
	13	170	508001
	26	140	1144001
	10	130	-
	10	150	724004
	2	140	-
	2	180	372001
	3	150	784305
	6	140	1622504
	28	130	-
	28	200	314301
Wrought machined	2	280	1051004
	3	270	-
	3	300	671206
	4	280	-
	4	320	750008
	5	290	-
	5	360	207758
	6	300	1716505
	7	290	1356501
	8	280	-
	8	340	413006
	9	290	-
	9	310	712007
	10	300	1804967
	10	330	778609
	11	290	-
	11	350	370001

Appendix B. Mesh convergence test

The convergence tests are conducted on the model containing a semi-circular defect with a radius of 5 µm. The model with the smallest defect is considered the most critical configuration to achieve convergence since the small geometrical defect requires more discrete elements to describe the heterogeneity in the vicinity of defect root. Cyclic tension loading with an amplitude of 100 MPa at R=-1 is applied. The model is meshed using three ordered elements of three different mesh sizes: 5 µm, 1µm and 0.1 µm representing coarse, fine, and super fine mesh quality respectively. For the configuration of mesh size equaling 0.1 µm, only a part of the mesh around the defect is refined since a global 0.1 µm mesh will generate about 10^{10} DOFs which far exceeds the capability of the computer cluster used.

The compared mechanical responses are the Dang Van stress from the non-local methods. To better present the results, minimums of the non-local parameters investigated in the study are used: 15 µm for the R* of the critical radius method and 1 for the N* of the neighbor layer method. The responses in the defect root from different models are listed in Table B-1.

For the neighbor layer method, as the results are averaged in the grain, the increase of mesh resolution has a negligible influence on the yielded results.

Concerning the critical radius method, slight differences can be observed. Considering the contour plots, jagged edges can be seen in the coarse mesh while the two refined meshes have similar smooth patterns. But the responses from 5 µm mesh and from 1 µm are similar. However, the critical radius method is sensitive to the mesh size since refining the mesh can increase the precision of results. But, the mesh size of 0.1 µm is not feasible for massive parallel simulations planned. Moreover, it can be expected the difference will reduce if larger R* is used.

Hence, the current choice of 2 µm is acceptable for balancing the computational expense and the precision.

Table B-1: Comparison of different mesh qualities

Mesh size (µm)	Responses in the defect root	
	Dang Van stress (N*=1) [MPa]	Dang Van stress (R*=15 µm) [MPa]
5	46.26	59.81
1	46.18	59.53
0.1	46.18	61.45

Appendix C. Application of the neighbor layer method

In Chapter V, we used the critical radius method to generate the fatigue prediction. The neighbor layer method, however, as discussed in Chapter IV, is expected to be an efficient alternative of the critical radius method. From the perspective of numerical implementation, the neighbor layer method requires less computational resources because it has less Time complexity and Space complexity compared to the critical radius method. However, current experimental investigations are insufficient for the identification and calibration of the parameter N* in different configurations. The simulations using the neighbor layer method are just trails of this non-local method.

C.1. Smooth models

Regarding the application of neighbor layer method, the results from tension loading categorized by the corresponding tessellation method and the value of N* are plotted separately according to the crystallographic orientations in the following Figure C-1. The presented figure is of the type of box-plot which has been explained in Chapter IV. For both the types of orientation, some general qualitative patterns can be observed. For N=1, the result is equivalent to the average response in one grain which is obvious lower than its counterpart for N >=2 in all the tessellation configurations and has a stronger scatter. The explanation is that the extreme value chosen as fatigue indicator is strongly dependent on the actual size of the considered effective area. If the effective area is considered as one grain, extreme value is probably found in a small grain on the free surface. For the Log-normal tessellated models, the distribution of grain size is more scattered compared to that of the quadrangle tessellated models which results in larger distribution ranges. The influence of small grain can be reduced by using larger N*. As the value of N* grows, the prediction tends to converge at a certain level which is consistent with the observation from critical radius method. Because the average grain size varies in different tessellated models, the results from Q2 tessellation are always higher than that from LN_V1 or LN_V2 models. By comparing the type of orientations introduced, similar trend that the textured microstructure leads to a 10% decrease of fatigue performance is seen. In the box-plot, blacker markers represent the out-of-range results. According to the definition of classical box-plot, the range is determined as (Q1-1.5ΔQ, Q3+1.5ΔQ). It is seen that in the realistic orientation sets, more outliers present. The outliers are often under the minimum estimation which demonstrates that the distribution of predictions for the realistic orientations are left-deviated. The finding confirms the rationality of using GEV distribution to fit the data. The predictions from critical radius method using parameter R*=60 μm are plotted to visually compare the difference of these two non-local methods. The value 60 μm was previously identified for it can yield approximate prediction under the condition of tension loading and isotropic orientations

which is the configuration of experimental test. In the models with equiaxed microstructure, the transfer from critical radius method to neighbor layer method is simply by division of grain size for the effective areas considered are usually similar. Nevertheless, in the presented models, neighbor layer parameter cannot be derived directly from the critical radius parameter. But analogy between R* and N* is still feasible. In the case of Q2 tessellation, the prediction from R=60µm is similar with that from N=2. For the Voronoi polygon tessellated models, a circular effective area with a radius of 60 µm is approximately equivalent to the case of N=4. The corresponding values of N* will be used in following simulations with more complex geometries.

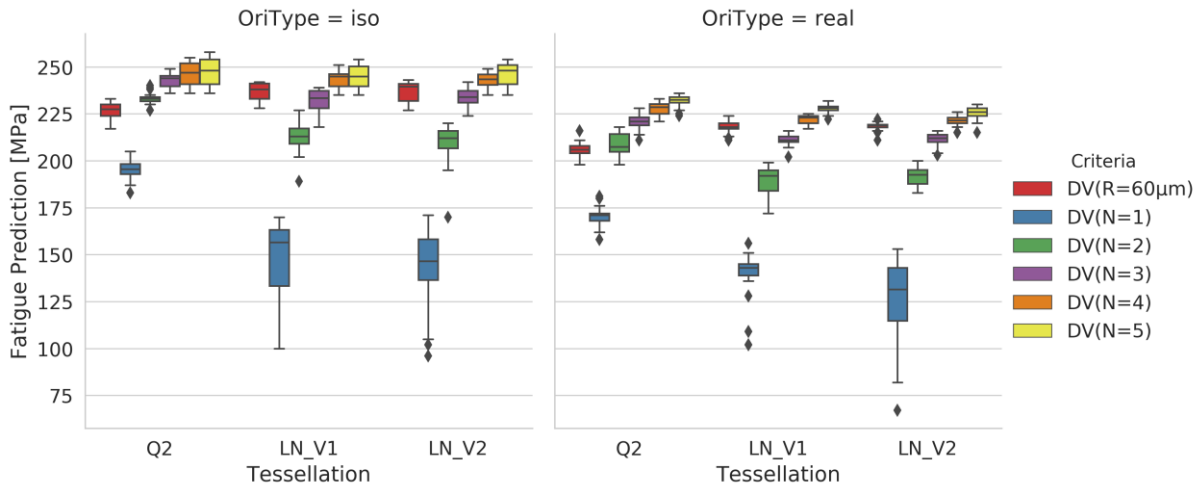

Figure C-1: Comparisons of predicted fatigue limit intervals under tension loading using different N* values for non-local Dang Van criterion

C.2. Models with artificial semi-ellipsoidal defects

Like in Figure V-23, similar contour plot using the neighbor layer method is presented (Figure C-2). With regard to the neighbor layer method, the grain shape and positioning are taken into accounts. The responses in each defect are even more different. Because the employed model has a non-constant grain size, the second defect from left to right are surround by several large grains whilst the rearmost defect has many small grains around. Therefore, the considered effective areas for these two defects are evidently different. The extreme values of FIPs in the critical radius method and in the neighbor layer method are very close to each other. Both methods predict the critical site in the root of the rearmost defect.

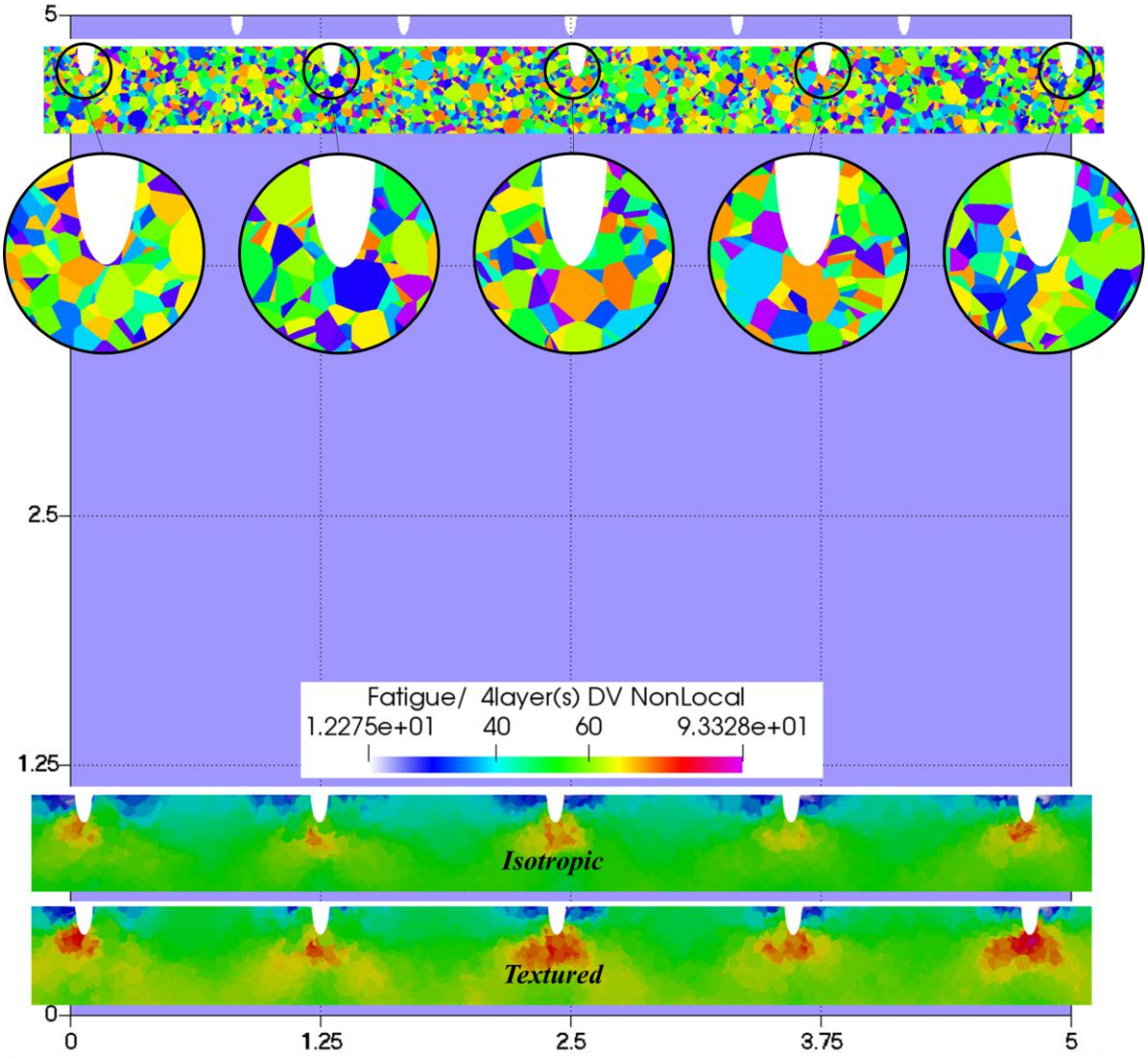

Figure C-2: Distributions of the non-local fatigue indicating parameters (Dang Van (N*=4)) in non-textured and textured numerical models under tension loading of 100 MPa

Similar investigation on the decrease of fatigue limit in models with geometrical defect is conducted by using neighbor layer method. N* is set to 2 for Q2 tessellation cases and 4 for Voronoi polygon tessellation cases. The choice of parameter's value is explained in previous section about smooth models. Generally, the percentage of fatigue limit decrease is similar with the result from critical radius method. Slight difference between the two log-normal Voronoi polygon tessellation can be observed which indicates the influence of the positioning of grains. Q2 tessellation using large quadrangles underestimates the effect of defect due to an overestimated effective area.

Table C-1: Mean values of predicted fatigue limits from models containing geometrical defects with same type of loading, tessellation and orientation using Neighbor layer Dang Van criterion

Configuration ("Tessellation", "Orientation", "Loading")	Smooth Model [MPa]	Pores model [MPa]	Drop of fatigue limit [%]
('LN_V1', 'Realistic', 'Bending')	220	165	25%
('LN_V2', 'Realistic', 'Bending')	219	155	29%
('Q2', 'Realistic', 'Bending')	211	170	19%
Experiments ('Realistic', 'Bending')	138	90	35%

C.3. Roughness models

In Figure V-24, we have shown the distribution of non-local Dang Van stresses using different R*. Similar results from the neighbor layer method are presented in Figure C-3. When the neighbor layer method is applied, slight differences are seen. If N*=1, as is the responses are averaged over each single grain, the extreme value appears in a small grain on the surface. However, this grain does not locate in or near any notable groove of roughness. The high value of response is due to the dimension and the conflict with other anisotropic neighbor grain. If using a larger N*, the hot spot is found to be in the comparable place as the critical radius method. In terms of the most critical grain, the prediction varies slightly. When the first layer of neighbor grains is taken into consideration, the critical value is from a grain in a deep valley in the roughness profile. As the considered neighbors increase, the prediction moves to a grain lying between two concave defects.

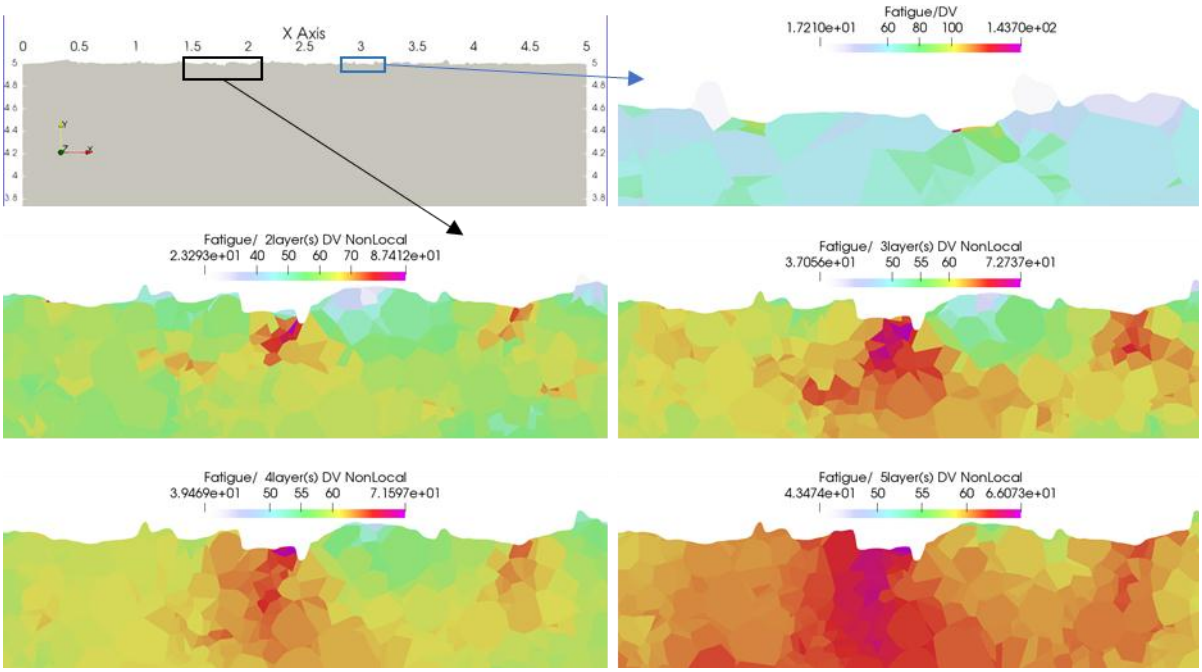

Figure C-3: Non-local Dang Van stresses using different N* (1, 2, 3,4 and 5) from a log-normal Voronoi-polygon-tessellated model with roughness

C.4. Combined models

Similarly, results from neighbor layer method are shown in Figure C-4. Only the two log-normal Voronoi polygon tessellated models are involved in the analysis because of the unequal grain size in the quadrangle tessellated model. The addition of roughness does not decrease evidently the fatigue strength. Nevertheless, the violin type markers indicating the distributions of probability density present the feature of bimodal distribution, especially when the N* is attributed a small value, due to the two instantiations of Voronoi tessellation. Hence, even though the stress distribution is strongly affected by the defects, the effect of grain morphology is still preserved by the neighbor layer method.

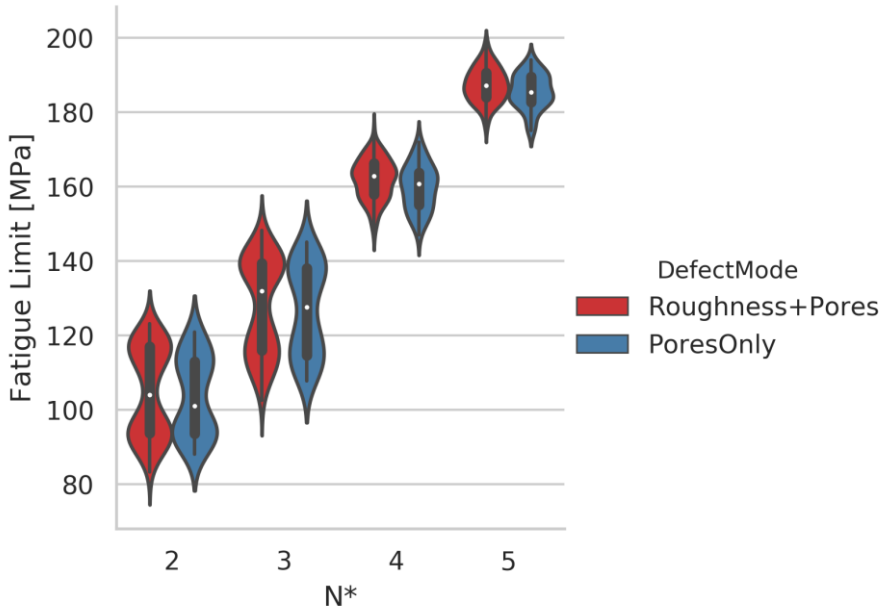

Figure C-4: Predictions of fatigue limit from Dang Van criterion using the neighbor layer method

Résumé substantiel

Chapitre I. Bibliographie 217
I.1. Introduction 217
I.2. Quelques éléments de la littérature relatifs au comportement en fatigue de l'acier SLM SS 316L 218
I.2.1. Etat de surface 219
I.2.2. Direction de fabrication et traitement thermique 220
I.2.3. Fraction de porosité et défauts de surface 221
I.3. Conclusion 222
Chapitre II. Fabrication et caractérisation du matériau de l'étude 224
II.1. Élaboration des échantillons : 224
II.2. Microstructural characterization 226
II.3. Caractérisation des défauts inhérents 231
II.3.1. Caractérisation de l'état de surface 231
II.3.2. Porosity characterization 232
II.4. La réponse mécanique 233
II.4.1. Mesure de dureté 233
II.4.2. Essai de traction monotone 233
II.4.3. Essai de traction cyclique 235
II.5. Conclusion 236
Chapitre III. Les expériences et analyses sur la tenue en fatigue 239
III.1. Analyse de la résistance à la fatigue à grand nombre de cycles 239
III.1.1. Effet de l'état de surface 241
III.1.2. Effet du mode de chargement 241
III.2. Analyse fractographique de l'amorçage de fissures de fatigue 242
III.2.1. Eprouvettes de flexion 242
III.2.2. Eprouvette de torsion 242
III.3. Corrélation entre la taille du défaut et le comportement en FGNC 243
III.3.1. Détermination de la taille des défauts 243

III.3.2. Diagramme de Kitagawa-Takahashi 245

III.4. Conclusion 248

Chapitre IV. Etude préliminaire de l'effet de la microstructure et des défauts sur la tenue en fatigue 251

IV.1. Modélisation et influence de la microstructure pour les matériaux à défauts 251

IV.2. Evaluation de la méthode non locale par rapport aux résultats expérimentaux 253

IV.2.1. Effet de la distribution des grains 257

IV.2.2. Effet de la taille de grain 261

IV.3. Conclusion 262

Chapitre V. Etude numérique de l'effet de la rugosité et de la porosité sur les performances en fatigue du 316L SLM 264

V.1. Modélisation du 316L SLM 264

V.1.1. Orientation cristallographique et morphologie des grains 264

V.1.1.1. Morphologie et taille des grains 264

V.1.1.2. Orientation des grains 265

V.1.1.3. Rugosité et pores 265

V.2. Configurations de modélisation 266

V.2.1. Conception de modèles géométriques 266

V.2.1.1. Modèles lisses 266

V.2.1.2. Modèles avec défauts 266

V.2.2. Modèles constitutifs 267

V.2.3. Conditions de chargement et critère de fatigue 267

V.3. Simulations de fatigue de modèles lisses 267

V.3.1. Discussion sur la référence expérimentale pour la simulation 267

V.3.2. Méthode statistique pour l'hétérogénéité microstructurale 267

V.3.3. Influence du R * 268

V.4. Simulations de fatigue utilisant des modèles avec rugosité et défauts 270

V.4.1. Modèles avec défauts semi-ellipsoïdaux artificiels 270

V.4.2. Modèles avec rugosité 271

V.4.3. Modèles contenant défaut artificiel et rugosité 273

V.5. Rôle de la plasticité dans la simulation de fatigue 275

V.5.1. Comparaisons entre les modèles constitutifs élastiques et plastiques dans les modèles lisses 275

V.5.2. Comparaisons entre les prédictions élastiques et plastiques dans les modèles défectueux 276

V.6. Conclusion 277

Chapitre I. Bibliographie

I.1. Introduction

Notre étude portant sur la caractérisation et la modélisation de la tenue en fatigue à grand nombre de cycles d'un acier inoxydable austénitique 316L obtenu par fabrication additive, il semble indispensable de proposer quelques éléments descriptifs relatifs à ce procédé de fabrication et de rappeler les spécificités du comportement en fatigue. Il est également important de préciser qu'il n'est nullement question ici de conduire une analyse bibliographique exhaustive relative à tous les alliages métalliques obtenus par fabrication additive. Il s'agit plutôt de se concentrer sur les caractéristiques microstructurales et le comportement mécanique de l'acier 316L obtenu par le procédé SLM (Selective Laser Melting).

Parmi les techniques de fabrication additive les plus étudiées et utilisées actuellement, le procédé "Selective Laser Melting" (SLM) appartient à la catégorie des procédés de type "Powder Bed Fusion".

Comme illustré en *Figure I-1*, il consiste, dans une enceinte à environnement contrôlé (gaz inerte), à utiliser un laser pour faire fondre, dans certaines zones, une fine couche de poudre métallique disposée à la surface d'un plateau. Après chaque passage de laser, le plateau est abaissé, une nouvelle couche de poudre est déposée et un nouveau passage de laser est effectué. L'opération est répétée jusqu'à obtention de la pièce sous sa forme finale.

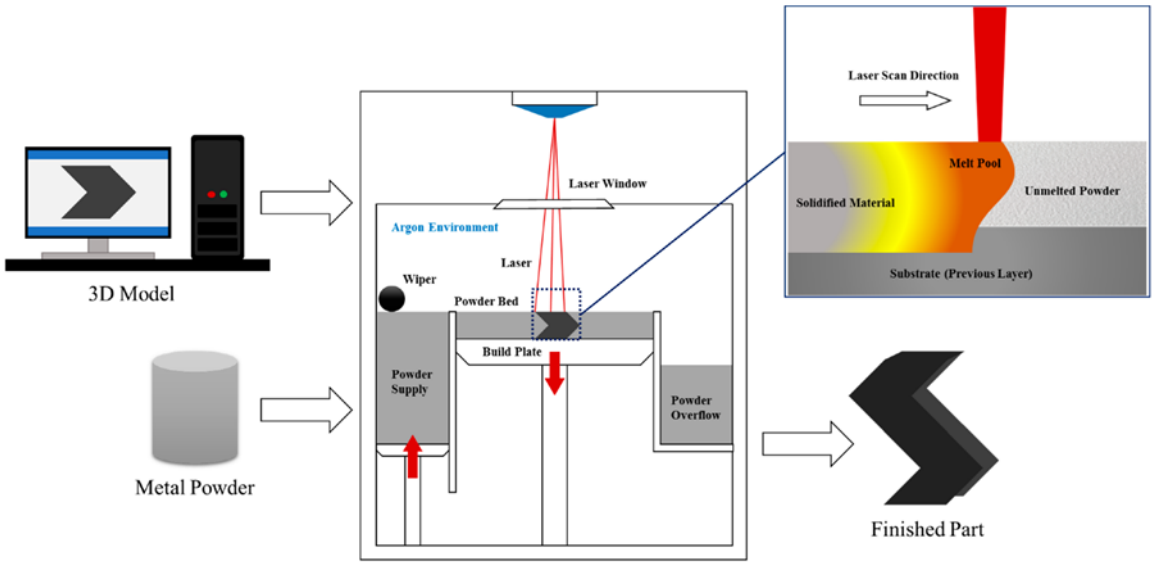

Figure I-1: Schematic illustrations of the SLM process (Patterson, Messimer and Farrington, 2017)

En comparaison d'autres procédés de fabrication additive, cette technique permet d'obtenir des caractéristiques très intéressantes en matière de fraction de porosité et de résistance (Tolosa *et al.*, 2010).

Le procédé SLM est également le procédé de fabrication additive conduisant au meilleur état de surface. Il n'en reste pas moins que la rugosité de surface dans l'état brut de fabrication est loin d'être satisfaisante du point de vue du comportement mécanique, notamment en fatigue.

Il est usuel de distinguer trois régimes de comportement en fatigue (*Figure I-2*), la plupart du temps au regard du nombre de cycles à rupture atteint. On parle de "Low cycle fatigue (LCF)" quand $N_f < 10^4$-10^5 cycles, de "High cycle fatigue (HCF)" dans la gamme 10^6-10^7 cycles et de "Very High Cycle Fatigue (VHCF)" au-delà de 10^7 cycles.

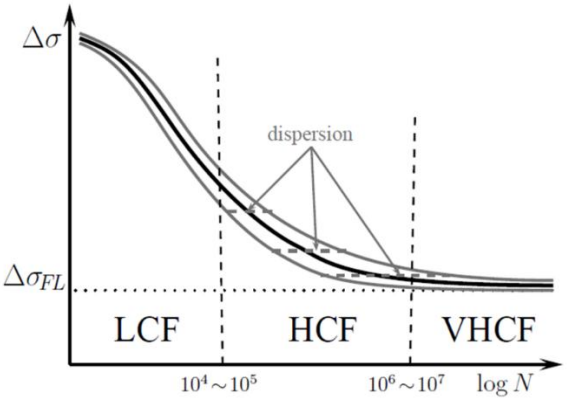

Figure I-2: Diagram of the various domains of fatigue and highlighting of the dispersion at low amplitudes of stress (Guilhem, 2011)

Notre étude porte sur le domaine HCF caractérisé par de faibles niveaux de déformation, de grands nombres de cycles et une très grande dispersion. La plupart du temps, le niveau de plasticité à l'échelle macroscopique est très faible. De plus, les fissures s'amorcent principalement en surface et la fraction de la durée de vie à l'amorçage est souvent importante.

I.2. Quelques éléments de la littérature relatifs au comportement en fatigue de l'acier SLM SS 316L

La variété des équipements et des conditions de fabrication additive type SLM utilisés est telle qu'il est parfois très difficile de comparer les travaux de la littérature traitant du comportement en fatigue. Les paramètres potentiellement influents sont très divers et il est souvent impossible de découpler chacun des effets associés. On observe en particulier des effets marqués de la direction de fabrication, du traitement thermique et des opérations de parachèvement. Les caractéristiques microstructurales et d'intégrité de surface, la population de défauts sont les principaux facteurs avancés pour expliquer les différences observées.

I.2.1. Etat de surface

L'ensemble des travaux de la littérature s'accorde sur le fait que l'état brut de fabrication est toujours associé à une résistance en fatigue bien plus faible que celles obtenues avec des procédés de fabrication conventionnelles (Yadollahi and Shamsaei, 2017). On a alors souvent recours à des opérations de polissage ou d'usinage qui permettent de découpler les effets de rugosité des effets de microstructure ou de défauts.

Des essais conduits en fatigue uniaxiale avec un rapport de charge R=0.1 par (Spierings, Starr and Wegener, 2013), (Solberg *et al.*, 2019) et (Davies, 2017) sur des échantillons de SS 316L obtenus par SLM (fabrication verticale) montrent par exemple des résistances en fatigue très dépendantes de l'état de surface (*Figure I-3*). Les niveaux les plus élevés obtenus sont comparables à ceux d'aciers 316L corroyés.

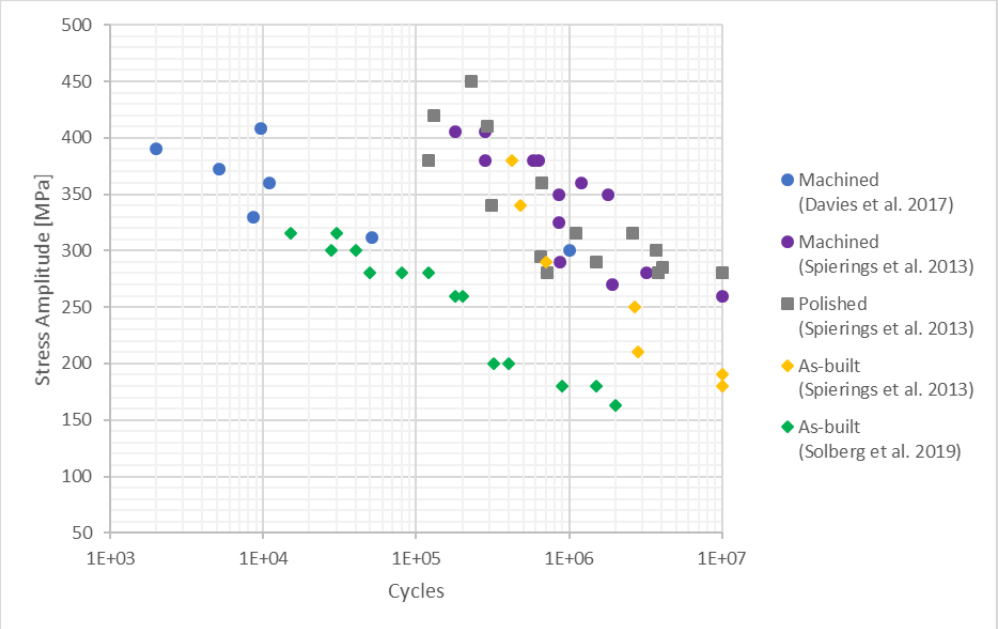

Figure I-3: S-N plots of vertically built SLM 316L under loading at R=0.1 with different surface treatments

La même constatation est faite en R=-1 par (Uhlmann *et al.*, 2017), (Elangeswaran *et al.*, 2019) et (Shrestha, Simsiriwong and Shamsaei, 2019) (*Figure I-4*). Il est important de faire remarquer que de faibles écarts sont parfois observés entre les lots « bruts de fabrication » et « usinés ». Une explication avancée est la présence de défauts de type « Lack of fusion » de grande taille très néfastes pour la tenue en fatigue.

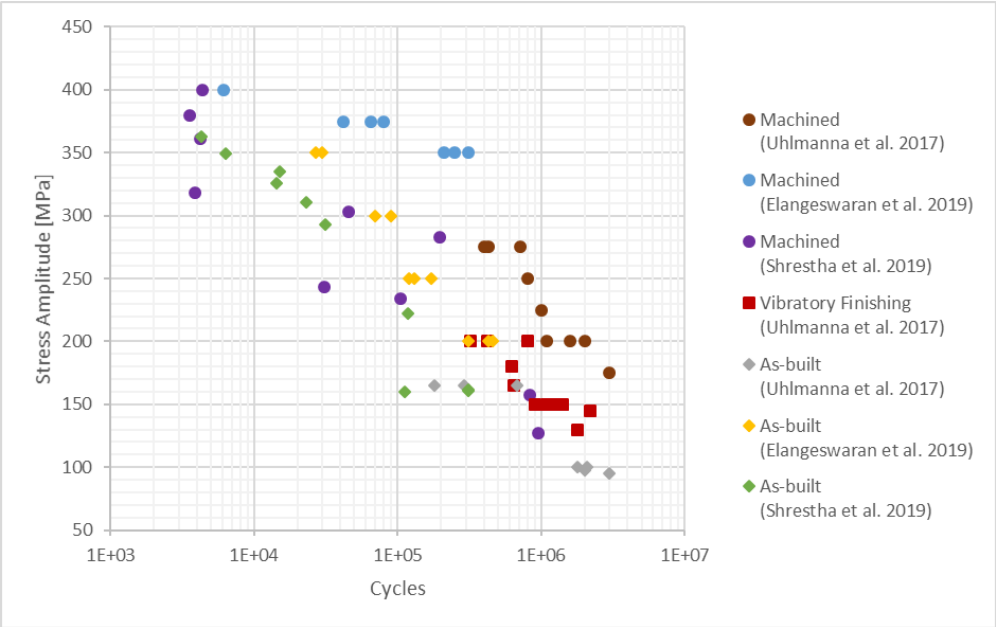

Figure I-4: S-N plots of vertically built SLM 316L under loading at R=-1 with different surface treatments

I.2.2. Direction de fabrication et traitement thermique

L'effet du paramètre direction de fabrication est étudié par plusieurs auteurs qui constatent des résultats parfois contradictoires.

Pour une configuration brute de fabrication, (Mower and Long, 2016) observent que les éprouvettes fabriquées horizontalement présentent des résistances trois fois meilleures que celles fabriquées verticalement (*Figure I-5*). Dans tous les cas, des défauts en surface ou en sous couche sont à l'origine de la fissure principale.

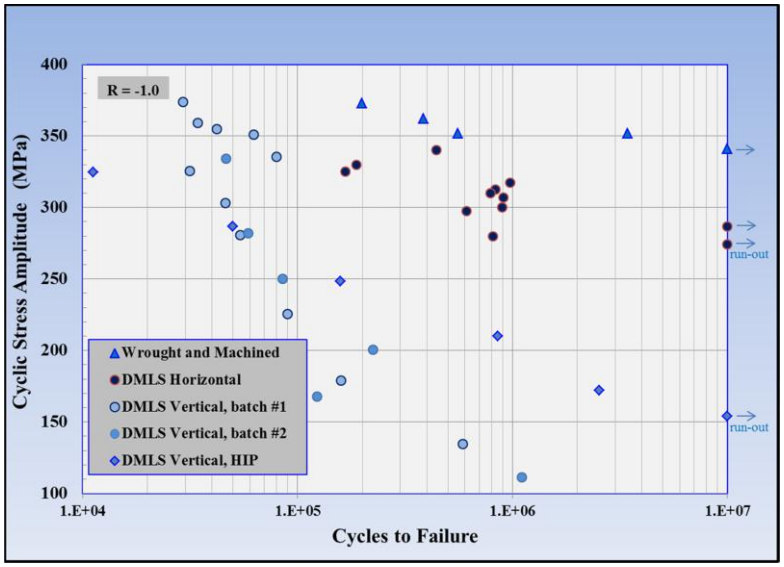

Figure I-5: S-N plots of DMLS 316L in bending fatigue at a frequency of 25 Hz with regards to building direction (Mower and Long, 2016)

(Blinn *et al.*, 2019) trouvent un résultat très différent (*Figure I-6(a)*) avec une meilleure résistance en fatigue pour les échantillons fabriqués verticalement. A noter que les éprouvettes sont usinées puis polies avant d'être testées. La *Figure I-6(b)* montre la microstructure très caractéristique obtenue par la technique SLM avec une texture morphologique prononcée dans le sens de la direction de fabrication.

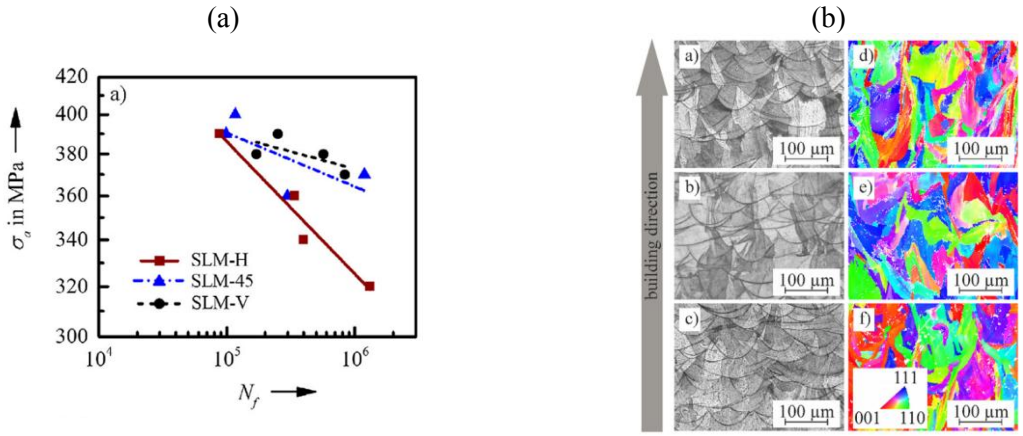

Figure I-6 : (a) S-N curves for differently oriented specimens; (b) Light optical micrographs and EBSD-mappings of SLM-H (a, d), SLM-45 (b, e) and SLM-V specimens (c, f). (Blinn et al., 2019)

Pour ce qui est des traitements thermiques, on a souvent recours à des recuits ou à des traitements de type « hot isostatic pressing (HIP) ». Ce dernier n'est pas forcément synonyme d'amélioration dans le domaine HCF (Riemer *et al.*, 2014).

I.2.3. Fraction de porosité et défauts de surface

Lors de l'optimisation des paramètres du procédé de fabrication additive (Cherry *et al.*, 2014; Ahmadi *et al.*, 2016; Lackey, 2016; Liverani *et al.*, 2017; Suryawanshi, Prashanth and Ramamurty, 2017), il est souvent question d'obtenir un état de surface acceptable ainsi qu'une fraction de porosité faible. Les paramètres de « laser hatching » et de « laser contouring » jouent un rôle fondamental à cet égard.

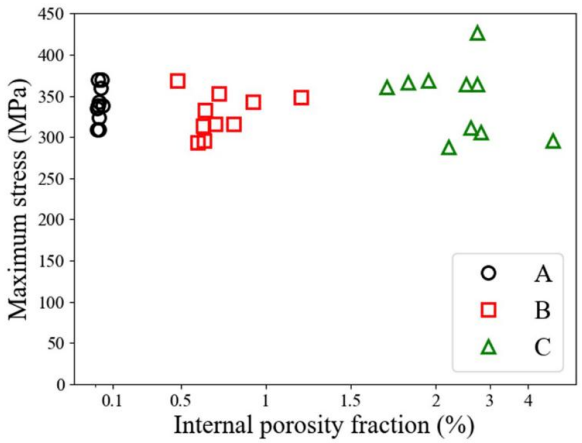

Figure I-7: Variation of Maximum stress at failure (MPa) with internal porosity fraction (%)(Andreau, Pessard, et al., 2019)

(Andreau, Pessard, *et al.*, 2019) étudient les effets des paramètres de hatching et de contouring lors de la fabrication SLM d'un acier 316L. Ils parviennent à obtenir des échantillons avec des fractions très diverses de porosité. Un résultat remarquable concerne la quasi indépendance de la résistance en fatigue vis-à-vis de la fraction de porosité (*Figure I-7*). Cela semble indiquer que la tenue en HCF est gouvernée par les hétérogénéités de surface présentes dans une couche de surface de quelques centaines de micromètres. La position des défauts relativement à la surface libre semble donc être un critère de premier ordre en fatigue pour ce type de matériaux.

I.3. Conclusion

Afin de mettre en évidence la complexité et la spécificité du comportement en fatigue de l'acier 316L obtenu par la technique de SLM, nous avons sélectionné des résultats importants de la littérature qui montrent le rôle fondamental joué par l'état de surface.

Ce rôle est d'autant plus marqué que, dans la configuration « brut de fabrication », les composants obtenus par SLM présentent des niveaux de rugosité très conséquents. D'après les éléments bibliographiques recueillis, les niveaux de résistance en fatigue les plus faibles sont toujours ceux associés aux lots « bruts de fabrication ». On constate également des résultats contradictoires quant à l'effet de la direction de fabrication et des traitements thermiques.

En première analyse, l'origine de cette résistance moindre pour les lots « as-built » pourrait être attribuée au seul rôle de la rugosité de surface. Il faut néanmoins garder à l'esprit que des défauts de type « Lack of fusion » sont souvent observés dans les zones d'amorçage des fissures de fatigue. Il est également important de souligner le caractère singulier de la microstructure en jeu avec des textures morphologique et cristallographique marquées.

Le défi majeur pour la compréhension et la modélisation des effets précités concerne la capacité à quantifier indépendamment le rôle de chacun des facteurs influents. C'est ce que nous nous proposons de décrire dans la suite du rapport avec les chapitres 2 et 3 dédiés à la descriptions d'une étude expérimentale complète et les chapitres 4 et 5 portant sur la simulation numérique des effets de rugosité, de défaut et de microstructure.

Chapitre II. Fabrication et caractérisation du matériau de l'étude

Ce chapitre est consacré à la présentation des propriétés mécaniques et métallurgiques du matériau de l'étude. Il s'agit de l'acier 316L austénitique obtenue par fusion laser sur lit de poudre (SLM). Dans ce chapitre, nous présentons le processus d'élaboration et de post-traitement des différentes éprouvettes ainsi que les différentes étapes de caractérisation de ce matériau. Dans la première section, les étapes d'élaboration et de préparation des éprouvettes de caractérisation et de fatigue sont détaillées en allant de la caractérisation de la poudre utilisée pour la fabrication jusqu'au post-traitement thermique des pièces fabriquées par SLM. Dans la deuxième section, la microstructure obtenue est analysée à plusieurs échelles. Dans la troisième section, les défauts surfaciques et volumiques issues de ce procédé de fabrication additive sont déterminés sur plusieurs échantillons. Enfin, la dernière section est consacrée aux propriétés mécaniques de ce matériau. Des essais mécaniques typiques ont été réalisés sur l'acier 316L : dureté, essai de traction monotone et des essais de traction-compression cycliques à déformation imposée. Ces données seront utilisées par la suite pour l'identification du comportement mécanique du matériau. Les données issues de ce chapitre constitueront un point de départ pour la partie modélisation présentée dans les prochains chapitres.

II.1. Élaboration des échantillons :

Les échantillons utilisés dans cette étude ont été fabriqués par la société PRISMADD (actuellement Weare Group), le protocole de fabrication et de post-traitement est celui appliqué par la société sur les pièces industrielles en acier 316L. Ce protocole consiste à utiliser une poudre neuve ou recyclée N fois (jusqu'à ce que le taux d'oxygène devienne supérieur à 1000 ppm). Les paramètres de fabrication sont également optimisés par l'entreprise en interne pour minimiser le taux de porosité. Un traitement thermique de détensionnement (à l'air) est ensuite effectué avant de séparer les échantillons du plateau de fabrication par électroérosion à fil (EDM). Cette section est consacrée à la fois à la description et à l'analyse de ce protocole de fabrication.

Deux plateaux d'échantillons identiques ont été fabriqués par Weare Group. La machine utilisée est la ProX DMP 320. Les paramètres optimisés par Weare Group pour l'acier 316L ont été utilisés, ces paramètres sont illustrés dans la *Table II-1*Table II-2. Le relasage du contour n'a pas été effectuée. Ce relasage du contour est configuré par défaut dans la machine et souvent utilisé dans la littérature car il a été prouvé que ce processus améliore l'état de surface de la pièce fabriquée et donc les propriétés en fatigue. Dans cette étude, notre objectif est d'étudier l'effet de l'état de surface sur la tenue en fatigue. Nous avons donc choisi de supprimer ce relasage du contour ce qui nous permet d'avoir une meilleure compréhension de l'effet de l'état de surface sur la tenue en fatigue.

Table II-1: SLM processing parameters for specimen's fabrication

Machine	**Paramètres énergétiques**					**Stratégie de lasage**	
ProX DMP 320	Taille du spot (µm)	Vitesse de lasage (mm/s)	Puissance laser (W)	Écartement (µm)	Epaisseur des couches (µm)	Trajectoire	Relasage contour
	70	700	275	70	30	Zone aléatoire	Non

Tous les échantillons avec les géométries illustrées dans la *Figure II-1* ont été fabriqués verticalement. Deux plateaux identiques ont été fabriqués, chaque plateau contient :

- 30 éprouvettes pour essai de fatigue en flexion,
- 30 éprouvettes pour essai de fatigue en torsion,
- 5 éprouvettes pour essai de traction et,
- 15 éprouvettes cylindriques de longueur 10 mm et de 3 diamètres différents (2, 4 et 8 mm) pour la microstructure et la caractérisation des défauts.

Un traitement de détensionnement appliqué habituellement par Weare Group a été réalisé sur l'ensemble avant la séparation des échantillons de chacun des deux plateaux. Ce traitement est optimisé par Weare Group pour réduire ou éliminer les contraintes résiduelles sans modifier les propriétés mécaniques de l'acier 316L. Il consiste à maintenir une température de 620 °C pendant 90 minutes suivie d'un refroidissement naturel pendant 800 minutes jusqu'à ce que la température atteint 180 °C. Ce traitement est effectué à l'air sans contrôle de l'environnement. Ensuite, la séparation des échantillons des plateaux a été effectuée en utilisant l'électroérosion à fil.

Même s'il a été prouvé dans la littérature (Leuders *et al.*, 2014; Riemer *et al.*, 2014; Zhang *et al.*, 2019) que l'état de contraintes résiduelles n'affecte pas les propriétés mécaniques de l'acier 316L ainsi que sa tenue en fatigue, ce traitement thermique est fréquemment utilisé. Nous avons donc choisi de le conserver dans cette étude.

(a) Éprouvettes de caractérisation (microstructure)

Cylindres de hauteur 10 mm et avec 3 différents diamètres (2; 4 et 8mm)

(b) Eprouvettes de traction (comportement cyclique)

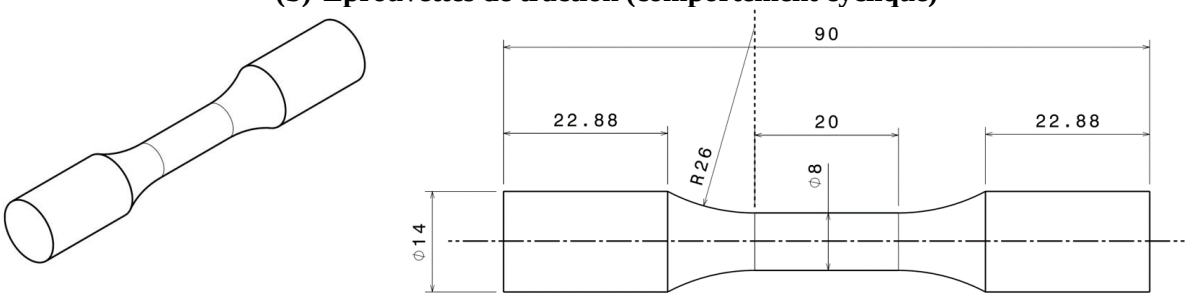

(c) Eprouvettes de flexion (fatigue)

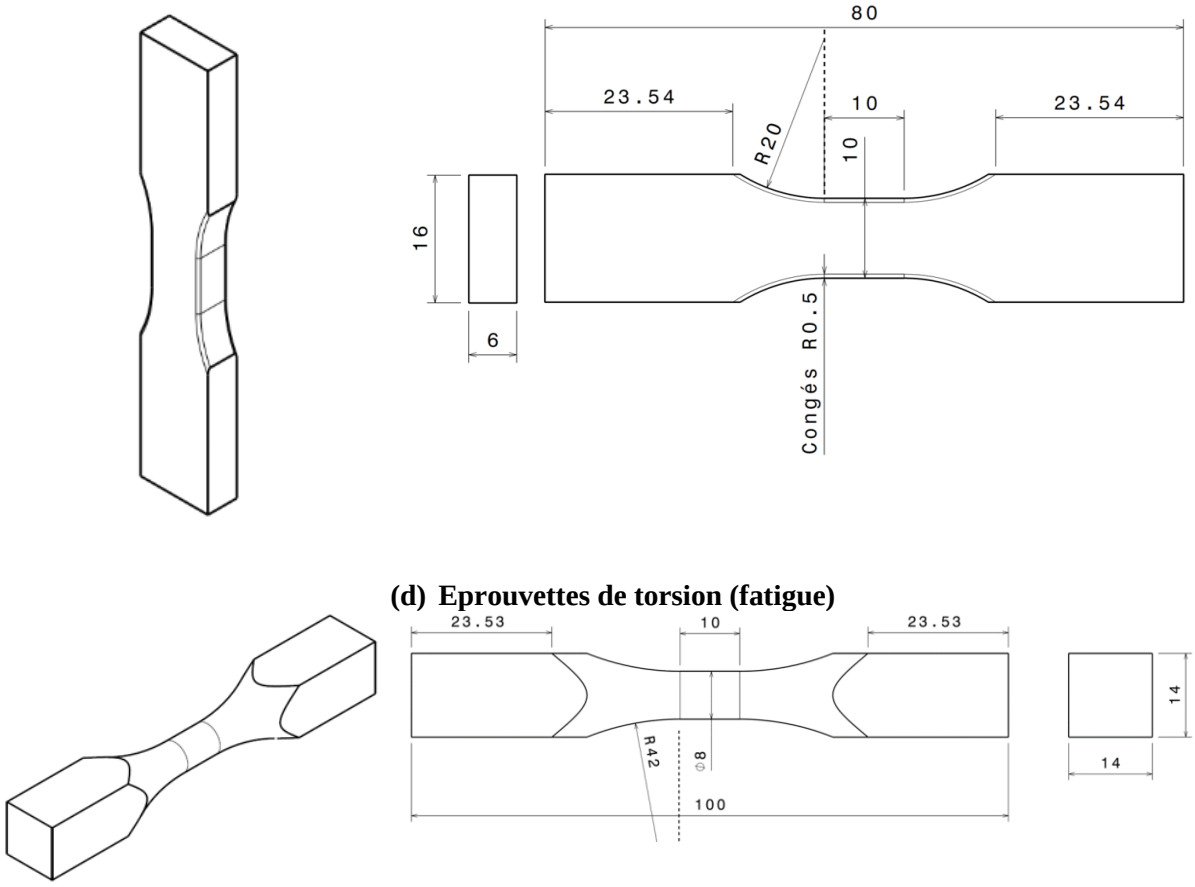

(d) Eprouvettes de torsion (fatigue)

Figure II-1: Geometries of specimens (dimensions in mm)

II.2. Microstructural characterization

Les microstructures générées par SLM peuvent être observées à deux échelles. Nous distinguons :

- La macrostructure générée par le passage du spot laser et constituée par les bains de fusion.
- La microstructure composée de grains traversant plusieurs bains de fusion et dont la morphologie et la texture cristallographique dépendent fortement de la cinétique de refroidissement.

Deux plans d'observation ont été étudiés : (i) les observations du plan Z aussi appelé plan de fabrication, c'est le plan perpendiculaire à l'axe de fabrication Z, il contient l'historique d'une seule couche ; (ii) les observations du plan X / Y, c'est le plan perpendiculaire à l'axe X ou Y. Ce plan contient donc l'historique thermique de toutes les couches.

La macrostructure du plan Z est illustré sur la *Figure II-2*. On distingue les cordons de soudure correspondant au déplacement du laser. Dans ce plan, la section des grains est quadrangulaire. Le trajet du laser est visible lors du changement de direction (voir « Laser spots » sur la *Figure II-2*).

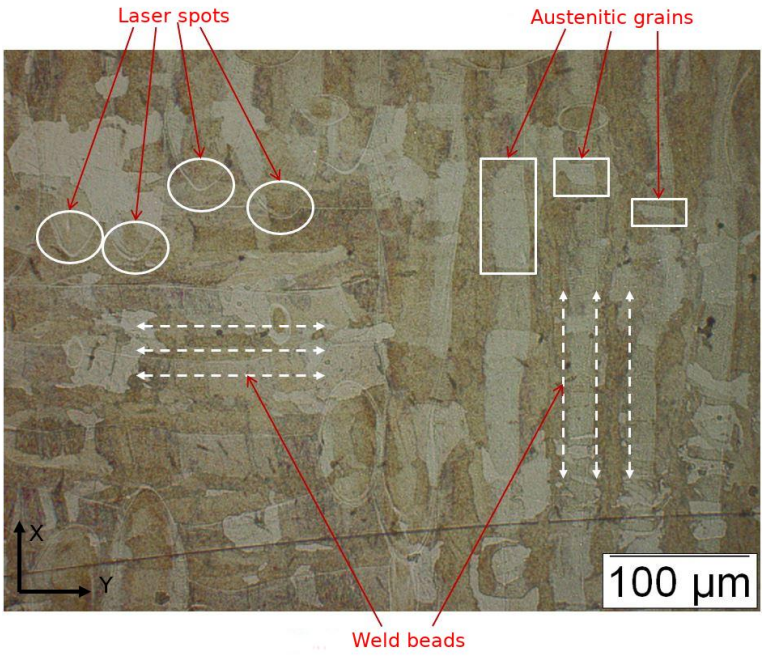

Figure II-2: Optical microscope observation on lasing plane Z

En ce qui concerne les plans X/Y (voir *Figure II-3*), nous pouvons voir des demi-ellipses, caractéristiques du processus SLM car elles représentent une section du bain de fusion qui apparaissent lors du passage du laser. La macrostructure ressemble à des écailles de poisson. L'observation de ces plans permet de distinguer clairement les interfaces entre les couches, ainsi que de voir la forme allongée des grains austénitiques traversant plusieurs couches. On peut également observer les grains qui se forment lors du processus de fabrication. Leur direction de croissance coïncide à peu près avec l'axe Z de l'échantillon.

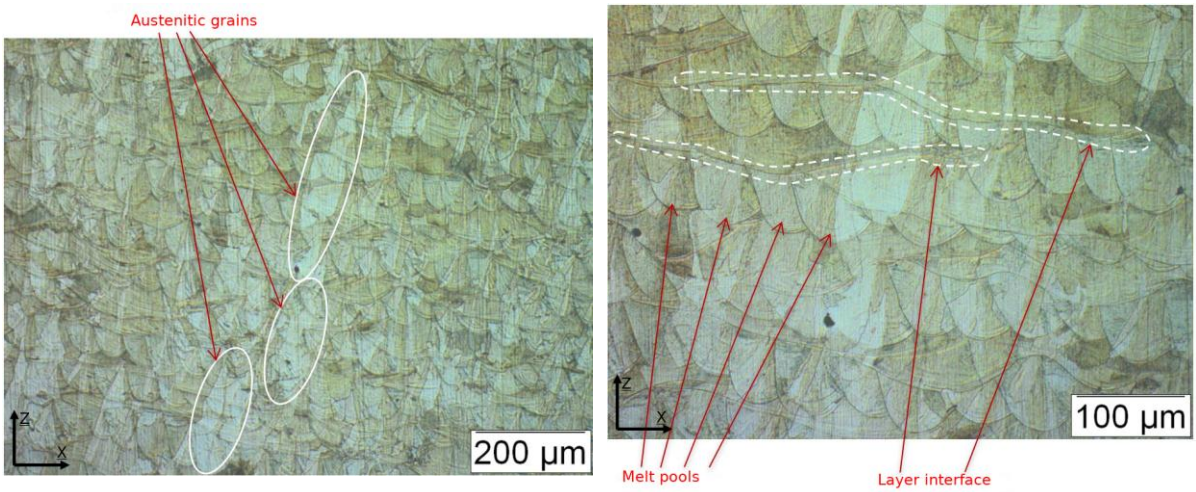

Figure II-3: Optical microscope observations on plane X/Y

La microstructure du plan Z est représentée sur la *Figure II-4*. A cette échelle, il devient possible d'observer la structure dendritique des grains austénitiques.

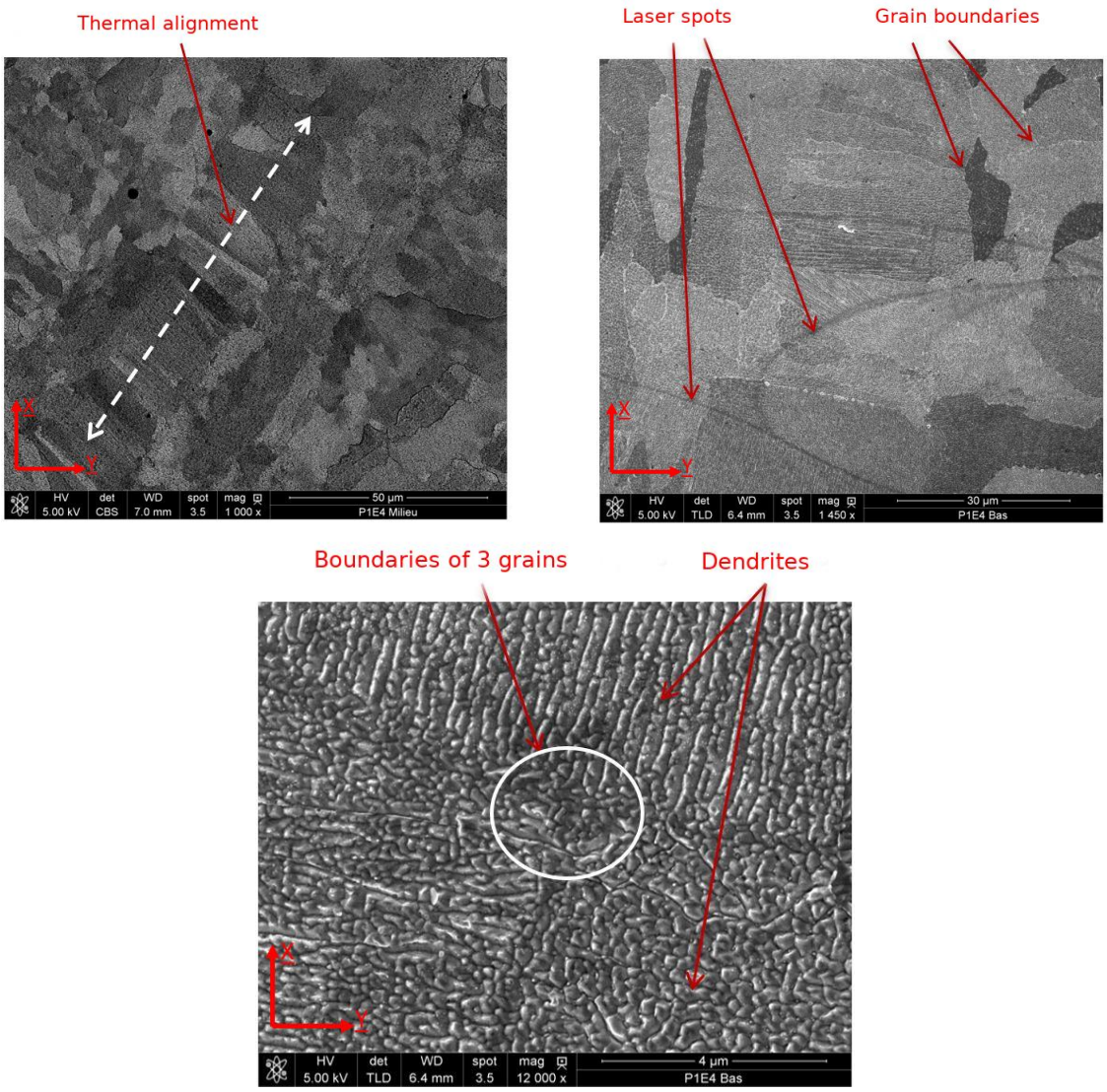

Figure II-4: SEM observations in the plane Z

La *Figure II-5* illustre la microstructure observée dans les plans X/Y. On peut observer les grains colonnaires allongés selon l'axe Z et traversant plusieurs couches. Classiquement, la direction préférentielle de solidification des matériaux CFC est la direction <100>. Il est orienté en fonction du gradient thermique local. En SLM, malgré les vitesses de refroidissement élevées (~ 10^6 K / s), cette direction de croissance privilégiée est respectée. On retrouve ainsi, dans toutes les études, une croissance des grains le long de <100> perpendiculaire au front de solidification formé par les bains de fusion. À une échelle plus fine, on peut voir des réseaux de dendrites traversant des bains de fusion.

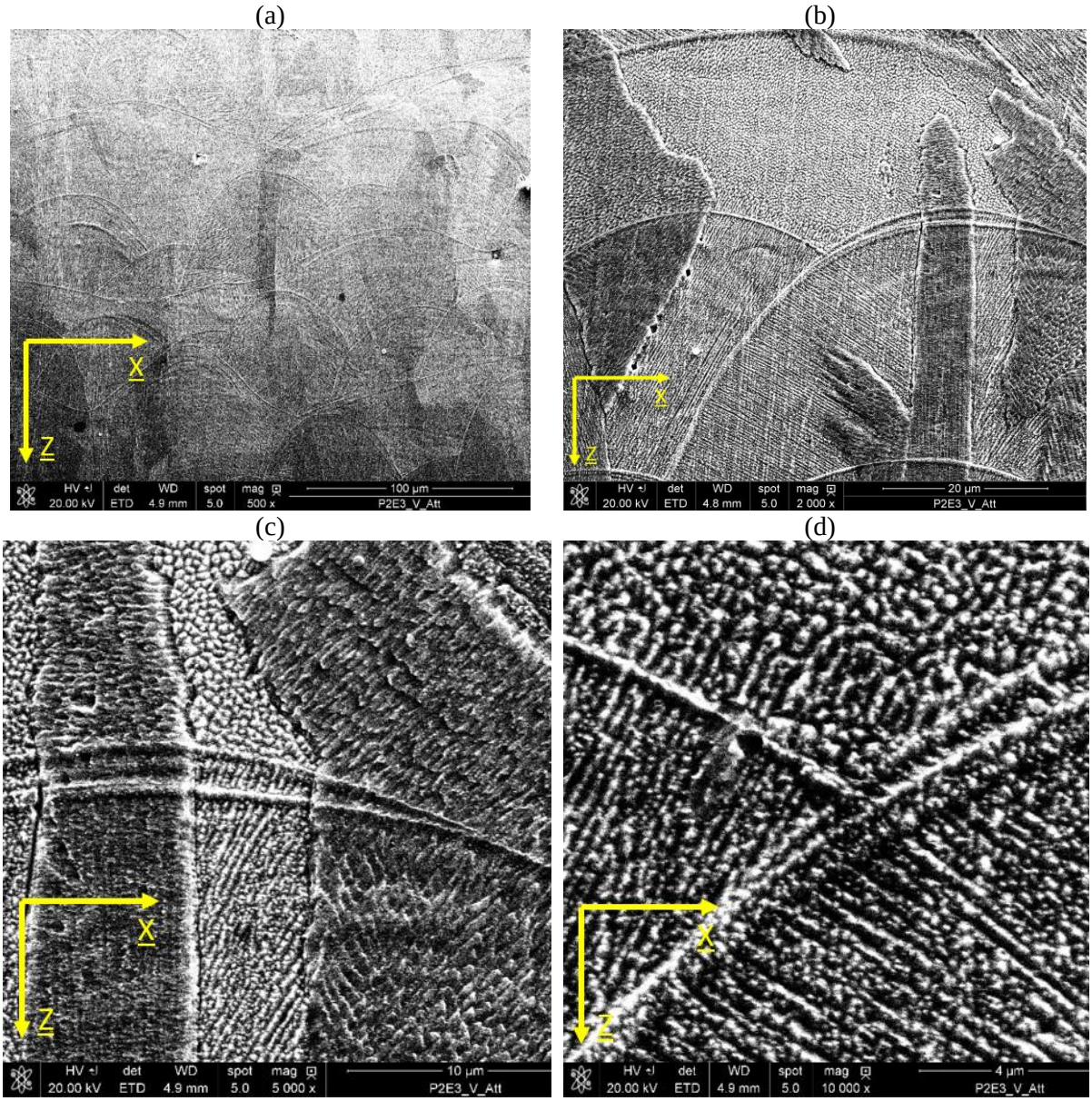

Figure II-5: SEM observations in the plane X/Y (long chemical attack)

Les observations ci-dessus montrent qu'il existe un alignement des grains austénitiques. Cet alignement est d'origine thermique. Les grains ont tendance à se développer le long du gradient thermique, c'est-à-dire selon le sens de la construction. Il s'agit d'une une croissance épitaxiale.

Pour déterminer la morphologie et l'orientation des grains des analyses par EBSD ont été réalisées sur un cylindre de diamètre 8 mm et de hauteur 10 mm. Le plan Z a été observé au centre de l'échantillon. Tandis que les plans X/Y ont été observés en bas (correspondant aux premières couches produites), au milieu et en haut (correspondant aux dernières couches produites). Le post-traitement des résultats a été réalisé en utilisant les bibliothèques MTEX. Ce post-traitement a permis d'obtenir la cartographie des grains reconstitués (*Figure II-6* et *Figure II-7*), les figures de pôles (*Figure II-8*a), et les figures de pôles inverses (*Figure II-8*b).

La granulométrie n'est pas homogène dans les échantillons observés. La morphologie prédominante ce sont des grains allongés (colonnaires). On peut constater également que les grains colonnaires ont une longueur supérieure à l'épaisseur de couche et donc traversent plusieurs couches. De plus, il n'y a pas de maclage typique de ce matériau CFC. Les cellules de dislocations sont piégées dans les cellules de micro-ségrégation dendritiques. Enfin, à l'exception des grains en contact avec le support et des grains de la surface extrême (où les cinétiques de refroidissement sont différentes), tous les autres grains ont une morphologie et une taille relativement identiques sur toute la longueur du cylindre. Il n'y a donc pas de gradient de microstructure le long de l'éprouvette.

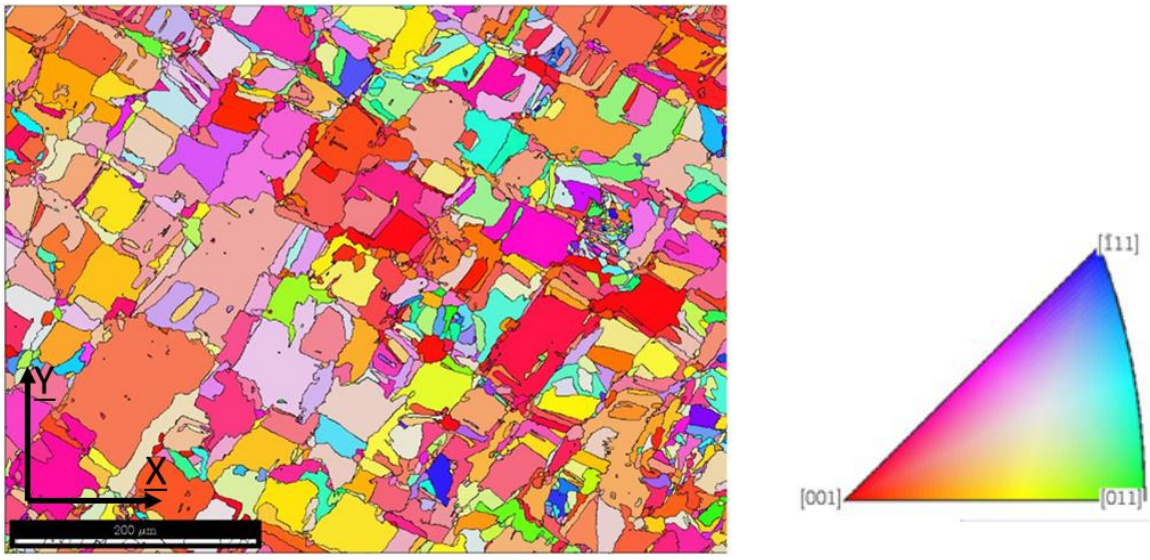

Figure II-6: Post-treated EBSD mapping of the Z-plane

(a) bottom (b) middle (c) top

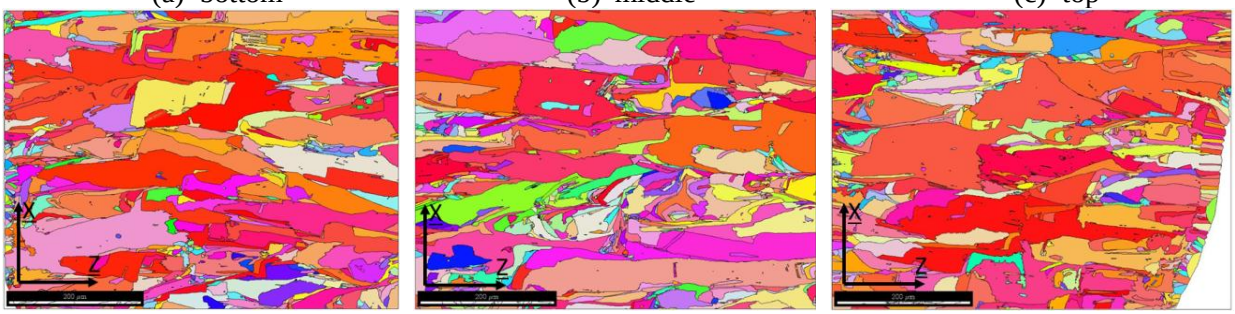

Figure II-7: Post-treated EBSD mappings of the X/Y-plane

Les figures de pôle et les figures de pôle inverses montrent que la microstructure générée est fortement texturée. On observe une orientation préférentielle très marquée de type <100> (l'axe <100> du cristal coïncide majoritairement avec l'axe de fabrication Z).

(a) Figures de pôle obtenues à partir de la cartographie du plan Z (grains)

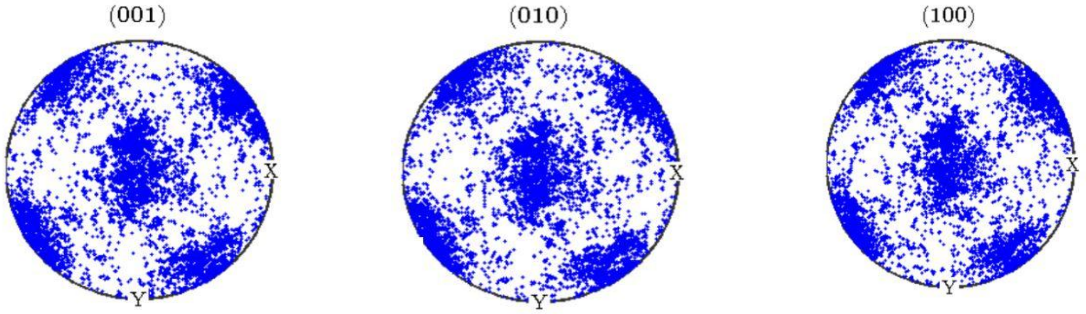

(b) Figures de pôle inverses obtenues à partir de la cartographie du plan Z (grains)

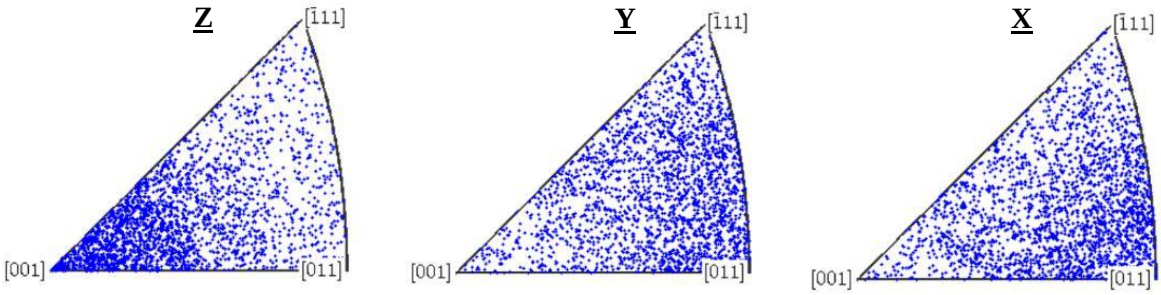

Figure II-8: (a) pole figures and (b) inverse pole figures representing the mean orientations of the grains observed in the mapping of Z-plane

L'orientation préférentielle des grains a un impact significatif sur leur comportement élastoplastique. Certes, les mécanismes de plasticité sont différents d'une orientation à l'autre. Il a été montré que les grains orientés <100> // Z se déforment par glissement plastique tandis que ceux orientés selon <110> // Z se déforment essentiellement par micro-maclage. Il en résulte une bien meilleure ductilité et résistance des matériaux avec une orientation <110> // Z prédominante (effet TWIP). Plusieurs composites cristallographiques lamellaires sont étudiés afin de combiner les effets bénéfiques de chacune des orientations (Sun *et al.*, 2019). Ce type de microstructure a également été obtenu par Andreau et al. (Andreau, Koutiri, *et al.*, 2019).

II.3. Caractérisation des défauts inhérents

Dans cette section, nous nous intéressons à la caractérisation et à la quantification des défauts de surface et de volume générés par SLM. Tout d'abord, les surfaces de plusieurs échantillons rectangulaires et cylindriques ont été caractérisées à l'aide du système de rugosité optique ALICONA. Ensuite, les défauts de volume ont été quantifiés en utilisant la technique de micro-tomographie aux rayons X (µCT).

II.3.1. Caractérisation de l'état de surface

Les pièces SLM à l'état de fabrication présentent une rugosité de surface élevée. Ceci est principalement attribué à l'effet d'étape d'escalier de ce processus. Dans ce travail, la rugosité surfacique et linéique de plusieurs échantillons a été étudiée. L'objectif est d'analyser l'effet de l'emplacement des

éprouvettes sur la rugosité de surface telle que construite. Pour chaque plateau, la rugosité est étudiée sur 3 éprouvettes de flexion (2 mesures par éprouvette correspondant à 2 faces) et 3 éprouvettes de torsion (1 mesure par éprouvette). Les résultats typiques pour chaque échantillon sont illustrés dans la *Figure II-9*.

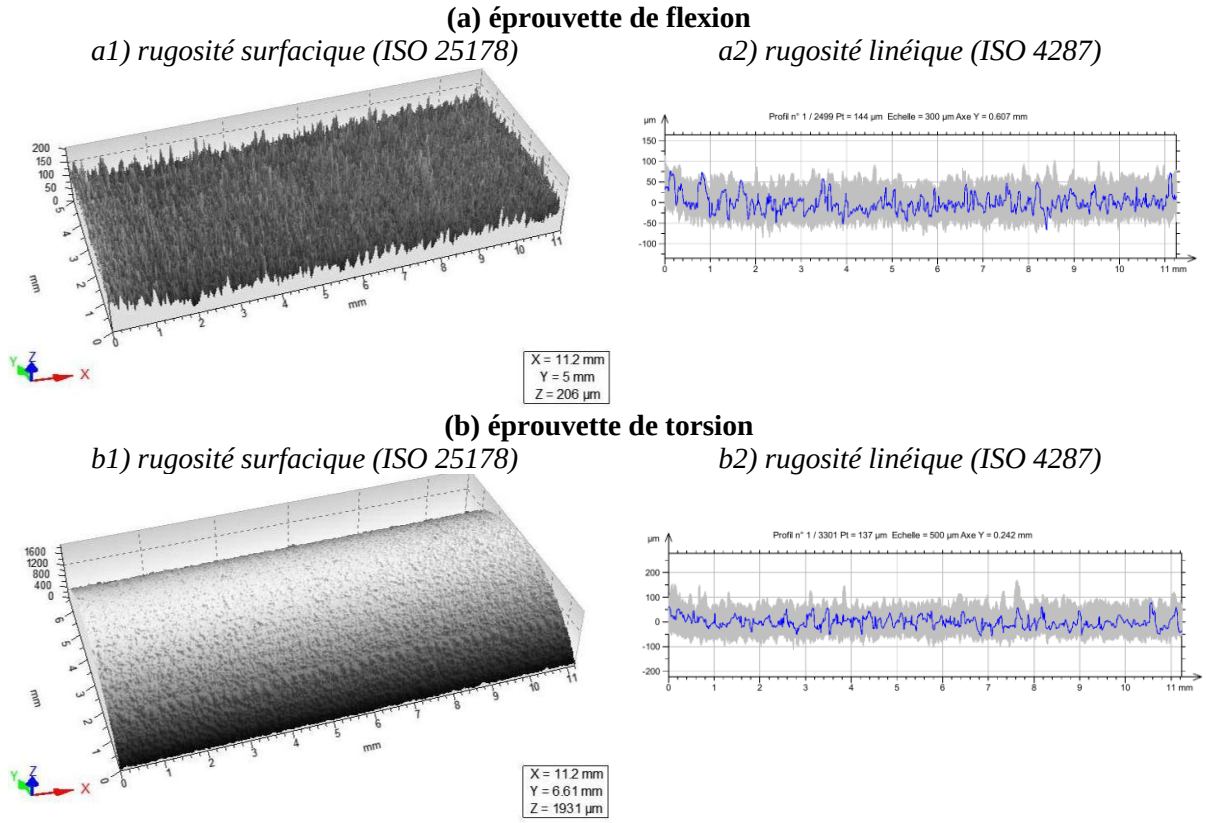

Figure II-9: Surface and linear roughness in (a) bending specimen and (b) torsion specimen

Plusieurs indicateurs de rugosité surfacique et linéique ont été calculés en utilisant les normes ISO 25178 (pour la rugosité surfacique) et ISO 4287 (pour la rugosité linéique). Cette analyse montre que la rugosité des éprouvettes est presque identique quel que soit leur emplacement dans le plateau de fabrication. Il est à noter que la rugosité linéique de l'échantillon tel que construit est relativement importante : Ra = 7~15 µm. Le nuage de points obtenu par cette analyse peut être utilisé pour créer une rugosité réaliste dans le modèle numérique.

II.3.2. Porosity characterization

La micro-tomographie a été réalisée sur 6 échantillons de 4 mm de diamètre et 10 mm de longueur. La capacité du dispositif utilisé, la taille de l'échantillon et les paramètres d'acquisition permettent de ne visualiser que les défauts supérieurs à 8 µm (correspondant à la taille d'un pixel). Les défauts de diamètre inférieur à 8 µm ne peuvent pas être détectés par cette méthode. Malgré cette limitation, cette technique est considérée comme suffisante car les défauts inférieurs à ce seuil n'ont aucun effet sur la résistance à la fatigue. En prenant les images dans les autres plans, il est possible de reconstruire le modèle 3D des défauts. Ce traitement a été réalisé à l'aide des logiciels *imageJ* et *slicing 4D*. Les défauts détectés ont un diamètre équivalent inférieur à 4 pixels (30 µm) et ils sont répartis aléatoirement dans le volume.

Enfin, le *Table II-2* illustre la porosité des échantillons correspondant aux plateaux 1 et 2. A partir des résultats de cette analyse, on peut conclure que le niveau de porosité moyen est généralement inférieur à 0,04%.

Table II-2: Porosity of the samples measured

Échantillon	Plateau 1 (Rayon= 1,8mm)			Plateau 2 (Rayon = 1,8mm)		
	S1	S2	S4	S2	S4	S5
Volume du vide (mm^3)	0,0051	0,0244	0,0244	0,0244	0,0019	0,1286
Porosité (%)	0,0074	0,0352	0,0352	0,0352	0,0027	0,1856

II.4. La réponse mécanique

II.4.1. Mesure de dureté

La microdureté du matériau a été mesurée dans la section d'un échantillon cylindrique dans trois directions différentes. Il n'y a pas de gradient de dureté en allant de la surface vers le cœur de l'échantillon. Les résultats de mesures de dureté (macro) dans le plan X/Y sont présentés dans le *Table II-3*. On constate qu'il n'y a pratiquement pas de différence entre le plan Z et le plan X/Y et d'un échantillon à l'autre. La valeur de la dureté est comparable à celles trouvées dans la littérature (Kruth *et al.*, 2010). En effet, Tucho et al. (Tucho *et al.*, 2018) ont étudié l'influence des paramètres du processus : puissance laser, vitesse de balayage, épaisseur de couche et distance entre les passages laser sur la dureté Vickers. Ils ont montré que cela peut varier de 185 à 282 Hv.

Table II-3: Macro-hardness of tested specimens

Échantillon	Moyenne de dureté (Hv)
Plateau2, S4 (milieu)	224
Plateau 2, S4 (haut)	223
Plateau 2, S3 (milieu)	231
Plateau 2, S3 (bas)	229
Plateau 2, S3 (haut)	222

II.4.2. Essai de traction monotone

Pour analyser les propriétés mécaniques de l'acier 316L étudié, des essais de traction monotone jusqu'à rupture ont été réalisés. Les essais ont été contrôlés à une vitesse de déformation à $10^{-3}\,s^{-1}$ à l'aide d'un extensomètre d'une longueur initiale de 12,5 mm. Les courbes contrainte-déformation sont tracées sur la *Figure II-10*. En raison de la limitation de la plage de l'extensomètre, l'extensomètre a été remis à zéro une fois que la déformation mesurée a atteint 15%. Le redémarrage de l'extensomètre a été répété 4 fois pour atteindre un allongement de l'échantillon à environ 60%.Le module de Young estimé est de 150 GPa en raison de l'anisotropie introduite par la microstructure fortement texturée.

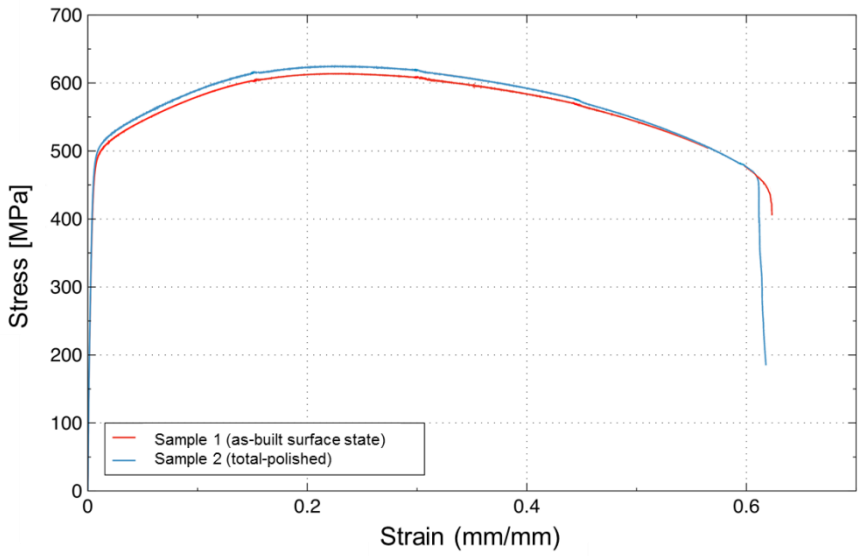

Figure II-10: Tension curves for the raw surface specimen (red) and for the polished surface specimen (blue)

Le comportement mécanique en statique a été étudié pour différentes directions de fabrication et différents paramètres dans la littérature. Une large dispersion sur ces quantités a été observée (*Table II-4*). Cette dispersion des propriétés mécaniques s'explique par la diversité des paramètres de fabrication choisis. Dans ce tableau, seules les valeurs des éprouvettes fabriquées verticalement sont collectées. L'augmentation significative (35 à 100%) de la limite d'élasticité (YS) de l'acier 316L obtenu par SLM, par rapport à celle obtenue classiquement, pourrait s'expliquer par la structuration multi-échelles de la microstructure, notamment grâce à la présence de sous-structures de dislocation cellulaire. Cette dernière permettrait un durcissement du matériau par effet Hall-Petch selon certains auteurs (Zhong *et al.*, 2016), mais, récemment, cette hypothèse est nuancée par Bahl et al. (Bahl *et al.*, 2019) ainsi que par Li et al (Li *et al.*, 2019). Ces derniers rapportent respectivement que la relation de Hall Petch ne peut pas être appliquée de manière aussi simple car le coefficient de franchissement des murs n'est pas le même pour les HAGB (> 15°) ou les parois cellulaires (environ 2°) et qu'en plus, pour des cellules plus petites, des résistances élastiques plus faibles ont été obtenues.Les valeurs de contraintes maximales (UTS) restent du même ordre de grandeur (mais souvent dans la fourchette supérieure) que pour les méthodes traditionnelles. Cependant, on sait que les défauts sont plus nombreux dans les matériaux obtenus par SLM (en particulier les porosités). Cela indique que le matériau 316L obtenu par SLM a une tolérance au dommage élevée. La particularité de l'acier 316L obtenu par SLM est son rapport YS / UTS élevé (*Table II-4*). En effet, il est généralement compris entre 0,7 et 0,9 alors qu'il est classiquement compris entre 0,4 et 0,5. Ceci est d'autant plus intéressant que, pour les matériaux classiques, une augmentation de ce rapport conduit généralement à une diminution de l'allongement à la rupture. Cependant, pour l'acier 316L obtenu par SLM, l'ordre de grandeur de l'allongement à la rupture reste généralement le même voire plus élevé que pour l'acier 316L classique. Cette valeur élevée du rapport YS / UTS est probablement associée au durcissement induit par le procédé SLM. Lors de la fabrication,

du fait des forts gradients thermiques, des contraintes apparaissent à l'échelle des grains ce qui implique la prolifération de nombreuses dislocations, elles-mêmes à l'origine de l'écrouissage.

Le module d'élasticité du 316L obtenu par SLM est généralement inférieur à celui du 316L forgé. Plusieurs explications existent dans la littérature. Certains auteurs lient cette baisse à la présence de défauts affectant la rigidité du matériau et d'autres liés à l'anisotropie cristalline du matériau. Dans cette étude, cette hypothèse est retenue et vérifiée par modélisation numérique. Enfin, l'acier 316L produit pour cette étude présente des propriétés de traction mécanique comparables à la littérature. On observe une légère augmentation de l'allongement à la rupture (60% contre maximum 54% dans la littérature).

Table II-4: Manufacturer and literature data of the mechanical properties in uniaxial tension of SS 316L obtained by SLM

	UTS (MPa)	YS (MPa)	YS/UTS	A%	E (GPa)
HT - Present study	**610 - 630**	**450 - 470**	**0.74**	**60**	**150 - 157**
As built- manufacturers data EOS (PILLOT, 2016)	540 ± 55	470 ± 90	0.87	50 ± 20	180
As built- SLM Solutions (PILLOT, 2016)	654 ± 49	550 ± 39	0.84	35 ± 4	169 ± 31
As built- Tolosa 2010 (Tolosa *et al.*, 2010)	570 - 590	530 - 560	0.94	42 - 45	
As built- Kuznetzov 2016 (Kuznetsov *et al.*, 2016)	685 - 708	567 - 582	0.83	34 - 35	
As built- Liverani 2017 (Liverani *et al.*, 2017)	540 - 570	420 - 500	0.84	40 - 70	
As built- Riemer 2014 (Riemer *et al.*, 2014)	565	462	0.82	54	
As built- Bahl 2019 (Bahl *et al.*, 2019)	565 ± 10	480 ± 20	0.85	44 ± 5	
As built- Spierings 2011 (Spierings, Starr and Wegener, 2013)	760	640	0.84	30	
As built- Salman 2019 (Salman *et al.*, 2019)	1016 ± 8	550 ± 10	0.54	50	
Forged, ASM Handbook (1993)	*620*	*310*	*0.5*	*30*	*205*

II.4.3. Essai de traction cyclique

Pour caractériser le comportement cyclique de l'acier 316L, une série d'essais de traction – compression a été réalisée sur les éprouvettes telles que construites pour les essais monotones. La vitesse de déformation utilisée est de 10^{-3} s^{-1}. Le *Table II-5* illustre les niveaux de déformation imposés, le nombre de cycles avant rupture et l'adoucissement moyen pour 100 cycles calculé pour la partie linéaire des courbes d'adoucissement (voir *Figure II-15*).

Table II-5: Low cycle tension-compression fatigue tests

Échantillon	Déformation (%)	Rupture (cycles)	Δσ par 100 cycles (MPa)
Plateau 2, S5	±0.30	81815	0.02
Plateau 1, S1	±0.45	10931	0.24
Plateau 2, S2	±0.60	5390	0.67
Plateau 1, S4	±0.75	2767	1.49

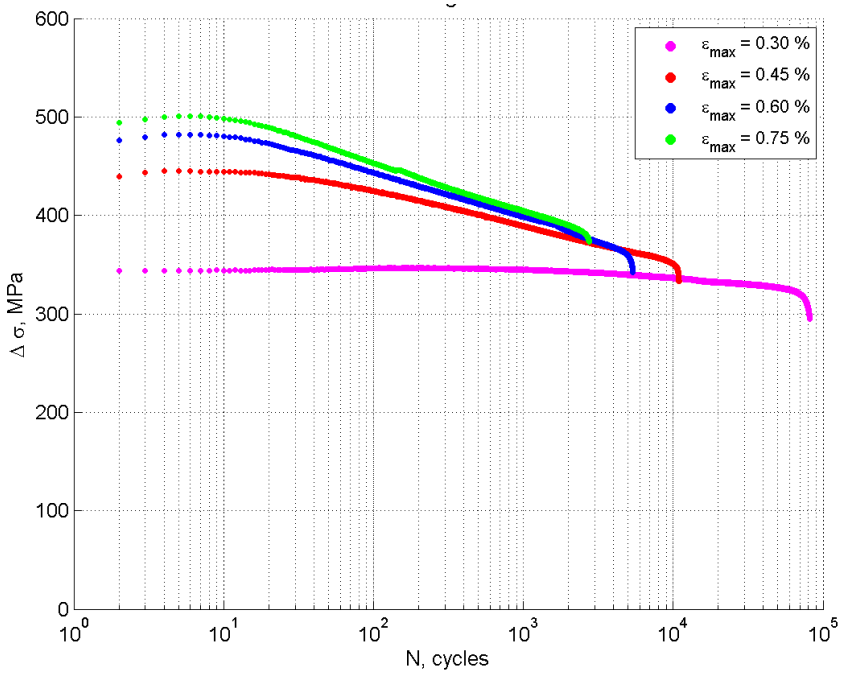

Figure II-15: Cyclic softening curves under different cyclic deformations

En traction-compression à déformation imposée, on observe classiquement un adoucissement cyclique du matériau comme illustré ci-dessus. Ce comportement est également observé sur l'acier 316L conventionnel (Mu *et al.*, 2013). Cependant, il est intéressant de noter une asymétrie de comportement entre la traction et la compression pour l'acier obtenu par SLM, cela peut être dû à un effet Bauschinger. De plus, le phénomène d'adoucissement est beaucoup plus prononcé en traction qu'en compression, à tel point que l'asymétrie traction-compression n'est plus observable après un certain nombre de cycles.

II.5. Conclusion

Les propriétés métallurgiques et mécaniques de l'acier 316L élaboré par SLM sont fortement dépendantes des paramètres de fabrication. Les observations microscopiques ont montré les défauts de surface et la micro-tomographie a mis en évidence la présence de pores dans le volume. D'après l'analyse de la macro et microstructure, on voit que le matériau est fortement texturé, avec des grains d'austénite colonnaires le long de l'axe de fabrication. Ces observations ont été confirmées par l'EBSD qui a permis de caractériser plus précisément la structure cristalline du matériau. Les mesures de rugosité de surface sur les échantillons bruts ont montré qu'à certains endroits, le niveau de rugosité pouvait dépasser 200 µm. Les résultats de dureté montrent que la dureté est dans la plage de 220 à 250 HV, ce qui est cohérent avec les résultats sur le même matériau fabriqué de manière conventionnelle. L'essai de traction monotone prouve que l'éprouvette SLM est similaire aux éprouvettes conventionnelles en termes d'UTS et d'allongement. Mais pour les modules de Young, la valeur déterminée est plus faible (environ 150 MPa) et inférieure à la valeur nominale du 316L. Des essais de comportement cyclique traction-compression ont été également réalisés. Quatre niveaux de déformation ont été imposés : ± 0,30%, ± 0,45%, ± 0,60%, ± 0,75%. Pour chaque essai, nous avons pu comparer les courbes d'hystérésis et les

courbes d'adoucissement cyclique. Selon l'analyse, avec l'augmentation de la déformation imposée, la courbe d'hystérésis devient plus ouverte et l'adoucissement plus exprimé. A titre de comparaison, l'adoucissement de l'éprouvette testée à $\varepsilon = \pm 0{,}30\%$ ne dépasse pas 0,02 MPa pour 100 cycles, tandis que celui de l'éprouvette $\varepsilon = \pm 0{,}70\%$ est de 1,49 MPa.

Chapitre III. Les expériences et analyses sur la tenue en fatigue

Les résultats des essais de fatigue sont présentés dans ce chapitre. Différents chargements ont été étudiés : traction, flexion et torsion. Pour chaque condition de chargement, différents états de surface sont étudiées pour révéler l'effet de l'état de surface sur les performances en fatigue à grand nombre de cycles (FGNC). Pour comprendre le mécanisme d'initiation des fissures de fatigue, des analyses fractographiques sont effectuées. Étant donné que des défauts ont été toujours observés sur le site d'amorçage de la fissure, on pense que la rupture par fatigue du 316L obtenu par SLM est générée par les défauts résultats du procédé. Les tailles des défauts observés sont ensuite mesurées et sont corrélées avec les limites de fatigue obtenues.

III.1. Analyse de la résistance à la fatigue à grand nombre de cycles

Les détails des essais de fatigue effectués lors de cet étude sont indiqués dans l'annexe A. Les données traitées sont reportées dans les figures suivantes pour les différents chargements. Le rapport de charge appliqué le long de cette étude est R=-1. Les limites de fatigue calculées par la méthode de l'escalier sont répertoriées dans le *Table III-1*.

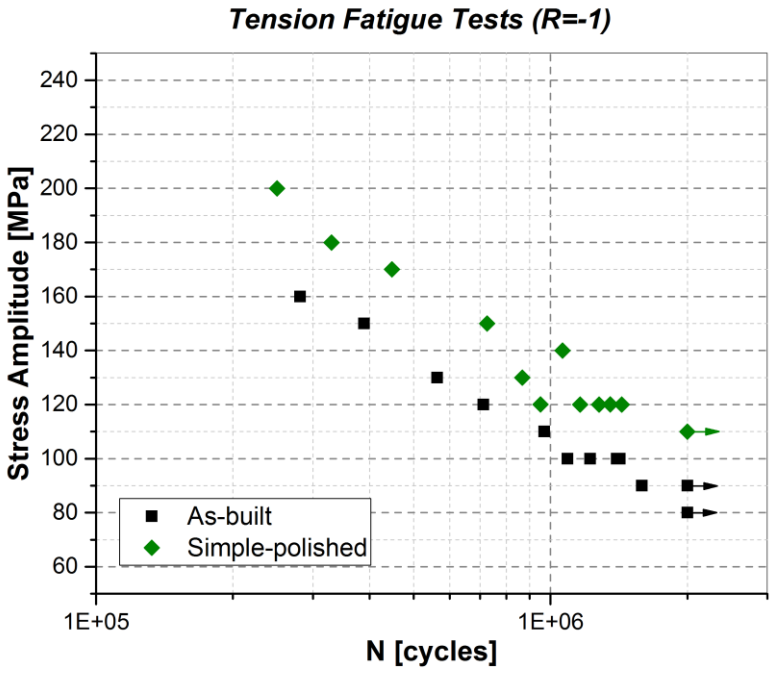

Figure III-1: S-N curves for two surface state conditions (As-built and Simple-polished) in fully reversed uniaxial tension/compression

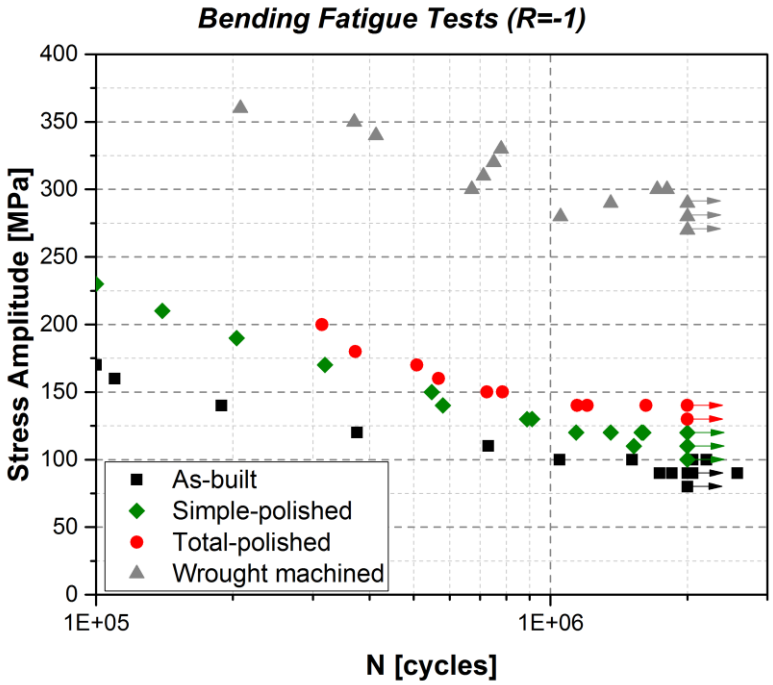

Figure III-2: S-N curves for three surface state conditions (As-built, Simple-polished and Total-polished) in fully reversed plane bending. The fatigue test results for machined specimens of wrought 316L steel are also given for comparison.

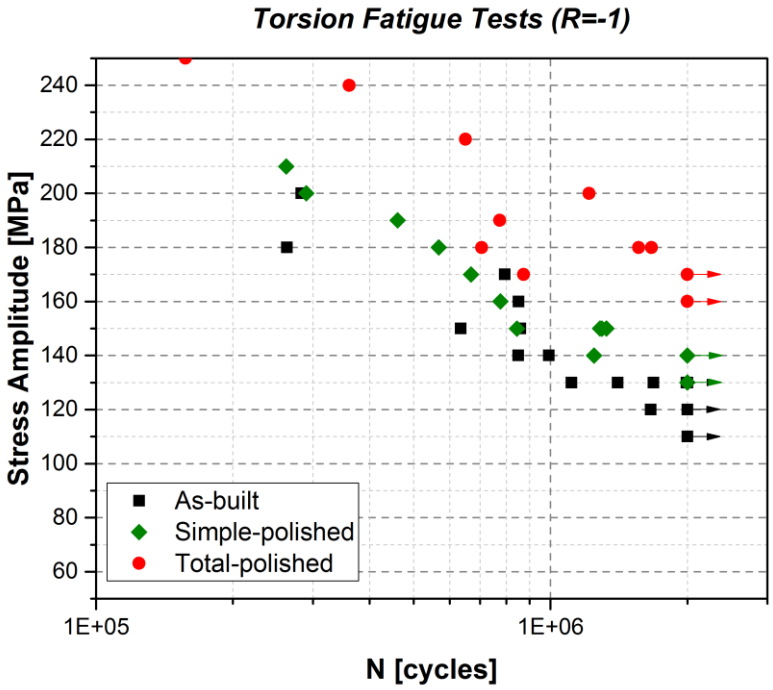

Figure III-3: S-N curves for three surface state conditions (As-built, Simple-polished and Total-polished) in fully reversed torsion

TableIII-1: Fatigue strength values assessed with the staircase method for different surface state conditions and different loading modes

État de surface	Chargement		
	Traction	Flexion	Torsion
As-built (AB)	**92.5**	**90**	**127**
Simple-polished (SP)	**115** (24% ↑)	**116** (29% ↑)	**143** (12% ↑)
Total-polished (TP)	-	**138** (53% ↑)	**172** (35% ↑)

Unit: MPa

III.1.1. Effet de l'état de surface

Dans la présente étude, deux traitements mécaniques de la surface nommés polissage simple (SP) et polissage total (TP) sont appliqués sur une partie des éprouvettes. Les éprouvettes brutes sont nommées les AB (As-Built). Le polissage simple (SP) indique le processus où l'échantillon est poli par papier de verre jusqu'à obtenir un état miroir. Les échantillons entièrement polis (TP) sont soumis à un polissage supplémentaire au papier de verre pour enlever environ 200 µm.

Un polissage simple augmente la résistance à la fatigue de 92,5 MPa à 115 MPa en traction et conduit donc à une augmentation de 24% de la limite d'endurance en traction. De même, les essais de flexion montrent une augmentation de 29% de la limite de fatigue pour les éprouvettes SP par rapport aux éprouvettes brutes (AB). Les résultats de la torsion sont légèrement différents. Les éprouvettes brutes (AB) ont une limite d'endurance de 127 MPa tandis que les éprouvettes SP donnent une estimation de 143 MPa. La différence est donc de 12% et est inférieure à celle des deux autres modes de chargement. L'élimination de la rugosité de surface optimise la résistance à la fatigue de l'acier 316L obtenu par SLM. L'amélioration est plus accentuée sous en traction ou en flexion.

III.1.2. Effet du mode de chargement

Aucune différence notable n'a été observée entre les essais de fatigue en traction et en flexion. Des recherches antérieures rapportent souvent que la limite de fatigue en flexion est supérieure à la limite de fatigue en traction en raison de l'effet de gradient de contrainte (Wentzel and Huang, 2015). Etant donné que dans l'étude actuelle, les limites de fatigue sous charge de traction et charge de flexion sont remarquablement inférieures aux limites de fatigue courantes du 316L fabriqué de manière conventionnelle, l'effet du gradient de contrainte pourrait être masqué par d'autres phénomènes. Les résultats obtenus révèlent également une découverte intéressante : l'acier 316L obtenu par SLM a une résistance à la fatigue plus élevée sous charge de torsion par rapport à sa limite d'endurance sous charge de flexion et de traction. Indépendamment de l'hétérogénéité microstructurale, le chargement en torsion provoque un état de cisaillement pur tandis que la charge en traction induit une contrainte de cisaillement perpendiculaire à sa direction de contrainte principale avec la moitié de son amplitude. On s'attend à ce que la limite de fatigue en traction soit supérieure à la limite de fatigue en torsion. Compte tenu de la microstructure distinguée du matériau obtenu par SLM, on peut supposer que l'orientation

préférentielle des grains, la taille des grains hétérogènes et la disposition des grains colonnaires sont responsables du résultat inhabituel. Aussi, si l'on tient compte du fait que l'élimination de la couche superficielle peut augmenter la limite de fatigue de façon remarquable, le positionnement et la disposition des défauts sub-surfaciques doivent être étudiés quant à leurs influences sur la répartition des contraintes.

III.2. Analyse fractographique de l'amorçage de fissures de fatigue

Les observations des faciès de rupture sont réalisées pour révéler les causes et les sites d'amorçage de la fissure de fatigue. D'après l'analyse précédente, les performances en fatigue de l'acier 316L obtenu par SLM sont plus faibles que celles du 316L forgé (classique). Une analyse fractographique, est menée donc dans cette section pour explorer le mécanisme de rupture par fatigue dans ce matériau. Toutes les éprouvettes de flexion et de torsion sont inspectées. Les éprouvettes de traction ne sont pas exploitables car les faciès de rupture sont endommagés lors des processus cycliques de traction-compression car le rapport de charge est de R=-1.

III.2.1. Eprouvettes de flexion

Toutes les fissures observées dans cette étude sont initiées principalement à partir d'un défaut de manque de fusion (LoF : Lack of Fusion). La porosité mesurée pour les échantillons utilisés dans cette étude est inférieure à 0,05%. Le défaut LoF est généralement de géométrie plate et indétectable par micro-tomographie (µCT). Mais la morphologie allongée et la pénétration profonde de ces défauts de LoF sont très néfastes en fatigue. Un simple polissage enlevant une fine couche de la surface ne peut éliminer que la rugosité. Les défauts de LoF peuvent encore être observés dans les faciès de rupture. Un polissage total (TP) éliminant une couche de 200 à 250 µm semble être insuffisante pour éliminer tous ces défauts de LoF sous la surface. On peut en déduire que la distribution des défauts LoF est fortement concentrée à l'extrême surface. Sous une certaine profondeur, la présence du défaut LoF diminue.

Dans la plupart des cas, nous avons observé qu'une seule fissure de fatigue tandis qu'une fissuration multiple a été observée plusieurs fois pour les échantillons bruts (AB) et avec polissage simple (SP). Un examen plus attentif de la fissure montre que plusieurs sites d'initiation de fissure peuvent être détectés sur les faciès. Tous les sites d'initiation se trouvent à la surface ou sous la surface. Le niveau de contrainte atteint sa valeur maximale en surface sous chargement de flexion. En revanche, le défaut de surface ne peut pas être totalement éliminé.

III.2.2. Eprouvette de torsion

Dans la théorie classique de la mécanique de la rupture, la propagation de la fissure est catégorisée selon trois modes : le mode d'ouverture, le mode de glissement et le mode de déchirement. Dans le cas de la fatigue à grand nombre de cycles sous traction ou flexion, le mécanisme de propagation des fissures de fatigue appartient toujours au mode I. En torsion, la fissure se fait en mode II dans la première étape.

L'éprouvette est à l'état de contrainte de cisaillement pure quelle que soit l'hétérogénéité des défauts. La contrainte de cisaillement agit sur le défaut et conduit à un chemin de fissure sur le plan de contrainte de cisaillement maximale. Après un certain seuil, la contrainte normale domine la propagation de la fissure et modifie le chemin de la fissure. La fissure se propage dans deux directions perpendiculaires aux deux extrémités ayant la contrainte normale maximale jusqu'à la rupture.

Tout d'abord, pour les échantillons de flexion et de torsion, les sites d'initiation de fissures se révèlent toujours être des défauts LoF. L'origine des pores de manque de fusion dans le contour n'est pas claire mais pourrait être attribuée à la combinaison de plusieurs phénomènes. Pour commencer, il peut se produire un manque de chevauchement entre les cordons de soudage suffisant entre le point de départ et le point d'arrivée d'un contour circulaire. De plus, une interaction entre le laser et des contaminants tels que des projections ou des nanoparticules dans des trajectoires laser spécifiques pourrait induire des hétérogénéités dans la forme du bain de fusion, et ainsi avoir un impact sur le chevauchement de ces bains de fusion. En particulier, les défauts ont souvent une forme allongée et pénètrent dans la surface libre de l'éprouvette. L'existence de défauts est généralement préjudiciable à la résistance à la fatigue, sans parler de la dimension et de la forme du défaut. Un autre problème est que la limite de fatigue de torsion est supérieure à la limite de fatigue de flexion. D'après les observations des faciès de rupture, nous savons que le mécanisme de rupture par fatigue est toujours la contrainte de cisaillement entraînée dans la première étape. La question soulevée par les essais de fatigue selon laquelle la limite de fatigue mesurée est inférieure aux attentes peut être partiellement répondue par les observations de fractographie. Même dans l'éprouvette entièrement polie, de gros défauts LoF peuvent encore être trouvés. Par conséquent, la limite de fatigue mesurée dans l'étude actuelle n'est pas comparable aux valeurs rapportées dans la littérature qui proviennent d'échantillons polis.

III.3. Corrélation entre la taille du défaut et le comportement en FGNC

III.3.1. Détermination de la taille des défauts

Outre la surface rugueuse des pièces brutes issues du procédé SLM qui apporte beaucoup de défauts de surface, la porosité de la phase solide apporte également des défauts internes. La porosité peut être classée en deux types : les pores de gaz et les pores de manque de fusion. Les pores de gaz ont généralement la forme d'une sphère et ont une taille inférieure à 100 µm. Les défauts manquent de fusion (LoF) sont souvent allongés et non sphériques. La forme irrégulière du défaut LoF rend difficile le choix d'un paramètre représentatif pour décrire sa dimension géométrique. Différentes méthodes de mesure sont proposées dans la littérature. Des illustrations schématiques sont présentées à la *Figure III-4*. Selon la définition originale du paramètre de Murakami (Murakami, 2002), la zone considérée doit être un contour lisse enveloppant le contour irrégulier du défaut. Romano et Beretta (Romano, Miccoli and Beretta, 2019) mesurent la surface réelle du défaut LoF et utilisent un cercle équivalent pour remplacer le défaut. Le et al. (Le *et al.*, 2018) utilisent le diamètre de Feret ainsi que le paramètre de Murakami

qui est la racine carrée de l'aire projetée sur le plan normal à la direction de chargement. El Khoukhi (El Khoukhi *et al.*, 2019) choisit la profondeur du défaut comme paramètre de description. Néanmoins, aucune des méthodes ci-dessus ne peut traiter plusieurs défauts sur le site d'initiation de la fissure. Dans les travaux d'Iben Houria (HOURIA, 2015), l'auteur a proposé une alternative pour considérer deux défauts en une seule initiation de fissure. Si les deux défauts sont proches l'un de l'autre, ils seront traités comme un seul gros défaut. Un rectangle est utilisé pour superposer ces deux défauts et sa $\sqrt{Area}$ est considérée comme la taille effective du défaut.

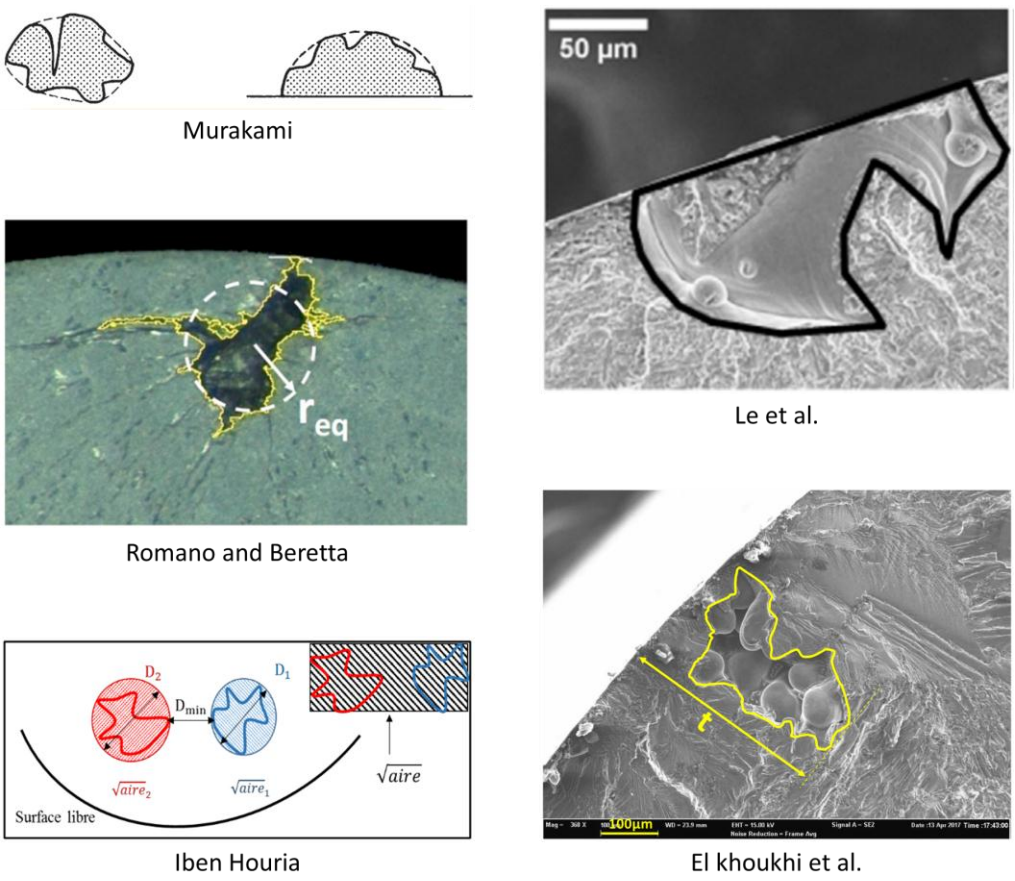

Figure III-4: Different methods proposed to measure irregular defect(s) (HOURIA, 2015; Le et al., 2018; El Khoukhi et al., 2019; Romano, Miccoli and Beretta, 2019))

Lors de l'observation des faciès de rupture en fatigue de l'acier 316L obtenu par SLM, plusieurs défauts sont fréquemment rencontrés, en particulier pour l'éprouvette brute (AB). Pour le cas où plus de deux défauts peuvent être trouvés sur un site d'initiation, aucun traitement approprié n'est trouvé dans la littérature. Afin d'avoir une compréhension statistique des défauts observés dans nos essais, nous proposerons un traitement pratique en modifiant les méthodes mentionnées. Nous utiliserons toujours une coque convexe comme zone efficace pour recouvrir les défauts. La description originale de la zone efficace est « un contour lisse », selon Murakami lui-même. Cependant, le choix d'un contour lisse est fortement déterminé par l'opérateur. En utilisant une coque convexe, la mesure sera cohérente sans l'influence de facteurs artificiels. Un autre avantage de la coque convexe est que le diamètre du Feret

restera inchangé comme celui de la forme du défaut d'origine. Nous utiliserons une stratégie différente pour mesurer et corréler les multiples défauts adjacents observés. La méthode conservatrice consiste à ne choisir que le plus gros défaut. La méthode extrême est de prendre en compte tous les défauts observés sur un site. La *Figure III-5* illustre deux exemples : un exemple de mesure de mesures conservatrice et un exemple de mesure extrême.

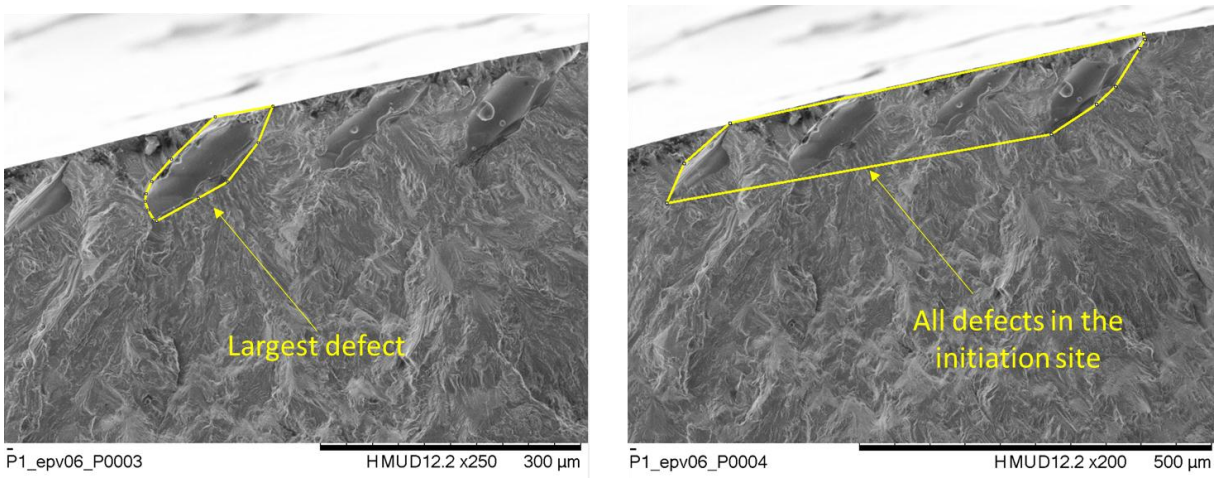

Figure III-5: Two different measurement techniques to assess the size of a cluster of adjacent defects

Compte tenu de la complexité de la forme du défaut LoF, même si elle est convertie en coque convexe, nous utiliserons plusieurs paramètres pour décrire les défauts critiques observés lors des expériences. Le paramètre de Murakami, le diamètre de Feret ainsi que la profondeur du défaut seront utilisés pour identifier la relation entre les performances de fatigue et la taille critique du défaut. De plus, nous définissons un nouveau paramètre appelé « Diamètre Féret modifié » qui est la racine carrée du produit du diamètre Féret maximum et du diamètre Féret minimum. Le produit du diamètre maximum de Feret et du diamètre minimum de Feret est équivalent à l'aire du rectangle minimum unique qui recouvre les défauts considérés. Ce paramètre est considéré comme la description la plus régulière du ou des défauts irréguliers.

III.3.2. Diagramme de Kitagawa-Takahashi

Les résultats des mesures conservatrices ne sont pas idéaux. On constate qu'aucun de ces paramètres ne permet de distinguer différentes finitions de surface. Les éprouvettes totalement polis (TP) sont représentées par des marques rouges ; Les éprouvettes SP sont indiquées par des marques vertes et les éprouvettes brutes (AB) sont indiquées par des marques bleues. Pour le plus gros défaut, les trois lots d'éprouvettes ne présentent pas de tendance significative entre la taille du défaut et la limite de fatigue.

En termes de profondeur du défaut critique, les deux lots polis ne peuvent pas être distingués. Les profondeurs des défauts sur la surface sont influencées par le polissage. Mais les pores de la sous-surface ne sont pas affectés et sont ramenés à la surface après le polissage. Surtout pour les échantillons totalement polis, les défauts critiques se trouvent souvent sous la surface. Malgré le fait que les défauts

de l'échantillon totalement poli sont de petite taille, ce qui peut être noté à partir d'autres paramètres décrivant la zone, les profondeurs peuvent être aussi grandes que celles des éprouvettes brutes (AB). Compte tenu des trois autres paramètres, les défauts dans les échantillons totalement polis sont toujours plus petits par rapport à leur homologue dans les deux autres lots. Mais les éprouvettes SP et AB ont des résultats similaires. L'explication est que le plus grand défaut trouvé sur le site d'initiation dans ces deux lots est proportionnel, mais les éprouvettes AB ont des défauts plus petits au voisinage du plus grand défaut. Par conséquence, la mesure conservatrice n'est pas un bon choix pour décrire la situation observée dans la présente étude où plusieurs défauts sont présents simultanément.

Les résultats des mesures extrêmes sont encourageants. D'après la *Figure III-6*Figure III-28, à l'exception de la profondeur, les trois autres paramètres présentent l'optimisation de l'état de surface par traitement de surface incrémental. La loi de puissance de Murakami (*Eq. III.1*) donne la prédiction de la limite de fatigue pour un matériau défectueux. Une formule de puissance similaire ($y = a * x^b$) est utilisée pour ajuster les résultats obtenus.

$$\sigma_w = 1.43(H_v + 120) * \sqrt{Area}^{-\frac{1}{6}} \qquad (Eq. III. 1)$$

En utilisant le diamètre de Feret, une pente ajustée d'environ -1/6 qui est en bon accord avec la constante de la loi de puissance de Murakami. Le paramètre Murakami et le paramètre Feret modifié donnent des résultats similaires. Cela démontre que notre mesure est stable. Les coques convexes utilisées dans la mesure du paramètre Murakami et le rectangle virtuel utilisé dans la mesure du paramètre du Feret modifié sont quantitativement approximatives.

(a) (b)

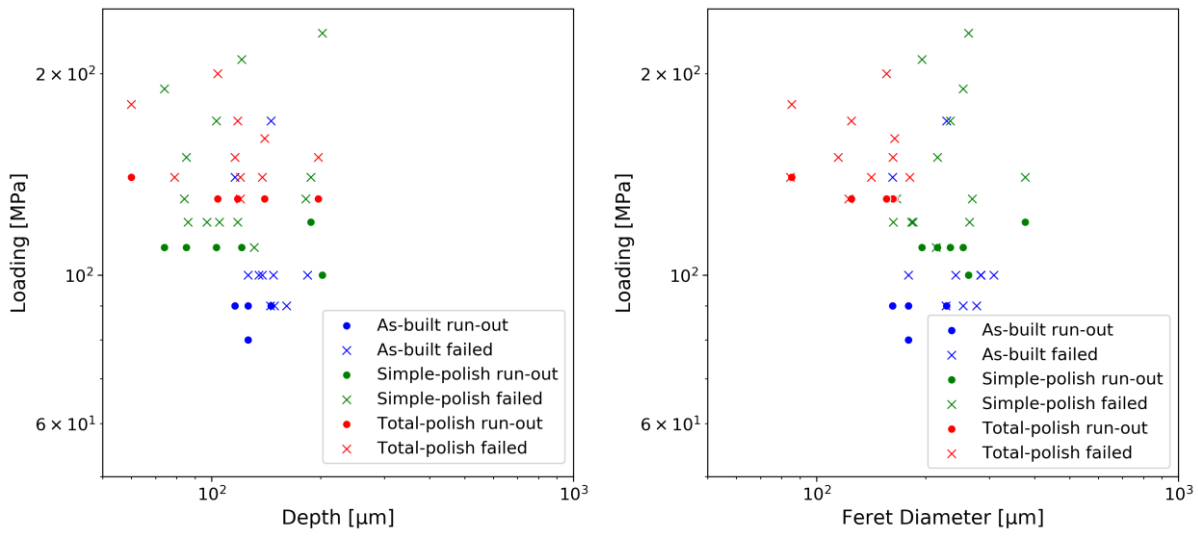

(c) (d)

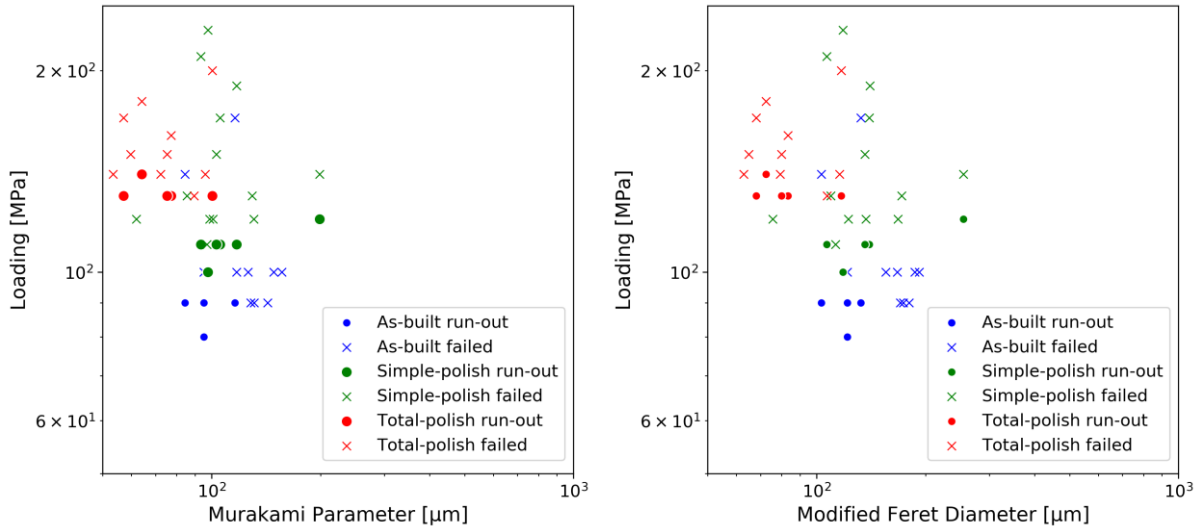

Figure III-5: Kitagawa diagram using the minimalist measurement methods with different parameters as effective defect size: (a) depth, (b) Feret diameter, (c) Murakami parameter, (d) modified Feret diameter

(a) (b)

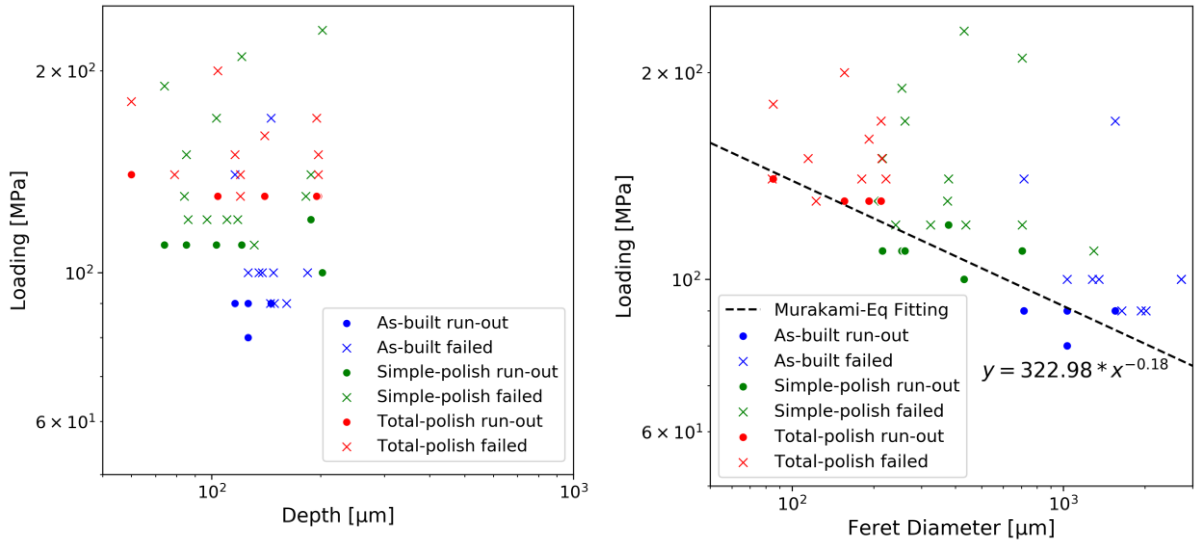

(c) (d)

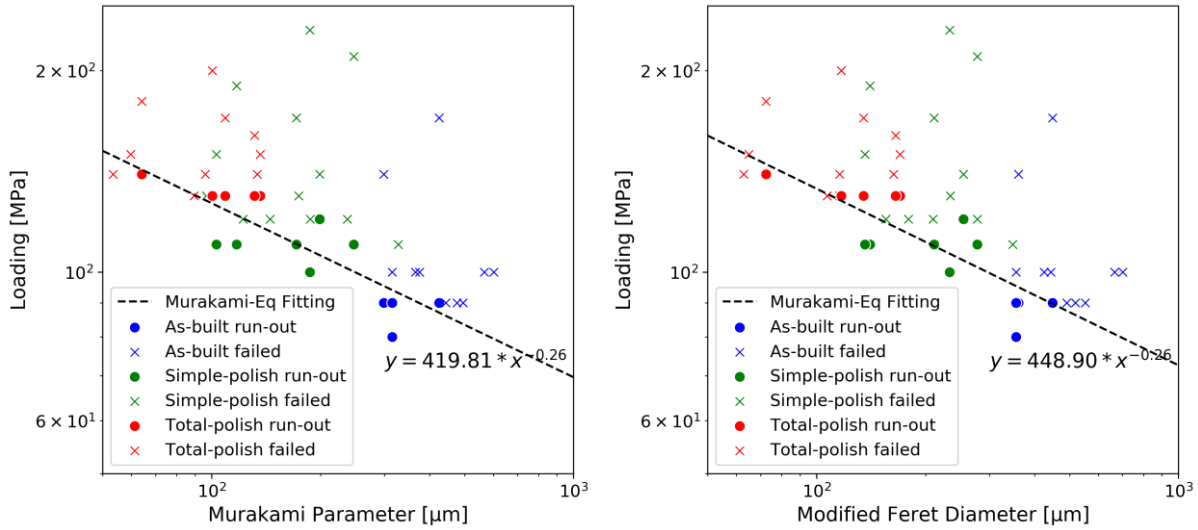

Figure III-6: Kitagawa diagram using the maximalist measurement methods with different parameters as effective defect size: (a) depth, (b) Feret diameter, (c) Murakami parameter, (d) modified Feret diameter

III.4. Conclusion

Le processus de relasage de contour est supprimé dans cette étude pour créer des surfaces plus rugueuses. Mais on constate que ce processus n'augmente pas considérablement la rugosité de la surface car les métriques sont cohérentes avec la littérature qui adopte ce processus, alors que de nombreux défauts de LoF sous la surface sont créés, ce qui modifie considérablement le comportement en fatigue.

L'effet du gradient de contrainte n'est pas observé dans la présente étude expérimentale puisque les essais de fatigue en flexion et en traction donnent des résultats similaires. On suppose que cet effet est secondaire donc dépassé par d'autres effets majeurs tels que la présence de gros défauts. Nous attribuons la faible résistance à la fatigue globale au défaut inhérent, en particulier au défaut de manque de fusion (LoF) en surface ou en sous-surface. Cependant, cela pourrait être controversé car d'autres facteurs potentiels peuvent affecter le comportement en fatigue.

En utilisant la théorie de Murakami pour le comportement à la fatigue des matériaux défectueux, la diminution de la résistance en fatigue est bien corrélée à l'augmentation de la taille effective des défauts. En particulier, pour faire face aux défauts de manque de fusion fréquemment rencontrés, une méthode de mesure modifiée est alors proposée. Une analyse plus approfondie révèle que les défauts adjacents à un site d'initiation agissent de manière intégrée sur la fissure de fatigue. En raison de la présence de plus grands défauts internes de LoF, les effets de la rugosité de surface sur l'amorçage des fissures de fatigue étaient mineurs dans cette étude. Tandis que le défaut LoF inhérent à la fabrication est la principale préoccupation.

En combinant les études expérimentales des chapitres II et III, on obtient une meilleure compréhension des propriétés du matériau, en particulier du comportement en fatigue. Le matériau

étudié partage de nombreuses similitudes avec son homologue conventionnel. La dureté, qui est considérée comme un paramètre indicateur de la résistance à la fatigue de l'acier, ne présente pas de différence évidente entre le 316L élaboré par SLM ou par fabrication conventionnelle (forgé). L'UTS et l'allongement sont également similaires. Même le comportement mécanique cyclique est conforme à celui du 316L forgé. Cependant, les observations de défauts de manque de fusion (LoF) provenant du processus de fabrication sur les faciès de rupture en fatigue, indiquent que ces défauts de surface/sous-surface ont affaibli sa résistance à la fatigue. De plus, un module de Young faible suggère que la microstructure texturée a une influence sur les propriétés mécaniques. La manipulation de la microstructure et des défauts par des moyens expérimentaux étant coûteuse et laborieuse, nous nous tournerons vers des outils numériques pour mieux évaluer l'effet de la microstructure et des défauts de surface.

Chapitre IV. Etude préliminaire de l'effet de la microstructure et des défauts sur la tenue en fatigue

Ce chapitre présente une étude numérique ayant pour but d'enrichir la modélisation en fatigue de matériaux à défauts avec une modélisation explicite de la microstructure. Les critères de fatigue sont utilisés avec une approche non locale afin de faire un lien entre distance critique et taille de microstructure. La comparaison des résultats obtenue est réalisée avec les travaux expérimentaux de Guerchais et al. (Guerchais *et al.*, 2015).

IV.1. Modélisation et influence de la microstructure pour les matériaux à défauts

L'objectif du modèle numérique est d'avoir une description proche de la réalité de la forme des grains ainsi que de leurs distributions cristallographiques. Pour ce qui est de la géométrie des grains, une tessellation de Voronoï est couramment utilisée dans la littérature (Robert and Mareau, 2015). Dans cette étude, une géométrie en 2 dimensions est utilisée car elle permet d'avoir des résultats acceptables tout en ayant besoin de ressources numérique beaucoup plus faible. A titre d'exemple, 1 mm^3 de notre matériau nécessiterais plus de 200000 grains en 3D. Trois lots de modèles sont construits. Le premier correspond à une taille moyenne de grain constant, qui correspond à celle travaux expérimentaux de Guerchais et al. (Guerchais *et al.*, 2015). Le deuxième lot de modèle prend un compte des distributions de taille de grains différente : distribution normale, qui correspond aux acier corroyés, distribution uniforme et distribution log-normale. Enfin le troisième lot prend en compte différente taille de grains. Les chargements sont en traction-compression purement alternée et le défaut est positionné sur la surface libre. L'hypothèse des déformations planes généralisées est faite, ce qui permet de prendre en compte tous les systèmes de glissement. Les orientations cristallographiques sont choisies pour avoir une texture isotrope.

Table IV-1: Characteristics summary of the different configured model

	Model Configurations				Number of simulations
	Defect size	Grain morphology	Grain orientation	Grain size	
Batch1	6 values 5,15,30,60,120,200 µm	4 kinds Voronoi tessellations*4	24 sets Isotropic*24	1 15 µm	576
Batch2	6 values 5,15,30,60,120,200 µm	4 kinds Uniform tessellation, Voronoi tessellation, Log-normal Voronoi tessellation *2	24 sets Isotropic*24	1 15 µm	576
Batch3	3 values 15,60,200 µm	4 kinds Voronoi tessellations*4	12 sets Isotropic*12	2 30,100 µm	288

Même si l'état de contrainte macroscopique est uniaxial, localement l'état de contrainte est multiaxial. Pour cette raison, 3 critères de fatigue multiaxial du type plan critique sont choisi : Matake, Dang Van et Papadopoulos.

Ces travaux sont basés sur la théorie de la distance critique. Elle suppose une zone dans laquelle la déformation plastique est suffisamment élevée pour initier une fissure de fatigue. Pour prendre en compte ce principe, plusieurs méthodes existent : méthode du point, ligne, surface et volume (Bellett *et al.*, 2005). Cette étude utilise une méthode surfacique. Le critère de fatigue est alors moyenné sur une surface avec la relation suivante :

$$\left(\int_S \sigma_{FIP}\, dS\right)/S \leqslant \beta \qquad (IV.7)$$

Avec σ_{FIP}, la contrainte équivalente au sens du critère de fatigue S la surface considérée et β le seuil du critère de fatigue.

Concernant la surface, 2 approches sont proposées. La première, nommée *R**, moyenne sur un disque de rayon R et centré sur le point considéré. La deuxième, *N**, moyenne par rapport au nombre de couches qui entoure le grain considéré. Ces deux approches reposent sur des mécanismes différent, *R** met l'accent sur une zone effective sans prendre en compte de manière explicite la microstructure, tandis que *N** met en avant l'interaction entre les grains adjacents et contient des caractéristiques microstructurales telles que la taille et la forme des grains. La *Figure IV-1* présente schématiquement ces deux approches.

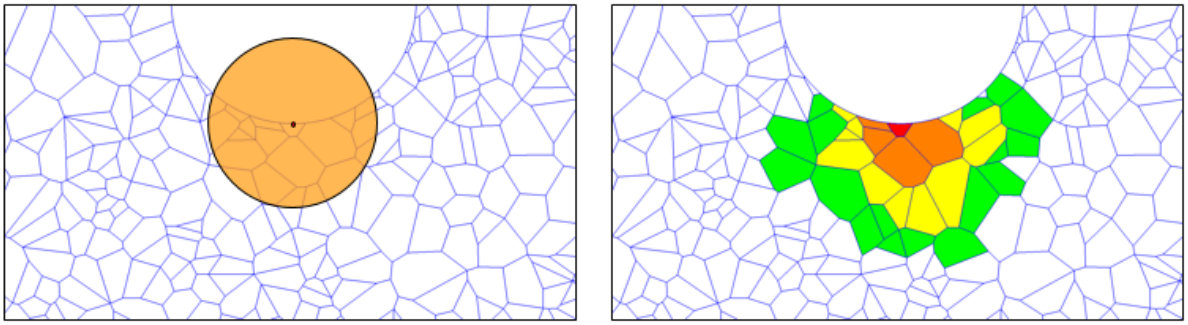

Figure IV-1: Schematic illustrations of non-local methods: (a) critical radius method and (b) neighbor layer method

L'identification des paramètres non-locaux peut être fastidieuse. Un compromis sur la précision des résultats est fait en ne prenant que quelques valeurs. Pour N*, 2, 3, 5, 9 et 13 sont pris en compte et pour R*, 15 µm, 30 µm, 60 µm,120 µm et 180 µm, ce qui correspond à 1, 2, 4,8 et 12 taille moyenne de grain.

IV.2.Evaluation de la méthode non locale par rapport aux résultats expérimentaux

Dans un premier temps, les valeurs locales de Kt sont analysées en fonction du rayon de défaut. Ce dernier varie de 5 à 200 µm. Chaque défaut est associé à un ensemble de 96 microstructures (4 tessellation avec 24 jeux d'orientations) pour permettre le calcul de la moyenne et de l'écart type. Le *Table IV-2* résume les différentes valeurs.

T*able IV-2: Local stress concentration factor with respect to different defect radius*

Defect Radius (µm)	5	15	30	60	120	200
Kt (isotropic model)	2.78	2.81	2.81	2.81	2.78	2.85
Kt (polycrystal models)	3.28 +/- 0.50	3.37 +/- 0.43	3.79 +/- 0.62	3.63 +/- 0.46	3.70 +/- 0.32	3.88 +/- 0.37

Le Kt moyen est toujours supérieur pour un polycristal à cause de l'interaction entre les grains voisins. Un petit défaut n'influence que peu de grain alors qu'un défaut plus grand a un effet sur un nombre plus élevé. C'est pourquoi la valeur relative de Kt entre le cas isotrope et le polycristal augmente avec un défaut plus grand.

Le paramètre $\sqrt{Area}$ est choisi pour décrire la taille des défauts. Afin de comparer les simulations en 2D avec les résultats expérimentaux en 3D sur des défauts semi-sphériques, les défauts 2D sont considéré comme des entailles dans un modèle 3D. La méthode proposée par Murakami (Murakami, 2002) pour estimer la surface effective d'une entaille peu profonde ou de la rugosité est adoptée. Grâce à cette méthode, le défaut semi circulaire de notre modèle à un paramètre de Murakami équivalent défini par la relation suivante :

$$\sqrt{Area} = \sqrt{10}\, r \qquad (IV.9)$$

Avec r le rayon du défaut 2D.

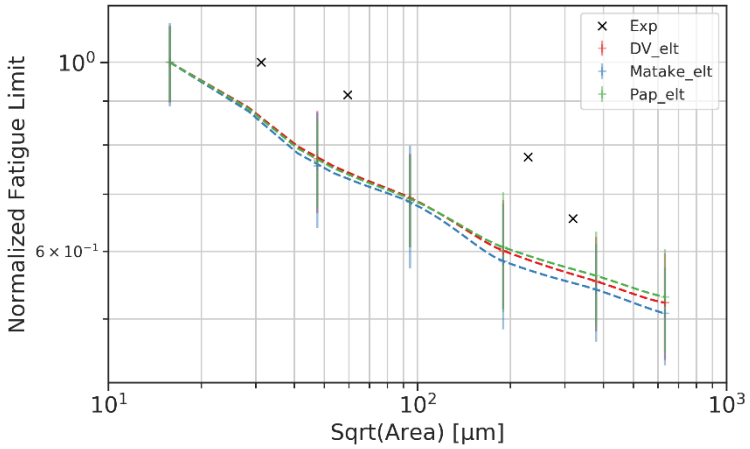

Figure IV-2: Kitagawa-Takahashi diagrams of local fatigue indicating parameters

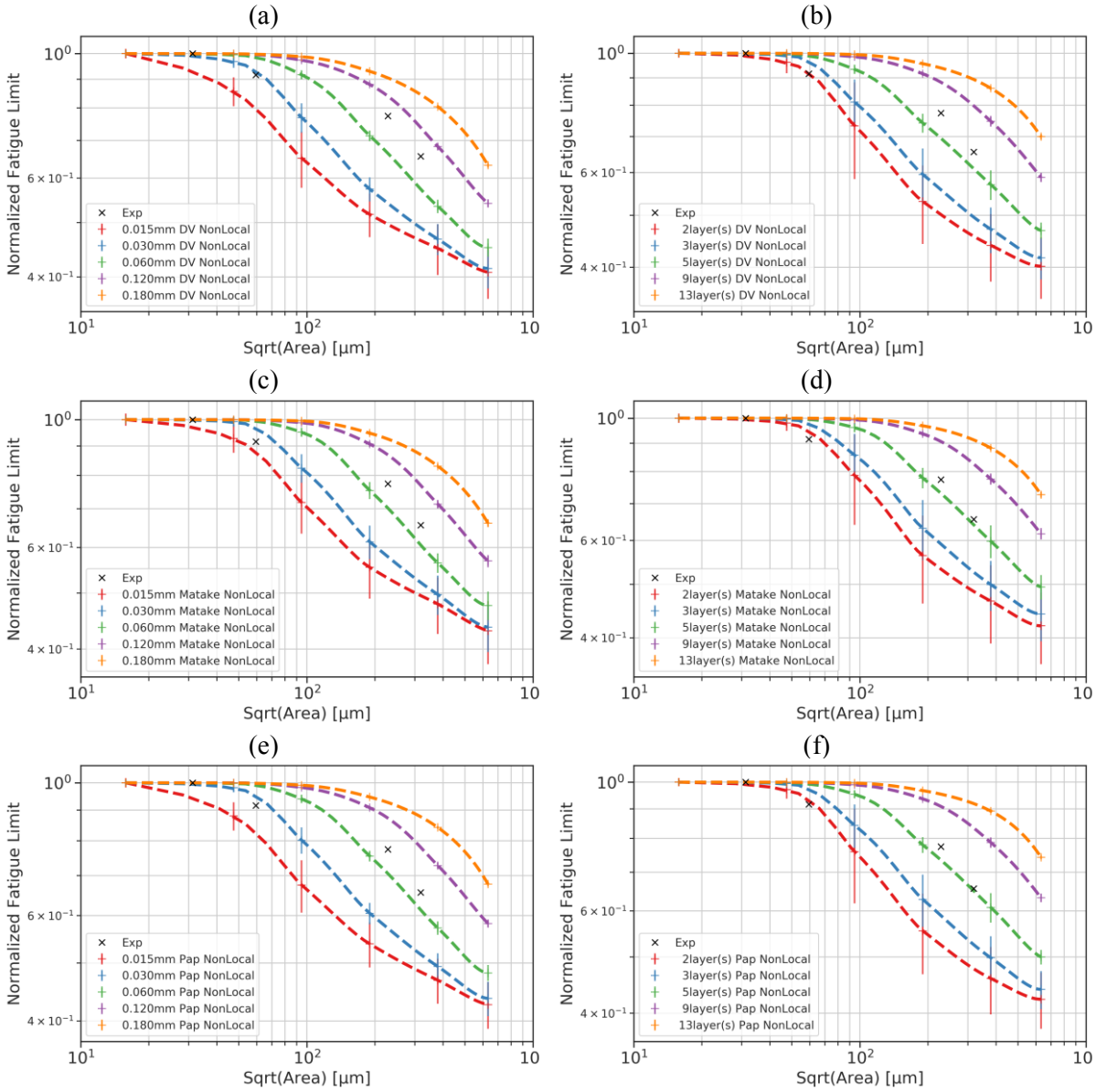

Figure IV-3: Normalized Kitagawa-Takahashi diagrams with the application of (a) critical radius Dang Van criterion;(b) neighbor layer Dang Van criterion;(c) critical radius Matake criterion; (d) neighbor layer Matake criterion; (e)critical radius Papadopoulos criterion; (f) neighbor layer Papadopoulos criterion

La *Figure IV-2* montre les prédictions de la méthode locale réalisés avec les valeurs extrêmes de chaque microstructure syntétique. Les barres représentent les valeurs moyennes avec +/- 1 écart type des limites de fatigue normalisée. Les points représentent les valeurs expérimentales observée par Guerchais. Pour les modèles avec défauts, les prédictions observée sont très conservatives à cause de la sensibilitée au facteur de concentration de contrainte.

Les résultats traités avec les méthodes R* et N* sont présentés sur la *Figure IV-3*. Ces méthodes donnent de bon résultats pour des défauts de petites tailles. Plus la valeur du paramètre non local augmente, plus la limite de fatigue prédite est élevée avec un écart type plus faible. La variation de l'écart type montre la sensibilitée de la microstructure en fonction du paramètre non locale. Les trois critères de fatigue étudiés donnent quand à eux des prédictions similaires. D'un point de vue qualitatif, les méthodes non locales permettent de bien décrire la tendance de l'effet d'un défaut sur la tenue en fatigue. D'un point de vue quantitatif, la valeur du paramètre non local peu être evaluée en comparant les prédictions avec les résultats expérimentaux. Globalement, aucunes des valeurs choisies ne permet une correspondance parfaite. Les petites valeurs de paramètres (R*=0.030 ou N*=3) donnent de bon résultats pour les petits défauts, mais se détériorent losque la taille des défauts augmente. Les valeurs intermédiaires (R*=0.06 ou N*=5) prédisent de bon résultats pour les défauts de grande taille mais surestiment les performances de petits défauts. Quand aux valeurs de paramètres plus élevés, la limites de fatigue est surestimée pour tous les cas étudiés. Un lien peu être fait entre le paramètre non local et la taille de défaut. Cependans l'erreur de la taille des défauts artificiels expérimentaux peux variée de +/- 20 µm. De plus a cause de la dispersion des résultats expérimentaux, il est difficile d'obtenir une valeur précise de la limite de fatigue moyenne. En raison de ces limites, il n'est pas possible de déterminer si le paramètre non local est une constante qui ne dépend que du type de matériau ou non. Considérant que l'objectif principal est de proposer une méthode numérique pour évaluer l'effet de défauts avec une taille de l'ordre de plusieurs centaines de micromètres, on peut considérer qu'une valeur de N* de 5 ou R* de 0,060 mm permet d'obtenir des prédictions acceptables.

La représentation en graphique box-and-whisker est utilisée dans la *Figure IV-4* pour présenter les limites de fatigue preditent ainsi que leurs dispersions pour les 3 critères. Le rectangle indique l'étandue entre le premier et troisière quartile et est coupé par la médiane. Les segments représentent l'étendue à 1.5 x l'intervalle interquartile du quartile inférieur et supérieure. Les marqueurs noirs sont les valeurs en dehors de la plage représentée. Chaque boite représente la distribution de la limite de fatigue prédite

à partir de 96 microstructures syntétiques (4 morphologies de grains x 24 jeux d'orientations). Parmis les 3 critères étudiés, le critère de Matake prédit une limite de fatigue plus élevée par rapport aux deux autres. La différence entre le critère de Matake et les deux autre est l'utilisation de la contrainte normale alors que le critère de Dang Van et celui de Papadopoulos utilise la pression hydrostatique. La différence entre le critère de Dang Van et le critère de Papadopoulos est le calcul de la cission. Le critère de Dang Van utilise la cission maximale, alors que le critère de Papadopoulos intègre la contrainte de cisaillement sur les systèmes de glissement. Cependant les différences obtenues entre ces trois critères sont faibles et ne permet pas de les juger en raison du nombre limité de configuration étudiées. La comparaison entre les méthodes non locales montre que la méthode N* est plus sensible à la microstructure. Pour les défauts de la taille de plusieurs grains, une dispersion plus forte indique la compétition entre le défaut et la microstructure. La modélisation explicite de la microstructure couplée à la méthode non locale peut expliquer l'observation expérimentale du comportement en fatigue des agrégats polycristallins métalliques où la principale source de dispersion provient des caractéristiques microscopiques.

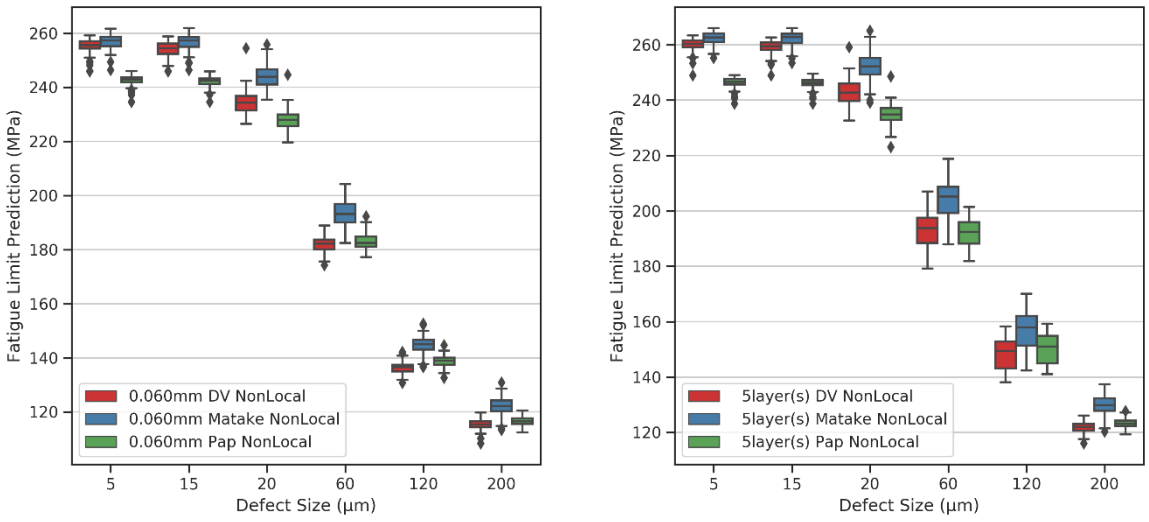

Figure IV-4: Fatigue limit intervals of 96 models containing the same defect but different microstructure from the criteria: Dang Van, Matake, Papadopoulos. (a) critical radius method (b) neighbor layer method

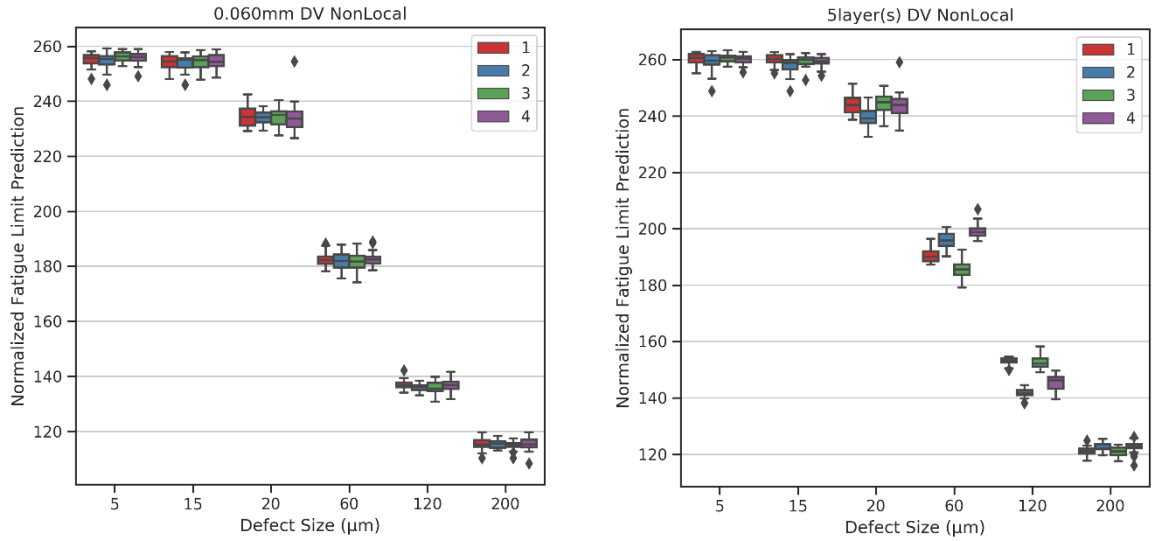

Figure IV-5: Fatigue limit intervals of 24 models containing the same defects and grain shapes but different grain orientations from the criterion: Dang Van. (a) critical radius method (b) neighbor layer method

La *Figure IV-5* montre l'influence de l'orientation cristallographique. Chaque boîte représente les prédictions du critère de Dang Van pour différent 24 jeux d'orientations cristallographiques différents. Les quatre boites associées à un défaut représentent quatre jeux de géométrie de grain différents. L'effet de l'orientation des grains peut être observé pour les résultats des deux méthodes. Une orientation de grains différentes peut entraîner une différence de 20 MPa de la limite de fatigue. Comme les grains ont une taille similaire, il serait intuitif que que la méthode R* et N* ait des résultats similaires pour le même arrangement de grain. Étonnamment, la méthode N* est plus sensible à la position et à la morphologie du grain tandis que la méthode du rayon critique donne des prédictions similaires indépendamment de la position et de la morphologie du grain. Cette comparaison montre différents scénarios d'application des deux méthodes.

IV.2.1. Effet de la distribution des grains

Dans les modèles FE polycristallins précédents qui ont servi de référence, la tessellation de Voronoï est utilisée avec une distribution gaussienne pour la taille des grains (distribution typique pour les aciers corroyés). Pour analyser l'effet de la distribution des grains sur les méthodes non locales proposées, des configurations différentes sont mises en œuvre. Tout d'abord avec une tessellation en quadrangles, identiques en taille et en forme, mais également une tessellation de Voronoï avec une distribution log-normale pour la taille des grains (distribution obtenue après recristallisation ou en fabrication additive, Toth et al., 2013). Deux distribution log-normale sont utilisées, la taille moyenne est constante (15 µm),

mais la deuxième est plus déviée ce qui conduit à une apparition de grains plus petits. Les 4 distributions sont présentées sur la *Figure IV-6*.

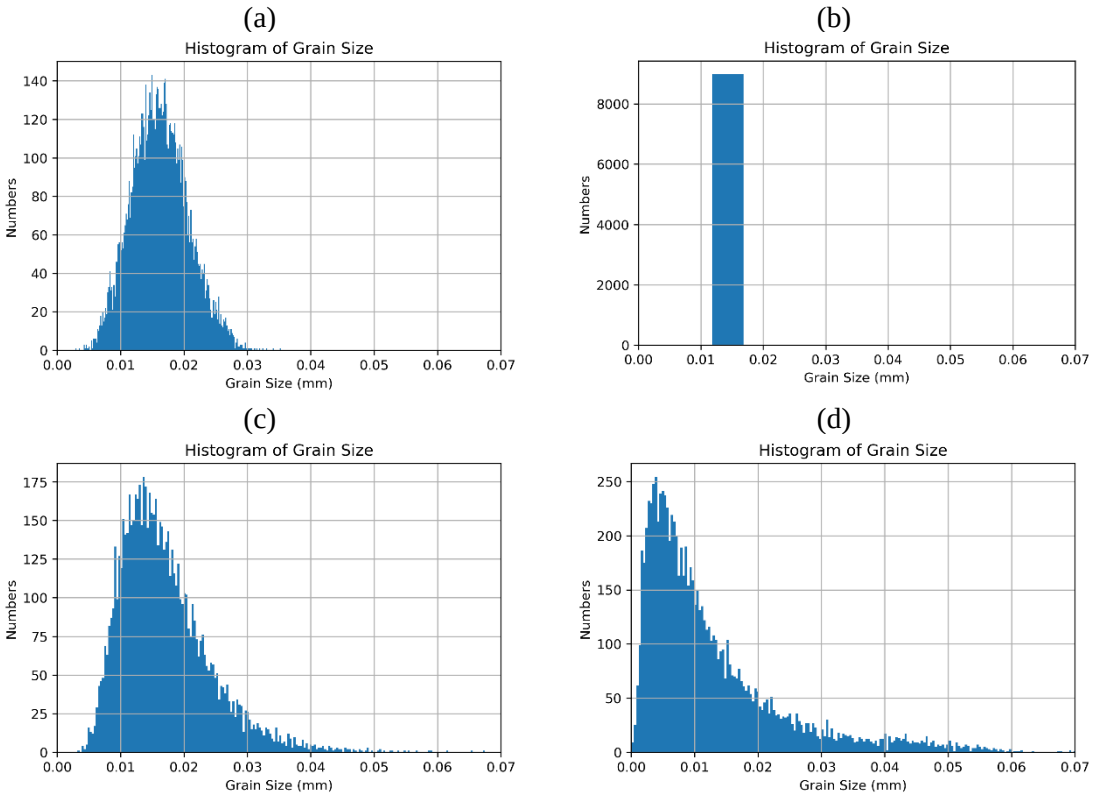

Figure IV-6: Histograms of grain size for different grain morphology configurations: (a) Gaussian distributed Voronoi polygon (b) uniform distributed quadrangle (c) log-normal distributed Voronoi 1 (d) log-normal distributed Voronoi 2

Les prédictions à partir des critères de fatigue de deux méthodes non locales sont présentées sur la *Figure IV-7*. En ce qui concerne la sensibilité de la morphologie des grains pour les petits défauts où la taille des défauts est inférieure à de deux fois la taille moyenne des grains, la distribution uniforme donne la prédiction la plus élevée. La distribution gaussienne donne un résultat intermédiaire. Enfin pour la distribution log-normale, plus la distribution est déviée, plus la limite de fatigue est faible. Pour les petits défauts, les 2 méthodes non locales diminuent les prédictions si le nombre de grains impliqués dans la zone de moyenne augmente. En comparant les valeurs numériques des prédictions, la différence des moyennes obtenues pour les différentes distributions est d'environ 1% dans la prédiction de la méthode N* et ne dépasse pas 5% pour R*. Les deux prédictions peuvent être considérées comme stables.

Lorsque la taille du défaut augmente pour atteindre la taille de plusieurs grains, des tendances différentes sont observées pour les deux méthodes. La méthode R* donne des prédictions similaires pour les quatre distributions, ce qui signifie que seule la taille du défaut a une influence sur les performances en fatigue par rapport à la morphologie des grains. La méthode N* montre la compétition entre le défaut

et la morphologie du grain. Par exemple, la différence entre la prédiction de la deuxième distribution log-normal et la distribution uniforme pour un défaut de 120 µm est supérieure à 20%. Ceci s'explique pour la taille de la zone effective qui, pour N*, est dépendante de la géométrie des grains, alors qu'elle n'en est pas dépendante pour R*.

L'analyse révèle que lors de l'utilisation de la méthode N*, la microstructure doit être prise en compte tandis qu'une tessellation simple peut être utilisée avec la méthode du rayon critique sans changer les prédictions.

Contrairement aux matériaux corroyés où des grains équiaxes sont fréquemment rencontrés, dans la fabrication additive, les pièces fabriquées ont souvent une morphologie de grain allongée ainsi que la présence de grains très fins près de la surface. La méthode N* pourrait être un meilleur choix dans cette situation car elle peut refléter davantage de caractéristiques microstructurales.

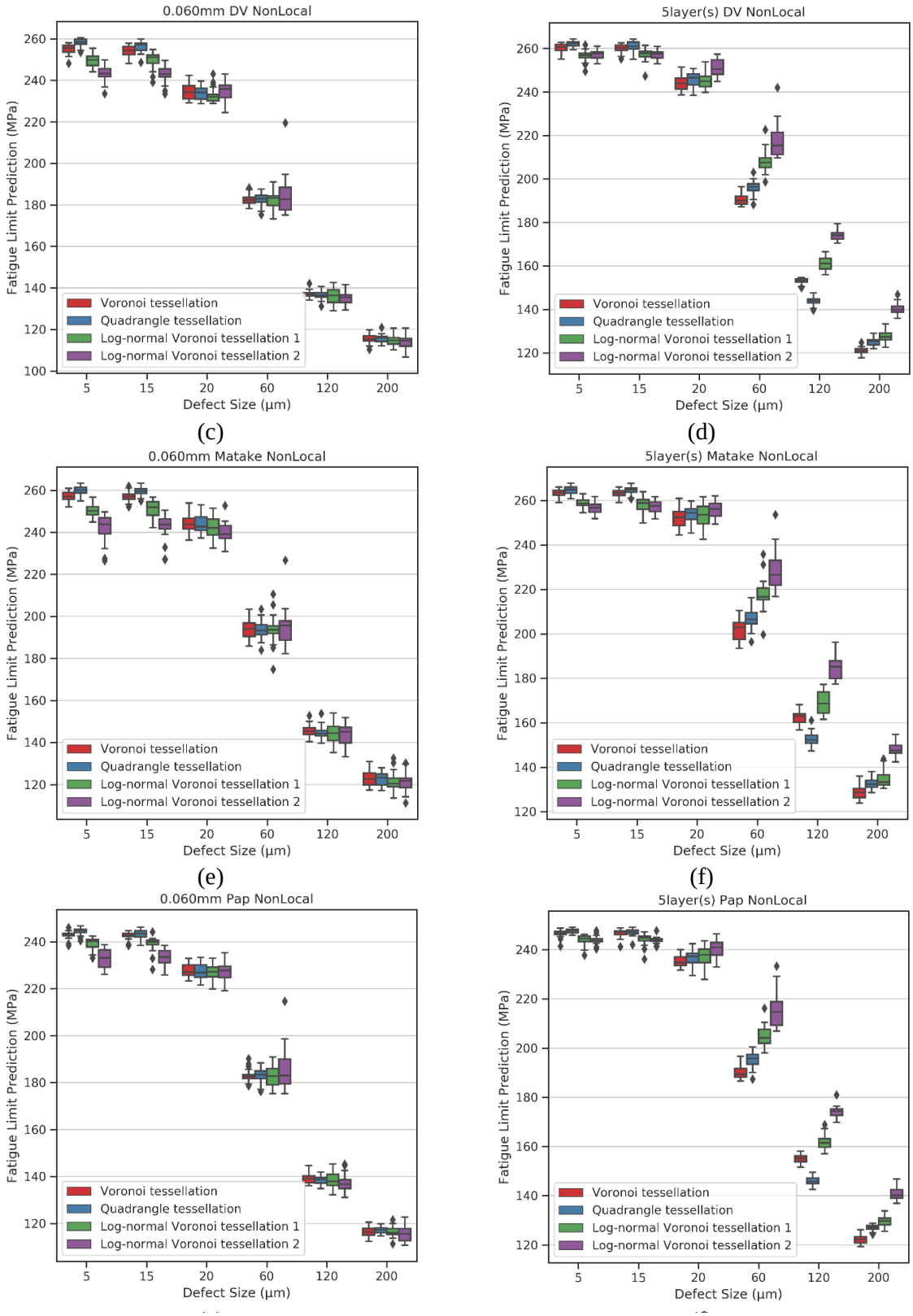

Figure IV-7: Fatigue limit intervals of 24 models containing same defects but different grain morphology from (a) critical radius Dang Van criterion;(b) neighbor layer Dang Van criterion;(c) critical radius Matake criterion; (d) neighbor layer Matake criterion; (e)critical radius Papadopoulos criterion; (f) neighbor layer Papadopoulos criterion

IV.2.2. Effet de la taille de grain

Grâce à la modélisation explicite de la microstructure, le rôle de la taille des grains peu être étudiée. En se basant sur les simulations précédentes, des microstructures contenant des grains de 30 µm et d'autres avec une taille de 100 µm sont construites.

Il est généralement admis que la résistance à la fatigue des matériaux ou le glissement est plan, comme l'acier et le laiton, augmente lorsque la taille des grains diminue, tandis que, dans les matériaux où le glissement est ondulé, comme le cuivre pur et l'aluminium pur, la résistance à la fatigue n'est pas affectée. Pour les matériaux à défauts, il est observé que la taille critique du défaut varie linéairement avec la taille des grains de l'acier (Masounave et Baflon, 1976). Néanmoins, la relation exacte entre la fatigue et la microstructure des matériaux à défauts reste une question ouverte en raison de peu d'études dans la littérature.

Le choix du paramètre de la méthode non locale pour cette partie ne peut pas être vérifié quantitativement en raison du manque de résultats expérimentaux. R* et N* sont définis respectivement à 60 µm et 5 à partir des résultats des modèles de référence (lot 1). La taille effective du défaut est définie comme la taille critique où la limite de fatigue chute de 10% par rapport à la prédiction du modèle sans défaut. En raison de la taille géométrique de notre modèle, la longueur de fissure effective définie par Haddad (El Haddad, Smith et Topper, 1979), qui correspond à un défaut provoquant une chute de la limite de fatigue de 70%, n'est pas réalisable. La valeur est interpolée linéairement à partir du diagramme Kitagawa-Takahashi basé sur la théorie de l'intensité de contrainte seuil. Comme on peut le voir sur la *Figure IV-8*, la méthode R* montre une forte sensibilité à la taille des grains. Elle correspond aux tendances expérimentales des aciers. Contrairement à la méthode R*, la méthode N* donne des résultats similaires lorsque la taille des grains varie. La méthode R* met l'accent sur l'influence de la taille des défauts tandis que la méthode N* accorde plus d'importance aux facteurs microstructuraux. Compte tenu tendances expérimentales, les deux méthodes ont leur scénario d'application, mais il faut faire attention lors du choix de la valeur du paramètre. Dans certaines circonstances où l'identification du paramètre non local n'est pas réalisable, pour des matériaux comme l'acier où une relation linéaire entre la taille du défaut critique et la taille du grain a été observée, une valeur approximative de R * peut être appliquée car elle affiche une sensibilité à la taille des grains. Pour d'autres matériaux comme l'alliage d'aluminium de coulé où la microstructure est souvent caractérisée non pas par la taille des grains mais par l'espacement des bras de dendrite, une valeur de N* similaire peut être utilisé car il y a peu d'influence par rapport à la taille des grains.

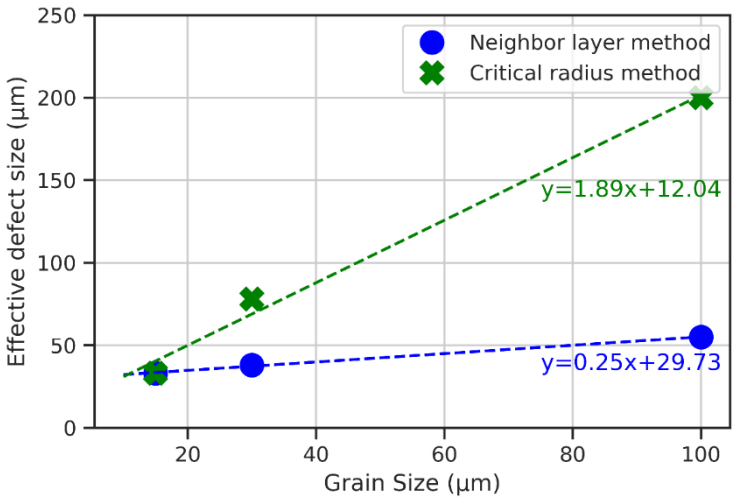

Figure IV-8: Effective defect sizes for different average grain size configurations of proposed realizations of non-local method and pre-fixed parameter values

IV.3.Conclusion

L'effet des défauts et de la microstructure, ainsi que leur compétition sur le comportement à la fatigue des agrégats polycristallins, sont étudiés avec une méthode non locale.

En créant un modèle numérique avec microstructure explicite, la réponse mécanique locale et la distribution des contraintes caractéristiques moyennes des grains est obtenues. Il ressort de l'analyse mécanique que la microstructure introduit une forte hétérogénéité car le défaut apporte une forte concentration de contraintes. Pour mieux évaluer l'effet des défauts sur le comportement en fatigue, la microstructure est un facteur essentiel. Cependant, une approche locale ne permet pas refléter correctement l'effet Kitagawa-Takahashi car les valeurs sont surestimées.

En introduisant la méthode non locale, la prédiction de limite de fatigue en tenant compte à la fois des défauts et la microstructure peut être obtenue. En termes d'influence de la taille des défauts sur les performances en fatigue, les simulations et expériences sont en bon accord. La tolérance des petits défauts et l'influence des défauts plus importants peuvent être clairement montré. La dispersion des résultats due aux attributs de microstructure est montrée et discutée. En particulier, pour le défaut de taille moyenne, la large dispersion montre la compétition entre le défaut et la microstructure.

Trois critères de fatigue multi-axiaux basés sur les contraintes sont utilisés et évalués. Les trois critères montrent qu'un très petit défaut a une influence négligeable sur la résistance à la fatigue. Le critère de Matake fournit toujours la limite de fatigue la plus élevée car il utilise la contrainte normale.

Concernant les méthodes non locales, la méthode N* est plus sensible à la microstructure. Des dispersions plus fortes peuvent être observées dans les résultats obtenus avec N* que ceux obtenus avec R*.

D'autres analyses sur la morphologie et la taille des grains ont permis d'observer que la sensibilité à la taille des grains dépend également du modèle non local utilisé. Chaque méthode a ses avantages dans différents scénarios d'application. Avec un choix approprié de paramètres non locaux et une compréhension de la sensibilité des matériaux à la microstructure, la méthode non locale devrait pouvoir être appliquée pour différents matériaux métalliques.

Chapitre V. Etude numérique de l'effet de la rugosité et de la porosité sur les performances en fatigue du 316L SLM

Les pièces de fabrication additive, en particulier celles non traités thermiquement, ont souvent une microstructure fortement texturée et non équiaxe. Ce chapitre à pour but de mettre en évidence de ces deux paramètres microstructuraux sur la tenue en fatigue. L'effet de la rugosité et des défauts du type lack of fusion (LoF) serons également pris en compte.

V.1. Modélisation du 316L SLM

V.1.1. Orientation cristallographique et morphologie des grains

V.1.1.1. Morphologie et taille des grains

La microstructure des agrégats polycristallins modélisés doit représenter objectivement la morphologie des grains (i.e. la forme et la taille). Il est possible, sur la base des résultats des analyses EBSD, de déterminer la taille moyenne des grains. Nous nous appuierons sur la définition recommandée par la norme NF EN ISO 643/2624 (Barralis et Maeder, 2005). Il est également intéressant de regarder comment la taille des grains est répartie. La définition de taille d'un grain choisi dans cette étude est définie par le diamètre du "cercle équivalent" Deq, c'est-à-dire le cercle de même surface que le grain.

Après élimination des très petits grains (Deq <2µm), la taille moyenne des grains est d'environ 25 µm. Les analyses EBSD montent que la microstructure est formée principalement par de gros grains allongés de forme quadrangulaire. Le premier modèle proposé prend en compte le rôle prédominant des grains allongés. Par conséquent, des quadrangles sont utilisés pour la tessellation. Les grains allongés ont un rapport de forme important. Les données brutes d'EBSD sont traitées en filtrant les petits grains pour ne considérer que les gros grains. Le seuil choisi est Deq inférieur à 5 µm. Les grains dépassant ce seuil occupent 98% de la superficie totale. La taille moyenne des grains calculée est de 54 µm. Cette valeur est utilisée comme valeur de référence pour le modèle avec les grains quadrilatéraux. Également, le rapport de forme est fixé à 3. Cette valeur a été choisie à partir d'un processus d'approximation par des ellipses des gros grains.

La tessellation de Voronoï est également utilisée pour construire d'autres modèles car, dans le modèle quadrangulaire, la taille des grains est presque homogène et la présence de petits grains qui pourraient avoir une influence est omise. Nous adoptons une autre modélisation de la microstructure en utilisant les polygones de Voronoï avec une distribution log-normal. Les paramètres de la distribution sont $\mu = 15$ (µm) et $\sigma = 0,6$, ont été choisi pour être en adéquations aux résultats expérimentaux

V.1.1.2. Orientation des grains

Dans la modélisation, un ensemble d'orientations cristallographiques est attribué aux grains. Dans l'étude expérimentale précédente, nous avons constaté que le matériau étudié présente une forte texture. L'essai de traction monotone révèle que le module d'Young est inférieur à la valeur nominale de l'acier conventionnel. Une étude préliminaire est effectuée pour choisir des ensembles d'orientation cristallographiques caractéristiques pour reproduire cette observation expérimentale.

L'analyse EBSD permet d'obtenir la taille et l'orientation réelles de chaque grain. Un modèle auto-cohérent (Robert et Mareau, 2015) est utilisé pour simuler l'essai de traction. Le comportement des grains est élastique cubique avec les paramètres du Fer alpha (Huntington, 1958). Les volumes et orientations déterminée expérimentalement sont également une donnée d'entrée du model. Les résultats du calcul donnent un module d'Young environ 10% plus faible que celui trouvé expérimentalement. Une explication possible est que les paramètres viennent de la littérature et n'ont pas été identifier sur notre matériau. Un tirage aléatoire des orientations, pondérée par le volume expérimental des grains est réalisée pour obtenir 24 jeux d'orientations texturé. Les modules d'Young obtenus par calculs éléments finis avec ces jeux d'orientations et celui obtenue par la méthode auto-cohérente ont une différence inférieure à 1%. On peut en conclure que les jeux d'orientations choisi sont en accord avec la texture réelle.

V.1.1.3. Rugosité et pores

En plus des attributs microstructuraux, la rugosité et les pores doivent êtres pris en compte dans notre modélisation.

La rugosité réelle est présentée au chapitre II. La surface numérisée renvoie des données 3D, ce qui signifie que les données brutes peuvent être discrétisées en milliers de profils 2D.

Pour définir quantitativement une rugosité, de nombreuses normes existes. Dans cette étude, nous utilisons le Ra comme paramètre prédominant et prenons également en compte d'autres paramètres (Rq, Rv, Rp, Rt, Rsk, Rsv et Rz). Les profils idéaux devraient avoir un Ra très similaire à l'ensemble de la surface balayée tandis que les autres paramètres doivent être dans des plages raisonnables. 5 Profiles sont choisis avec des caractéristiques différentes. P1 est un profile relativement lisse compte tenu de ses paramètres caractéristiques. Tous les paramètres de P2 se situent à l'intérieur de l'écart-type des résultats moyens de l'ensemble de la surface scannée, ce qui fait de ce profil le plus représentatif. P3, au contraire, est celui dont les paramètres s'écartent des références. P4 et P5 sont choisis de manière à avoir les mêmes valeurs Ra que celles expérimentales. P4 a un grand Rv tandis que P5 a un grand Rp.

La microtomographie présentée au chapitre II a permis de mesurer la porosité inhérente de notre matériau. La plupart des pores sont très petits et le plus grand détecté a un diamètre équivalent de 46

µm. Compte tenu de l'effet Kitagawa-Takahashi, ces pores de gaz internes sont susceptibles de ne montrer aucun effet. Par conséquent, les pores internes ne sont pas pris en compte dans la modélisation.

Sur les surfaces de rupture des éprouvettes ayant subi une rupture de fatigue, des défauts du type LoF sont toujours observés et sont considérés comme le facteur le plus nocif d'amorçage de fissures. Mais ce type de défaut n'est souvent pas détectable par µCT. Pour prendre en compte ce type de défaut, l'estimation d'une taille critique est nécessaire. Plus précisément, nous devons représenter les défauts 3D observés aux sites d'initiation des fissures par un défaut 2D équivalent. Une solution utilisant l'équation de Murakami est appliquée. Un défaut semi-elliptique d'une profondeur de 100 µm avec un petit axe de 30 µm est alors utilisé pour modéliser ce type de défaut.

V.2. Configurations de modélisation

V.2.1. Conception de modèles géométriques

V.2.1.1. Modèles lisses

Des modèles lisses contenant des attributs de microstructure explicites sont construits pour étudier l'effet de la morphologie et des orientations des grains. Cinq tessellations sont utilisées pour comparer différentes morphologies de grains. Deux types d'orientation des grains sont utilisés. Les détails de chaque configuration de modèle sont répertoriés dans le *Table V-1*. La tessellation quadrangulaire 1 et la tessellation Voronoï sont purement basées sur l'estimation approximative de la taille des grains. Deux tessellations de Voronoï log-normales sont utilisés pour représenter la microstructure du matériau en fabrication additive. La structure quadrangulaire 2 permettra de montrer l'influence des grains allongés.

Table V-I: Configurations of the models employed in the simulations

	Tessellation		Orientation		Loading	
Name	Grain number	Average grain size [µm]	Isotropic set number	Realistic set number	Tension	Bending
*Quadrangle 1	5070	25	50	50	✓	×
*Voronoi	5070	25	50	50	✓	×
#Log-normal Voronoi 1	8400	19	24	24	✓	✓
#Log-normal Voronoi 2	8400	19	24	24	✓	✓
#Quadrangle 2	1080	54	24	24	✓	✓

*: only used in smooth models; #: used in all models

V.2.1.2. Modèles avec défauts

Les modèles avec défauts semi-ellipsoïdaux permettrons de simuler l'effet des défauts du type LoF. Rappelons que pour les éprouvettes polies, la rugosité est éliminée mais les défauts LoF restent sur ou

près de la surface polie. Comme mentionné précédemment, des défauts 2D équivalents sont introduits dans les modèles pour refléter le rôle des défauts LoF.

Les cinq profils de rugosité sélectionnés discutés précédemment sont ajoutés aux modèles lisses par des opérations booléennes géométriques. Les modèles construits permettent d'avoir une rugosité importante mais également des défauts LoF. Les modèles avec rugosité et défauts géométriques visent à prendre en considération les deux facteurs néfastes.

V.2.2. Modèles constitutifs

Les équations constitutives sont de deux type : élasticité et plasticité. En ce qui concerne l'élasticité cubique, les mêmes valeurs que celles utilisées au chapitre IV sont utilisées. Pour ce qui est de la plasticité, les paramètres de la loi de Méric et Cailletaux ont été identifiée à partir d'un modèle autocohérent, en utilisant un algorithme génétique composé de 768 individus évoluant sur 50 générations. Les courbes cycliques à mi durée de vie pour une déformation imposée de 0.30% et 0.45% sont utilisées comme référence.

V.2.3. Conditions de chargement et critère de fatigue

Les chargements sont de deux types, traction et flexion, avec un rapport de charge de -1.

Les critères de fatigue choisi sont les même que précédemment, c'est-à-dire Dang Van, Matake et Papadopoulos.

V.3. Simulations de fatigue de modèles lisses

V.3.1. Discussion sur la référence expérimentale pour la simulation

Les limites de fatigues de références doivent être choisies. Cependant, celles de la littérature pour le 316L SLM ne sont pas toujours cohérentes (voir chapitre I). Bien que les campagnes expérimentales menée dans ces travaux fournissent des résultats en traction et en torsion, l'analyse fractographique à montrer que les LoF n'ont pas été totalement supprimées et le pallier sur le diagramme Kitagawa-Takahashi n'est pas atteint (voir chapitre II et III). Au chapitre IV, les limites de fatigues utilisées pour la calibration sont de 230 MPa en traction et de 147 MPa en torsion (résultats de Guerchais). Ce choix de limite sera donc également utilisé comme référence dans ce chapitre pour les modèle lisse sans défaut. Il est important de souligner que, dans l'étude de Riemer et al., La limite de fatigue du 316L SLM est de l'ordre de 250 à 280 MPa en flexion. De plus, les simulations numériques sont réalisées en élasticité linéaire, les tendances observées restent valables même si la limite de référence est différente.

V.3.2. Méthode statistique pour l'hétérogénéité microstructurale

D'après les résultats présentés dans les chapitres précédents, les performances en fatigue semblent dépendre de plusieurs facteurs tels que l'état de surface, les orientations cristallographiques, la

morphologie des grains, etc. Il est difficile de connaître le rôle réel joué par chacun de ces facteurs car le nombre limité d'expériences et d'observations ne nous permet pas de les évaluer quantitativement. Nous nous tournons donc vers les résultats de la simulation pour mieux comprendre leur rôle. L'utilisation des outils numériques nous permet de générer de nombreuses configurations. Pour analyser les paramètres microstructuraux ainsi que l'état de surface, la méthode des statistiques des extrêmes est utilisée (Fisher et Tippett, 1928; Freudenthal et Gumbel, 1954).

Une démarche similaire aux travaux de Hor et al., 2014, est réalisée dans un premier temps pour traiter la relation entre la réponse de locale et seuil macroscopique. Premièrement, le paramètre indicateur de fatigue (FIP), c'est-à-dire la contrainte de Dang Van dans ce cas, est défini à l'échelle mésoscopique. C'est-à-dire que le FIP est calculé en moyenne dans chaque grain de l'agrégat. Deuxièmement, la partie droite du critère est remplacée par un nouveau paramètre β* qui est le seuil de fatigue à l'échelle mésoscopique. 100 volumes statistique représentatifs (SVE) avec des textures isotropes sont utilisées pour générer l'évolution des valeurs extrêmes. La moitié des SVE sont tessellées par des quadrangles et l'autre moitié sont tessellées par des Voronoï. Le chargement est en traction purement alterné avec une amplitude de 230 MPa. Les travaux de Hor montrent que pour le critère de Dang Van, β* est proche de β. C'est pourquoi β* est pris égale à la limite de fatigue expérimentale en torsion. Les résultats de la statistique des extrêmes montrent que la limite de fatigue estimée est nettement inférieure à la limite de fatigue expérimentale. Cet écart peut être dû à de nombreux facteurs. Premièrement, supposer que β et β* sont égaux est peut-être discutable. Deuxièmement, la définition de β* est basée sur la validité de la FIP moyenné dans les grains. Les réponses moyennées dans les grains doivent être analysées plus en détail pour vérifier les mécanismes de fatigue sont à une échelle d'un grain.

La variabilité de la microstructure dans les modèles quadrangulaires ne se distingue que par les orientations cristallographiques tandis que les modèles Voronoi montrent une plus grande variabilité dans forme et taille des grains. Autrement dit, les réponses obtenues pour les modèles quadrangulaires sont moins dispersées par rapport aux Voronoï. Concernant l'estimation de β*, la plupart des valeurs extrêmes se situent entre 167,5 et 217,5 MPa. Néanmoins, dans certains cas, les valeurs extrêmes s'écartent fortement de cette plage, ce qui conduit à des estimations de contrainte Dang Van plus élevées et à des limites de fatigue plus faibles. Dans ce qui suit, la méthode non locale présentée au chapitre IV est utilisée.

V.3.3. Influence du R *

L'approche non locale utilisant l'intégration sur une sphère de rayon critique R* a été présentée au chapitre IV. Les résultats précédents montrent que cette méthode n'est pas très sensible à la morphologie et à la taille des grains.

Dans un premier temps, nous avons choisi comme référence la tessellation de Voronoï avec une texture isotrope. Les simulations sont réalisées avec un ensemble 50 jeux d'orientations. Le critère de Dang Van est utilisé avec différentes valeurs de R* (15 µm, 60 µm et 100 µm). L'application de la statistique des extrêmes est ensuite réalisée. En partant de l'hypothèse que la limite de fatigue critique est la valeur à laquelle 50% des fissures se déclenchent, nous utilisons la valeur médiane pour représenter la limite de fatigue prédite. Les résultats montrent que prendre un R* de 60 permet d'être en accord avec les résultats expérimentaux. La limite de fatigue obtenue est de 232 MPa avec un intervalle de confiance à 95% de 227 à 242 MPa.

Pour les autres modèles étudiés, on peut se demander si une la même valeur de R* peut être utilisée car plusieurs tessellations avec des tailles de grains différentes sont adoptés. Il convient de rappeler que l'objectif principal est de comparer l'effet des attributs microstructuraux d'un point de vue qualitatif. L'étude précédente du chapitre IV montre que, pour le modèle lisse, le même R* peut entraîner des valeurs FIP différentes pour différents modèles tessellés, mais la sensibilité à la morphologie et à la taille des grains de la méthode R* n'est pas significative. Également, nous avons vu que les distributions log-normales ont tendance à donner des prédictions inférieures par rapport aux Voronoï standard. D'un point de vue qualitatif, ces différences sont négligeables puisque la différence entre les limites de fatigue prédites est de quelque dizaines de MPa. Dans cette étude, nous garderons 60 µm comme choix de R* pour toutes les simulations.

Les prévisions des limites de fatigue à partir du critère de Dang Van, Matake et Papadopoulos montrent que la différence entre les deux types de texture (isotrope et réelle) est notable tandis que l'effet du mode de chargement est négligeable. Les modèles avec des textures isotropes donnent des prédictions dans la plage de 220 à 250 MPa, ce qui est cohérent avec la limite de fatigue de référence. Les modèles contenant des textures de fabrication additive ont des performances plus faibles.

Les trois critères produisent des résultats similaires. Par conséquent, nous utilisons uniquement les prédictions du critère de Dang Van pour effectuer une analyse quantitative plus approfondie. Les valeurs médianes des limites de fatigue prédites à partir de modèles ayant le même type de chargement, de tessellation et d'orientation sont calculées. On peut conclure que la texture de fabrication additive peut conduire à une baisse de la limite de fatigue prévue d'environ 10%. Il est à noter que la taille moyenne des grains de chaque lot n'est pas équivalente. Mais les résultats obtenus sont proches les uns des autres.

Les mêmes traitements sont réalisés avec les différentes valeurs de R*. Lorsque la valeur de R* augmente, la limite de fatigue prédite augmente. En ce qui concerne la texture, l'effet de l'orientation du grain est plus élevé lorsque le R* diminue.

V.4. Simulations de fatigue utilisant des modèles avec rugosité et défauts

V.4.1. Modèles avec défauts semi-ellipsoïdaux artificiels

Dans cette partie, des défauts sont ajoutés aux modèles pour prendre en compte les LoF. Ces défauts modélisés par des demi-ellipses construits par rapport au paramètre équivalent de Murakami

Les modèles sont classés par tessellation, chargement (traction ou flexion) et orientation cristallographiques (isotrope ou texturée). Pour chaque configuration, 24 simulations avec différentes réalisations d'orientations cristallographiques sont réalisées. Tous les défauts ont la même taille et la même forme. Ils sont situés en surface et sont éloignés les uns des autres. Nous supposons qu'aucune interaction n'existe entre eux.

La *Figure V-1* montre les distributions la contrainte de Dang Van en utilisant le modèle non local (R*). Les résultats avec une texture isotrope et une autre du type acier SLM sont présentés. On peut constater que les réponses du modèle texturé sont plus élevées que celles du modèle isotrope, ce qui montre un effet de l'orientation des grains. Bien que les points chauds soient toujours dans la racine du défaut, la texture cristallographique modifie la distribution des contraintes de Dang Van.

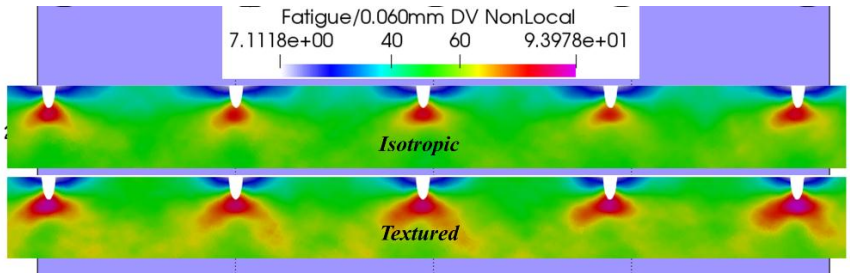

Figure V-1: Distributions of the non-local fatigue indicating parameters (Dang Van (R=60µm)) in non-textured and textured numerical models under tension loading of 100 MPa*

Dans l'étude expérimentale présentée au chapitre III, les échantillons polis soumis à un chargement de flexion ont une limite de fatigue approximative de 138 MPa et les échantillons as-built ont une limite de fatigue d'environ 90 MPa. Les défauts entraînent une diminution de la résistance à la fatigue d'environ 35%. En comparant les résultats de simulation de modèles lisses et de modèles avec défauts, l'influence des défauts peut être révélée. Pour maintenir la cohérence des résultats, R* est égale à 60 µm. Les résultats montrent que les défauts artificiels ajoutés entraînent une diminution d'environ 25% pour toutes les configurations. Compte tenu du nombre limité d'expériences conduisant à une incertitude concernant la limite de fatigue réelle du 316L SLM, la différence entre les expériences et les simulations est acceptable. L'effet de la texture cristallographique peut être mis en évidence en comparant les deux ensembles d'orientation des grains. Les différences sont de l'ordre de 10 MPa. Le mode de chargement ne montre pas de différence significative.

V.4.2. Modèles avec rugosité

L'influence de la rugosité seule est difficile a quantifié expérimentalement. Cette partie vise à en montrer l'influence numériquement.

29 profils de rugosité différents sont utilisés pour créer des surfaces rugueuses. Pour chaque profil est associé à 24 ensembles d'orientations de grains texturer et le chargement est en traction. Différentes valeurs, 15, 30, 45 et 60 µm, sont utilisés pour moyenner la contrainte de Dang Van. Les résultats montent que l'effet de la concentration de contrainte du est accentué avec une faible valeur de R*, et à mesure que le R* augmente, la position critique se déplace de la racine du défaut de surface aux joints de grains. Le changement de position du point critique est dû à la compétition entre la rugosité et la microstructure. Pour ce qui est des orientations cristallographiques, les modèles texturées conduisent à une baisse d'environ 10% de la limite de fatigue par rapport textures isotropes. Concernant les critères de fatigue, les résultats avec un R* de 15 µm montent que la valeur maximale de la contrainte de Dang Van est inférieure à celle de Matake tandis que la contrainte de Papadopoulos est la plus importante. Le critère de Papadopoulos prédit également un plus grand nombre de points critiques comparé aux deux autres.

Les prévisions des 5 profils présentés au début du chapitre sont tracés sur la *Figure V-2*. En comparant les profils sélectionnés, plusieurs résultats peuvent être obtenus. Comme le profil P1 est relativement lisse comparé aux autres, les prédictions sont toujours les plus élevées. Concernant le profil P2 qui correspond le mieux à la rugosité réelle, les prédictions sont toujours intermédiaires. Les profils P4 et P5 ont des Ra identiques. P4 à un Rv élevé, c'est-à-dire une grande profondeur de vallée maximale, tandis que P5 a un Rp élevé, i.e. une grande valeur de crête maximale. Il semble que le défaut concave soit plus nocif que le défaut convexe car les résultats de P4 sont toujours inférieurs à ceux de P5. P3 est un profil sensiblement plus rugueux que les autres. Cependant, les résistances à la fatigue les plus faibles ne sont pas toujours de P3. À l'exception des cas où R* = 60 µm, les prédictions les plus conservatrices sont attribuées à P4. Mais en comparant le Rv (50 µm pour P3 et = 43 µm pour P4), on constate que P3 a une profondeur de vallée maximale plus élevée.

Il semble que les performances de fatigue prévues ne puissent pas être directement liées aux mesures de rugosité. Pour mieux montrer la relation entre les performances de fatigue et la rugosité de surface, les résultats des 24 profils choisis au hasard sont également pris en compte. Sur la *Figure V-3*, les limites de fatigue prédites par rapport à leurs mesures de rugosité correspondantes sont tracées. Chaque point se réfère à la valeur moyenne de 96 microstructures utilisant le même profil de rugosité. Les paramètres de rugosité étudiées sont Ra, Rq, Rv et Rt. Ra et Rq qui décrivent globalement l'état de surface ne présentent pas de corrélation évidente avec les prévisions de limite de fatigue. Rv semble avoir une corrélation négative avec les limites de fatigue prévues. Cependant ce paramètre a ses limites car le point critique ne se situe pas nécessairement au point le plus bas du profile. Rt montre une tendance similaire

avec Rv avec une dispersion plus forte. Comme Rt est la somme de Rv et Rq, on peut penser que Rt et Rv sont étroitement liés.

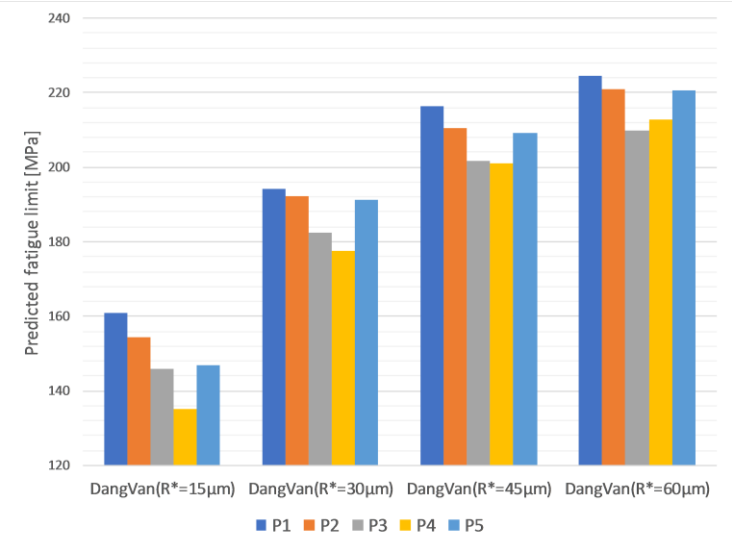

Figure V-2: Medium values of predicted fatigue limits using different non-local FIPs with respect to different roughness profiles

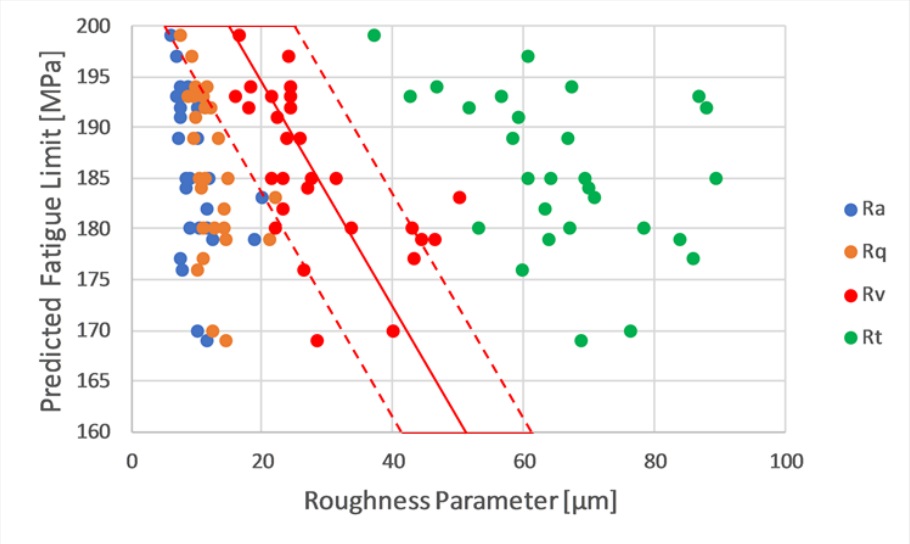

Figure V-3: Predicted fatigue limit of models containing surface roughness versus roughness characteristic parameters

En conclusion, cette étude révèle que les paramètres caractéristiques de la rugosité ont une certaine pertinence avec les performances en fatigue, mais un lien direct entre la résistance à la fatigue et un ou plusieurs paramètres de rugosité est introuvable. La proposition d'un nouveau paramètre caractéristique de rugosité décrivant la fatigue nécessite une étude plus approfondie et sort du cadre du projet actuel. L'approche de simulation construite dans cette étude peut néanmoins être un outil utile pour mener une telle étude.

V.4.3. Modèles contenant défaut artificiel et rugosité

Selon les résultats expérimentaux, l'effet des LoF est supposé être beaucoup plus préjudiciable que l'effet de la rugosité puisqu'un simple polissage n'améliore pas significativement la résistance à la fatigue. Un lot de modèles contenant à la fois des défauts artificiels imitant le défaut LoF et la rugosité est analysé.

La *Figure V-4* montre les distributions de FIP (contrainte de Dang Van) de modèles avec les mêmes configurations de microstructure (morphologie et orientation du grain). Pour mieux prendre en compte l'effet de la rugosité, R* est fixé à 30 µm. Pour le modèle avec rugosité uniquement, la contrainte maximale est située dans la plus grande vallée. Cependant, les défauts génèrent des valeurs FIP beaucoup plus élevées. La valeur maximale de FIP dans le cas avec défaut + rugosité s'avère un peu inférieure à celle avec défaut uniquement, ce qui conduit à une conclusion contre-intuitive que la rugosité peut avoir un effet positif sur la résistance à la fatigue. Quoi qu'il en soit, ce cas de figure rare en raison de la disposition de ces irrégularités dans le profil de rugosité. Généralement, les zones fortement sollicitées sont dominées par les LoF. Les irrégularités dues à la rugosité génèrent des concentrations de contraintes ainsi qu'une diminution des contraintes dans certaines zones. Pour mieux évaluer l'effet apporté par la rugosité sur l'effet de gros défauts, davantage de simulations sont nécessaires.

Des simulations avec des modèles contenant des défauts géométriques avec ou sans rugosité sont effectuées. Le mode de chargement est en flexion. Les orientations réalistes sont utilisées. Les contraintes de Dang Van, évaluées à partir de la méthode R*, sont représentées sur la *Figure V-5*. Premièrement, aucune des microstructures ne montre une différence évidente avec les autres. LN_V1 et LN_V2 sont deux tessellations différentes en termes de positionnement des grains. Mais les résultats des deux modèles sont similaires. Deuxièmement, les comparaisons entre modèles avec ou sans rugosité montrent que dans les configurations testées où le défaut géométrique est important par rapport à la rugosité, la rugosité semble être négligeable. Bien qu'elle ne puisse pas encore être observée par les expériences, la tendance est montrée par des simulations.

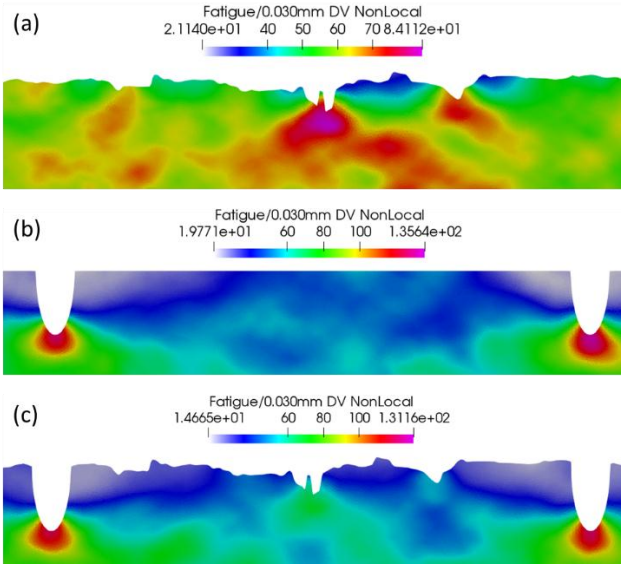

Figure V-4: Distributions of FIP (non-local Dang Van stress with R = 30 µm) of models with the same microstructure configurations (morphology and orientation of grain) but different defect(s): (a) surface roughness, (b) LoF defects, (c) surface roughness + LoF defects*

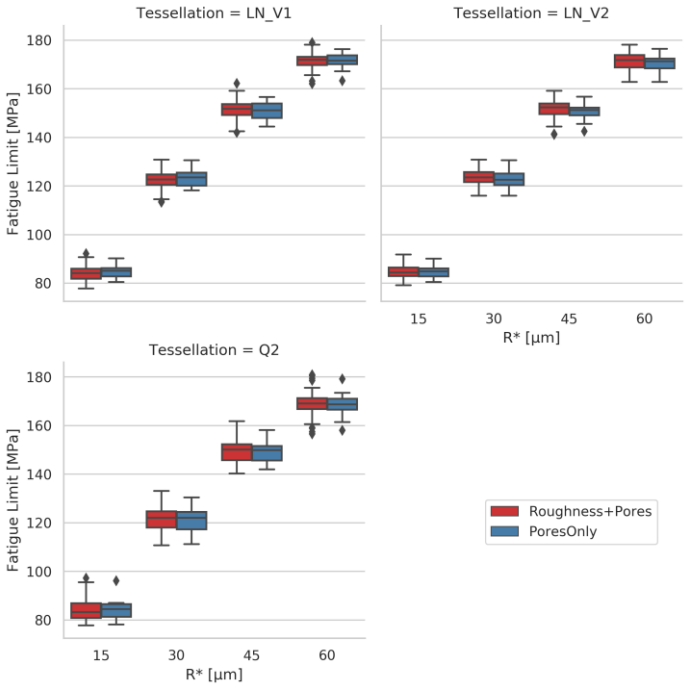

Figure V-5: Predictions of fatigue limit from Dang Van criterion using the critical radius method categorized by the tessellation type

Bien que de nombreuses hypothèses sont faites pour les simulations (transition de la 3D à la 2D, la forme et la disposition des défauts…), les résultats montrent que l'effet sur la résistance à la fatigue de la combinaison de plusieurs gros défauts et une série de petits défauts est principalement contrôlés par les gros défauts.

V.5. Rôle de la plasticité dans la simulation de fatigue

Une étude qualitative du rôle de la plasticité dans les simulations est réalisée dans cette partie. Pour cela, seul certains niveaux de chargements représentatifs sont choisis. Il est cependant important de noter que pour une étude quantitative, des simulations itératives sont nécessaire pour prédire la limite de fatigue avec la prise en compte de la plasticité.

V.5.1. Comparaisons entre les modèles constitutifs élastiques et plastiques dans les modèles lisses

Le modèle lisse avec une texture isotrope est considéré comme un 316L corroyé dont la limite de fatigue a été déterminée dans les recherches de Guerchais. Le niveau de charge de tension est ainsi fixé à 232 MPa. Afin de montrer l'effet de la texture, le modèle lisse texturé est soumis au même chargement. 5 cycles de chargement sont simulés, et les résultats sont post-traiter sur le dernier.

En comparaison avec uniquement un modèle élastique, la plasticité ne présente pas de différence notable dans la distribution de la contrainte équivalente de von Mises, et elle réduit la contrainte équivalente de moins de 20 MPa. Néanmoins, dans certains joints de grains, les différences peuvent atteindre 70 MPa.

Les distributions de la contrainte de Dang Van avec la méthode non locale appliquée sont présentées dans la *Figure V-6*, avec un R* égal à 60 µm. Les deux modèles constitutifs génèrent des résultats très similaires. En comparant les valeurs maximales, la réponse obtenue est de 136 MPa dans le modèle plastique alors qu'elle est de 140 MPa dans le modèle élastique. Le modèle élastique surestime la réponse aux contraintes, mais la différence peut être négligée.

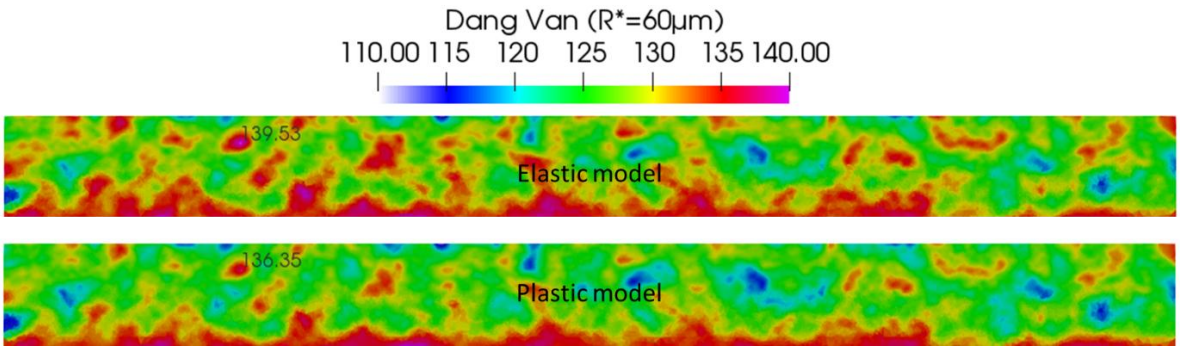

Figure V-6: Distribution of the Dang Van stress (R=60 µm) in smooth polycrystal aggregates using plastic and elastic constitutive models respectively with isotropic texture after a cyclic tension loading at 232 MPa*

Des analyses similaires sont effectuées pour le modèle lisse texturé. La microstructure fortement texturée du 316L SLM entraine un état plus sollicité (160 MPa en élasticité et 150MPa en plasticité). Une diminution de 4,3% de la valeur maximale de la contrainte non locale de Dang Van est observée,

dans le cas d'un comportement élasto-plastique. Pour les deux configurations, les résultats indiquent que la charge actuelle est supérieure à la limite de fatigue. On peut supposer que la limite de fatigue réelle doit être inférieure à 232 MPa.

L'absence de plasticité dans les précédentes simulations de modèles lisses ne change évidemment pas l'analyse des résultats. Cependant, avec la présence de défauts, une concentration de contraintes se produit. Le rôle de la plasticité est ainsi évalué pour les modèles avec défauts dans la section suivante.

V.5.2. Comparaisons entre les prédictions élastiques et plastiques dans les modèles défectueux

Dans les simulations précédentes, trois types de modèles ont été utilisés : avec rugosité, avec défaut artificiel et avec rugosité combinée à un défaut artificiel. Les géométries sont conservées ainsi que les ensembles d'orientation des grains. Trois niveaux de chargement représentant les limites de fatigue des éprouvettes en flexion pour les éprouvettes as-built, avec polissage simple et avec polissage total sont testés : 90, 120 et 150 MPa.

Pour la configuration la plus critique dans laquelle apparaissent à la fois la rugosité et les défauts, la distribution des contraintes non locales de Dang Van est représentée sur la *Figure V-7*. Avec une valeur R* de 60 µm, aucune différence évidente existe entre le modèle plastique et élastique. L'hétérogénéité de la microstructure n'entraîne pas de déformation plastique perceptible. En terme d'isovaleurs, les deux modèles donnent des distributions similaires.

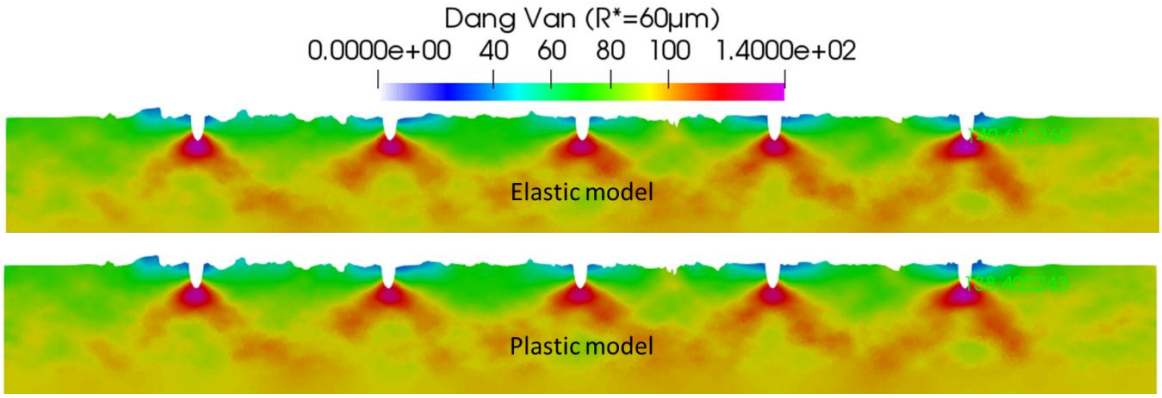

FigureV-7: Distribution of the Dang Van stress (R=60 µm) in defective polycrystal aggregates using plastic and elastic constitutive models respectively with realistic texture after a cyclic tension loading at 150 MPa*

Une comparaison est effectuée pour tous les modèles avec défauts. Dans les trois configurations, les réponses relatives de la prédiction de la fatigue dans le modèle plastique par rapport à celle du modèle élastique sous une charge de tension cyclique à 150 MPa sont répertoriées dans le *Table V-2*. Il convient de noter que certaines données ne sont pas disponibles car le la convergence n'est pas atteinte dans ces configurations.

Table V-2: Predictions from a crystal plasticity model and a purely elastic model under a cyclic tension loading at 150 MPa

		R* (µm)			
		15	30	45	60
Roughness	Dang Van	-	98.8%	99.5%	99.5%
	Matake	83.7%	98.0%	99.3%	99.3%
	Papadopoulos	87.0%	98.9%	99.5%	99.6%
Defect	Dang Van	-	95.3%	97.8%	98.5%
	Matake	-	95.1%	97.1%	98.3%
	Papadopoulos	-	95.6%	97.8%	98.4%
Roughness + Defect	Dang Van	-	94.7%	97.0%	98.4%
	Matake	88.7%	94.5%	96.8%	98.3%
	Papadopoulos	90.6%	95.1%	97.7%	98.9%

La rugosité qui peut être considérée comme une série de petits défauts présente la plus petite différence après l'ajout de plasticité dans la simulation. Néanmoins, même si les grands défauts géométriques sont combinés avec la rugosité de surface, les résultats générés ne changent pas de manière significative. Différents R* sont comparés. Globalement, plus R* augmente, plus la différence entre le modèle plastique et le modèle élastique diminue. Dans l'ensemble, l'effet de la plasticité est négligeable si R* est relativement grand.

Pour les niveaux de chargement inférieurs, des comparaisons similaires sont également effectuées. Comme on pouvait s'y attendre, avec un niveau de charge plus faible, la différence introduite par la plasticité est réduite.

V.6. Conclusion

Une modélisation explicite de la microstructure du 316L SLM est proposée en tenant en compte de la texture et de la morphologie des grains. La rugosité ainsi que les défauts du type LoF sont également pris en compte. Quatre lots de modèles sont étudiés. Pour les modèles avec défauts géométriques (LoF), les résultats sont comparés aux données expérimentales. Les modèles avec rugosité sont fictifs puisque les expériences ont révélé que les défauts LoF dominent l'amorçage de fissure de fatigue et existent également avec la rugosité. En combinant la rugosité et les défauts géométriques, un dernier lot de modèles est utilisé. Il semble que la rugosité n'ait pas influence perceptible sur la résistance à la fatigue. On suppose que l'effet de la texture cristallographique sur le comportement à la fatigue du 316L SLM réduit la limite d'endurance de 10% quelles que soient les valeurs des paramètres du modèle non local. Les résultats concernant l'effet de la morphologie des grains dépendent de la configuration des méthodes non locales. Cependant, cet effet s'avère faible par rapport à d'autres effets tels que la texture ou les défauts. Plusieurs tests préliminaires ont été effectués pour montrer l'effet de la plasticité. Les résultats montrent que la plasticité est négligeable avec notre approche non locale. Par conséquent, pour le

matériau étudié, ne pas tenir compte de la plasticité réduit les coûts de calcul sans perte notable de précision.

Xiaoyu LIANG

High cycle fatigue behavior of additive manufactured stainless steel 316L: free surface effect and microstructural heterogeneity

Résumé

Cette étude vise à étudier l'influence de la microstructure, de la rugosité et des défauts de surface sur le comportement en fatigue à grand nombre de cycles (FGNC) d'un acier inoxydable 316L obtenu par fabrication additive (FA). Composée d'un volet expérimental et d'un volet numérique, elle est motivée par le fait que les matériaux issus du procédé de FA présentent souvent un état de surface et une microstructure très distincte des couples procédés de fabrication / matériaux conventionnels. Afin de clairement identifier le rôle joué par chacun des facteurs influents sur la réponse en fatigue, différentes techniques de caractérisation (Profilométrie, EBSD, Tomographie RX, dureté …) sont employées et permettent de mettre en évidence un niveau de rugosité important après fabrication ainsi que des textures morphologiques et cristallographiques marquées. Pour ce qui est du comportement sous chargement mécanique, des essais cycliques à déformation totale imposée mettent en évidence un écrouissage cyclique avec durcissement puis adoucissement. Une importante campagne d'essais en fatigue est conduite sous différents modes de chargement (traction, flexion, torsion) et pour différentes configurations d'état de surface (brut de fabrication, poli). L'analyse des faciès de rupture fait apparaître le rôle prépondérant joué par les défauts de type « lack of fusion » sur les mécanismes d'amorçage en surface des fissures de fatigue. Un diagramme de type Kitagawa-Takahashi est construit à partir de l'observation de la taille des défauts à l'amorçage et le rôle des amas de défaut est clairement démontré. L'étude numérique comporte deux parties distinctes avec, d'abord, un travail préliminaire relatif à la construction d'une méthode non locale adaptée à la prise en compte des effets de microstructure en fatigue dans le cas d'un acier 316L corroyé. A partir des données collectées lors de la campagne expérimentale portant sur l'acier SLM 316L, un modèle d'éléments finis tenant compte de la rugosité, des défauts et de la microstructure est construit. Les calculs sont conduits en utilisant un comportement de type élasticité cubique associé ou pas à de la plasticité cristalline. À l'aide d'une approche faisant appel à la statistique des extrêmes, les résultats des simulations EF sont analysés de manière à quantifier les effets respectifs de la rugosité de surface, de la taille et morphologie des grains, de la texture cristallographique et des défauts.

Mots clés : Fatigue à grand nombre de cycles, Fabrication additive, Selective Laser Melting, Acier inoxydable 316L, Défaut de surface, Microstructure, Kitagawa-Takahashi, Méthode des éléments finis, Elasticité cubique, Plasticité cristalline, Méthode non locale

Résumé en anglais

This study aims at investigating the influence of both defect and microstructure on the high cycle fatigue (HCF) behavior of a 316L stainless steel obtained by additive manufacturing (AM). Surface defects and microstructure are dominant factors of fatigue behavior, while the AM materials often exhibit distinguished surface state and microstructure compared to conventional materials. The current study begins with an investigation of the material properties that are related to fatigue behavior. Microstructure observations of the powder and fabricated specimens are undertaken. Profilometry and tomography analyses make the inherent defects visible. The hardness, elastic behavior and elastic-plastic behavior are studied via mechanical tests. Then, load-controlled fatigue tests concerning different surface-treated specimens under different loading types are conducted. To reveal the mechanism of fatigue failure in the studied specimens, a comprehensive fractography analysis is carried out. Experimental research reveals the weakening of fatigue strength due to lack-of-fusion defects. Yet, the effect of the microstructural attributes is difficult to evaluate without numerical tools. A preliminary numerical study about the application of the non-local method in an explicit microstructure sensitive model is undertaken to complement the microstructure-sensitive modeling framework. Based on the data collected in the experimental campaign, a finite element model that takes into account the defects and the microstructure of the SLM SS 316L is built up. Finite element analyses are performed with both cubic elasticity and polycrystal plasticity constitutive laws. With the help of the statistical method, the results from the FE model are used to quantitatively assess the influence of surface roughness and microstructural attributes on the fatigue performance of SLM SS 316L.

Keywords: High cycle fatigue, Additive manufacturing, Selective Laser Melting, Stainless steel 316L, Surface defect, Microstructure, Kitagawa-Takahashi effect, Finite element method, Cubic elasticity, Crystal plasticity, Non-local method